Rui Pedro César Marreiros
Mestre em Engenharia de Estruturas

PRECAST CONCRETE WALL-FOUNDATION CONNECTION

Development of a seismic dissipative connection

Dissertação para obtenção do Grau de Doutor em Engenharia Civil, Especialidade Estruturas

Orientador: Válter José da Guia Lúcio,
Professor Associado, FCT/UNL
Co-orientador: Stefano Pampanin,
Associate Professor, UC, Christchurch, NZ

Júri:

Presidente: Prof. Doutor António Manuel Flores Romão de Azevedo Gonçalves Coelho
Arguentes: Prof. Doutor Jorge Miguel Silveira Filipe Mascarenhas Proença
Prof. Doutor Filipe Pimentel Amarante dos Santos

Vogais: Prof. Doutor Válter José da Guia Lúcio
Prof. Doutor António Manuel dos Santos Baptista
Prof. Doutor Carlos Manuel Chastre Rodrigues
Profª. Doutora Ana Rita Faria Conceição de Sousa Gião Gamito Reis

FACULDADE DE CIÊNCIAS E TECNOLOGIA
UNIVERSIDADE NOVA DE LISBOA

Outubro 2014

To my family

Acknowledgments

This dissertation would not have been accomplished without the support of many people who have either helped me to solve problems or encouraged me. For all those people, my most profound thanks. Some of those will be referred to in the following text.

I would like to express my gratitude and recognition to my supervisor, Professor Válter Lúcio, for his guidance and commitment, which allowed me to pursue this quest.

I am truly grateful to my co-supervisor, Professor Stefano Pampanin, for his priceless scientific teaching and invaluable guidance, which have made this experience so meaningful.

I would like to express my immense gratitude to Dr. José Santiago, Eng. Romeu Reguengo and Eng. Pedro Lopes, from Concremat - Prefabricação e Obras Gerais, S.A., for all the support concerning the construction of the concrete specimens.

I would like to thank Eng. Manuel Pipa and Eng. Ana Sofia Louro, who helped me with the experimental tests on the steel angles and generously allowed me to use LNEC's (Laboratório Nacional de Engenharia Civil facilities.

I thank Eng. Carlos Moniz, Eng. Vitor Marchão, Eng. Miguel Coutinho and Eng. Joana Marreiros, from VSL Portugal, for all the help and materials provided.

I kindly acknowledge Eng. André Oliveira for all the help with the equipment in the rocking wall experimental tests.

I would like to show my true appreciation to Professor Ana Brás for helping with the grout testing.

I would also like to thank Eng. Hugo Fernandes, Eng. André Almeida, Eng. Micael Inácio and Eng. David Lucas for the precious help in the laboratory works, namely in the assembly of laboratory tests, as well as to the laboratory technicians José Gaspar and Jorge Silvério.

I would also like to thank Fernando Alves for his support in making the laboratory specimens.

I am also indebted to Professor João Rocha de Almeida and I thank him for his unconditional support. I truly thank Maria da Luz Sousa for the help in overcoming all the bureaucratic issues.

I would like to show my true appreciation to Professor António Pinho Ramos and Professor Carlos Rodrigues for all the help in experimental tests, brainstorming sessions and friendship.

I truly thank Eng. André Barbosa for all the help in finding information, all the things that taught me, all the brainstorming sessions and friendship.

To Professor Luís Neves and Professor Yury Fonseca, a special thanks for the unconditional help in general problem solving. For Eng. Eduardo Cavaco, Professor José Varandas and Professor Filipe Santos a word of appreciation for their availability to help me.

I acknowledge the financial support of FCT/MCTES through the Project PRECA-SEISMIC (PTDC/ECM/116161/2009) and a PhD scholarship (SFRH/BD/46114/2008).

I sincerely thank me colleagues and friends Eng. Carla Marchão and Professor Ana Rita Gião for their support and advice.

I thank my parents and my brother for all their love and everlasting devotion.

Finally, I would like to give a special word to my wife for the unconditional love and patience, and also for the precious reviews of the work. Finally my son, who cost me many hours of sleep at night, but who gave me motivation to keep going.

Abstract

Seismic events are a major factor to consider in structural design of buildings in many countries. With the purpose of saving lives, most of the design codes lead to structural solutions that withstand large seismic actions without collapsing, but without taking into account a possible usage of the structures after the earthquake. As a result, it is necessary to consider the time needed to repair/retrofit the damaged structures (i.e. the downtime) since this period of inactivity may result in huge financial implications for the occupants of the buildings. In order to minimise the damages and simplify repair operations, structural solutions with rocking systems and negligible residual displacements have been developed during the last two decades.

Systems with precast concrete rocking walls were studied with the aim of investigating suitable and convenient structural alternatives to minimise the damage in case of an earthquake. Experimental, numerical and analytical analyses on post-tensioned solutions, with and without energy dissipation devices, were carried out in this research.

The energy dissipation devices were made from steel angles that were further developed during the research. Different solutions for these devices were experimentally tested under cyclic loading and the results are presented. Numerical and analytical work on steel angles was also carried out.

Regarding the concrete rocking wall systems, two concrete rocking wall systems were studied: post-tensioned walls and post-tensioned walls with energy dissipation devices. In the latter, the solution was to fix them externally to the wall, allowing their easy replacement after an earthquake. It is shown that the dissipaters are a viable solution for use in precast concrete rocking wall systems.

A building case study is presented. The comparison between a traditional monolithic system and a hybrid solution was carried out, allowing the evaluation of the efficiency of the solution that was developed.

Keywords

Rocking, Precast Concrete Walls, Wall-Foundation Connection, Seismic Behaviour, Energy Dissipation, Cyclic Test

Resumo

Os fenómenos de carácter sísmico são significativos em muitos países, e um factor importante a considerar no dimensionamento estrutural de edifícios. A maior parte das normas de dimensionamento preconizam soluções que permitem que a estrutura resista à acção sísmica sem colapsar, com a finalidade de salvar vidas. Todavia, a possível utilização da estrutura após o sismo não é, na maioria das vezes, considerada. O tempo necessário para reparação/reforço dos elementos estruturais danificados poderá corresponder a custos financeiros elevados, por interrupção no funcionamento e utilização do edifício. Para minimizar os danos e reduzir as acções de reparação, soluções estruturais com sistemas de *rocking* e deslocamentos residuais desprezáveis têm vindo a ser estudadas e desenvolvidas ao longo das últimas duas décadas.

Com o objectivo de investigar alternativas estruturais adequadas à minimização de danos em caso de sismo, neste trabalho foram estudados sistemas de paredes pré-fabricadas de betão com comportamento de *rocking*. Foram desenvolvidas análises de carácter experimental, numérico e analítico de soluções pós-tensionadas, sem e com dissipadores de energia.

Os dissipadores de energia eleitos para o presente estudo foram cantoneiras de aço. Ao longo do desenvolvimento dos trabalhos, foram utilizadas e testadas experimentalmente várias soluções sujeitas a carregamento cíclico, apresentando-se os resultados obtidos. Foi também desenvolvido trabalho analítico e numérico para estes elementos.

No que concerne às paredes com comportamento de *rocking* foram estudados dois tipos de sistema pós-tensionado: paredes sem e com dissipadores de energia. Neste último, as cantoneiras são fixadas externamente à parede, privilegiando-se a facilidade de substituição após o sismo em caso de necessidade. É demonstrado que os dissipadores de energia se constituem como uma solução viável para utilização em paredes pré-fabricadas com comportamento de *rocking*.

Ainda no contexto do presente traballho, são apresentados os resultados do caso de estudo de um edifício. A avaliação da eficiência da solução desenvolvida foi realizada por comparação da solução híbrida com um sistema monolítico tradicional.

Palavras Chave

Rocking, Paredes de Betão Pré-fabricadas, Ligação Parede-Fundação, Comportamentos Sísmico, Dissipação de Energia, Ensaio Cíclico

Contents

List of Figures

List of Tables

Nomenclature

Capital Roman Letters

A_e area of effectively confined core concrete

A_p area of the post-tensioning steel

A_s area of the reinforcing steel under tension

A_v shear area

A_{cc} area of core within centre lines of perimeter transverse reinforcement excluding area of longitudinal reinforcement

A_g section gross area

A_{shy} total area of transverse reinforcement in the y direction

A_{shz} total area of transverse reinforcement in the z direction

A_{sj} area of the bars in position j

E_c concrete tangent modulus of elasticity at a stress of $\sigma_c = 0$

E_p prestressing steel modulus of elasticity

E_r resin and cork tangent modulus of elasticity at a stress of 10 MPa

E_s steel modulus of elasticity

E_{cm} secant modulus of elasticity of concrete between $\sigma_c = 0$ and $\sigma_c = 0.4f_{cm}$

E_{d1} energy dissipated for positive displacements

E_{d2} energy dissipated for negative displacements

$E_{r,m}$ resin and cork mean value of the tangent modulus of elasticity at a stress of 10 MPa

E_{s1} elastic strain energy for positive displacements

E_{s2} elastic strain energy for negative displacements

E_{sec} secant modulus of elasticity of the concrete

F steel angle force

$F(d)$ total angle force

F_c total concrete compressive force

F_H horizontal force in the angle vertical leg

F_i horizontal force at floor i

F_p force in the post-tensioning bars

F_s tensile force in the reinforcing steel

F_y steel angle yielding force

F_1 force at maximum cycle displacement for positive displacements

F_2 force at minimum cycle displacement for negative displacements

F_{acj} steel angles compressive force in position j

F_{atj} steel angles tensile force in position j

F_{ci} compressive force on the concrete fibre i

F_{geom} geometrically nonlinear angle force

F_{mh} angle force including material hardening

$F_{p,m}$ force installed in the post-tensioning bar m

$F_{p0.1k}$ characteristic 0.1% proof-force of prestressing steel

F_{pi} initial post-tensioning force

F_{scj} steel bars compressive force in position j

F_{sc} total compressive force in the steel bars

F_{stj} steel bars tensile force in position j

F_{st} total tensile forces in the steel bars

G shear modulus

H horizontal actuator's height

h_n height of the roof level

I second moment of area

I_O moment of inertia about the point O

K_e effective stiffness of a SDOF system at the design displacement

M total mass of the block

$M(c)$ bending moment after the yield point

M_a contribution of the steel angles to the bending moment

M_N contribution of the axial load to the bending moment

M_P plastic bending moment

M_s contribution of the steel bars to the bending moment

M_t total section bending moment

M_w wall bending moment demand

M_{atj} contribution of the steel angles in position j to the bending moment

M_p contribution of the post-tensioning bars to the bending moment

M_{stj} contribution of the steel bars j to the bending moment

N_w wall axial load demand

P_{DxDy} average position of the displacement transducers Dx and Dy relatively to the wall southern corner

P_{max} maximum concrete compressive force

R distance between the corner of the block and the centre of gravity

R_a angle fillet radius

S soil factor

$S_e(T)$ elastic acceleration response spectrum

T vibration period of a linear single-degree-of-freedom system

T_B lower limit of the period of the constant spectral acceleration branch

T_C upper limit of the period of the constant spectral acceleration branch

T_D value defining the beginning of the constant displacement response range of the spectrum

T_e effective period of a SDOF system at the design displacement

V base shear

V_B design base shear

V_w wall base shear demand

Small Roman Letters

$\mathrm{d_{max}}$ ultimate steel angle displacement

a constant

a_g design ground acceleration on type A ground

a_{gR} reference peak ground acceleration

b steel angle length

b_w wall width

b_y concrete core dimension to centre line of transverse reinforcement in the y direction

b_z concrete core dimension to centre line of transverse reinforcement in the z direction

c distance between the yield strain and the maximum strain in the section

cc concrete cover

d angle displacement

d_0 bolt hole diameter

d_a distance between the centroid of the tensile steel angles and the most compressed concrete fibre

d_{aj} distance from the steel angles j to the most compressed concrete fibre

d_{bl} diameter of the reinforcing bar

d_{ci} distance from the concrete fibre i to the most compressed concrete fibre

d_{el} steel angle elastic displacement

d_p distance between the centroid of the post-tensioning bars and the most compressed concrete fibre

d_{sj} distance from the bars j to the most compressed concrete fibre

d_{xy} absolute distance between displacement transducers Dx and Dy

f_y steel yield strength

$f_{cm,cubes}$ mean concrete compressive strength in cubes

$f_{cm,c}$ compressive strength of confined concrete

f_{cmax} maximum concrete compressive stress

f_{cm} mean value of concrete cylinder compressive strength

f_{ly} effective lateral confining stress in the y direction

f_{lz} effective lateral confining stress in the z direction

$f_{p0.1k}$ characteristic 0.1% proof-stress of prestressing steel

f_{p0} initial prestressing stress

f_{pk} characteristic tensile strength of prestressing steel

f_{sh} transverse reinforcement stress

f_t ultimate tensile strength of the reinforcing steel

f_{yd} design yield strength of the reinforcing steel

f_{yh} transverse reinforcement yield stress

f_y steel yield stress

g distance between the inner part of the vertical leg and the centre of the bolts holes in the horizontal leg

g_1 distance between the inner part of the horizontal leg and the centre of the bolts holes in the vertical leg

h_e effective height of a SDOF system

h_i height of floor i

k material hardening factor

k_c concrete strength enhancement factor

k_e confinement effectiveness coefficient

l_w wall length

l_{cant} length until the point of contraflexure (cantilever length)

l_p plastic hinge length

l_{sp} strain penetration length

l_{ub} post-tensioning unbonded length

m mass per unit area of the block

m_e effective mass of a SDOF system

m_i mass of floor i

r impact reduction of energy ratio

s longitudinal spacing between transverse reinforcement

s' clear longitudinal spacing between transverse reinforcement

t steel angle thickness

t_{washer} washer plate thickness

w'_i i^{th} clear transversal spacing between longitudinal reinforcement

x neutral axis depth

x_{cg} distance from the resultant compressive force to the most compressed concrete fibre

z lever arm between the tensile and compressive forces

z_a lever arm between angles tensile force and compression forces

z_j position coordinate in z axis

Capital Greek Letters

Δ displacement

Δ_d substitute structure design displacement

Δ_i displacement of floor i

Δ_p plastic displacement

Δ_r residual displacement

Δ_1 maximum cycle displacement for positive displacements

Δ_2 minimum cycle displacement for negative displacements

Δ_{σ_p} stress variation in the post-tensioning bars

Δ_{F_p} force variation in the post-tensioning bars

Δ_{mon} displacement in the equivalent monolithic element

Δ_{yi} displacement of floor i at yield

Θ angle horizontal leg rotation

Small Greek Letters

α angle that the line R makes with the vertical

α_{OTM} post-tensioning force and axial load moment ratio

β_{OTM} energy dissipaters moment ratio

δ_{DxDy} average displacement measured by the displacement transducers Dx and Dy

δ_{Dx} displacement measured by displacement transducer Dx

η damping correction factor

μ_{δ} displacement ductility factor

ϕ section curvature

ϕ_p section plastic curvature

ϕ_u ultimate curvature

ϕ_y yield curvature

ϕ_{dec} curvature at the decompression point

ψ_2 factor for quasi-permanent value of a variable action

ρ_{cc} ratio between the longitudinal reinforcement area to and the section core area

ρ_v ratio between the transverse reinforcement area and the section core area

ρ_y ratio between the transverse reinforcement area and the section core area in the y direction

ρ_z ratio between the transverse reinforcement area and the section core area in the z direction

$\sigma(\varepsilon_{max})$ stress at the fibre with the maximum strain

σ_c compressive concrete stress

$\sigma_{c1.5\%}$ 1.5% proof-stress of the resin and cork

σ_{cc} compressive concrete stress including confinement

$\sigma_{cm1.5\%}$ mean value of the 1.5% proof-stress of the resin and cork

σ_{max} maximum steel tensile stress

σ_{sj} steel bars stress in position j

$\sigma_{t,max}$ maximum tensile stress from the bending test

$\sigma_{t,m}$ mean of the maximum tensile stresses from the bending test

θ base rotation

θ_p plastic hinge rotation

θ_{yn} roof level drift at yield

ε_y steel yield strain

ε_{acj} steel angles strain in position j

ε_{c1} compressive strain in unconfined concrete at the peak stress

ε_{cc} strain corresponding to confined concrete compressive strength

$\varepsilon_{cu,c}$ ultimate confined concrete compressive strain

ε_{cu1} ultimate compressive strain in the unconfined concrete

ε_{max} steel strain at maximum tensile stress

ε_{sj} steel bars strain in position j

ε_{su} ultimate tensile steel strain

ξ_{eq} equivalent viscous damping ratio

Abbreviations

$DDBD$ Direct Displacement-Based Design

$EC1$ Eurocode 1

$EC2$ Eurocode 2

$EC3$ Eurocode 3

$EC8$ Eurocode 8

FRP Fiber Reinforced Polymer

$LNEC$ Laboratório Nacional de Engenharia Civil

$MDOF$ Multi-Degree-Of-Freedom

$SDOF$ Single-Degree-Of-Freedom

ULS Ultimate Limit States

CAM Active Confinement of Masonry

CCC Crushing of Confined Concrete

CF Coulomb Friction

DBD Displacement-Based Design

DEC DECompression at the base of the wall

DIS-CAM DISsipative Active Confinement of Masonry

ELL Elastic Limit of the Linear-elastic response of the wall

FBD Force-Based Design

GLULAM GLUe LAMinated timber

LLP Linear Limit of Proportionality of the prestress steel

LNEC Laboratório Nacional de Engenharia Civil

LVL Laminated Veneer Lumber

NIST National Institute of Standards and Technology

NLE NonLinear Elastic

PRES-LAM PREStressed LAMinated

PRESSS PREcast Seismic Structural Systems

SY Shear Yield

TCY Tension-Compression Yield

Chapter 1

Introduction

1.1 Background and motivation

Earthquakes are events that can lead to chaotic situations. The conception and design of structures to resist a major earthquake is mostly done to avoid collapse and save lives without taking into account the structural damage and a possible usage after the earthquake. The main exceptions to this design philosophy are important structures, such as hospitals or important bridges. This approach has been changing, as the costs associated with the period of inactivity may result in huge financial implications for the occupants of the buildings. As a result, structural systems with reduced level of damage and negligible residual displacements (recentring) have been developed. Within these types of systems are the precast concrete dry connections with controlled rocking, which started to be studied in a research cooperation between the United States of America (USA) and Japan, the PREcast Seismic Structural Systems (PRESSS) research program (Priestley et al., 1999), in the 1990s. Since then, many studies have been carried out, essentially in the USA (e.g., Kurama (1997), Perez (2004), Smith (2012), Belleri et al. (2014), Christopoulos et al. (2002b), Christopoulos et al. (2002a), Rojas et al. (2005), Lin et al. (2013), Ricles et al. (2001), Ricles et al. (2002), Garlock et al. (2005), Garlock et al. (2007), Kurama et al. (2006), Weldon and Kurama (2010) and Shen (2006)) and New Zealand (e.g., Holden et al. (2003), Restrepo and Rahman (2007), Marriott (2009), Palermo et al. (2005), Palermo et al. (2006b), Palermo et al. (2006a), Iqbal et al. (2007), Smith et al. (2007), Iqbal et al. (2008), Iqbal et al. (2010) and Smith et al. (2014)).

A connection with controlled rocking concentrates the nonlinear response in the joint between the elements of the structure. The rocking means that the joints are designed to open and close between the two elements. To be able to recentre, these connections are built with unbonded post-tensioned tendons which should remain elastic and ensure that the gap closes. If the connection is made using only post-tensioning to connect the

elements, a nonlinear elastic response is expected. To achieve a structural response including damping, energy dissipaters can be added to the system, resulting in a hybrid system (Stanton et al. (1997), fib (2003)). When a structure is constructed using these systems, instead of the multiple plastic hinges, there will be multiple gap openings controlled by the post-tensioning. This leads to structures with controlled damage and reduced repair costs.

In the final phase of the PRESSS program, a 60% scale building with five floors was tested using frame and wall systems developed in the program. Both systems provided excellent performance. Since then, the PRESSS technology has been used in several buildings world-wide. In California, an apartment building with 39 floors, the Paramount, used precast hybrid frames (Englekirk, 2002). In New Zealand, two more examples can be mentioned, a teaching and research building of the Victoria University in Wellington (Cattanach and Pampanin (2008) and NZCS (2010)) and a medical building in Christchurch (NZCS, 2010). Other on site applications can be found in Italy and in the Dominican Republic (Marriott, 2009). There are also some design provisions that take into account these systems in the USA (ACI-T1.2-03, 2003) and New Zealand (NZS3101, 2006).

The initial hybrid systems consist of dry joints with unbonded post-tensioned tendons and steel reinforcing bars (energy dissipaters) with an unbonded length. The post-tensioned tendons were designed to remain elastic, but the steel reinforcing bars were designed to go beyond the yield stress and dissipate energy. As a result, the steel reinforcing bars should be replaced after an earthquake. This operation is very difficult if the bars are placed inside the concrete structure. To overcome this problem, replaceable external dissipater solutions have been studied (Marriott (2009), [Kurama et al. (2006), Weldon and Kurama (2010) and Smith et al. (2014)).

1.2 Objectives

The objective of this dissertation is to develop replaceable external energy dissipaters and apply them to precast concrete rocking walls. For this study, experimental and numerical tests were carried out.

Energy dissipater devices made from steel angles were studied. The requirement is to sustain cyclic actions with stable hysteretic behaviour. The strength and ductility of the devices are also important if they are to be used in precast concrete walls. For this reason, an estimation of the maximum displacement and the required force is made to design the steel angles properly. An important requirement of these devices is that they should be easily replaceable, which means that the connections have to be designed taking this into account.

In this dissertation precast rocking walls with and without energy dissipaters were experimentally and numerically analysed. In both solutions low damage and negligible residual displacements were expected. In the hybrid system the damage was expected to be confined to the energy dissipater devices. The post-tensioning shall be in elastic range within the design drift to maintain its recentring capacity.

A design example using the developed hybrid structural solution is presented. This design uses the displacement-based design method to estimate the seismic displacements and forces acting in the structure. The objective was to evaluate the efficiency of the system under development using a comparison with a traditional monolithic system. It is also important to discuss the design method, as the design of these systems depend on the estimation of the displacements.

1.3 Dissertation organisation

The dissertation is composed of the following six chapters, including the present one:

Chapter 2 presents a general view of the present state of the art of the dissertation subject. The solutions developed during the PRESSS research program on wall and frame structures and the evolution since then are the main focus of the chapter. In this program several rocking systems were developed and tested and a large 5 storey structure tested to validate the research. After this large program, the chapter focus on the research done essentially in the United States of America and New Zealand, places where this subject has mostly been studied. A brief summary on rocking motion and the related damping is also shown. A main subject of this chapter is the state of the art on steel angles used for connections, especially when used as dissipation devices. Finally, an integration of the studied systems with the demand performance of the structures and the seismic actions is made.

Chapter 3 focus on the experimental, numerical and analytical work done to develop and design the energy dissipaters made from steel angle. Special importance was given to a good cyclic behaviour of the energy dissipaters with the aim of applying them to hybrid rocking walls. Five experimental specimens are presented, in which the first three do not present the desired cyclic behaviour and the last two achieve the desired response. A numerical study with finite elements is shown using 2D solid elements to model the steel angles. The models presented here are calibrated using the experimental specimens and then a parametric study is presented to extrapolate the results for specimens with other dimensions. In the analytical work expressions to estimate the energy dissipaters force as a function of the displacement are deduced for elastic and plastic ranges, taking into account physical and geometrical nonlinearity.

In Chapter 4 the precast concrete rocking wall solutions are shown. A total of six wall specimens are presented. Three preliminary post-tensioned rocking walls, with the purpose of evaluating the experimental difficulties and optimising the experimental setup, are presented. The first two specimens have no energy dissipation devices while in the third specimen, wedges made of resin and cork are included for that purpose. The fourth and fifth specimens are post-tensioned walls with energy dissipation devices. The development of these devices is shown in Chapter 3. The final specimen is a post-tensioned wall without energy dissipaters. To complement the experimental work, numerical models are presented and the results are compared with the experimental ones.

In Chapter 5 the developed system is applied to a case study. A 6 storey precast concrete residential building with 21 x 14 m2 floor plan dimensions is used to exemplify the use and design of structures with the solution being developed. A comparison between a traditional monolithic system and a hybrid solution is made to evaluate the efficiency of the solution that was developed. To calculate the seismic forces, direct displacement-based design was used.

Chapter 6 presents the main conclusions of the dissertation, a synthesis of the design proposals as well as suggestions for future researches on this dissertation scope.

Chapter 2

Literature review

2.1 PRESSS program

In the 1990s, from a research cooperation between the USA and Japan, a PREcast Seismic Structural Systems (PRESSS) research program was developed. During this program precast structural systems were developed and tested to enhance the behaviour of the concrete precast structures in seismic zones. Design recommendations were part of the scope of this program. This work had the contribution of over a dozen different research teams across the United States of America (Nakaki et al., 1999), with the coordination carried out by Professor Nigel Priestley, University of California at San Diego.

When the PRESSS program started, the solutions for reinforced concrete precast structures were mainly though to emulate the cast in place reinforced concrete, which is still the main option in most places nowadays. That design option guaranties a good behaviour of the reinforced concrete precast structures in seismic zones but discards some advantages that can be found in precast structures. When an emulative solution is the alternative to a cast in place reinforced concrete, the main advantages of the precast are the speed of construction and a better quality control. For both design solutions, significative structural damage is expected with formation of plastic hinges in critical regions. This damage can imply a downtime with huge indirect costs. To mitigate this consequence one of the main goals of the PRESSS program was to develop solutions with minimal residual damage and that were easy to repair after an earthquake.

This project had three phases. According to Priestley (1996), Phase I consisted of concept development, connection classification and modelling, analytical platform development, preliminary design recommendations and research coordination, and was completed in 1993. Phase II consisted of experimental testing and analytical work of precast connection systems and also the development of design procedures for precast buildings

in seismic zones. Phase III was centred on using the systems developed in the former two phases in two large scale tests, one using frame systems and another one using wall systems. From this last phase, design recommendations were proposed.

In Phase II, four generic types of connection systems were considered with the following designations: nonlinear elastic (NLE) connection systems; tension-compression yield (TCY) connection systems; shear yield (SY) connection systems and coulomb friction (CF) connection systems. The main goal of Phase II was to study the viability of these systems (Priestley, 1996).

These systems have a rocking behaviour. This characteristic means that the joints are made to open and close a gap (also referred to as a "crack") between two elements. To explain this behaviour a rigid block oscillating between two corners can be imagined. If the block is not rigid, it will not be supported only in the corner but there will be an area under compression where the contact will be made between the two elements. For example, in a beam-column joint (see Figure 2.1), if a precast column and a precast beam are to be connected using only interior unbonded prestress, the build sequence can be to put the beam in contact with the column and clamp one against the other using post-tensioning. During a cyclic horizontal displacement action, this joint will open and close for both sides, stretching the unbonded tendons inside each time the gap opens. The post-tensioning force will ensure that the gap closes every time.

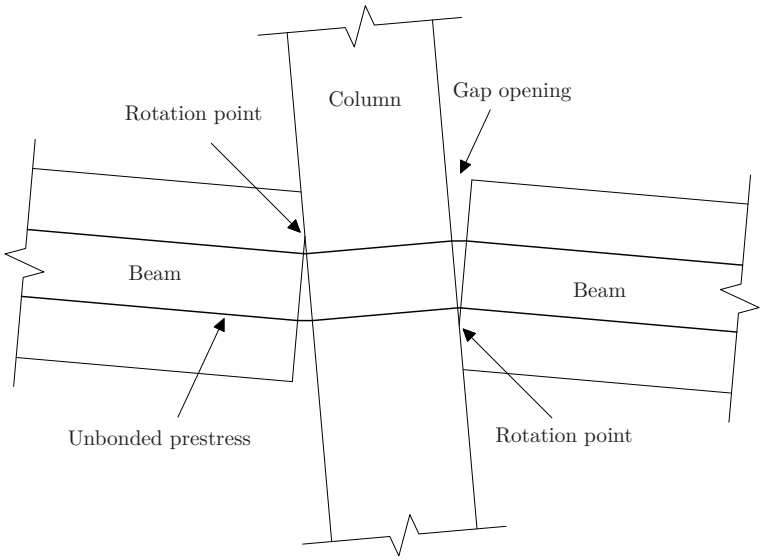

Figure 2.1: Beam-column joint rocking behaviour.

These rocking systems without any dissipation devices are the NLE systems and exhibit reduced residual displacements after an earthquake and a nonlinear behaviour due to rocking. These systems were developed with unbonded prestress that should remain elastic during an earthquake. The opening of a gap will elongate the tendons, resulting in an increase of tension in them. A high initial stiffness of the connection after an earthquake is

expected. The opening and closing of the gap on the connection will result in a nonlinear elastic behaviour. The expected equivalent viscous damping ξ_{eq} is between 5% and 10% (see Figure 2.2b), slightly higher than the 2-5% expected for a linear elastic system (see Figure 2.2a), which means that the advantages of recentring and high initial stiffness after the earthquake have to be balanced against the reduced equivalent viscous damping.

The TCY systems have a similar response to the monolithic reinforced concrete connections. These systems are designed to have steel yielding under tension and under compression during the push and pull of the seismic action. The expected ξ_{eq} is between 25% and 35% (see Figure 2.2c). The advantage of these systems is the high energy dissipation capacity, whilst the disadvantages are the expected residual displacements and the loss of initial stiffness after an earthquake.

A way to overcome the weaknesses of these two systems is to combine both in a hybrid system. The solution of simultaneously using both systems is to balance the strengths of each one to have as much energy dissipation as possible with minor residual displacements. The result expected for ξ_{eq} is between 10% and 25% (see Figure 2.2d). In a hybrid system the NLE, with unbonded prestress and/or other axial loads, is responsible for the reduced residual displacements and high initial stiffness after an earthquake. The TCY is responsible for most of the energy dissipation and for most of the residual displacements that the system may have after an earthquake. In this system the elements should act as rigid bodies, concentrating the deformations at the joints. The hysteretic behaviour of this system is called "flag-shape" because of the shape of the diagram. Hybrid connections were tested at the National Institute of Standards and Technology (NIST) in one-third scale specimens. Details of this work can be found in Stanton et al. (1997).

The SY systems are activated by shear and can be used, for example, with vertical joints between panels of shear walls. The expected energy dissipation is similar to TCY systems.

The CF systems are based on friction sliding and can be considered rigid-perfectly plastic, corresponding to an expected ξ_{eq} of 64% (see Figure 2.2e). This systems can be combined with linear elastic systems resulting in a ξ_{eq} of between 10% and 60% (see Figure 2.2f).

In Phase II several connections were developed according to the generic types already referred to above. Experimental tests and analytical simulations were carried out. Most of the work done in this phase will be summarised below.

Priestley and Tao (1993) developed a theoretical study of the seismic response for a NLE beam-column joint system. Figure 2.3 shows the generic joint with partially unbonded tendons studied. To allow a relative rotation between the beam and the column (opening of a gap) without yielding the tendons, the unbonded length needs to be large

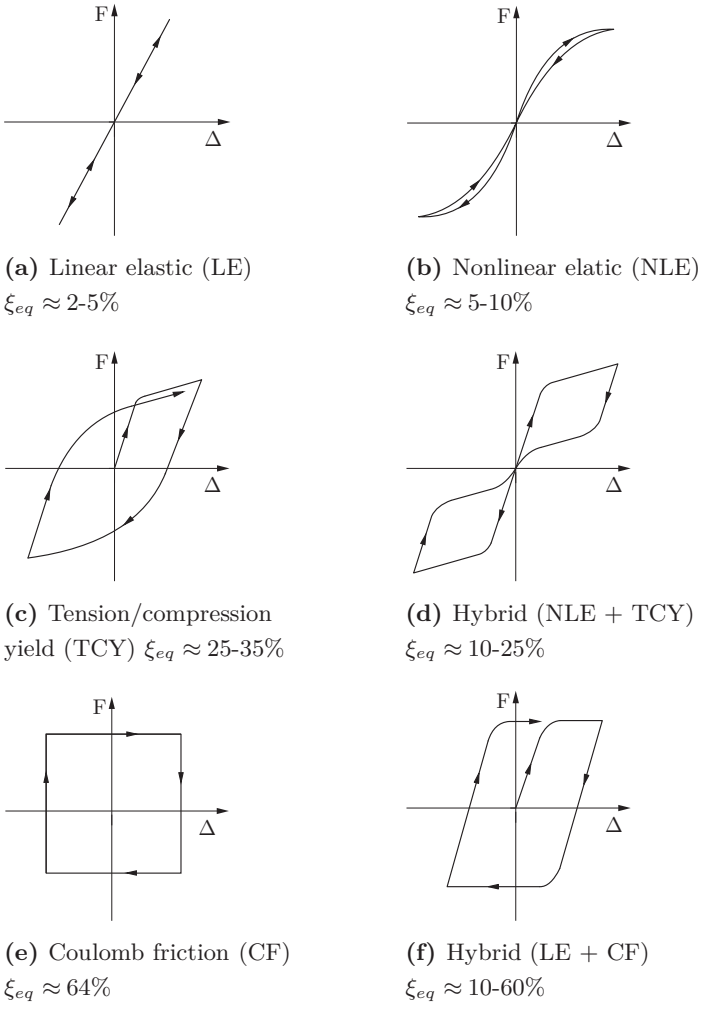

(a) Linear elastic (LE)
$\xi_{eq} \approx$ 2-5%

(b) Nonlinear elatic (NLE)
$\xi_{eq} \approx$ 5-10%

(c) Tension/compression yield (TCY) $\xi_{eq} \approx$ 25-35%

(d) Hybrid (NLE + TCY)
$\xi_{eq} \approx$ 10-25%

(e) Coulomb friction (CF)
$\xi_{eq} \approx$ 64%

(f) Hybrid (LE + CF)
$\xi_{eq} \approx$ 10-60%

Figure 2.2: Hysteretic characteristics for generic PRESSS connection systems (adapted from Priestley (1996)).

enough for the tendons to accommodate the elongation. As a result the prestress will not be lost during the cycles and a constant shear strength due to friction is expected. Another characteristic of the system is the simplicity of the design of the joint, since the horizontal shear forces are transferred by a diagonal strut, as no force is transferred by bond action (Figure 2.4). When a structure reaches large drifts, the rotation on the connection tends to be large as well, leading to concentrated compressions in small areas at the bottom and top of the beams, causing high strains that can degrade the concrete. As a result, the bottom and top of the beam may need special confinement for the concrete. In this numerical study, confinement spirals were considered as in Figure 2.5. Dynamic time history analyses with single degree of freedom models were carried out resulting in a minor hysteretic energy dissipation and a peak displacement slightly higher than was expected for an equivalent monolithic reinforced concrete system. This difference in displacements was expected to be larger, as the unbonded prestress systems have no energy dissipation.

To explain this fact, Priestley and MacRae (1996) pointed to the less efficient loops of the reinforced concrete plastic hinges when compared with an ideal elasto-plastic system, leading to a higher vibration period of the equivalent monolithic reinforced concrete structure. Having two structures with a similar vibration period, one with unbonded prestress and other with an equivalent monolithic reinforced concrete system, the less efficient loops of the reinforced concrete plastic hinges will force the vibration period to grow as well as the displacements in this system.

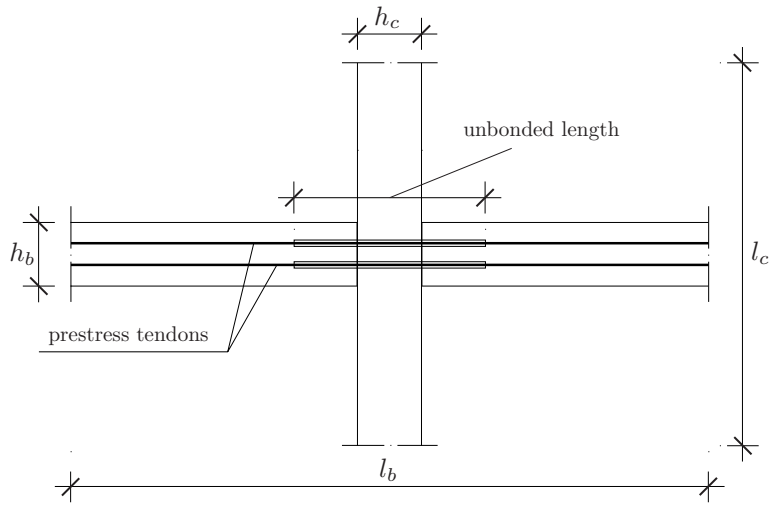

Figure 2.3: Beam-column joint with partially unbonded tendons (adapted from Priestley and Tao (1993)).

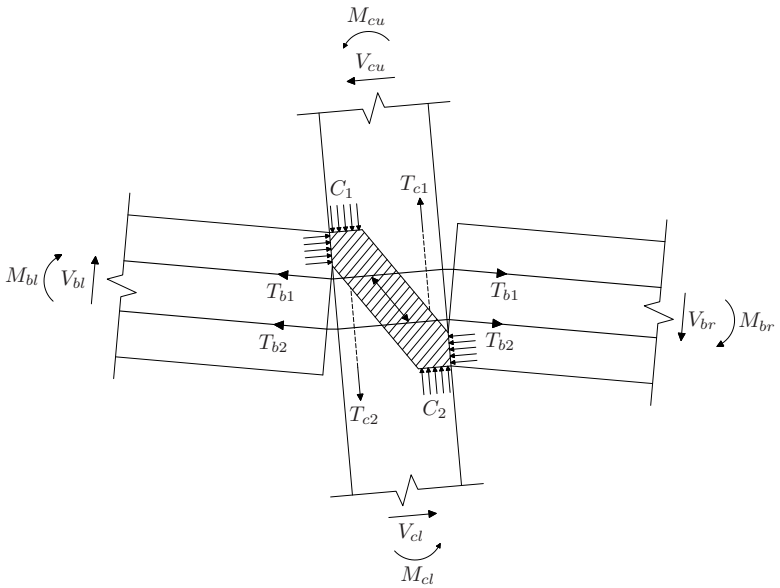

Figure 2.4: Forces contributing to joint shears on beam-column joint with partially debonded prestress (adapted from Priestley and MacRae (1996)).

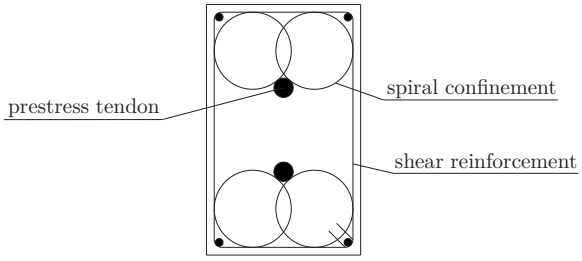

Figure 2.5: Spiral confinement on a beam near the column (adapted from Priestley and Tao (1993)).

Beam-column joints were tested at the University of Minnesota and at the University of Texas, Austin. The tests were made with half-scale specimens, four of them with TCY systems, one with CF system and three with NLE systems. At the University of Minnesota the specimens tested were two with NLE systems and two with TCY systems. The two NLE tests were one using unbonded Dywidag bars crossing the joint and another one with monostrands, the design and detailing was made according to Priestley and Tao (1993). In the two TCY units, one had a gap connection system (Figure 2.6), whilst the other had block-outs (to be cast in place) through the beams and embedded corrugated pipes in the column for the reinforcement. At the University of Texas, Austin, the specimens tested were one with NLE system, two with TCY systems and one with CF. In the NLE specimen, the beam was precast in one piece with pretensioned strands, before being connected to the column. The two TYC systems tested differed in that one had a gap between the column and beam (Figure 2.7), whilst the other had an increased beam depth to accommodate the high strength thread bars used to connect the beams to the column. The CF system was a friction system where a brass plate was used between all the sliding surfaces. All the NLE systems were designed to have no yielding of the prestress within the design drift ratio, ensuring the recentring capability with small energy dissipation. This was not achieved with the unit tested at University of Minnesota with monostrands that had a strand failure for the design drift ratio. As expected, the CF was the system that proved to be more capable of dissipating energy. The units that performed worst where the unit with the beam depth variation tested at the University of Texas, Austin and the gap unit tested at the University of Minnesota. These units did not performed well for design drifts of 3.0%. The second had a bar failure at 2.0% and the first suffered crushing of the concrete in the area of the beams with increased depth. In the gap connection systems tested, the lower edge of the beam cross section acts as a pivot, whilst the gap in the upper part of the beam opens and closes during a cyclic action. This system can be used to protect a floor, if the pivot is located in the upper part of the beam. More details of these tests can be found in Palmieri et al. (1996) and Priestley (1996).

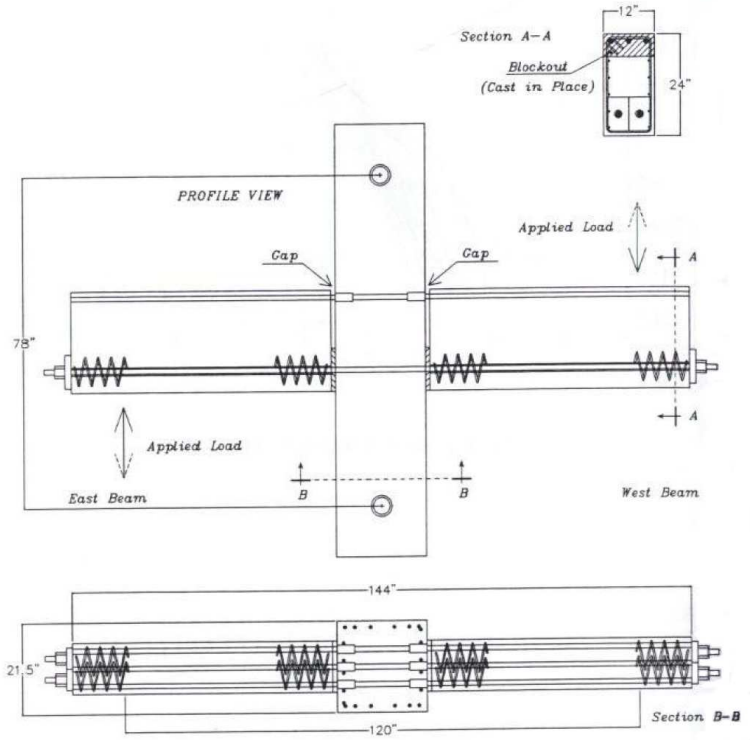

Figure 2.6: Gap joint from the University of Minnesota (extracted from Palmieri et al. (1996)).

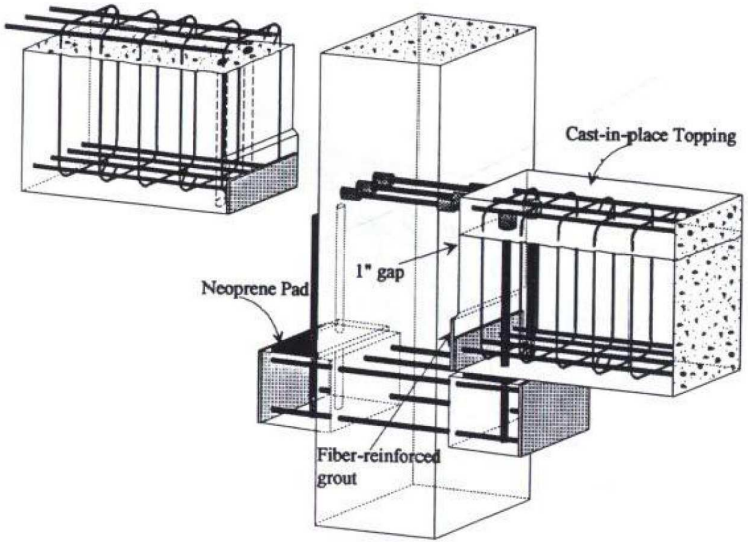

Figure 2.7: Gap joint from the University of Texas at Austin (extracted from Palmieri et al. (1996)).

Beam-column joints were also tested at the University of California at San Diego. Precast joints were tested with unbonded prestressing tendons. The specimens were designed for a precast building constructed with a seismic frame on the perimeter. These

seismic frame had single bay precast beams, connected with unbonded post-tensioned tendons for the full length of the building and multi-storey columns. Priestley and MacRae (1996) report the tests on an interior and an exterior joint. In these tests little energy was dissipated, as expected from a NLE system, and it showed very good shear behaviour with reduced shear reinforcement compared with equivalent monolithic joints. Figure 2.8a shows the minor degradation of the joint after a 2.8% drift ratio and in Figure 2.8b the self centring capacity of the joint during the test. Another important conclusion was that the stiffness decreased during the tests, but it still remained much higher than what would have been expected for an equivalent monolithic reinforced concrete system (Priestley and MacRae, 1996). For example, for one interior connection, the stiffness at a drift ratio of 2%, that corresponded to the design drift, was 35% of the initial stiffness.

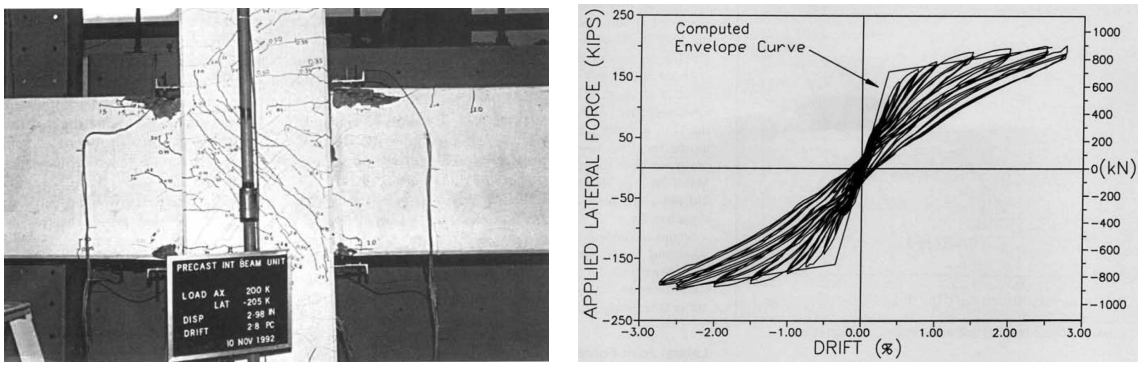

(a) Crack pattern **(b)** Lateral force-displacement response

Figure 2.8: Beam-column interior joint at maximum tested drift ratio of 2.8% (extracted from Priestley and MacRae (1996)).

At NIST, connections for vertical and horizontal joints between precast shear walls were tested. In this study, the generic TCY, SY and CF systems were used to connect and dissipate energy in the joints. Figures 2.9 and 2.10 show tested welded and bolted connections, respectively. According to Priestley (1996), the connections using a brass friction device and a U-shaped flexure plate presented the most reliable response.

During Phase II new materials were also studied. High performance fiber reinforced concrete (FRC) was used in the University of Michigan to improve the beam-column joint.

The development of design procedures was took two different directions. The first was to develop design recommendations for the already existing reinforced concrete systems. The second was to develop a displacement-based design (DBD) procedure for precast seismic systems. The need for this alternative design procedure was related to the inadequacy of force-based design (FBD) procedures to deal with the energy dissipation characteristics and yielding displacement of these systems, since FBD assume an elasto-plastic behaviour (Priestley, 1996).

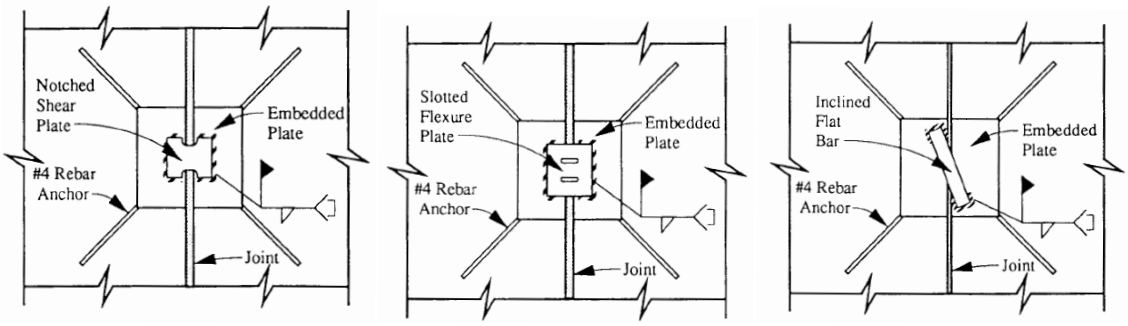

(a) Notched Shear Plate **(b)** Slotted Flexure Plate **(c)** Inclined Flat Bar

Figure 2.9: Welded connections for precast shear wall joints tested at NIST (extracted from Schultz et al. (1994)).

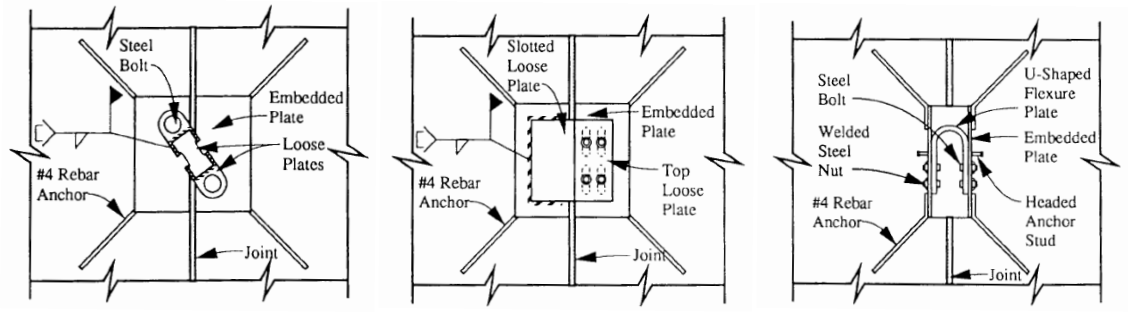

(a) Pinned Tension Strut **(b)** Brass Friction Device **(c)** U-Shaped Flexure Plate

Figure 2.10: Bolted connections for precast shear wall joints tested at NIST (extracted from Schultz et al. (1994)).

The Phase III of the PRESSS program consisted of validating the technology developed in the former Phases I and II by building and testing two large scale structural systems, a precast frame system and a precast shear wall system. According to Priestley (1996) the work would consist of design studies, analytical studies, a large scale test and final design recommendations for each building. The structure built was a 60% scale building with five floors, having four different frame systems in one direction and a jointed shear wall system in the other direction (see Figure 2.11). The floor systems were pretopped double tees for the bottom three floors and topped hollow-core slabs for the top two floors. In Figure 2.12 a plan view of the floor is shown, where the two seismic frame systems in the x direction can be seen, one with prestress (hybrid frame) and the other without prestress (TCY gap frame), and a seismic jointed wall system and two gravity frame systems in the y direction. The design of the building was made using Direct Displacement-Based Design, as Force-Based Design is not suitable for this type of structure, as mentioned above. To evaluate the seismic behaviour of the structure a pseudo-dynamic test procedure was adopted to simulate the action of an earthquake. Cyclic testing using a force vector in the form of an inverted triangle was also applied to complement the tests. The test was carried out at

the Charles Lee Power Structural Laboratory of the University of California, San Diego (Priestley et al. (1999) and Nakaki et al. (1999).

Figure 2.11: General view of the test building (extracted from Conley et al. (2002)).

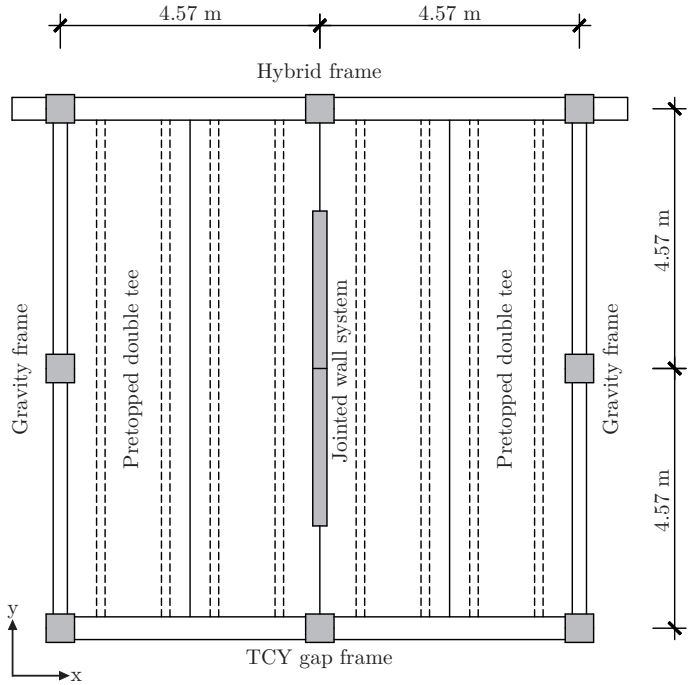

Figure 2.12: Plan view of test building showing lower three floors (adapted from Priestley et al. (1999)).

The four chosen frame systems included in the test were a TCY gap, a TCY, a hybrid and a pretensioned. The TCY systems were in the same frame, the TCY gap for the first three floors and the TCY for the top two floors. The construction method was multi-storey columns with single-bay beams. The frame using prestress was built with hybrid connections for the first three floors and pretension on the top two floors. The hybrid connections were constructed using the same method as the TCY connections. The pretensioned beams were multi-bay, while the columns were single-storey (Priestley et al., 1999).

The jointed wall system is shown in Figure 2.13a and was a hybrid system using vertical prestress bars to recentre and maintain a high stiffness at the end of each cycle and U-shaped plates (see Figure 2.13b) to dissipate energy until the 2.0% design drift ratio was reached. The vertical joint used the U-Shaped connection developed at NIST (see Figure 2.10c) and the horizontal joints were prestressed with unbonded bars, that were coupled with bar connectors in the horizontal joints. The jointed wall panels when horizontally pushed or pulled will lift (rocking), resulting in the elongation of the prestress bars and in the deformation of the U-Shaped Plates due to the relative vertical displacement between adjacent panels (see Figure 2.13b). More details of this building can be founded in Priestley et al. (1999), Nakaki et al. (1999) and Conley et al. (2002).

(a) Shear wall system (extracted from NZCS (2010).

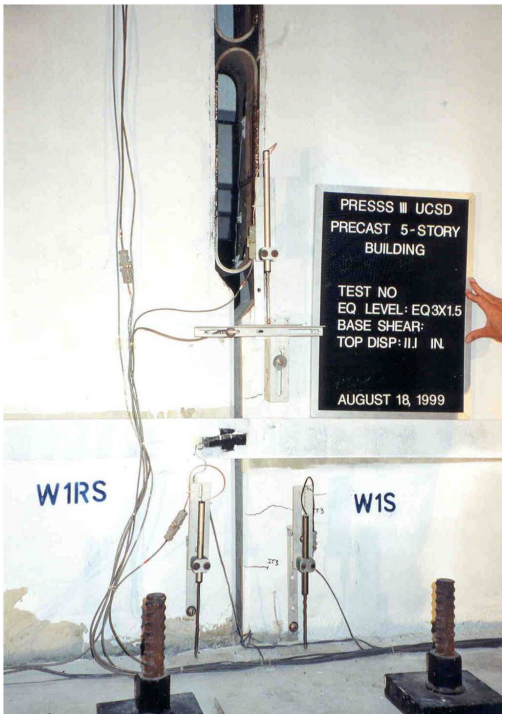

(b) Deformed U-shaped flexure plate (extracted from Conley et al. (2002)).

Figure 2.13: Jointed shear wall system tested in PRESSS program .

The seismic behaviour of the large test building was good. The 2.0% design drift ratio was reached with minor damage in both directions. The overall damage was much less than the expected for an equivalent monolithic reinforced concrete structure. The jointed wall suffered minor spalling at the base and fine cracking of floor slabs. The frame systems performed very well, although the TCY gap was the system that performed the worst and was most damaged. This problem with the TCY gap connection could be solved by using a higher post tension clamping force in the bottom of the connection and an improved detailing to avoid premature spalling of the concrete cover. In the frame direction the drift ratio reached 4.5% with minor loss of strength. In the wall direction the test ended when the forces acting in the precast reaction wall exceeded the maximum safety values. Every system with unbonded prestress resulted in very low residual drift ratios, resulting in low overall residual drifts in both directions, which were higher in the frame direction. It should be noted that the x direction (Figure 2.12) had a frame with unbonded prestress and another without prestress. This last one suffered a higher residual drift ratio and higher level of damage (Priestley et al., 1999).

With regards to the design, the displacement-based design predicted accurately the structure behaviour. When compared with force-based design, the strength needed for the shear base was only 40% and 60% of the correspondent calculated by conventional force-based design for wall and frame directions, respectively (Priestley et al., 1999).

Since the PRESSS program began, the PRESSS technology as been evolving and some real applications have been made. In San Francisco, California, the Paramount, a 39 storey-high reinforced concrete apartment building (see Figure 2.14a) was designed. It was constructed using a shear wall system and a precast and cast in place moment frame bracing system below the eighth floor and perimeter seismic frames above the eighth floor. The seismic frame systems used were a precast hybrid moment resistance frame and a Dywidag ductile connector system that is shown in Figure 2.14b (Englekirk, 2002). The approach was also used in New Zealand, where a building was built with more recent PRESSS technology. Figure 2.15 shows that external energy dissipaters were used instead of the usual internal mild steel energy dissipaters. The major advantage of using external dissipaters is the quickness of the inspection and eventual replacement after an earthquake, resulting in minor downtime and mitigating the associated costs (Cattanach and Pampanin (2008) and NZCS (2010)).

(a) View of Paramount building (extracted from Wikipedia (2013))

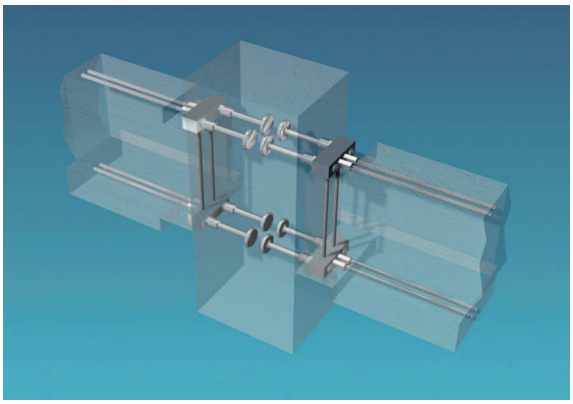

(b) Dywidag ductile connector (extracted from Dywidag (2014))

Figure 2.14: Paramount building in San Francisco, California (Englekirk, 2002).

(a) Column with external dissipaters

(b) Beam-column joint with external dissipaters

Figure 2.15: Two applications of external dissipaters on the first multi-storey PRESSS building constructed in New Zealand (Cattanach and Pampanin (2008) and NZCS (2010)).

2.2 Walls with rocking system

During the PRESSS program, a coupled wall was used in the large scale test described in Section 2.1. In that structure, the coupled wall was vertically prestressed to the foundation with unbonded bars and coupled with U-shaped plates in the vertical joint between adjacent panels. Other studies have been made on precast reinforced concrete walls with PRESSS technology. Most of the research has been carried out in the United States of America and in New Zealand.

Quasi-static tests

At the University of Canterbury, New Zealand, five half-scale walls (1350x125x4000 mm^3) were tested. The tests were cyclic and the horizontal actuator was located 3.75 m above the base of the walls. Restrepo and Rahman (2007) describe the first three rocking walls tested. The first wall was designed using only prestress (Unit 1R), the second with prestress and internal mild steel as energy dissipaters (Unit 2R) and the third with prestress, energy dissipaters and a gravity load of 200 kN (Unit 3R). The prestress and the gravity loads are restoring forces that contribute to the recentring of the wall. The energy dissipaters used in Units 2R and 3R were mild steel dissipaters crossing the joint with a dogbone shape to concentrate the non linear behaviour on a specific unbonded length (see Figure 2.16d). The hysteretic response of these walls is shown in Figures 2.16a, 2.16b and 2.16c. In terms of damping Unit 1R dissipated a negligible amount of energy; Units 2R and 3R presented a "flag-shape" hysteretic diagram with a ξ_{eq} of 14%. There were some losses of prestress recorded at the end of the tests, Unit 2R reached 12% loss and Unit 3 19.3% loss. The structural damage of the walls was minimal and was due to compression near the edge of the walls as can be seen in the Figures 2.16a, 2.16b and 2.16c. The three walls had a good recentring behaviour.

Holden et al. (2001) and Holden et al. (2003) describe the other two of the five referred walls, the Units 1H and 2H (see Figure 2.17a). The first was designed to emulate a cast in place reinforced concrete wall (Unit 1H) and the other to be similar to Unit 3R but prestressed with carbon fibers instead of steel tendons and cast with a steel fiber reinforced concrete for crack control (Unit 2H). Units 3R, 1H and 2H were designed for the same forces, but due to a scaling problem with the reinforcement of Unit 1H, this one was built 30% stronger than the others (Restrepo et al. (2001)). The hysteretic response diagrams are shown in Figures 2.17b and 2.17c. The Unit 2H had a push-out failure on the dissipater bars, which affected the results, achieving very small ξ_{eq} values. At 2.5% drift ratio Unit 1H responded with a ξ_{eq} of 23.5% while Unit 2H with approximately 5.0%. Apart from the dissipater failure on Unit 2H, the two walls had a good behaviour, the Unit 1H reached 2.5% drift ratio without losing strength and the Unit 2H reached 3.0% with minor damage.

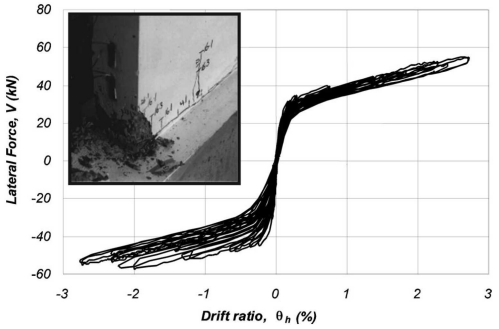

(a) Unit R1 only with prestress

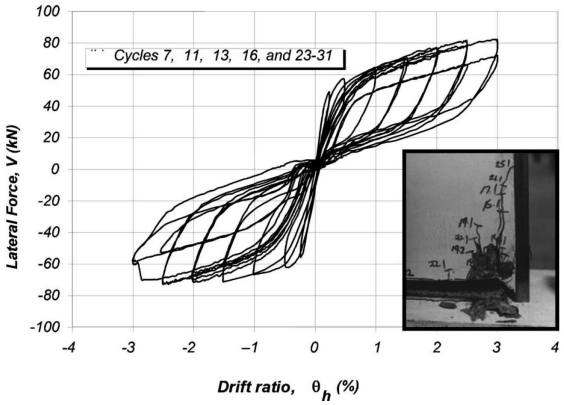

(b) Unit R2 with prestress and dissipaters

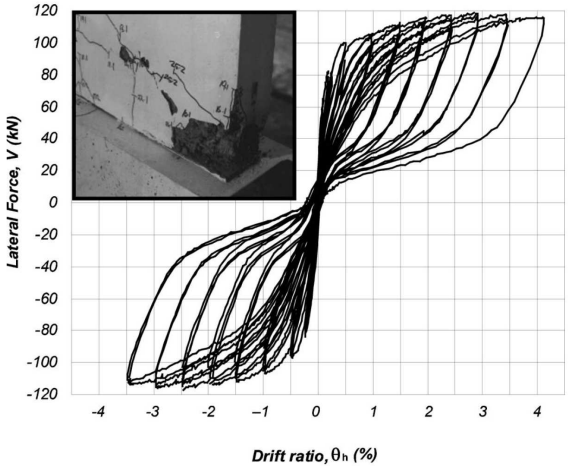

(c) Unit R3 with prestress, dissipaters and 200 kN of gravity load

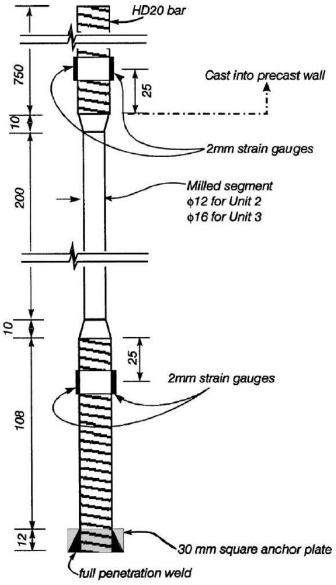

(d) Dissipater used in Units R2 and R3

Figure 2.16: Hysteretic response of three walls tested by Restrepo and Rahman (2007).

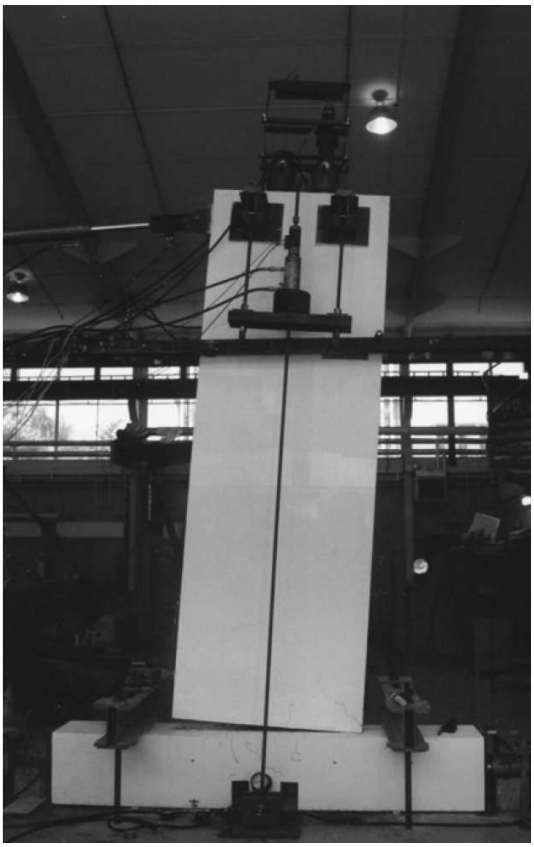

(a) View of unit 2H during the cyclic test

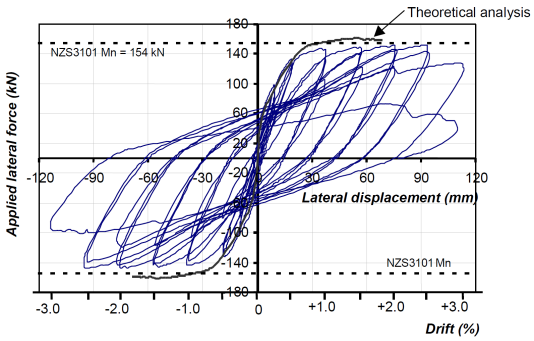

(b) Hysteretic response of Unit 1H

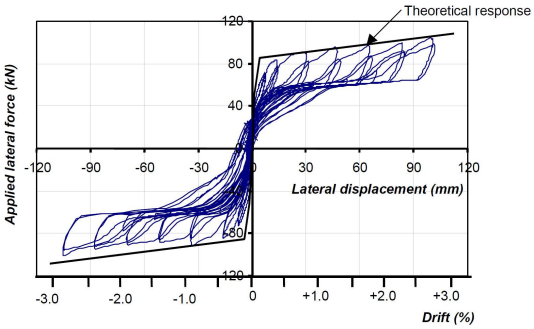

(c) Hysteretic response of Unit 2H

Figure 2.17: Hysteretic response of two walls tested by Holden et al. (2003) (extracted from Holden et al. (2001).

A sequence of studies on post-tensioned rocking walls was carried out by Kurama (1997), Perez (2004) and Smith (2012). In the first study, numerical models were developed and the design of prototype walls was made. In the second study, large-scale post-tensioned wall specimens were tested. The post-tensioning force was applied using high strength steel bars. In the third study, hybrid walls with and without openings were tested. The post-tensioning force was applied using strands.

Shaking table tests

More recently, dissipation devices have been tested on the outside of the structures to facilitate their inspection during the life-time of the structure, or their eventual replacement after a major earthquake or even a possible retrofit. The building in New Zealand mentioned above (see Figure 2.15) is a good example of an application of the technique in a new structure.

In the scope of a PhD work developed at the University of Canterbury, New Zealand, external dissipaters were used in LVL (laminated veneer lumber) and concrete post-tensioned rocking walls (Marriott, 2009). Both walls were tested on a shaking table. In the case of the LVL walls, the action was a high-speed cyclic action and consisted of applying different sinusoidal displacements. In the case of the concrete walls, the action was dynamic and consisted of applying different recorded earthquake ground motions scaled to satisfy the New Zealand seismic design spectrum. The concrete walls were connected at the top to a concrete mass of 3840 kg. For both wall types, five combinations of viscous and hysteretic damping were used. Figure 2.18 shows two concrete walls, one using four viscous dampers and the other using four viscous dampers and two mild steel hysteretic dampers. Free vibration tests were also carried out using the concrete specimens and based on these tests, it was possible to evaluate the contact damping for a post-tensioned wall without dissipaters where a mean value of ξ=2.4% was reached (Marriott, 2009).

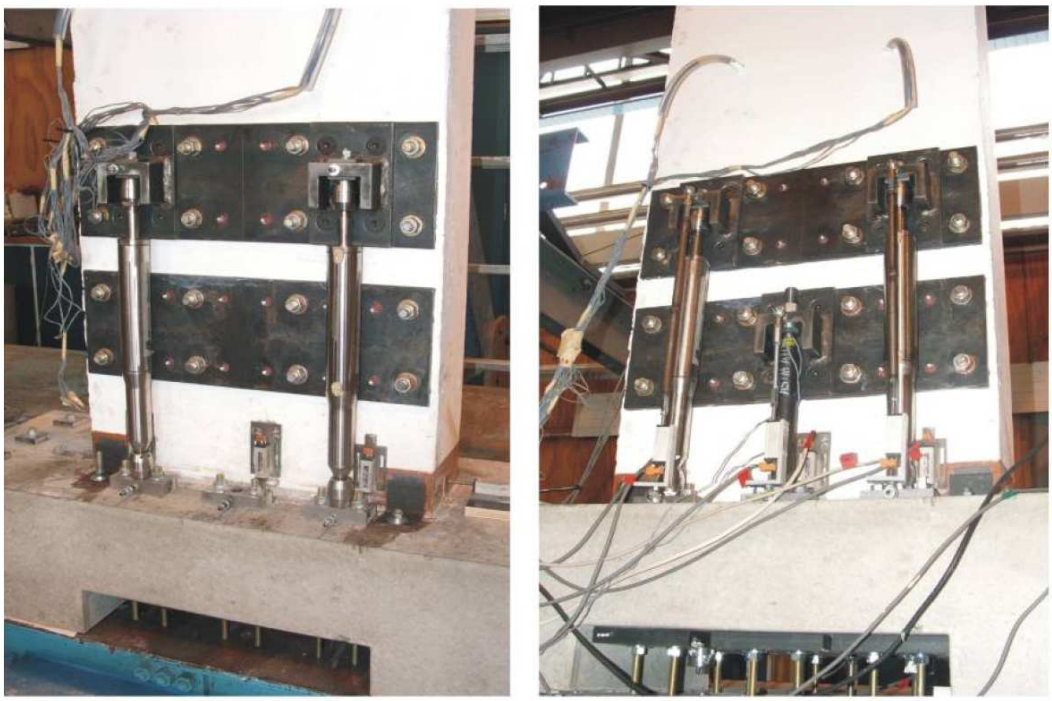

Figure 2.18: Walls tested with different external dampers solutions. Left: Four external TCY mild steel dampers, Right: Four external TCY dissipaters and two viscous dampers (adapted from Marriott et al. (2008).

The mild steel and the viscous dampers were used together with the purpose of having devices to respond to displacements and to velocity inputs, respectively. Using only viscous dampers resulted in a low energy dissipation capacity, but the dampers were affected by a lack of efficiency, due to tolerances in the connections, that resulted in pinching. The test using the viscous dampers was compromised by the limit of the velocity of the

shaking table (Marriott et al., 2008). Combining viscous dampers with mild steel was considered a good solution for resisting different earthquake actions. Another advantage is that without velocity the viscous dampers respond with zero force, meaning that they do not contribute to residual displacements, thus the recentring capacity of the system results from the balance between the moment of the post-tensioning and the hysteretic dissipaters (Marriott, 2009).

In the NEES (Network for Earthquake Engineering Simulation) large high-performance outdoor shaking table at the Englekirk Structural Engineering Research Centre, University of California, a three-storey precast structure at half-scale was tested. The plan dimensions of the structure were 17.07×4.88 m^2. The walls had a cross section of 2.44×0.20 m^2 and a total height of 7.01 m. The structural vertical elements were two precast walls to resist the seismic actions and ten columns to resist the gravity loads. The three floors had different precast systems, the first one had a field-topped double tee system, the second one a field-topped hollowcore system and the third one a pretopped double tee system. The building is shown in Figure 2.19 and the seismic action was applied in the direction of the precast rocking wall. The ground motions used for testing were from regions of low, moderate and high seismic hazard in the United States of America. For the low seismic hazard earthquakes the wall did not have active energy dissipaters, meaning that the wall was designed to have the same elastic response as a post-tensioned rocking wall. For the other dynamic actions the energy dissipaters that were located inside the wall were active and the wall was a hybrid wall with an expected flag shaped hysteretic response. The floors were connected to the walls in a way that only horizontal shear was transmitted to allow relative vertical displacements without restrictions (Belleri et al. (2014) and Schoettler et al. (2009)).

Belleri et al. (2014) considered the response of the structure as consistent with expectations, however an unpredicted response was also observed. For the low seismic hazard actions the response was as desired and no damage was observed. For the moderate seismic hazard a diaphragm tension chord failed in three tests, although the fourth was a successful test. No cracks were observed at this point. For the high seismic hazard, two levels of earthquakes were used, a design level ground motion and a maximum considered earthquake. For the design level ground motion, a strand failed for an average stress corresponding to 45% of the nominal ultimate tensile strength. This failure lead to a 10% loss of the post-tensioning force and compromised the subsequent tests. In the subsequent test, for the maximum considered earthquake, a complete failure of the tendons was reached in both walls, resulting in uncontrolled rocking of the walls, failure of the columns-foundation connections bolts and impact of the structure with the restraint towers. This failure resulted in the recommendation to grout the strand duct ends after post-tensioning, to be able to reach the ultimate capacity of the tendons. After this failure, the structure was repaired and more tests were carried out. Another conclusion was that the wall base shear

demand and resistance were affected by the dynamic wall-building interaction. The timing of the closure of the gap was considered more critical for the base shear than the timing of the maximum gap opening. The vertical and horizontal accelerations amplify the base shear and the yielding of the energy dissipaters under compression reduces the base shear capacity (Belleri et al. (2014) and Schoettler et al. (2009)).

Figure 2.19: 3-floor high shaking table test of precast building at university of California, San Diego (extracted from Schoettler et al. (2009)).

2.3 Damping of rocking motion

Figure 2.20 shows a block rotated about one corner (point O) to analyse the behaviour of a rocking block. If the block is rotated with an angle θ and released, it will rotate backwards about the point O until the vertical position is reached and, after impact, will continue rotating about the point O'. Assuming an inelastic impact (no bouncing) and that the angular momentum about the point O' is conserved, Housner (1963) presented the equation 2.1 to calculate the relation between the kinetic energy before and after the impact. This ratio corresponds to a relative loss of energy, as in the impact instant there is only kinetic energy. Housner (1963) concluded that this energy loss changes the vibration period of the rocking system during the motion.

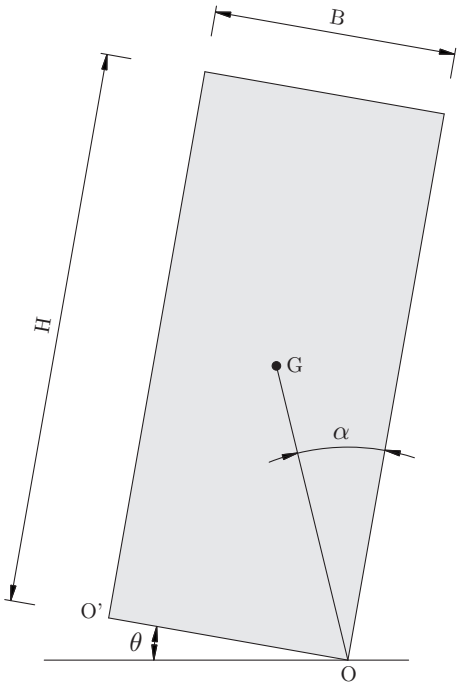

Figure 2.20: Rocking block (adapted from Housner (1963).

$$r = \left[1 - \frac{MR^2}{I_O}(1 - cos(2\alpha))\right]^2 \tag{2.1}$$

$$I_O = m\left(\frac{BH^3}{12} + \frac{B^3H}{12}\right) + MR^2 \tag{2.2}$$

where,

r is the impact reduction of energy ratio;
I_O is the moment of inertia about the point O, obtained by equation 2.2;
α is the angle that the line R makes with the vertical;
R is the distance between the corner of the block and the centre of gravity;
m is the mass per unit area of the block;
M is the total mass of the block.

The parameter r was also named apparent coefficient of restitution by Ma (2010). The Table 2.1 was adapted from Ma (2010), where the theoretical results calculated with equation 2.1 are compared with experimental studies made by several authors. The table shows a generally good agreement between theoretical and experimental, but most of the experimental values exceeded the theoretical ones, suggesting that the actual energy dissipation tends to be smaller that the one assumed by the equation 2.1. The bigger differences correspond to the less slender specimens. In addition to the materials and the slenderness of the specimens, Ma (2010) concluded that the energy dissipated by impact

also depends on the angular impact speed, whilst having no apparent relationship with the impact force.

Table 2.1: Comparison of experimental and theoretical apparent coefficient of restitution values (adapted from Ma (2010)).

Block dimension		Material at the contact	r	
H × B	H/B	interface (model/base)	Experimental	Theoretical
200 × 100 mm^2 [a]	2	Wood / steel	0.624	0.490
300 × 100 mm^2 [a]	3	Wood / steel	0.774	0.723
400 × 100 mm^2 [a]	4	Wood / steel	0.884	0.831
1000 × 250 mm^2 [b]	4	Granite / granite	0.876	0.831
762 × 152 mm^2 [c]	5	Aluminium / steel	0.856	0.888
950 × 190 mm^2 [d]	5	Steel / concrete	0.844	0.888
1000 × 167 mm^2 [b]	6	Granite / granite	0.946	0.921
1000 × 125 mm^2 [b]	8	Granite / granite	0.956	0.954
900 × 190 mm^2 [e]	4.9	Steel / concrete	0.720-0.970	0.890

[a] Ogawa (1977); [b] Peña et al. (2007); [c] Aslam et al. (1980); [d] ElGawady et al. (2006); [e] Ma (2010).

Based on Priestley et al. (1978), Ma (2010) presented equation 2.3 to relate the equivalent viscous damping to the apparent coefficient of restitution. Using this equation, the mentioned ξ_{eq}=2.4% obtained by (Marriott, 2009) for a post-tensioned wall would correspond to an apparent coefficient of restitution of r=0.932, in other words 6.8% of energy would have been lost due to impact.

$$\xi_{eq} = -0.34\, ln(r) \tag{2.3}$$

2.4 Connections using steel angles

2.4.1 Rigid, semi-rigid and flexible steel frames

Steel angles are structural elements that are frequently used in steel construction for beam-column joints or column-foundation joints. The angles can be used on the beam or column flanges to contribute to the bending capacity or in the web to contribute to the shear capacity, however in both cases bending moment and shear forces are resisted.

A joint may be classified as rigid, semi-rigid or flexible according to its rotational stiffness. Typically, when the angles are welded it is considered as rigid, when the top and seat steel angles are bolted the joint is considered semi-rigid and when the bolted steel angles are used in the web the joint is considered to be flexible.

Astaneh et al. (1989) presented an experimental study on the cyclic behaviour of double angle connections. The solution was to use two angles, one on each side of the web, welded to the beam web and bolted to the column flange. They used two types of bolts, structural ribbed bolts from an existing building and high strength bolts. The ribbed bolts did not performed as desired, having failed and the high strength bolts performed satisfactorily and in a ductile way. In these tests, two types of failure modes were observed, the failure of the bolts, which is never to be desired and fracture of the angles in the zone adjacent to their fillets.

To compare structures with rigid, semi-rigid and flexible connections, a one-storey, one-bay structure was constructed to evaluate the dynamic behaviour of different solutions in shaking table tests (Nader and Astaneh-Asl (1991) and Nader and Astaneh-Asl (1996). Figure 2.21 shows the steel structure mounted on the shaking table. The flexible connections were obtained using double angles fixed to the web of the beam. A semi-rigid connection can be seen in Figure 2.22a which had double angles bolted to the web plus bolted top and seat angles. The rigid connections were made using a double angle solution in the web, with the angles welded to the beam web and the top and bottom flanges welded to the column (Figure 2.22b). The main objective of this work was to study other alternatives to the rigid connections that the author considered as being the most used connection type at that time.

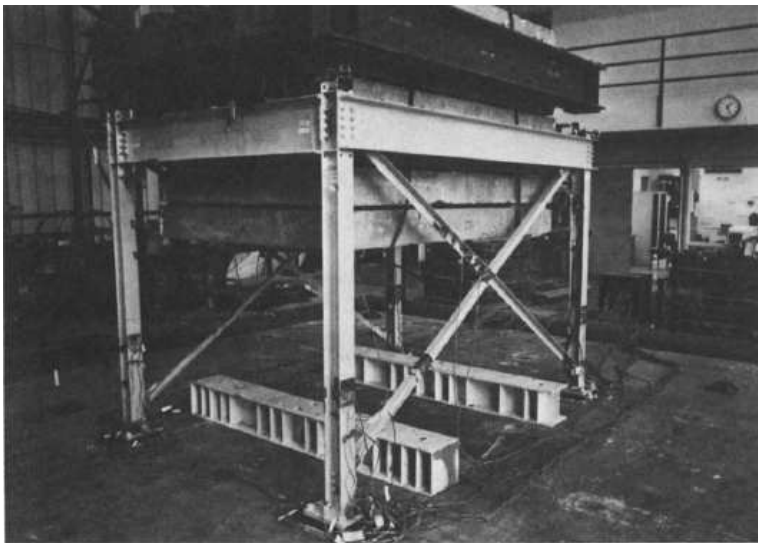

Figure 2.21: Steel structure on the shaking table (extracted from Nader and Astaneh-Asl (1991)).

The authors concluded that the semi-rigid connections do not result in larger lateral displacements or in more damage than the rigid solutions. It was also concluded that a well designed semi-rigid connection with ductile behaviour can make a positive contribution to the nonlinear behaviour of the structure, resulting in a more ductile structure. The authors refer that the semi-rigid connections had a response similar to the rigid connections for low

and moderate earthquake levels. For more severe earthquakes, the semi-rigid connections reached large rotations with minimal damage due to the top and seat angles yielding and the slippage of the bolts. It was mentioned that even the flexible connections solution have potential to resist a earthquake. In the semi-rigid connections, the plastic bending moment capacity was approximately twice that of the authors expectations, meaning that the nonlinear response of the steel angles used on top and bottom flanges needed more study (Nader and Astaneh-Asl (1991) and Nader and Astaneh-Asl (1996).

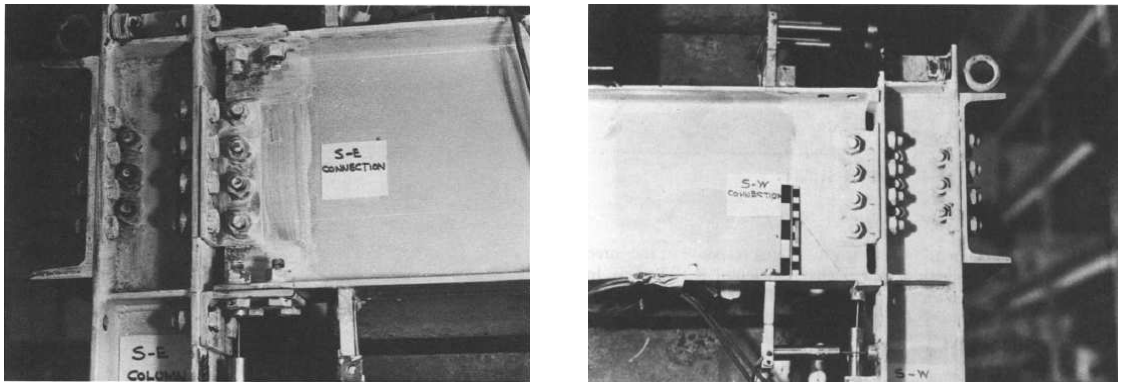

(a) Semi-rigid joint. **(b)** Rigid joint.

Figure 2.22: Steel connections tested on the shaking table (extracted from Nader and Astaneh-Asl (1991)).

Following on from the previous studies, Shen and Astaneh-Asl (1999) investigated the response of steel angles by testing 8 specimens. Figure 2.23 shows the authors intention of simulating the actions on the top and seat steel angles with cyclic tension and compression. The main objectives of the work were to study the hysteretic behaviour, the nonlinear inelastic patterns and failure modes, the energy dissipation capacity and to compare monotonic and cyclic behaviour.

In the tests described by Shen and Astaneh-Asl (1999), the deformation patterns and failure modes of the specimens depended mostly on the relative strength between the angle and the bolts. Two different deformation patterns and four failure modes are shown in Figure 2.24. Deformation pattern 1 was the result of having relatively strong bolts and deformation pattern 2 because of the relatively strong angles. In deformation pattern 1 the steel angle edge presented plastic deformation, leading to no prying resistance. This phenomenon resulted in a reduced stiffness at the beginning of the following cycles. In pattern 2 the bolts reached the plastic range, leading to a pinching in the hysteretic diagram. The comparison between cyclic and monotonic loading was made by having two equal specimens that deformed according to the deformation pattern 1 and the other two equal specimens according to deformation pattern 2. In the first comparison the monotonic specimen presented 30% more strength and ductility, but in the comparison for the specimens with deformation pattern 2 there was no significant difference between monotonic

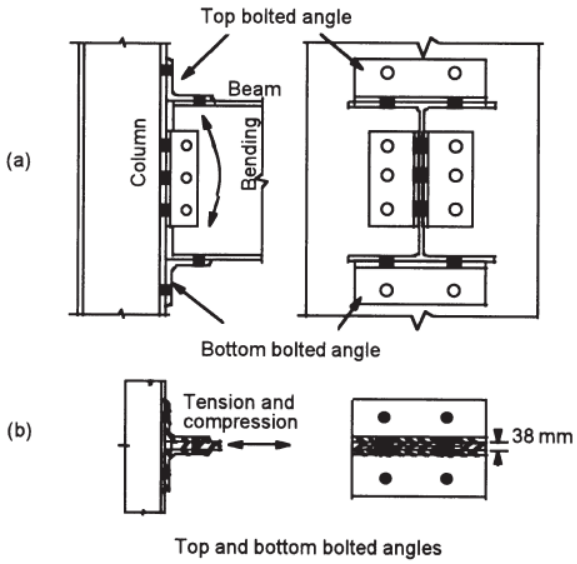

Figure 2.23: Tests simplification: (a) beam-column connection and (b) experimental test of the angles (extracted from Shen and Astaneh-Asl (1999)).

and cyclic loading. This means that the low-cycle fatigue depends on the deformation pattern. The authors concluded that, for these specimens, the energy dissipation was associated with the steel angles and the sizes of the bolts and not with other parameters. The geometric and strain hardening resulted in rupture forces 2 to 3 times the yielding forces and the cyclic ductility achieved was between 8 and 10.

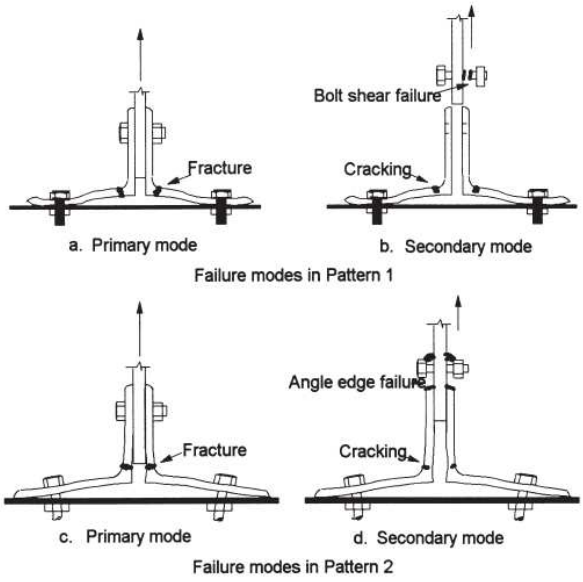

Figure 2.24: Failure modes associated with deformation patterns (extracted from Shen and Astaneh-Asl (1999)).

Yang and Tan (2013a) carried out a study on the progressive collapse of steel frames. To that end, steel angles were investigated in Yang and Tan (2013b). The work on angles had the objective of developing an analytical model to predict their response. To calibrate the model fourteen tests were made and the bolts position, the angle thickness, the bolt size and the material properties were the studied parameters. The thickness of the tested angles ranged from 7 mm to 11 mm and the lengths of the legs from 90 mm to 150 mm. The authors used two solutions for the bolts, one in the horizontal leg plus one in the vertical leg and one in the horizontal leg plus two in the vertical leg. The bolts sizes were M20 or M24 and the load was incremented monotonically. As has already been mentioned, the failure mode depends on the relative strength between the angle and the bolts, have five different types been observed by Yang and Tan (2013b). The failure modes were: (1) angle failure at horizontal leg bolt holes; (2) angle failure on the horizontal leg close to the fillet (see Figure 2.25); (3) angle failure at horizontal leg bolt holes with bolts yielded; (4) angle failure on the horizontal leg close to the fillet with bolts yielded; (5) bolts failure with angles yielded. The authors also concluded that the relative bolt/angle strength influenced the position of the plastic hinge near the bolts of the horizontal leg. For the same bolts, the plastic hinge can be closer to the angle fillet for more flexible angles or closer to the edge for stiffer angles (see Figure 2.26), as had previously been reported by Shen and Astaneh-Asl (2000). Yang and Tan (2013b) highlights that the force at failure is significantly higher than the yielding force.

Figure 2.25: Yang and Tan (2013b) angle failure close to fillet (extracted from Yang and Tan (2013b)).

2.4.2 Unbonded prestressed beam-column connection

Several authors have studied steel rocking beams with unbonded post-tensioning. To exemplify other solutions besides steel angles, Christopoulos et al. (2002b) and Christopoulos

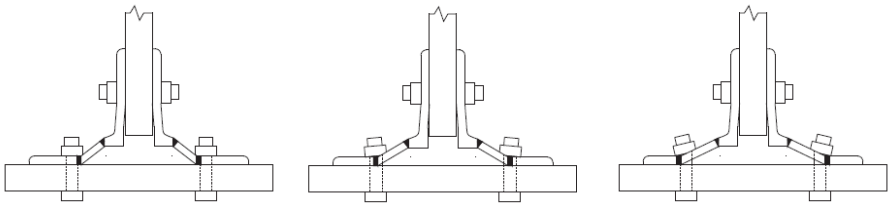

Figure 2.26: Influence of relative strength bolt/angle on plastic hinge position (extracted from Yang and Tan (2013b)).

et al. (2002a) studied beam-column joints using tension-compression yield steel bars as energy dissipaters, Rojas et al. (2005) and Lin et al. (2013) used friction devices as energy dissipaters.

Steel beams using top and seat steel angles as energy dissipaters were studied in the following five papers: Ricles et al. (2001) developed analytical models to estimate the response; Ricles et al. (2002) presented experimental work with large scale unbonded prestressed steel beams; Garlock et al. (2003) described the development of the steel angles; then Garlock et al. (2005) made full-scale post-tensioned steel connection specimens; Garlock et al. (2007) added more parameters to the prior research, as the interaction between the floor and the beam and a performance-based seismic design.

Ricles et al. (2001) and Ricles et al. (2002) studied moment-resisting frames, using unbonded post-tensioned connections between beams and columns with steel angles in the top and bottom of the beam to dissipate energy and give redundancy under seismic loading. The authors compare these solutions to the welded solutions, that were the typical solutions for seismic zones at that time. These hybrid systems presented a stiffness similar to the welded connection solutions. These systems respond with self-centring capability and the damage is confined to the angles, that can be easily replaced.

Figure 2.27 shows two connections tested by Ricles et al. (2001). Shim plates were used to force the contact between the beam flanges and the column and prevent contact between the beam web and the column, even after the flanges yield. A reinforcing plate was used in the flanges to prevent the flanges from yielding too early. Washer plates were used in the vertical legs of the angles to control the plastic hinge location and to to reduce the prying force on the column bolts (Garlock et al., 2003). Two types of columns were used, wide flange columns and concrete-filled steel tube columns.

Figure 2.28a shows a specimen (PC6) in the deformed position with unbonded post-tensioning and with steel angles connected to a concrete-filled steel tube column, presenting damage in the steel angles at 3.0% drift ratio. Figure 2.28b shows the same specimen hysteretic diagram for the same specimen (PC6) compared with other specimen (PC8)

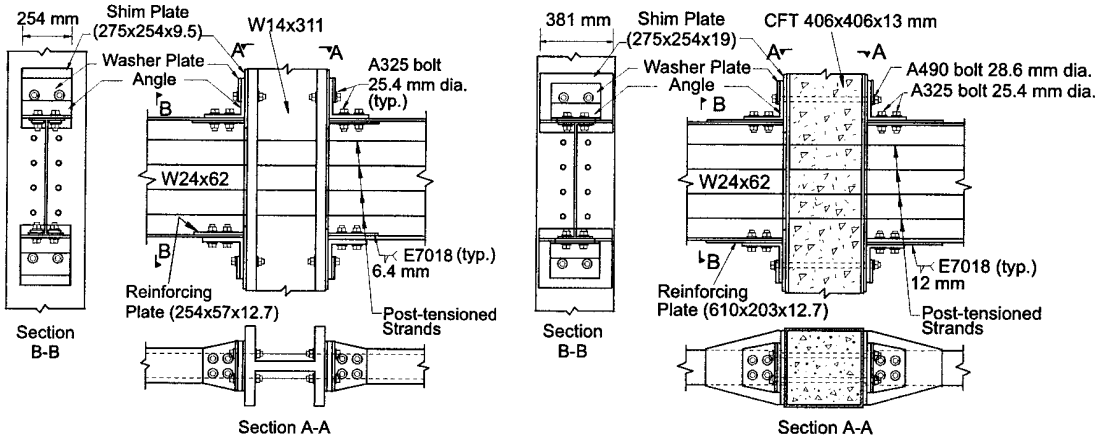

(a) Specimen with wide flange column. **(b)** Specimen with CFT column.

Figure 2.27: Two types of hybrid connection specimens (extracted from Ricles et al. (2002)).

without post-tensioning. These figures help to support the conclusion that a connection with the proper design responds very well to cyclic actions. To increase the bending moment capacity and energy dissipation of the connections, the thickness of the steel angles can be increased or the gage length (the distance between the bolt in the column leg and the heel of the angle) decreased. However, these parameters also influence the accumulated plastic strain in the angles and may result in low-cycle fatigue. It is also important to have the post-tensioning always in the elastic range to maintain the self-centring capability (Ricles et al., 2002).

In parallel with the previous studies (Ricles et al. (2001) and Ricles et al. (2002)), the steel angles that were used were developed and that study is described in Garlock et al. (2003). The authors tested seven specimens to investigate the influence of the thickness and gage length of the steel angles on the connection stiffness, strength, energy dissipation and resistance to low-cycle fatigue. The tests setup were similar to the ones used by Shen and Astaneh-Asl (1999) shown in Figure 2.23. The steel angle solution was the one shown in Figure 2.27 and of the seven angles, one was tested without washer plate. The mechanism that formed included three plastic hinges, one in the bolts of the column leg and the other two near the fillet, in the column leg and beam leg. Garlock et al. (2003) concluded that the washer plate had no major effect on the bolt prying force neither in the plastic hinge location for small gage lengths and thick angles, thus the authors do not recommend its use, however, no alternative solution to control the prying action was given. In terms of low-cycle fatigue, stiffer angles with smaller ratios between gage length and thickness correspond to less resistance to low-cycle fatigue. Garlock et al. (2003) also presented expressions to estimate the force at yielding and the force in the post-yielding range. The force after yielding is a function of the geometric and material hardening.

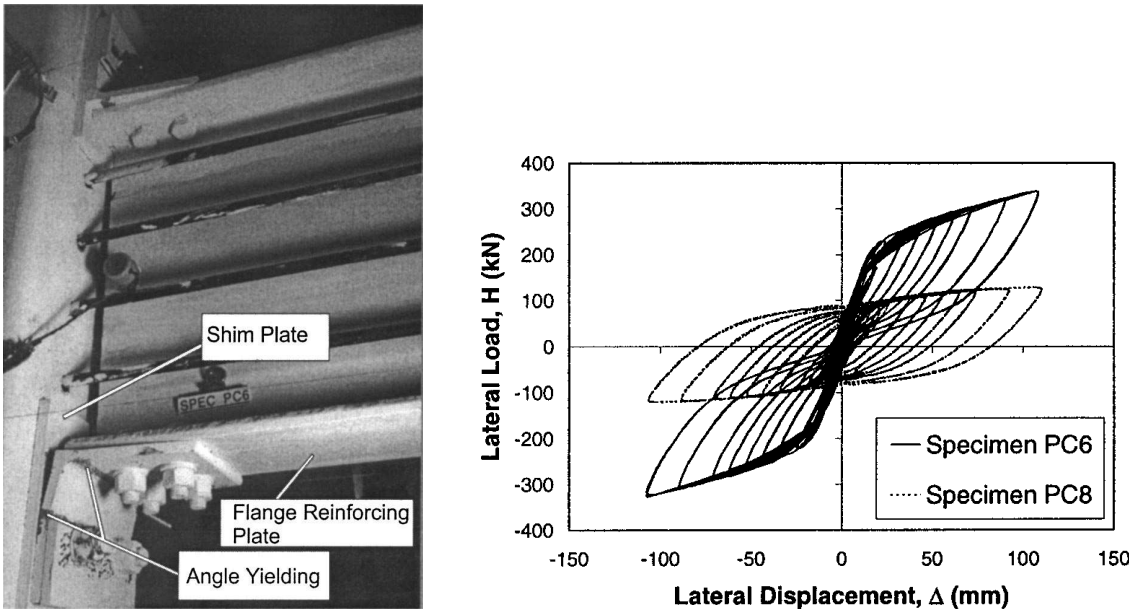

(a) Specimen PC6 at 3.0% drift ratio. **(b)** F-d of specimens PC6 and PC8, with different PT.

Figure 2.28: Tests of connections with and without post-tensioning (extracted from Ricles et al. (2002)).

After the work of Ricles et al. (2001), Ricles et al. (2002) and Garlock et al. (2003), six full-scale connections were tested and are described by Garlock et al. (2005). The tests were similar to the ones presented by Ricles et al. (2002), but with larger specimens, steel wide flange elements and steel angles without washer plates, as recommended by Garlock et al. (2003). The tests were conducted until a drift ratio of 4.0%. The specimens presented a self-centring response, and the plastic deformation was concentrated in the top and seat steel angles.

2.4.3 Concrete coupled wall systems

Two studies on concrete walls with coupling beams using angles as energy dissipaters are described in Kurama et al. (2006) and Weldon and Kurama (2010). The experimental work of these studies was carried out at the University of Notre Dame. Steel coupling rocking beams were used in the study described in Kurama et al. (2006) and concrete coupling rocking beams in the study described in Weldon and Kurama (2010).

The usual method of building coupled walls using steel beams is to embed the beams into the walls. In Shen and Kurama (2002) a method was analytically studied considering steel beams connected to concrete walls using post-tensioning and steel angles, avoiding the need to embed the beams into the walls. From this work, the results were positive, and a seven storey high prototype was modelled and subsequently presented in Kurama and

Shen (2004). From the model, it was concluded that the hybrid coupling beams, due to the post-tensioning force, gives a self-centring capacity to the concrete wall that reduces the residual displacements of the structure after a nonlinear response. A disadvantage of this solution is the lower energy dissipation capacity compared with a beam embedded construction, as the energy dissipation is concentrated in nonlinear behaviour of the the top and seat angles. The authors refer this system as a retrofit and strengthening solution for existing concrete walls.

Kurama et al. (2006) describes eleven tests of half-scale specimens of the prototype described in Kurama and Shen (2004). The test setup can be seen in Figure 2.29, where the block that simulates the wall on the left was fixed and the one that simulates the wall on the right was used to apply the vertical displacements. The rotation in the loading block was not allowed to maintain the two blocks parallel. The horizontal displacement was not restrained, as the walls can get closer to each other when horizontal displacements are applied. The beams axial load was not considered. The connection of the steel angles to the walls was made using prestressed strands to avoid tension stresses in the concrete. From Figure 2.29, it can be seen that the solution used was similar to the one used by Ricles et al. (2002), having a shim plate and a cover plate (or flange reinforcing plate) for the same reasons. The differences were that Kurama et al. (2006) used angles with different legs, the connection to the beam was made using only one line of bolts instead of two and the connection to the vertical element was made using two or four prestressed strands instead of a line of bolts.

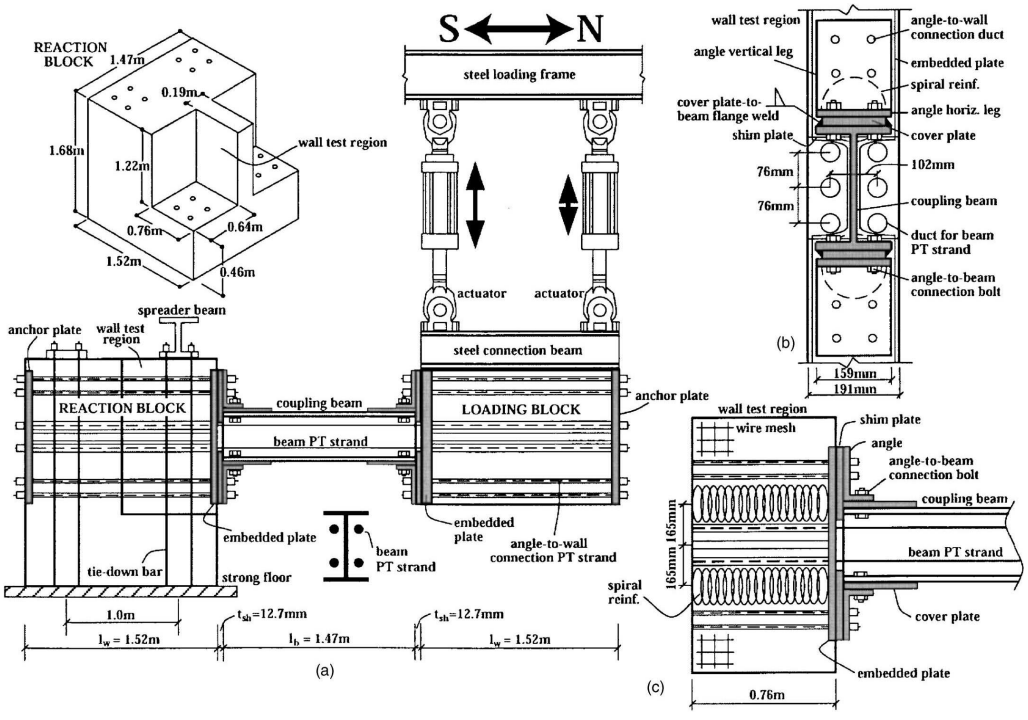

Figure 2.29: Kurama et al. (2006) test setup (extracted from Kurama et al. (2006)).

From a general point of view, Kurama et al. (2006) concluded that the tested specimens can be designed for large reversed cyclic loading. The initially used cover plates were used only in four tests, as the compressions in the flanges did not justify the presence of these plates. The beam rotations achieved were very large with minor losses of prestress or degradation of the systems. Figure 2.30a shows a deformed specimen for 8.0% beam rotation and Figure 2.30b an angle failure in the same specimen for 9.0% beam rotation. It was observed for cyclic loading that thicker angles lead to low cycle fatigue cracks for smaller rotations. Another conclusion was that the damage was confined to the angles, allowing a reuse of the coupling steel beams.

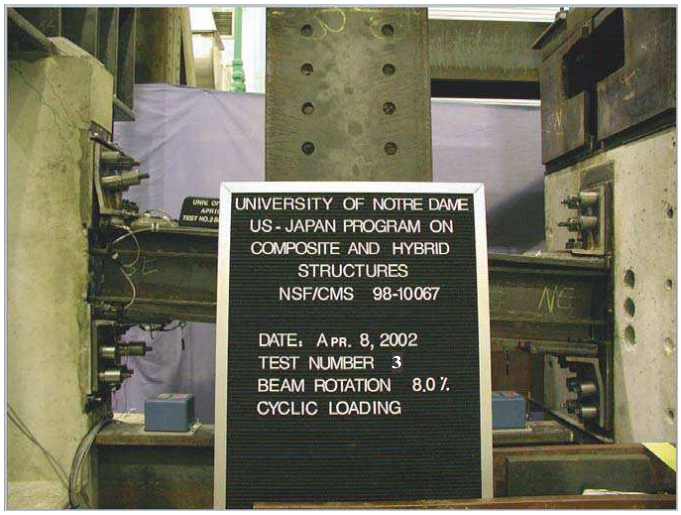

(a) Deformed specimen at 8.0% beam rotation.

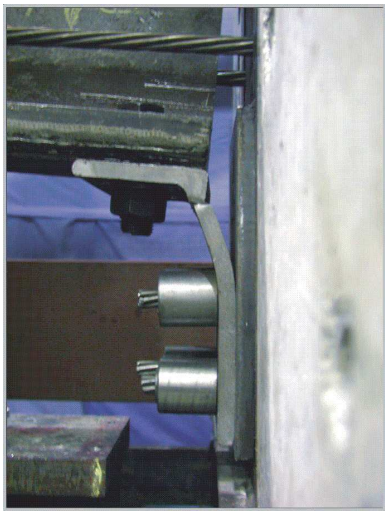

(b) Angle failure at 9.0% beam rotation.

Figure 2.30: Steel coupling beam test (extracted from Shen (2006)).

For the work on coupled walls using concrete coupling beams, a prototype with only one beam was modelled in Weldon and Kurama (2007) to make parametric variations. Weldon and Kurama (2010) describes the tests of eight half-scale specimens. The general setup used for these tests was similar to the one previously mentioned and shown in Figure 2.29. Some changes were introduced, such as the exclusion of the cover plate and the use of two prestressed strands in the vertical legs and four bolts in the horizontal legs of the steel angles. A centred tendon was used for the post-tensioning. The concrete beams had special confinement near the connection to protect the compressive concrete. As for the steel coupling beams, the concrete coupling beams presented a good behaviour and can be designed for large reversed cyclic loading. The specimens sustained large rotations with damage located in the steel angles and cover concrete near the connection. In one specimen there were premature losses in the post-tensioning forces due to the fracture of wires. These losses reduced the self-centring capacity of the specimen.

2.4.4 DIS-CAM system and timber beam-column connections

Steel angles have been used in a system described by Dolce et al. (2006) named DIS-CAM (DISsipative Active Confinement of Masonry). This system is an evolution of the CAM (Active Confinement of Masonry) system, where the columns are confined with angles along the corners and post-tensioned steel ribbons wrapping the columns (Dolce et al., 2003). The DIS-CAM system adds steel angles as energy dissipaters to the CAM system. The dissipative angles are welded to the angles in the corners of the beams and columns. Figure 2.31a shows a corner of the one-fourth scale 3D reinforced concrete model made to test this solution in a shaking table. This model was initially designed only for gravity loads, then tested, repaired and strengthened with the DIS-CAM system. Figure 2.31b shows the developed angle solution, with one zone where the angle is thinner and with holes to provide the desired strength and stiffness. The maximum achieved drift ratio was about 8.0% and the structure did not collapse, although many dissipaters failed. In general the test was considered to be positive, with good energy dissipation and a high ductility capacity.

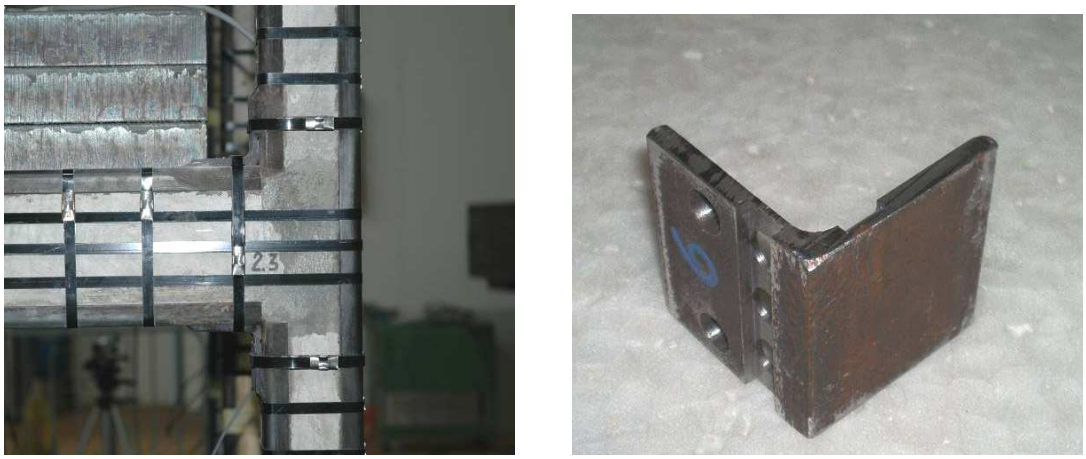

(a) Beam-column joint. **(b)** Steel angle.

Figure 2.31: DIS-CAM system in a 3D reinforced concrete model (adapted from Dolce et al. (2006)).

At the University of Canterbury in Christchurch, New Zealand, timber solutions using laminated veneer lumber (LVL) have been studied for frame and wall structures (Palermo et al. (2005), Palermo et al. (2006b), Palermo et al. (2006a), Iqbal et al. (2007), Smith et al. (2007), Iqbal et al. (2008) and Iqbal et al. (2010)). These systems are a continuation of the PRESSS technology and are known as PRES-LAM. In the work described in Smith et al. (2014), Smith et al. (2011) and Smith et al. (2012), a post-tensioned full-scale glue laminated (GLULAM) timber beam-column joint was tested. This test was carried out in the structural laboratory of the University of Basilicata, Italy. The system used for

this connection was post-tensioned and had steel angles to give additional strength and energy dissipation. The steel angles used were developed based on the DIS-CAM system. A general view of a test is shown in the picture of Figure 2.32a. Four types of tests were carried out: using only post-tensioning; using post-tensioning with steel angles; using only post-tensioning plus gravity load and using post-tensioning with steel angles plus gravity load. Parametric variations were made for the post-tensioning force and the quantity of steel angles was also variable, resulting in a total of twenty one tests. The steel angle used in these tests can be seen in Figure 2.32b, in a deformed position showing cracks in the column leg near the fillet. The post-tensioning was applied using a 7 wire strand 0.6" for forces below 170 kN or a 26 mm diameter bar for larger forces.

From a general point of view, the connection behaviour was good, with the maximum applied drift 2.5%. A steel angle fatigue failure was observed at the maximum drift (see Figure 2.32b). Concerning the post-tensioned tests without dissipaters, the response was as expected, with an elastic and recentring behaviour of the connection. With the addition of the steel angles, the bending moment increased as well as the energy dissipated. An important conclusion was that with a decrease in the post-tensioning force, the gap opens sooner and the displacement demand in the angles increases for the same drift. The plastic behaviour was confined to the steel angles, as desired. Finally, the tests including gravity load resulted in a response similar to the ones without gravity load. The gravity load essentially increased the demand on the shear that was transmitted by friction, steel angles and an interior steel tube designed to resist the shear force and to allow the presence of the post-tensioning inside the beam (Smith et al. (2014) and Smith et al. (2011)).

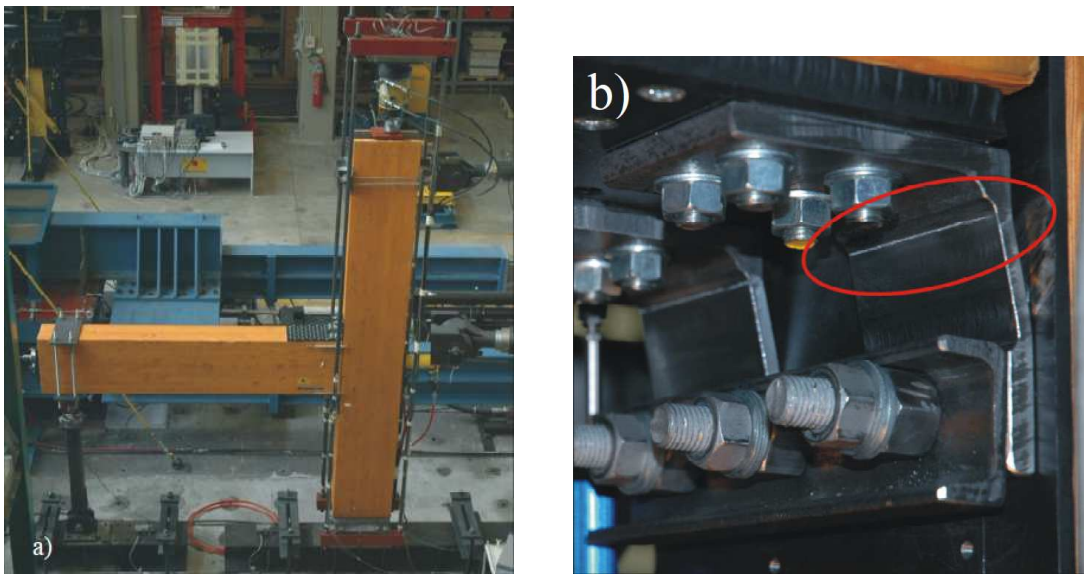

(a) Picture of the test.

(b) Deformed and cracked angles.

Figure 2.32: GLULAM beam-column joint test (extracted from Smith et al. (2011)).

2.5 Performance based design

The seismic design of a structure can be made using "Performance Based Design", a general term that can be associated with "Limit States Design", according to Priestley (1998). The structures have to behave inside imposed limits or performance limits.

A more common way of designing is known as "Force-Based Design" (FBD), where the strength of the structure is the main parameter to be controlled. The elastic stiffness is used to characterise the structure and the demand forces are obtained based on a 5% damping acceleration spectrum and a behaviour factor, to reduce those demand seismic forces. The main problem with this method is determining the stiffness to be used. The elastic stiffness is not real and will result in unreal estimations of demand forces and displacements. To take into account the cracking of the elements, Priestley (1998) states that a reduction of 50% in the moment of inertia of the gross is used in many cases. Priestley (1998) also suggests that for more rigorous design, different reductions should be used for different types of elements and suggests, based on Paulay and Priestley (1992) that 40%, 70% and 30% of the gross area inertia may be used for beams, columns and walls, respectively. More details of the Force-Based Design procedure are discussed in Priestley (1993) and Priestley (2003).

The FBD estimates the internal forces caused by the seismic action on the elements of the reinforced concrete structure. The seismic action is not a force itself, it is a history of displacements applied in the foundation of a structure that will be transmitted from floor to floor through the vertical elements of the structure. This means that the seismic action is not a force applied but the forces are a consequence of the stiffness of the structure. Theoretically, a structure with no stiffness would have no seismic forces demand! Therefore, during an earthquake the stiffness will be reduced due to damage and the seismic forces should not be obtained based on elastic analyses but taking into account the nonlinear behaviour of the structure. This led to a use of a behaviour factor to reduce the elastic forces obtained from considering an elastic behaviour of the structure. The problem with FBD is that the displacements associated to the real behaviour are difficult to obtain. Based on this, alternative procedures to design structures with the objective of achieving better estimations for the displacements/deformations were developed and called "Performance-Based Design".

In the case of rocking walls, the non-linearity is concentrated in the connections and the post-elastic behaviour is also taken into account explicitly, so the usual FBD considering an initial stiffness and a behaviour factor is not an appropriate way to design it. In this case a DBD method has to be used. More generally it can be said that for precast structures the FBD should be used only for emulative structures (Nakaki et al., 1999).

2.5.1 Direct Displacement-Based Design (DDBD)

Direct Displacement-Based Design (DDBD) is a DBD method used for the seismic design of structures. In the DDBD procedure the structure is characterised by a single degree of freedom (SDOF) representation of performance at peak displacement response, rather than by the initial elastic characteristics, as in FBD (Priestley et al., 2007).

In Figure 2.33 a resume of the DDBD design is shown. The first step is to assume a critical drift ratio and estimate an equivalent damping for the structure. The damping can be estimated based on the type of structure and the displacement ductility (Fig. 2.33(c)). With this and considering a deformed shape that depends on the type of structure, it is possible to obtain the SDOF structure (Fig. 2.33(a)) and a design displacement on the effective mass, Δ_d. With the design displacement and the displacement spectrum for the equivalent damping, the SDOF vibration period is obtained (Figure 2.33(d)) with which the SDOF effective stiffness, K_e is calculated. As can be seen in Figure 2.33(b), with the K_e and Δ_d, the shear base can be calculated, $V_b = K_e \times \Delta_d$. At this point, the real structure has to be considered and designed. The design seismic forces are obtained by distributing the V_b for each floor as a function of the displacements along the height of the structure. The plastic hinges at critical sections have to be designed as well as the rest of the structure. The next step is to verify the assumed damping. With the structure designed, it is possible to model the real behaviour and obtain a hysteretic diagram to calculate the equivalent damping. With the real damping, the need to iterate is evaluated comparing it with the initial damping. If the initial damping is not correct a different displacement spectrum needs to be considered with the new damping value, if not the structure is detailed according with capacity design (Priestley (1998), Priestley (2002), Priestley (2003) and (Priestley et al., 2007)).

2.5.2 Empirical methods for force-displacement diagrams and structural limit states

During the application of a displacement in the top of a precast post-tensioned concrete rocking wall or frame, several main points can be defined to draw a force-displacement diagram. After the initial linear-elastic response, decompression is reached and a gap is opened in the base connection. At this stage there is no significant modification to the stiffness of the structure, what happens when the neutral axis is much deeper into the section or when the concrete has a nonlinear response under compression. After the change to the stiffness there are three options: the yielding of the energy dissipater (if present); reaching the limit of proportionality of the post-tensioning steel and excess of compression on the concrete. This last stage corresponds to the ultimate limit state and the three options can be achieved sequentially.

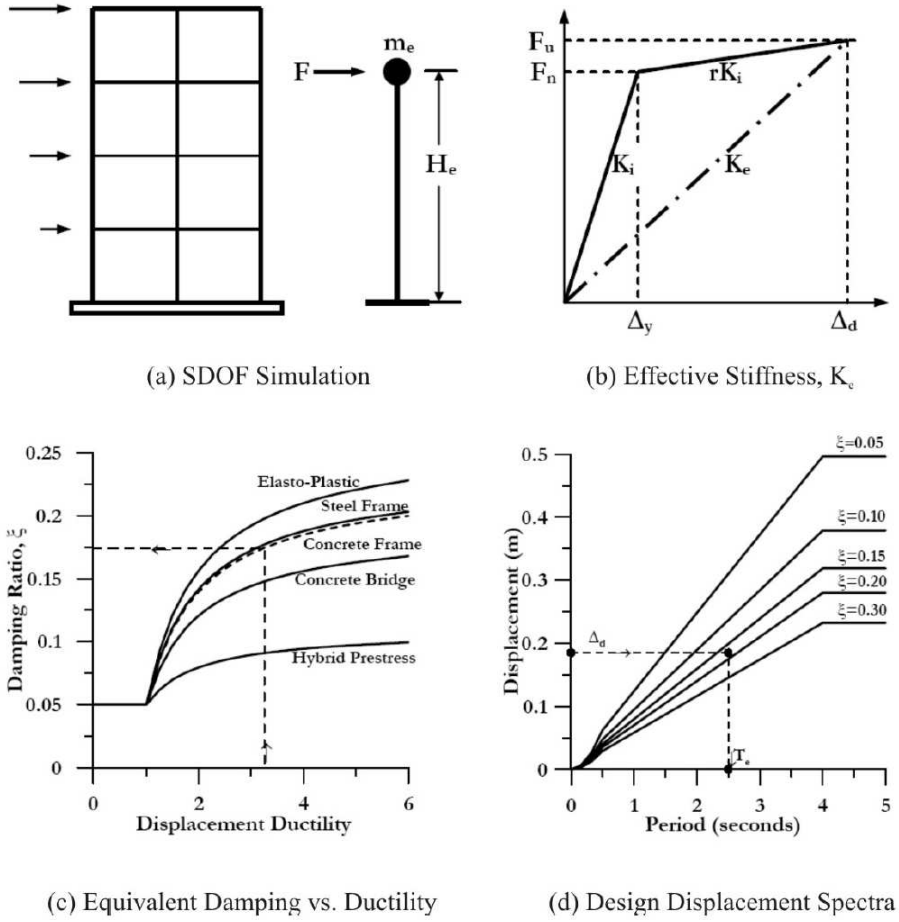

Figure 2.33: Fundamentals of Direct Displacement-Based Design (extracted from Priestley et al. (2007)).

Priestley and Tao (1993), developed a bilinear idealisation, considering the limit of proportionality of the prestress as the ultimate state. In this study, a precast prestressed frame with partially debonded tendons without dissipaters was considered, as can be seen in Figure 2.34a. To define the bilinear idealisation (Fig. 2.34b), three points are needed, the first is the origin, point one, then the end of the initial stiffness, point two and the limit of proportionality of the prestress, point three. Point two is obtained considering that the stiffness changes when the gap opening has propagated to the centroidal axis, unless the average initial stress in the concrete due to prestress is higher than $0.25f_{cm}$. This point corresponds to a moment twice the one related to the decompression of the cross section. The author considers that the prestress should remain elastic, thus point three is when the limit of proportionality of the prestress is reached. In this example no dissipation device is considered, what means that only an excess of compression stress in the concrete can change this bilinear idealisation.

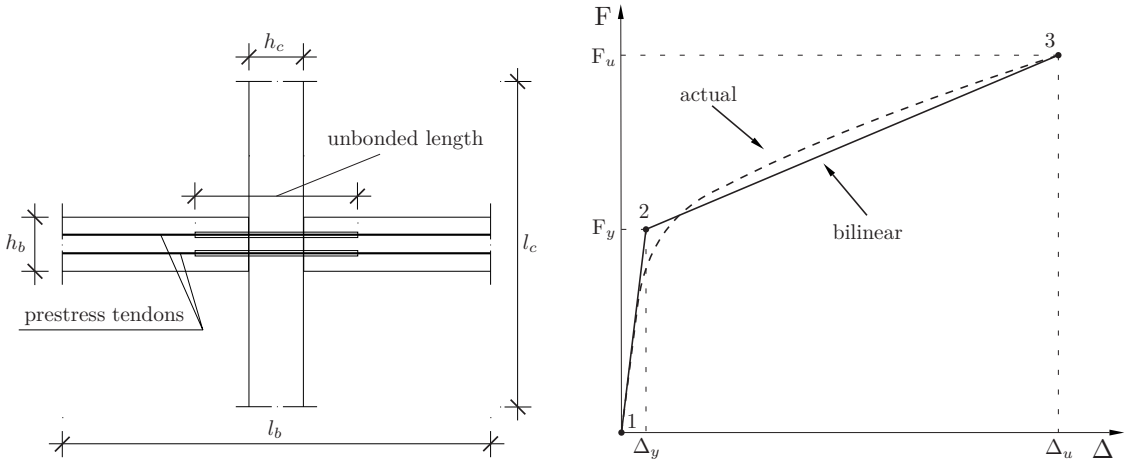

(a) Beam-column connection with partially debonded tendons

(b) Bilinear force-displacement

Figure 2.34: Beam-column connection with partially debonded tendons (adapted from Priestley and Tao (1993)).

Perez (2004) made an approach similar to Priestley and Tao (1993), using some of their conclusions and added the possibility of the prestress steel to reach stresses beyond the limit of proportionality. Based on Kurama (1997), Perez (2004) presented seven wall stages for the behaviour of an unbonded post-tensioned precast prestressed wall:

1. decompression at the base of the wall (DEC);
2. elastic limit of the linear-elastic response of the wall (ELL);
3. limit of proportionality of the prestress steel (LLP);
4. base shear capacity;
5. loss of prestress under cyclic lateral load;
6. crushing of confined concrete (CCC);
7. rupture of prestressing steel.

1. DEC is when the wall starts to lift on one side and opens a gap in the connection. As already mentioned, at this stage there is no significant change to the wall stiffness. The initial compressive force is due to the prestressing force and the other vertical loads.

2. ELL is when the wall changes stiffness, this occurs by the growing of the opening of the gap or by a nonlinear behaviour of the concrete in compression. According to El-Sheikh et al. (2000) the value of the bending moment that corresponds to this stage should be calculated as the minimum value considering two possible situations: the concrete nonlinear response in compression, assuming an extreme fiber (including the concrete cover) strain of the concrete equal to 0.003 and a prestressing force equal to the initial one; the geometric softening, that is considered to be reached when the gap opening length propagates beyond 75% of the cross section depth, corresponding to 2.5 times the

decompression bending moment. This last situation, that corresponds to the geometric softening, is different from the one previously suggested by (Priestley and Tao, 1993), where the effect of the gap opening on the stiffness is considered small until the neutral axis reaches the section centroid.

3. LLP is when the limit of proportionality of the prestress steel is reached. Beyond this limit the prestress force begins to have losses and the structural initial elastic stiffness is reduced. The prestress can be applied with several bars or tendons, which means that the first bar or tendon to reach the limit of proportionality may not impose a significant loss of stiffness due to prestress. Either way, LLP is considered to be reached when the first bar or tendon reaches the limit of proportionality.

4. The base shear capacity is the maximum base shear that can be reached. Considering that there is no sliding, the base shear is controlled by the overturning capacity of the wall and is achieved when the prestress reaches the limit of proportionality (LLP), neglecting the strain-hardening effects in the steel.

5. As mentioned above, the loss of prestress occurs when the wall is unloaded from a drift after the prestress had went beyond the limit of proportionality. Prestress losses can also be associated with local damage or system adjustments during loading, especially in short length bars or tendons.

6/7. CCC is a limit state that should be avoided. To delay this limit state beyond the design drift ratio, the concrete should be conveniently confined. Priestley and Tao (1993) recommend interlocking spirals as confinement for rectangular beams (Figure 2.5), that can also be used in the walls. As well as CCC, rupture of post-tensioning steel should never occur within the design drift ratio.

Using ELL, LLP and CCC limit states, Perez (2004) presented the tri-linear idealisation, base shear vs drift ratio, that is shown in Figure 2.35. The difference for the idealisation presented by Priestley and Tao (1993) is essentially by considering the structure beyond LLP.

2.5.3 Performance levels

Perez (2004) states that according to FEMA-273 the performance levels are: (1) the immediate occupancy performance level, and (2) the collapse prevention performance level. In immediate occupancy the structure has an essentially elastic behaviour with minor post-earthquake structural and non-structural damage. In collapse prevention, damage is expected without the collapse of the structure. The immediate occupancy level is expected to be reached if the drift ratio associated with the LLP is not exceeded during an earthquake. The collapse prevention is expected to be accomplished if there is no

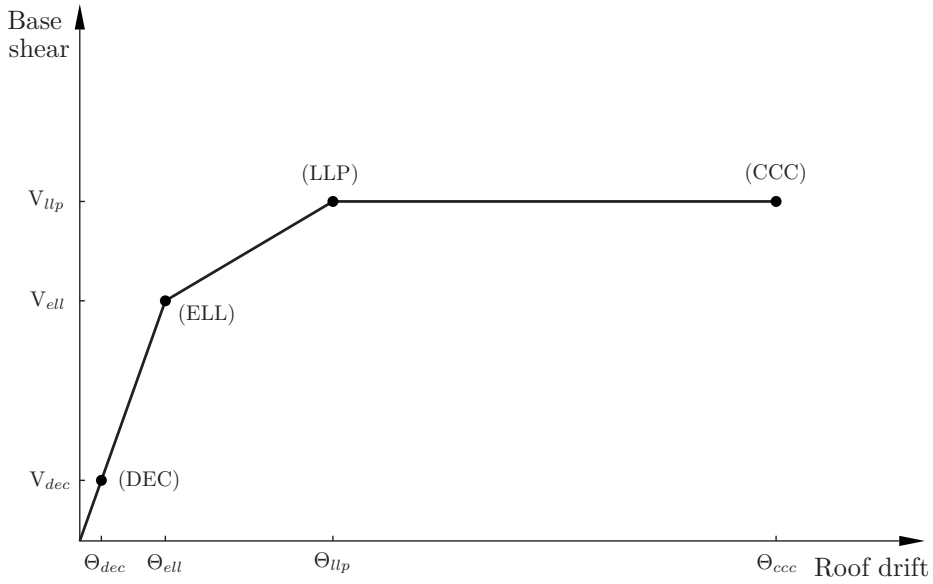

Figure 2.35: Tri-linear idealisation (adapted from Perez (2004)).

crushing in the confined concrete. If the demand drift ratio goes beyond CCC limit state, the structure is expected to completely or partially collapse.

Having the structure limit states associated with the desired performance levels it is needed to link it with the seismic demand levels. Perez (2004) associates the immediate occupancy with the design level ground motion and the collapse prevention with the maximum considered ground motion. The maximum considered ground motion has a 2% probability of being exceeded in 50 years, corresponding to a 2500 year return period, and the design level ground motion a ground shaking intensity of 2/3 of the maximum considered earthquake ground motion according to IBC-2003.

Chapter 3

Steel angles as energy dissipation devices

3.1 Introduction

This chapter focuses on the development of energy dissipaters for hybrid rocking precast wall systems. The energy dissipaters developed in this work were to be used externally to the wall, having the advantages of being easy to inspect and replace after an earthquake. The work had the goal of achieving dissipaters that presented a good cyclic behaviour, adequate strength and enough ductility to sustain the displacements applied by a major seismic event without failure. Experimental work using steel structural angles as dissipaters was done and solutions presenting the desired behaviour were achieved. To support and complement the experimental tests, 2D numerical models were analysed using a finite element software and an analytical method is presented for elastic and plastic ranges.

3.2 Experimental tests

The steel angles studied were to be used as external dissipaters in the connection of a hybrid rocking precast concrete wall to the foundation. The rocking of the wall-foundation joint has a relative displacement between the wall and the foundation that the steel angles have to follow (Figure 3.1a).

Cyclic tests were made applying a vertical displacement to two identical steel angles at the same time, in order to produce a symmetric specimen. This action is not exactly identical to the action on the hybrid wall (Figure 3.1b) because the wall has a small rotation, as is shown in Figure 3.1. This simplification is needed to allow the testing of

the specimens in a standard universal testing machine. A test with both displacement and rotation would have the disadvantage of being specific for each pair of effects and the rotation effect is small and may be neglected.

The experimental tests were made at Laboratório Nacional de Engenharia Civil (LNEC), using a universal testing machine that can be seen in Figure 3.2. Five specimens, with two angles each, were tested with an imposed cyclic displacement history, each specimen being a variation of the previous one to include improvements between specimens. The main problem to overcome during this work was achieving a stable cyclic hysteretic behaviour, specially in the reloading part of the test.

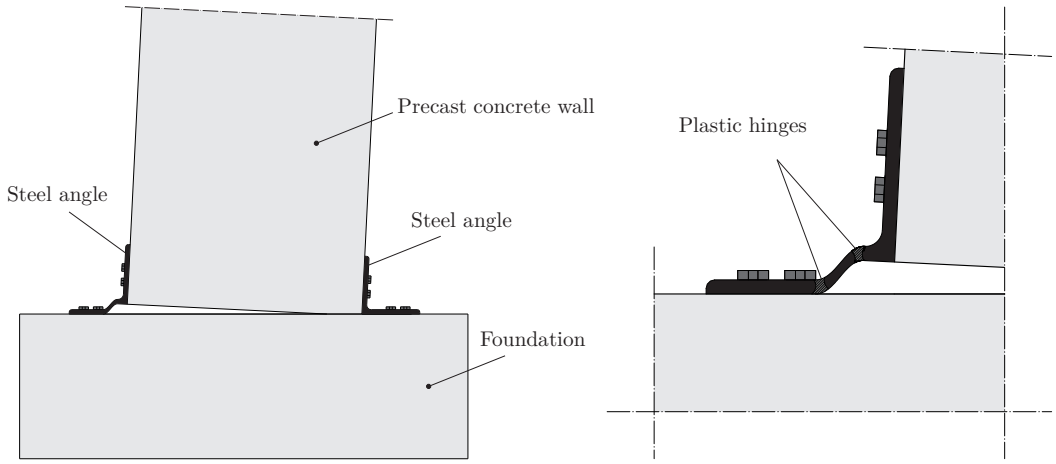

(a) Precast wall rotated. **(b)** Steel angle deformation.

Figure 3.1: Precast concrete wall with steel angles.

3.2.1 Specimens

The steel angles tested were cut from a 6 m long structural laminated steel bar. In Figure 3.3a the L150x150x15 used in specimens A1 to A4 is shown as well as the position of the bolts and washer plates used. It should be noted that specimen A4 did not have a washer plate. In Figure 3.3b the L200x200x16 used in specimen A5 is shown as well as the position of the bolts. In Figures 3.3a and 3.3b the distance g is defined as the distance that indirectly controls the lever arm between the expected plastic hinges in the bottom leg of the angles. Table 3.1 presents the main characteristics of the five tested specimens.

3.2.1.1 Steel angles conception

The steel angles were designed to be used as energy dissipaters in the precast rocking walls described in Chapter 4. After preliminary calculations to predict the walls response, the desired steel angle should have a good cyclic behaviour of up to 15 mm of displacement

Figure 3.2: Universal testing machine.

and a resistance not higher than 140 kN. The first angle solution to be tested was designed based on Garlock et al. (2003) and resulted in specimen A1. Although the use of washer plates is not recommended in that study, specially for very rigid angles, they were included in the horizontal leg bolts to avoid having a plastic hinge in the bolt zone, thus avoiding stress concentrations near the holes and to have better control of the location of the plastic hinge. The washer should also help to reduce the negative effects of the prying action during cyclic displacements that can occur if the end of the horizontal legs lift during unloading and compression. The forces involved in this are shown in Figures 3.4a and3.4b, where it is shown that the stiffness of the washer plates and bolts play a major role in this issue.

3.2.1.2 Specimen A1

The specimen A1 was a L150x150x15 (mm) angle with a length of 125 mm (Figure 3.3a). The vertical legs had four M16 threaded rods, class 8.8, inserted in circular holes of 18 mm diameter. The horizontal leg of each angle had two M20 bolts, class 8.8, with a 10 mm

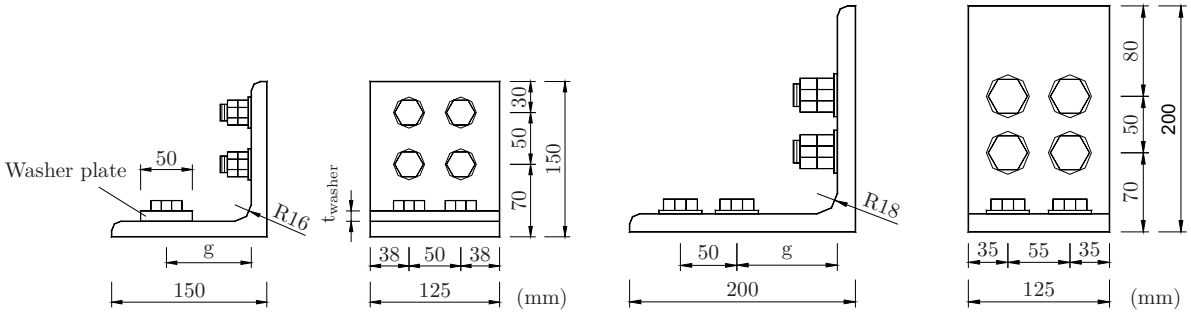

(a) Angles for specimens A1 to A4. **(b)** Angles for specimen A5.

Figure 3.3: Dimensions of the specimens.

Table 3.1: Main characteristics of the angles tested.

	Holes ovalization		Bolts		t_{washer}	g	t_{angle}	Prying action
	Vertical legs	Horizontal legs	Vertical legs	Horizontal legs	(mm)	(mm)	(mm)	control
A1	No	Longitudinal	M16 CL8.8	M20 CL8.8	10	85	15	Washer/bolt
A2	No	Longitudinal	M16 CL10.9	M20 CL10.9	15	81	15	Washer/bolt
A3	Transversal	No	M16 CL10.9	M20 CL10.9	15	85	15	Washer/bolt
A4	Transversal	No	M16 CL10.9	M20 CL10.9	-	80	15	Welding
A5	Transversal	No	M20 CL8.8	M20 CL10.9	-	89	16	Bolts

thick washer plate. The holes of the angles' horizontal legs were longitudinally oval, with a length of 32 mm and a width of 22 mm, for assembly tolerances. All the bolts were prestressed according to EN 1993-1-8 (2005) limits. The main characteristics of this solution can be found in Figures 3.3a and 3.5 and in Table 3.1.

3.2.1.3 Specimen A2

The specimen A2 was initially designed to have a smaller g distance, leading to a stiffer and stronger specimen. The bolts and washers of specimen A2 were only decided after

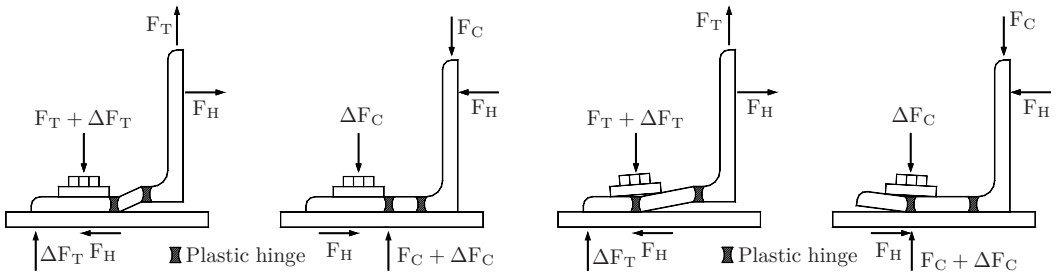

(a) Rigid bolt and a rigid washer plate. **(b)** Flexible bolt and a rigid washer plate.

Figure 3.4: Tensile and compression situations for a rigid washer plate.

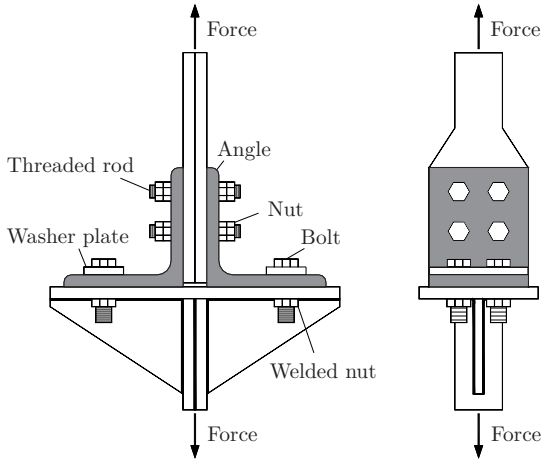

Figure 3.5: Specimen A1 test setup.

the test of specimen A1. Stiffer and stronger washer plates were used, with a thickness of 15 mm instead of 10 mm, because they were shown to be insufficient in the previous test. The class of resistance of the steel used in the bolts and threaded rods was changed to class 10.9 and additional standard washers were used. The main characteristics of this solution are shown in Figures 3.3a and in 3.6 and Table 3.1.

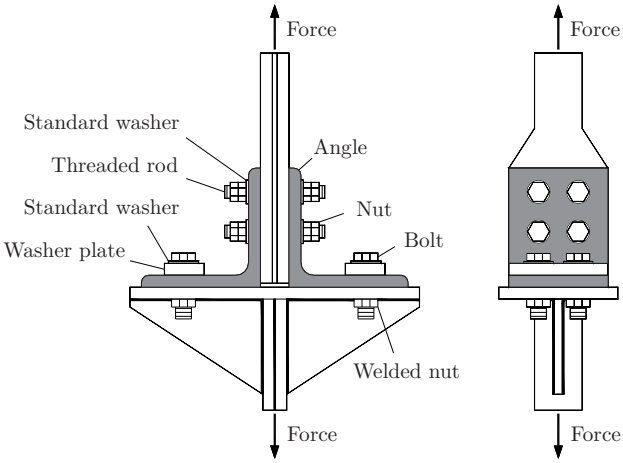

Figure 3.6: Specimen A2 test setup.

3.2.1.4 Specimen A3

The specimen A3 had bolts in the same position as in specimen A1. The differences between the specimen A2 and A3 were the geometry of the holes and a different g distance. The holes were circular in the horizontal legs and horizontally oval, with a length of 23 mm and a width of 18 mm, in the vertical legs to allow for assembly tolerances. The position of the bolts was the same as in specimen A1 and the washer plates, standard washers, bolts and threaded rods were the same as in specimen A2. The main characteristics of

this solution can be found in Figures 3.3a and 3.7 and in Table 3.1.

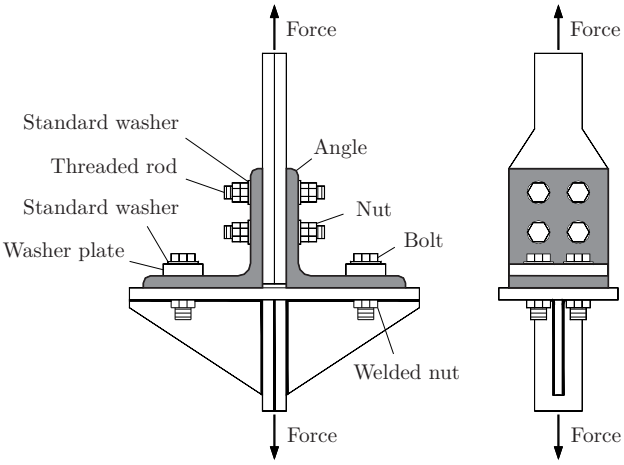

Figure 3.7: Specimen A3 test setup.

3.2.1.5 Specimen A4

In specimen A4 two main improvements were made, the edges of the horizontal legs were welded to the base plate and the washer plates were not used. The purpose of the welding was to restrain the vertical displacement of the edges of the horizontal legs. The exclusion of the washer plates, as will be seen in Section 3.2.5, was because they were unable to accomplish the functions that were explained above. The hole geometry was similar to specimen A3. The positions of the bolts in the horizontal legs were closer to the vertical leg, with a smaller g dimension than the first three specimens, in order to compensate for the lack of washer plate in terms of stiffness and strength. The main characteristics of this solution are shown in Figures 3.3a and 3.8 and in Table 3.1.

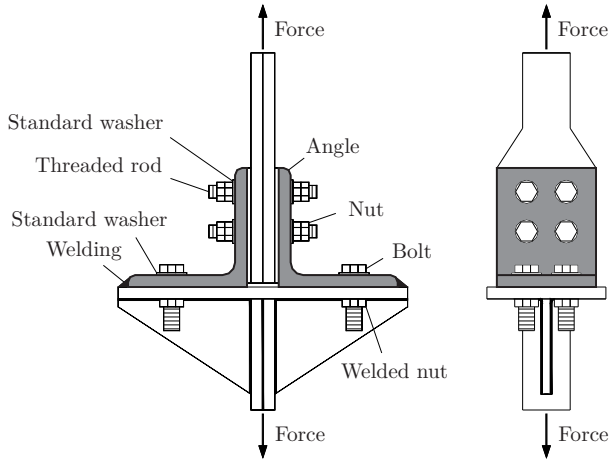

Figure 3.8: Specimen A4 test setup.

3.2.1.6 Specimen A5

Specimen A5 was designed to have a response similar to specimen A4, without the welding along the edges of the horizontal legs. For that reason, a steel angle with a longer horizontal leg was needed to accommodate a second row of bolts. The second row of bolts was located at the same distance from the first row of bolts as the welding in specimen A4. The specimen was a L200x200x16 (mm) steel angle with a length of 125 mm. In this specimen all the bolts and threaded rods were M20, the bolts being in steel class 10.9 and the threaded rods in steel class 8.8. As the threaded rods were M20, the holes were horizontally oval with a length of 27 mm and a width of 22 mm. The main characteristics of this solution are shown in Figures 3.3b and 3.9 and in Table 3.1.

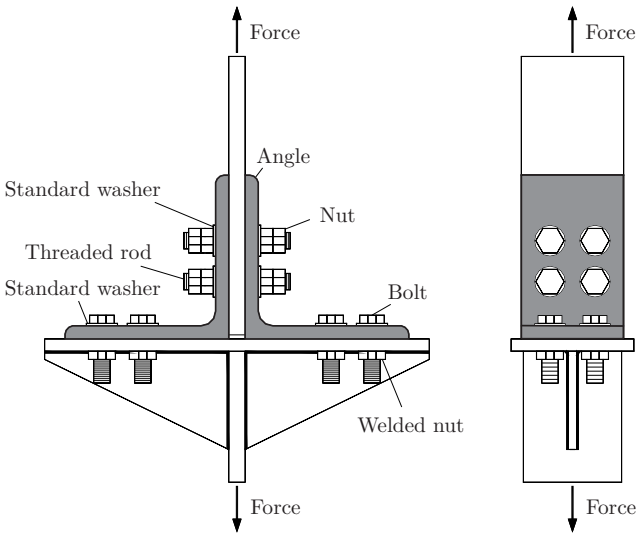

Figure 3.9: Specimen A5 test setup.

3.2.2 Instrumentation

The instrumentation was prepared to record the total force and relative displacements during the tests. The total force was monitored by the universal testing machine load cell. The displacements were monitored by displacement transducers attached to the vertical legs above the top row of bolts. The displacement transducers were placed to measure the relative displacements between the angle and the base and to monitor the deformation of the bolts, that was supposed to be negligible.

In the first four tests of specimens A1 to A4, the displacements were monitored by four displacement transducers. In the fifth test of specimen A5, six displacement transducers were used. The relative displacements from the angle vertical legs to the base and to the heads of the bolts in the horizontal legs were measured. The location of the displacement transducers is shown in Figure 3.10a for the specimen A1, which was similar to specimens

A2, A3 and A4 and in Figure 3.10b for the specimen A5. For each angle a threaded rod was screwed in the angle vertical leg to attach the transducers.

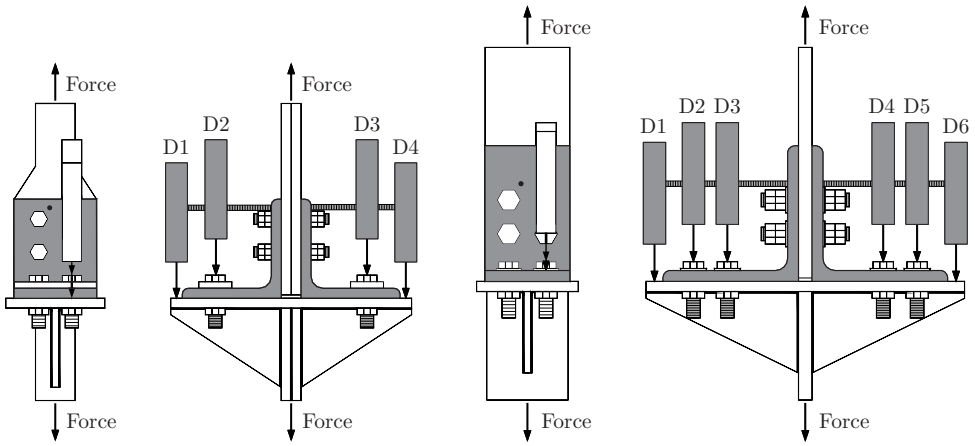

(a) Instrumentation of specimens A1 to A4.

(b) Instrumentation of specimen A5.

Figure 3.10: Transducers used for displacement monitorization.

3.2.3 Test protocols

The main purpose of the experimental tests was to develop an optimised design solution for steel angles to be used in hybrid walls systems with cyclic actions. This was achieved by applying a cyclic protocol with one cycle per amplitude. Figure 3.11a shows the protocol used in the specimen A1 test and Figure 3.11b shows the protocols in the other specimens. The first test was different only in the first cycle, where two cycles with smaller amplitude were made instead of the 5 mm amplitude cycle. This difference was due to the need to test the response of the whole system in the first test. The tests of specimens A2 to A5 did not finish with the same displacement; the maximum achieved displacement was 30 mm for specimens A2 and A5, as is shown in Section 3.2.5.

When the rupture was not achieved, the test end criteria was always safety regarding the laboratory equipment and technicians. The tests were performed using displacement control, which led to a problem with the unloading part of the test, where it was important to avoid the angles touched the base. If the referred contact was permitted, there was a risk of a sudden rise in the force that could break the horizontal bolts in the vertical leg of the angles. For that reason, the angles under compression never reached zero displacement, there always remained a residual displacement.

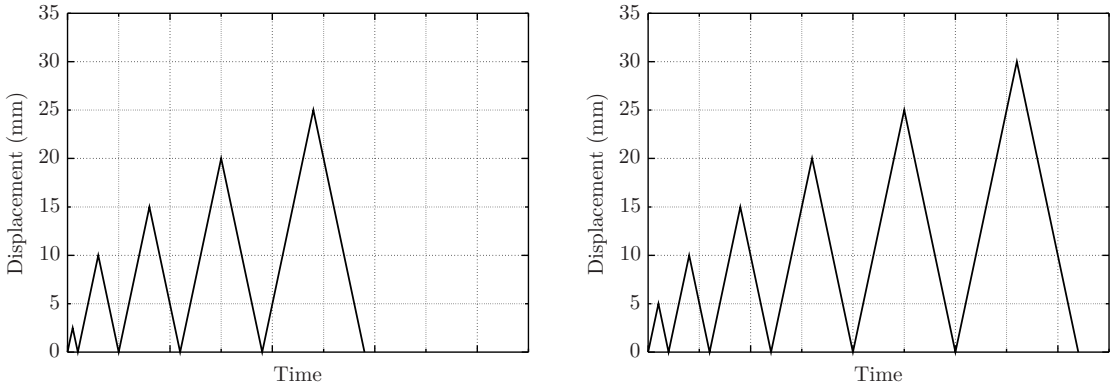

(a) Specimen A1. **(b)** Specimens A2 to A5.

Figure 3.11: Steel angles cyclic test protocol.

3.2.4 Materials

The steel prescribed for both angles was S275 grade. To obtain the mechanical characteristics of the steel, dog-bone specimens were made according to EN 10002-1 (2001) as shown in Figures 3.12a and 3.12b and tensile tests were performed (Figure 3.13). The results for four tested specimens of each type are shown in Figures 3.14a and 3.14b and summarised in Table 3.2. In Figure 3.13a a general view of a tensile test is shown with the mechanical and electric gauges. Figure 3.13b shows a specimen after failure.

From the stress-strain diagrams shown in Figure 3.14a, it can be seen that the results for the four specimens were similar. However, the results in Figure 3.14b present two different responses for two pairs of specimens. The explanation for this fact is that the bigger legs of the L200x200x16 angle made possible the fabrication of two dog-bone specimens from each leg instead of one as in the L150x150x15 angle. As a result of this, the steel tested from the L150x150x15 angle was always from the same region of the angle section while in the L200x200x16 angle two dog-bone specimens were from a region closer to the fillet whilst the other two were from a region closer to the exterior edge of the angle section. In Figure 3.14b the two specimens with higher yield stress were from the region closer to the exterior edges of the angle section.

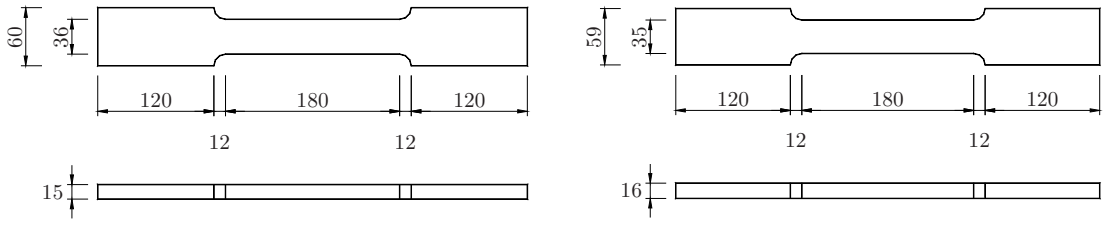

(a) Specimen of L150x150x15 angle. **(b)** Specimen of L200x200x16 angle.

Figure 3.12: Dog bone specimens for tensile tests.

(a) Dog bone specimen in machine. **(b)** Specimen after rupture.

Figure 3.13: Pictures of the tensile steel tests of L150x150x15 angle.

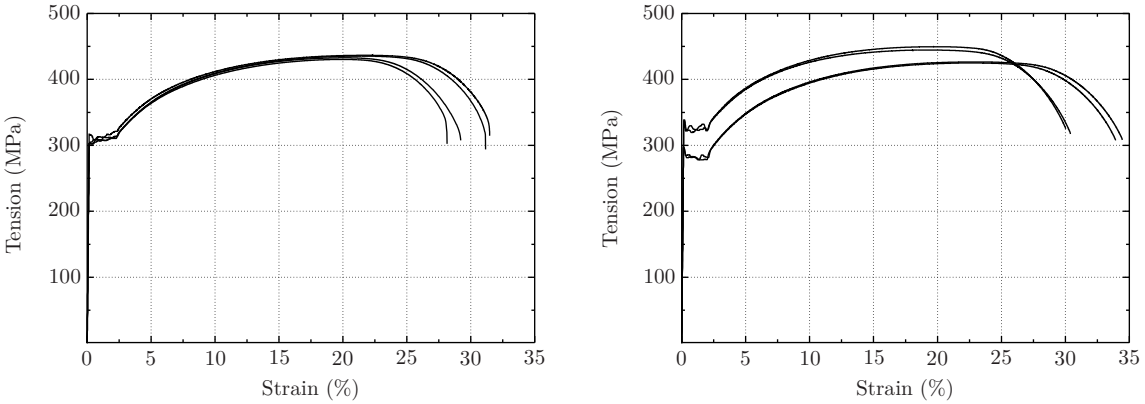

(a) Angle L150x150x15 steel. **(b)** Angle L200x200x16 steel.

Figure 3.14: Stress vs strain diagram of angles steel under tensile test.

3.2.5 Results of the steel angles tests

This experimental work was used to develop the steel angles as external dissipaters and the design of the dissipaters evolved throughout the testing. The first three specimens did not have the desired behaviour that was achieved in the last two specimens. The main parameters that will be discussed here are the achieved forces, ductility and cyclic behaviour. The achieved force for a target displacement is the main parameter for the design of the dissipater. The ductility is important because the dissipaters work mainly in

Table 3.2: Tensile tests for steel used in specimens.

	f_y (MPa)	ε_y (%)	σ_{max} (MPa)	ε_{max} (%)	ε_{su} (%)	E_s (GPa)
L150x150x15	309.9	0.15	433.8	21.46	30.70	201.1
L200x200x16	311.8	0.15	436.6	21.94	33.22	214.9

a plastic range, needing ductility to achieve the design displacement. The achieved forces and displacement are summarised in Table 3.3. The cyclic behaviour is evaluated by the shape of the hysteretic diagram in each cycle, which gives the information on the stability of the dissipater along the cycles, the energy dissipated and the response in tension and compression.

Table 3.3: Forces for one angle and maximum sustained displacement.

	F(kN) - Maximum force for different displacements						**d_{max}(mm)**
	5 mm	**10 mm**	**15 mm**	**20 mm**	**25 mm**	**30 mm**	
A1	104	116	127	138	148	-	>25
A2	123	143	156	175	188	192	30
A3	116	138	154	176	193	181	25
A4	100	122	136	149	135	-	20
A5	103	125	138	152	165	188	30

3.2.5.1 Specimen A1

The deformed shape of specimen A1 is shown in Figure 3.15. From this picture it should be highlighted that the contact between the angles and the base starts in the middle of the washer plates and the washer plates were bent by flexure. This means that the washer plates and the bolts were not able to control the position of the plastic hinges position, that formed below the washer plates instead of next to them. Another consequence of this fact can be observed in Figure 3.16, that shows the lack of contact between the base and the edge of the angles. The lack of contact that occurred in the compression phase and in the beginning of the next tension phase, was due to the residual deformation left by the prying action responsible for the plastic hinge near the bolts of the horizontal leg.

The hysteretic response diagram is shown in Figure 3.17. The displacements were measured between the vertical legs and the base using transducers D1 and D4 (Figure 3.10a). The displacements shown are the average of transducers D1 and D4. The maximum achieved force for a given displacement can be obtained from the hysteretic diagram or from Table 3.3. The cyclic behaviour was not the desired one, because in the reload part of the cycles, when the specimen goes from compression to tension, the stiffness decreases significantly, compromising the cyclic response. The maximum achieved displacement was 25 mm with no evidence of failure.

The problem referred to in the cyclic behaviour was associated with three possible causes: the prying action forces that resulted in the lifting of the edges of the angles, which can be observed in Figure 3.16; an eventual yielding of the bolts in the horizontal legs submitted to bending and tensile forces and the longitudinal ovalization of the holes

in the horizontal legs which allows the angles to slip. The washer plates suffered plastic deformations and were not able to impose the plastic hinges position in the angles or to control the prying action. To mitigate these problems, the specimen tested after this had three main differences: thicker washer plates; more resistant bolts and standard washers in all bolts and threaded rods. The use of thicker washer plates and the more resistant bolts intended to control the position of the plastic hinges and to keep the edges from lifting. The standard washers should allow a more uniform distribution of the stresses applied by the head of the bolts to the washer plates. All these changes were made to improve the behaviour of the washer plates and bolts on the horizontal legs of the angles and mitigate the first two possible causes of the cyclic behaviour problem outlined above.

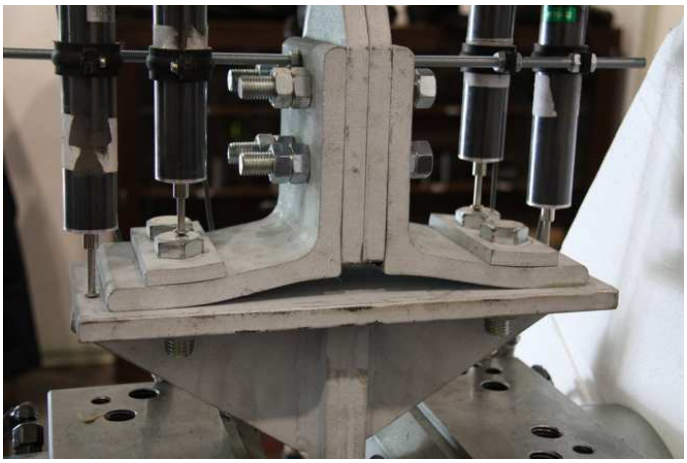

Figure 3.15: Picture of deformed specimen A1.

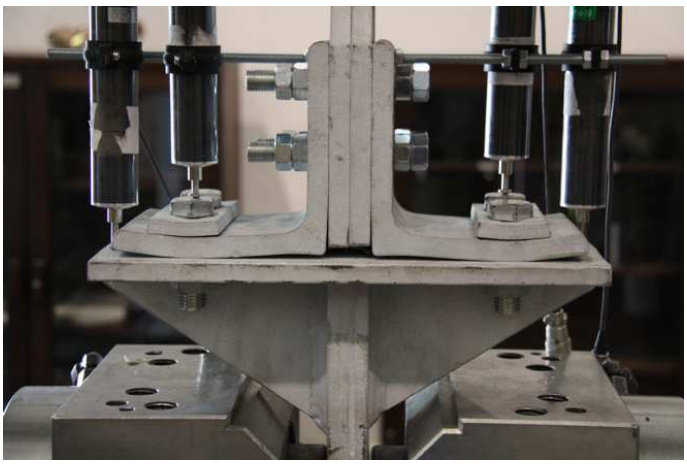

Figure 3.16: Plastic residual deformation of specimen A1.

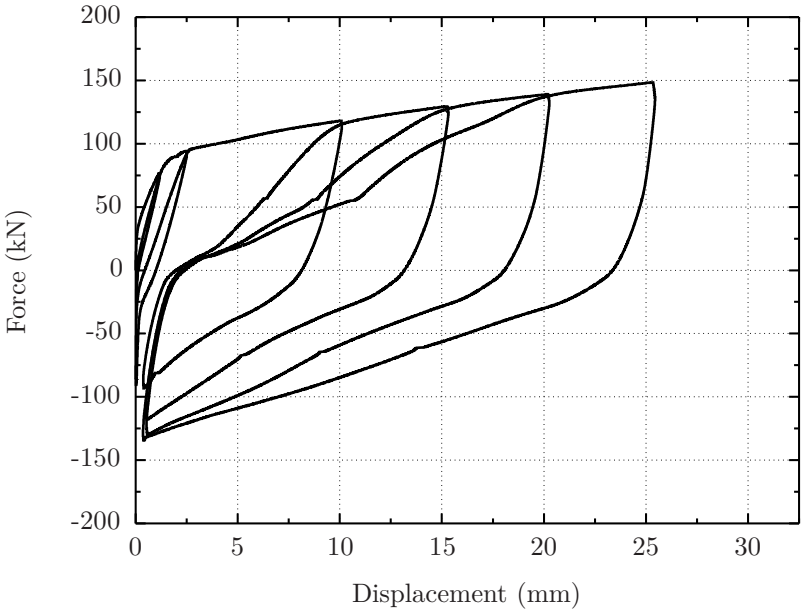

Figure 3.17: Hysteretic response diagram of specimen A1 cyclic test.

3.2.5.2 Specimen A2

The deformed position of specimen A2 test is shown in Figure 3.18. In this specimen the washer plates had rigid body behaviour but the angles lifted from the base in the middle of the washer plates, meaning that the plastic hinges in the angles horizontal legs still formed below the washer plates. Figure 3.19 shows the residual deformation of these angles. This figure shows that the edges of the angles still lifted up. In this test it was also possible to notice some slippage of the angles below the washer plates.

The hysteretic response diagram is shown in Figure 3.20. The displacements were measured between the vertical legs of the angles and the base using transducers D1 and D4 (Figure 3.10a). The displacements shown are the average of transducers D1 and D4. The cyclic behaviour was not as desired, because when the specimen went from compression to tension the stiffness decreased significantly, compromising the cyclic behaviour. This means that despite some improvements, the main problem detected in specimen A1 remained. The maximum achieved displacement was 30 mm, with imminent rupture. Observing the response diagram it is possible to see an horizontal plateau near the maximum force and a crack is shown in Figure 3.21 in the plastic hinge below the washer plate zone, meaning that this specimen was near failure. The horizontal leg holes were oval, allowing slippage of the angles and this could influence the variations of stiffness during the test. These holes were changed to circular in the next tested specimen.

Figure 3.18: Picture of deformed specimen A2.

Figure 3.19: Plastic residual deformation of specimen A2.

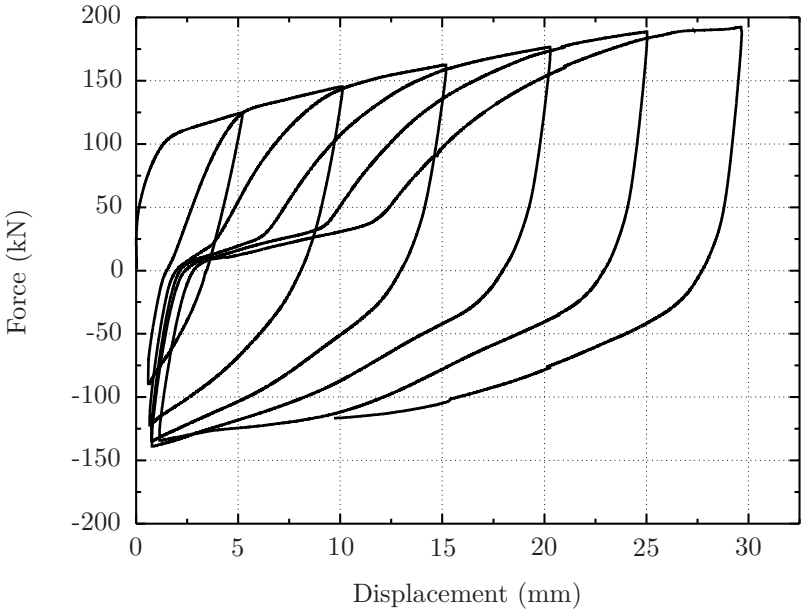

Figure 3.20: Hysteretic response diagram of specimen A2 cyclic test.

Figure 3.21: Picture of a crack in specimen A2.

3.2.5.3 Specimen A3

As in specimen A2, in specimen A3 the washer plates had rigid body behaviour (Figure 3.22) and the angles started to lift up from the base in the middle of the washer plates, meaning that the plastic hinges were still forming below the washer plates, as may also be seen in Figure 3.23. No slip was observed in the horizontal direction in this specimen because the holes in the horizontal legs were drilled circular instead the oval ones used in specimens A1 and A2.

In the hysteretic response diagram shown in Figure 3.24, the displacements were measured between the vertical legs and the base using transducers D1 and D4. When the specimen went from compression to tension the stiffness decreased significantly, compromising the cyclic behaviour. This means that despite the improvements made, the main problem detected in specimens A1 and A2 remained. After this test it seemed clear that the problem could only be solved by restraining vertical displacements on the edge of the horizontal legs. The maximum achieved displacement can be considered 25 mm, since failure was already achieved for 30 mm displacement, as can be seen in the hysteretic response diagram. From Figure 3.25 it is also possible to see the rupture in the plastic hinge below the washer plate zone. Both angles presented a similar rupture.

After three tests with continuous detailing improvements, but without solving the main cyclic response problem, some changes in the design solution of the next specimen had to be made. The first change was the exclusion of the washer plates. The introduction of washer plates was explained in Section 3.2.1 but for the relative stiffness between the angles and the washer plates and bolts used, the washer plates were not able to fulfill their purpose. Without washer plates it is clear that the plastic hinges in the horizontal legs should be in the line of the bolt holes. To restrain the edges from lifting, the edges were welded to the base.

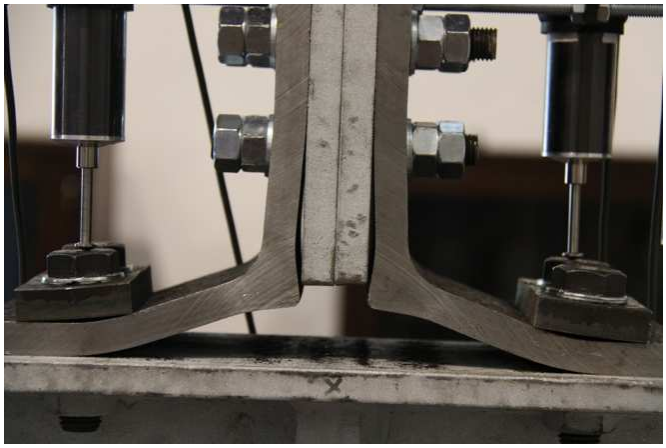

Figure 3.22: Picture of deformed specimen A3.

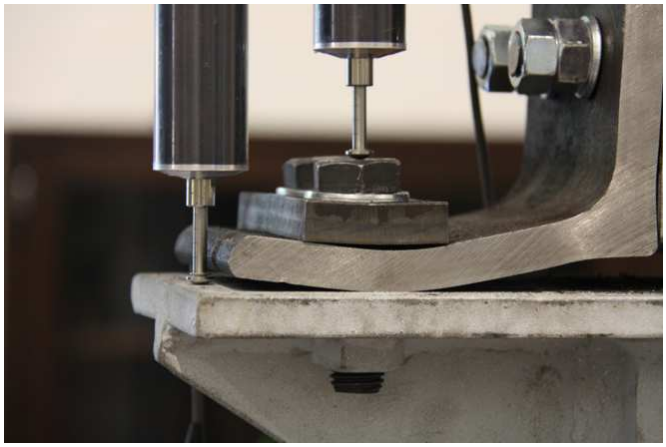

Figure 3.23: Angle edge lift on specimen A3.

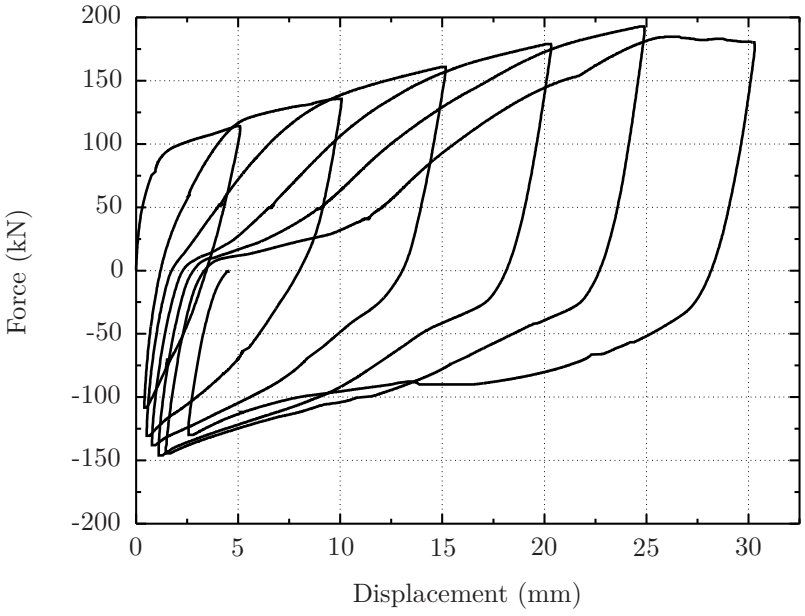

Figure 3.24: Hysteretic response diagram of specimen A3 cyclic test.

Figure 3.25: Picture of cracking in specimen A3.

3.2.5.4 Specimen A4

The deformed shape of specimen A4 test is shown in Figure 3.26. The specimen without washer plates presented the plastic hinge in the line of the bolt holes, as expected, and the contact between the angles and the base started in the line of the bolts. From the residual deformation in the angles shown in Figure 3.27 it is clear that the edge of the angles did not lift, thus the welding fulfilled its purpose.

The hysteretic response diagram is shown in Figure 3.28. The cyclic behaviour was as desired once the stiffness problem recorded in the first three specimen was solved by the use of the welding. The maximum displacement was 20 mm. Observing the response diagram it is clear that for 25 mm displacement, failure had already been achieved. From Figure 3.29 it is also possible to see the rupture in the plastic hinge below the bolts of the horizontal leg, being the same in both angles. This specimen was the one that achieved the smallest maximum displacement, this fact is assigned to the welding, that restrains not only the vertical displacements, but also the horizontal displacements, increasing the tension in the horizontal legs. In the previous tests, the horizontal displacements were a function of friction, the tolerances of the bolt holes and the stiffness of the bolts, resulting in some small horizontal displacements.

Specimen A4 was considered a good solution and was applied in a hybrid rocking wall system that is described in Chapter 4. After this test it was decided that a solution without any welding should be considered, thus a second alignment of bolts was introduced in specimen A5 to substitute the welding. In construction it is recommended that only bolted solutions are used on site to facilitate the assembly and guarantee the quality of the execution.

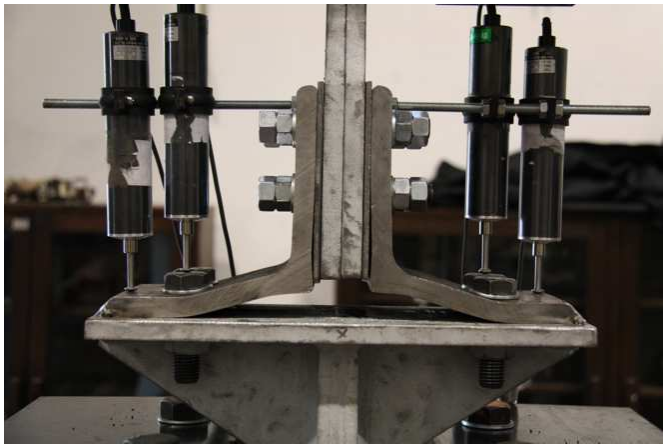

Figure 3.26: Picture of deformed specimen A4.

Figure 3.27: Plastic deformation of specimen A4.

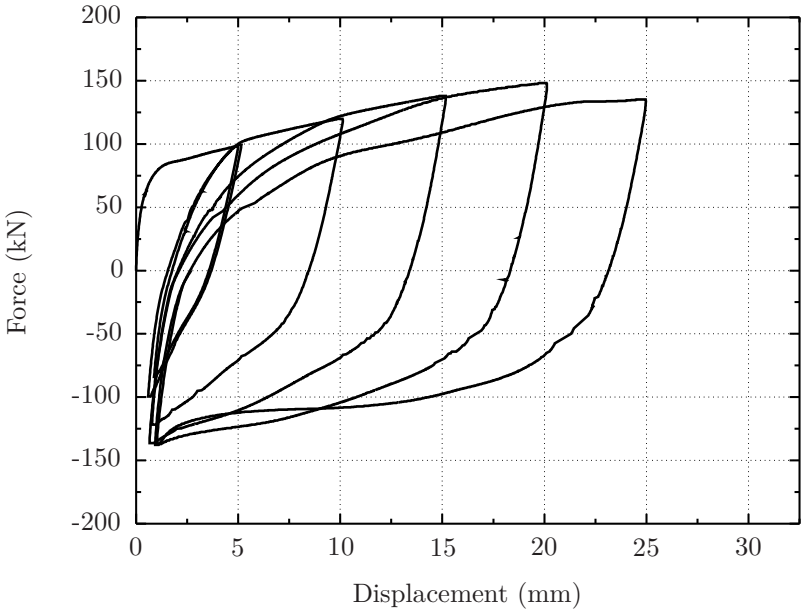

Figure 3.28: Hysteretic response diagram of specimen A4 cyclic test.

Figure 3.29: Picture of cracking in specimen A4.

3.2.5.5 Specimen A5

To avoid the lifting up of the edges of the horizontal legs without welding, it was decided to use two lines of bolts. For that reason, a larger angle (L200x200x16) had to be used in specimen A5.

The deformed shape of specimen A5 test is shown in Figures 3.30 and 3.31. The deformation pattern was similar to the one of specimen A4, with the plastic hinges of the horizontal legs located along line of the bolts. From the residual deformation in the angles shown in Figure 3.32 it is clear that the edge of the angles did not lift, thus the second line of bolts fulfilled its purpose.

The displacements of the hysteretic response diagram (Figure 3.34) were measured between the vertical legs and the base, using transducers D2 and D5 instead of D1 and D6, due to a problem in last cycles when the transducer D6 suffered an unexpected rotation (Figure 3.10b). These two transducers were located in the second line of bolts and the displacements measured are similar to transducers D1 and D6 until the moment when D6 rotated. The cyclic behaviour was the desired one as the stiffness problem observed in the first three specimens was solved by the use of the second line of bolts. The achieved displacement was 30 mm and observing the response diagram it is not possible to see any evidence of failure. However, in Figure 3.33 it is possible to see cracks in a plastic hinge located near the fillet of the angle, meaning that this specimen was close to failure.

The results of specimen A5 are considered as good and this solution was used in a hybrid rocking wall system that is described in Chapter 4. This solution was the final and recommended solution for the angles as energy dissipaters for cyclic action.

Figure 3.30: Picture of general deformation of specimen A5.

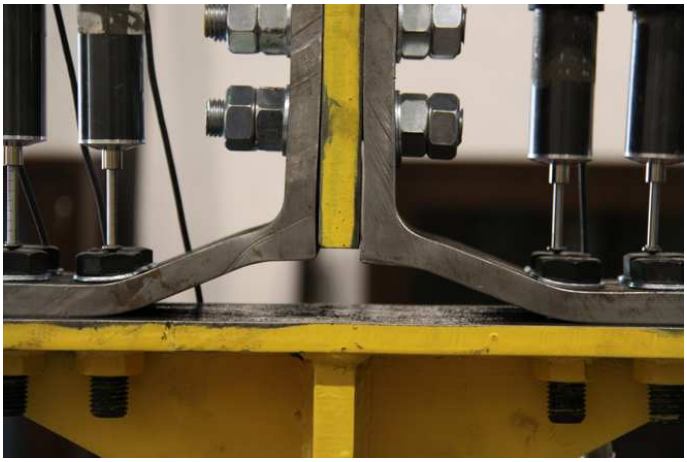

Figure 3.31: Picture of deformed specimen A5.

Figure 3.32: Plastic residual deformation of specimen A5.

Figure 3.33: Picture of cracking in specimen A5.

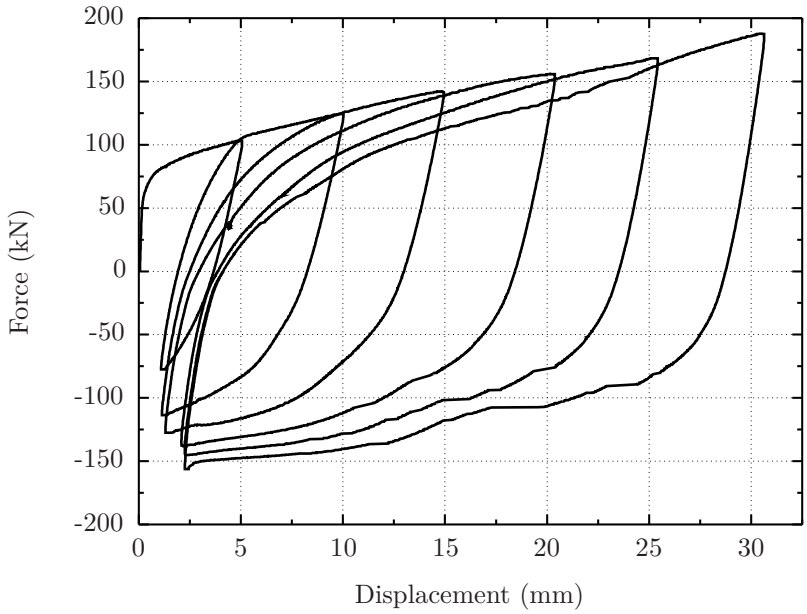

Figure 3.34: Hysteretic response diagram of specimen A5 cyclic test.

3.3 Numerical models

To help and support the experimental optimisation process described in Section 3.2, finite element models were used. A parametric study to produce force-displacement diagrams for other cases was also made. The finite element program Adina (Bathe, 2010) was used for the modelling.

The two final solutions of the experimental specimens, specimens A4 and A5, were used to calibrate the numerical modelling. These two specimens had respectively, welding along the edges of the horizontal legs and an additional line of bolts in each horizontal leg.

The numerical results presented in this section are the result of several model iterations and simplifications. The first simplification introduced was the development of 2D models instead of 3D. The 3D model would have been more precise, and an initial attempt at 3D modelling was made. This option was dropped because of the aim of developing a parametric study, which would have been a much harder task, due to the corresponding huge increase in computational effort.

With reference to the 2D model, simplifications were made and some alternative models were studied. The bolts were modelled only in the horizontal legs, but models with bolts in the vertical legs with prestress were also considered leading to the conclusion that restraining the horizontal displacements was a simplification with minor influence in the angles final response. To apply prestress in the bolts of the horizontal legs, linear elements with pipe sections were used to model the bolt bodies and 2D solid elements to model the bolt heads. Standard washers were not modelled in the final solutions, but were tested. The option for not modelling the standard washer was due to two reasons: the post-yield response changed with the inclusion of the standard washer, but not significantly and the steel characteristics of the standard washer were not experimentally obtained.

The mesh was also analysed. The 2D models did not present computational problems, the monotonic models took around fifteen minutes to run, so the meshes used had relatively large areas with small elements and there was no need for a more refined optimisation. The fillet was the region where the mesh raised more doubts and more variations were made to get confidence in the final results. To have confidence in the modelled fillet, a model where the mesh in the corner was generated all at once, including the fillet, was made, and the results were not influenced by that.

3.3.1 Modelling of the specimens

The modelling of specimens A4 and A5 was made with cyclic and monotonic actions. The cyclic action had the intention of reproducing the experimental tests. The monotonic action was applied to obtain a force-displacement diagram, to estimate maximum forces and to calibrate the models in order to do the parametric study presented in Section 3.3.2.

The dimensions of the modelled specimens are presented in Figure 3.35. The angles had already been described in Section 3.2.1, but in the parametric study the distance g, between the centre of the bolt in the horizontal leg and the face of the vertical leg as well as the angle thickness t, were variable. In the case of the tested specimens, the distance g was 80 mm for specimen A4 and 89 mm for specimen A5.

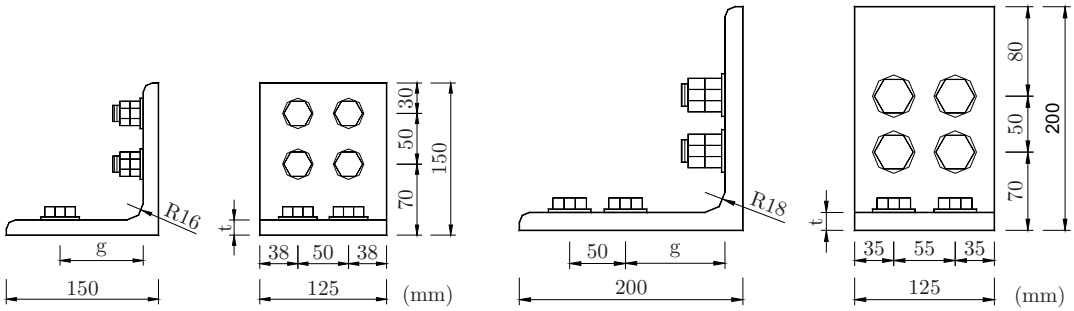

(a) Angle for specimen A4. **(b)** Angle for specimen A5.

Figure 3.35: Dimensions of the angles used for modelling.

3.3.1.1 Specimen A4

The 2D mesh of specimen A4 is shown in Figure 3.36. Two symmetry simplifications were used: one in the middle plan between angles and the other in the middle plan of the angles, resulting in the model of only half an angle. The modelled angle had two bolts in the vertical leg and one bolt in the horizontal leg and a weld along the edge of the horizontal leg.

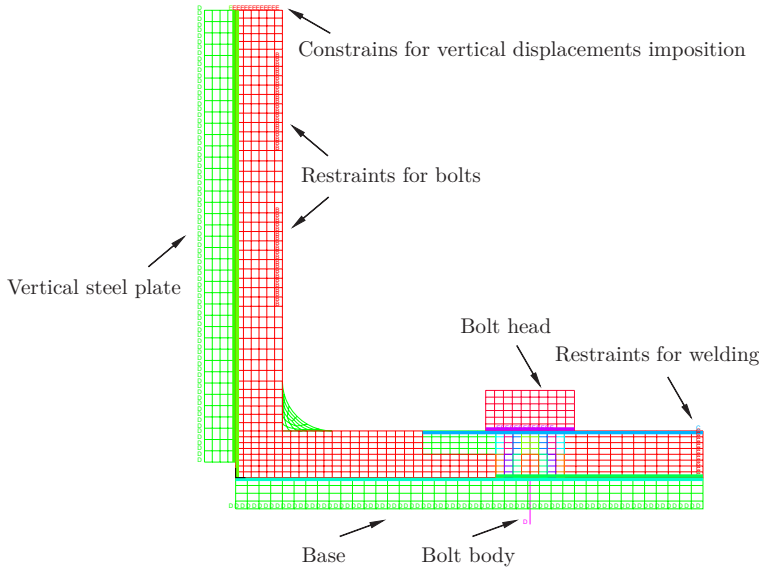

Figure 3.36: Adina mesh for the L150x150x15 A4 tested specimen (different colours correspond to different finite elements).

The steel angle was modelled with 2D solid elements, having a 625 mm width. In the horizontal leg, the 22 mm diameter M20 bolt hole was modelled through the variation of the 2D solid elements width. The hole was modelled using 8 different widths, in a total of 64 solid elements. The angle was modelled with 633 elements, using 9 nodes 2D solid elements and a stress-strain relation made to fit the experimental tests results as can be seen in Figure 3.37.

In some particular regions, namely below the left corner of the bolt head and in the angle fillet the strain was allowed to go beyond the limit shown in the diagram. This solution was needed to solve numerical problems due to stress concentrations.

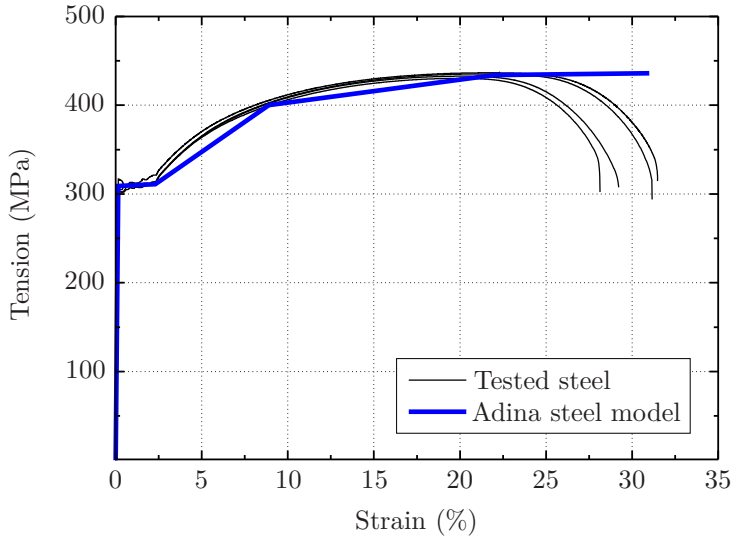

Strain (%)	Stress (MPa)
0.0	0.0
0.15	309
2.3	311
8.9	400
22.0	434
31.0	436

Figure 3.37: Stress vs strain relation of steel used in Adina for specimen A4.

The bolt in the horizontal leg of the angle was modelled with two different solutions for the head and for the body. To model the bolt head, 60 2D solid elements of 9 nodes were used with 30.0 mm width. The bolt body was modelled using a solid pipe section element with 17.7 mm diameter and 30 mm length, corresponding to the thickness of the angle plus the base steel plate. The head and the bolt body were connected by rigid links between the top of the bolt body and the base of the bolt head. For the bolt, an elastic stress-strain relation was used considering an elastic modulus of 210 GPa. A prestress force of 140 kN was applied to the body of the bolt.

The boundary conditions of the angles were the bolts in the horizontal and vertical legs, the welding along the edge of the horizontal leg, the base in contact with the horizontal leg and the vertical steel plate in contact with the vertical leg.

The bolt in the horizontal leg was modelled as described due to its importance in the stiffness of the angle. The bolts in the vertical leg were simulated by blocking the horizontal displacements. Some changes were made to evaluate the importance of modelling these bolts in the vertical leg and the conclusion was that blocking the horizontal displacements was good enough. The welding was modelled by blocking all the possible movements of the edge of the horizontal leg.

The base plate below the angle and the vertical steel plate were modelled with 2D solid elements which were fixed.

Contact surfaces and contact pairs were introduced to only allow compression between the angle and the other parts. Three contact pairs were defined: one between the angle and the bolt head, another between the angle and the base plate and a third one between the angle and the vertical steel plate. The Coulomb friction coefficient between surfaces was considered as 0.2.

Two different actions were applied: one cyclic to compare directly with the experimental tests and one monotonic to provide an upper boundary of the load for a given displacement. The cyclic action was similar to the one shown in Figure 3.11b, with the adjustments needed to have the same displacements as the experimental tests.

The actions were displacements imposed to a point connected with rigid links to the top of the vertical leg of the angle.

The global response of the numerical model of specimen A4 is shown in Figures 3.38 and 3.39, where the force-displacement can be seen respectively for the cyclic and monotonic actions. The cyclic behaviour is generally good, with the exception of at the end of the unloading/compression part, where the numerical model is more rigid, and in the reloading, where the model is not able to exhibit with much precision the stiffness degradation from cycle to cycle as can be seen in the experimental test. The monotonic response presents a good agreement with the maximum force values obtained in the experimental cyclic test. It has to be highlighted that the rupture displacement of 22 mm reached is an estimation and is sensitive to the chosen mesh. It is also true that the rupture in the cyclic action is different than in the monotonic action and the load path is important to evaluate the correct rupture point.

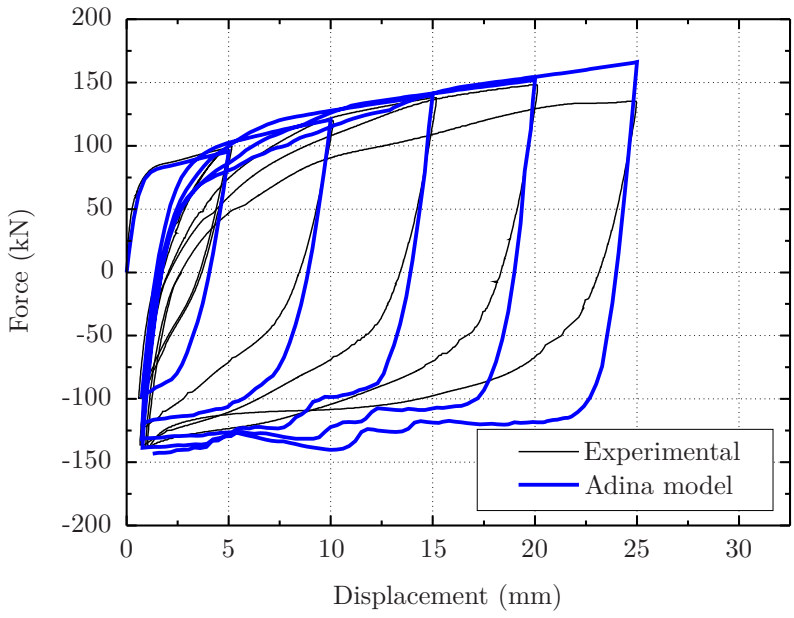

Figure 3.38: Numerical cyclic response for specimen A4.

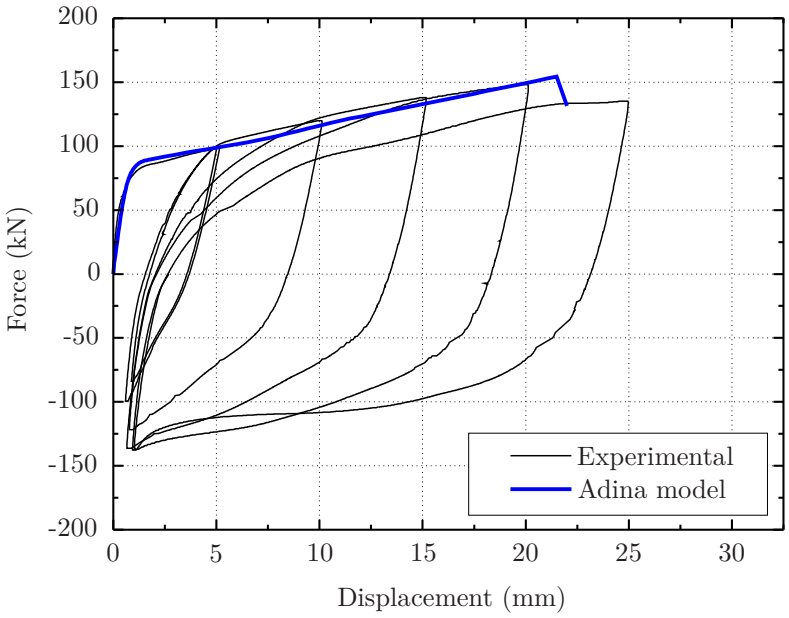

Figure 3.39: Numerical monotonic response for specimen A4.

The distribution of normal stresses in the horizontal and vertical directions are presented respectively in Figures 3.40a and 3.40b for the maximum displacement, one step before the beginning of rupture. In these figures the four regions where the plastic stresses emerge and where rupture may occur, depending on the relative dimensions of the angle can be easily seen. The shear stresses are not shown as they do not affect the failure and are taken into account in the effective stresses.

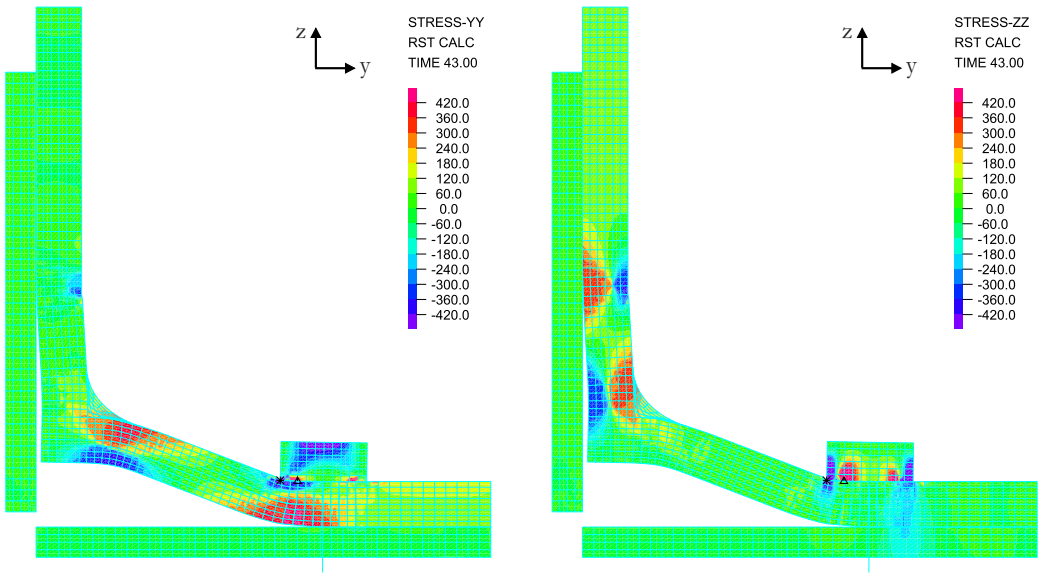

(a) Normal stresses in yy direction.

(b) Normal stresses in zz direction.

Figure 3.40: Numerical stresses, in MPa, for horizontal (yy) and vertical (zz) directions for specimen A4 at maximum displacement.

Figures 3.41a and 3.41b show the effective stresses, obtained according to von Mises yield criteria, one step before the rupture and where an element reaches its maximum strain. The rupture occurs when the strain limit, defined in Figure 3.37, is reached. In this model, the rupture starts simultaneously below the bolt and near the corner of the angle in the horizontal leg, as can be seen inside the two black circles drawn in Figure 3.41b, for a displacement of 22 mm. In the particular case of specimen A4, the rupture occurred below the bolts in the horizontal leg, as can be seen in Figure 3.29.

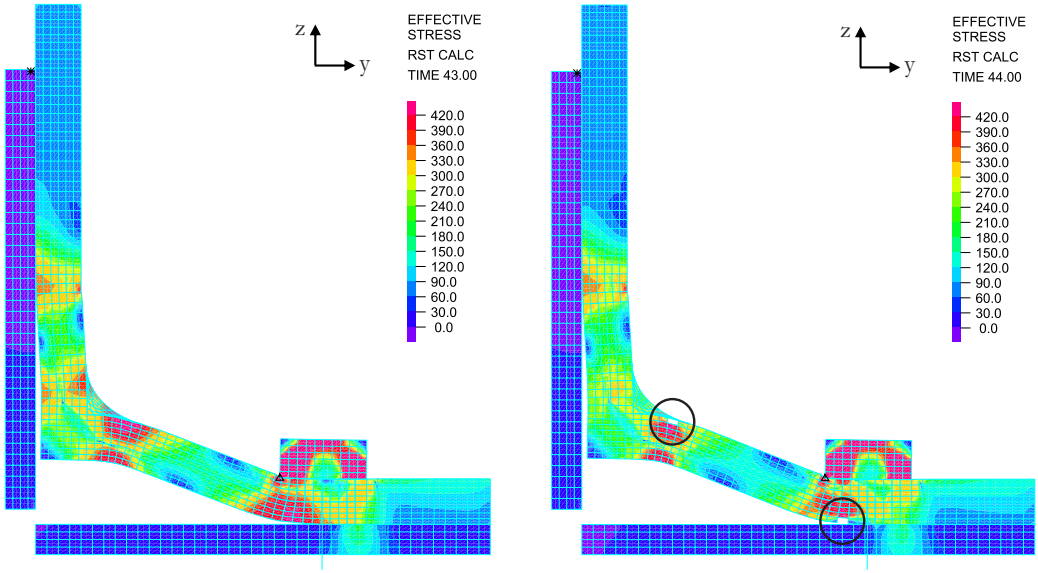

(a) Effective stresses at maximum displacement.

(b) Effective stresses after failure.

Figure 3.41: Effective stresses, in MPa, for specimen A4.

3.3.1.2 Specimen A5

The 2D mesh used for specimen A5 is shown in Figure 3.42. The steel angle was modelled with 2D solid elements with a width of 625 mm. In the horizontal leg, the M20 bolt hole of 22 mm diameter was modelled through the variation of the 2D solid element width. Each hole was modelled using 8 different widths, in a total of 64 solid elements. The angle was modelled with 757 elements, using 9 nodes 2D solid elements and a stress-strain relation made to fit the experimental tests results as can be seen in Figure 3.43.

The bolts were modelled as for specimen A4. The prestress in both bolts of the horizontal leg contribute to mobilise the friction between the angle and the base plate. The bolts in the vertical leg were simulated by blocking the horizontal displacement for the same reasons as in specimen A4.

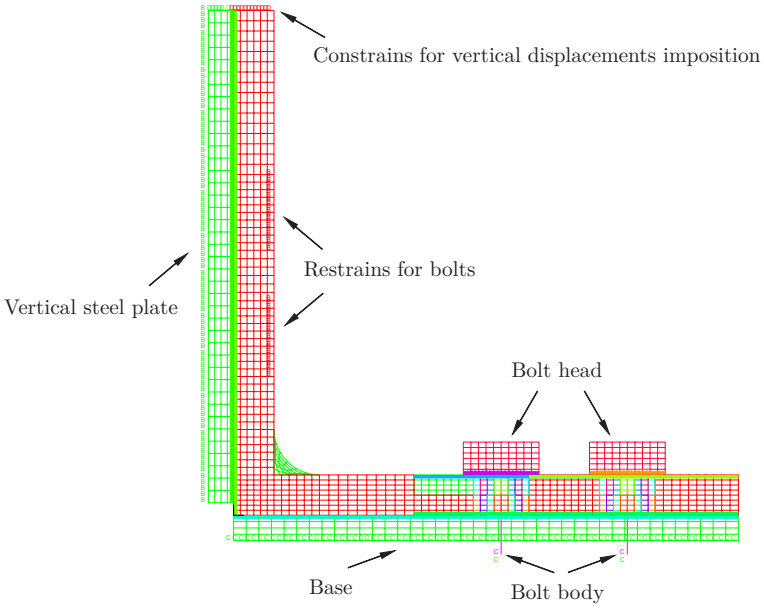

Figure 3.42: Adina mesh for the L200x200x16 A5 tested specimen (different colours correspond to different finite elements).

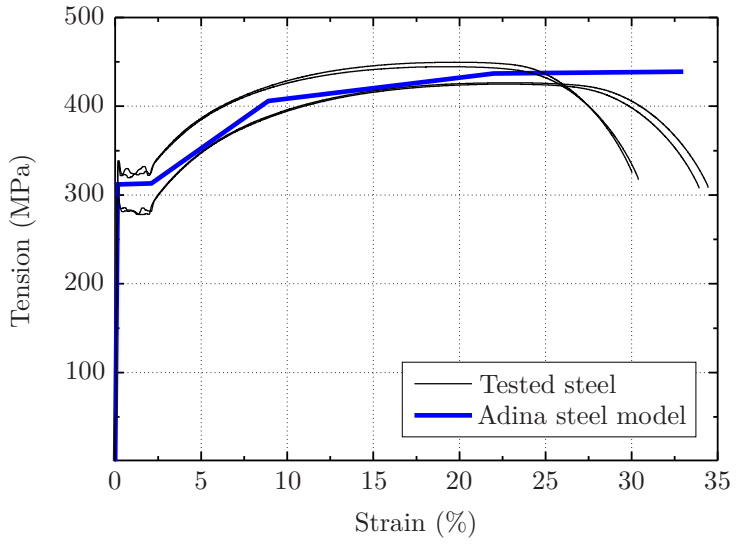

Strain (%)	Stress (MPa)
0.0	0.0
0.15	312
2.1	313
8.9	406
22.0	437
33.0	439

Figure 3.43: Stress vs strain relation of steel used in Adina for specimen A5.

The boundary conditions as well as the actions, were similar to specimen A4. The exception was the vertical steel plate, that in this specimen was modelled to follow the displacements of the vertical leg. This improvement did not have influence in the final result, was made during a search for a more precise model.

The results of the numerical model of specimen A5 are shown in Figures 3.44 and 3.45, where the force-displacement plot can be seen respectively for the cyclic and monotonic actions. The comparison of the numerical results with the experimental ones shows the

same problems as for the specimen A4, described in Section 3.3.1.1. Figure 3.45 shows that the response of the numerical model is less stiff than the response of the experimental specimen, with the force always being lower for the same displacement. This difference can be due to the simplifications used in the numerical model and/or due to the assembly process of the angles tests, that introduced prestress in the angles due to imperfections in the specimens.

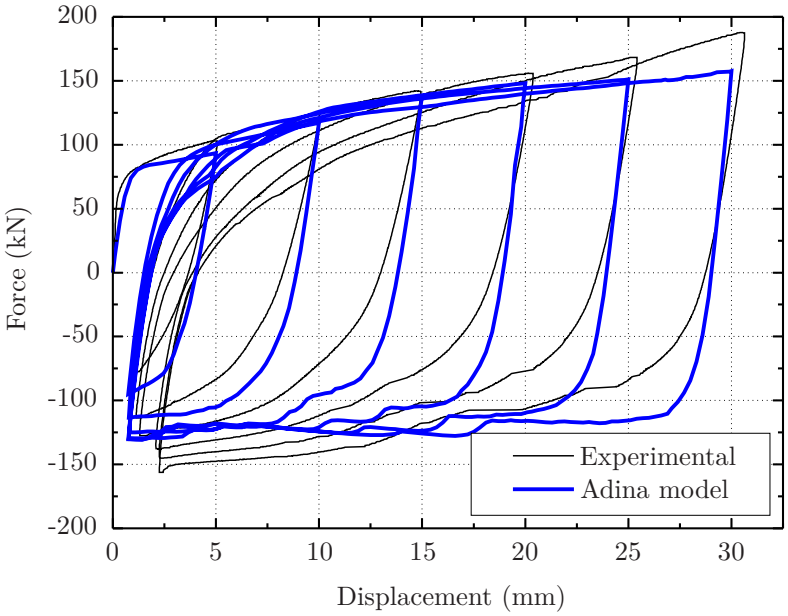

Figure 3.44: Numerical cyclic response for specimen A5.

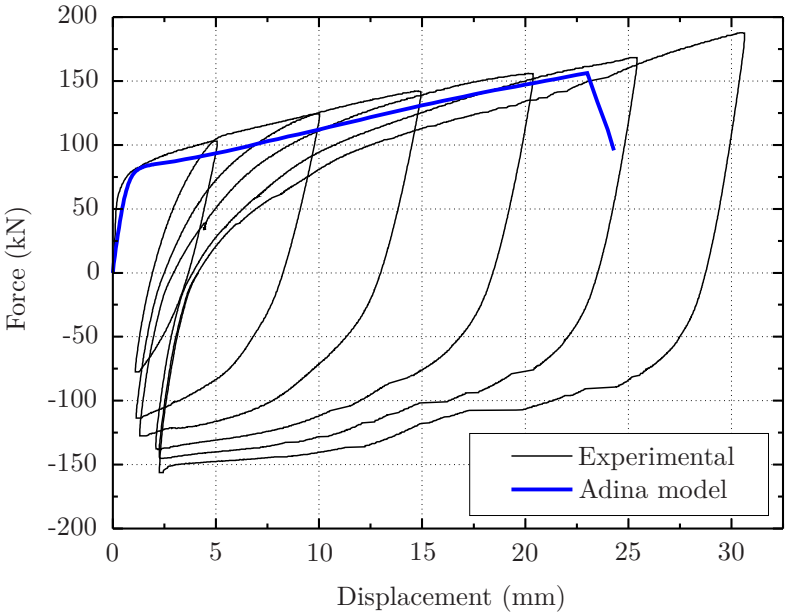

Figure 3.45: Numerical monotonic response for specimen A5.

The distribution of normal stresses in the horizontal and vertical directions are presented respectively in Figures 3.46a and 3.46b for the maximum displacement one step before the beginning of rupture. In these two figures the four regions where the plastic stresses emerge, and where it is possible the failure to occur, may be seen.

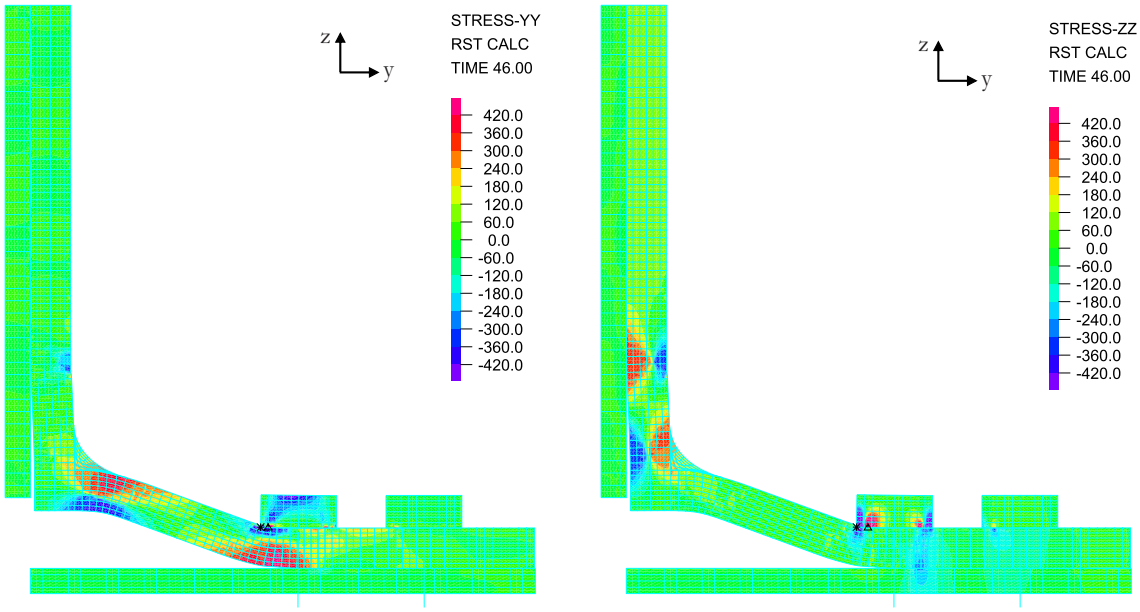

(a) Normal stresses in yy direction.

(b) Normal stresses in zz direction.

Figure 3.46: Numerical stresses, in MPa, for horizontal (yy) and vertical (zz) directions for specimen A5 at maximum displacement.

Figure 3.47a shows the effective stresses at the step just before the rupture. Figure 3.47b shows the step corresponding to the rupture. The first element that reaches its maximum strain is deleted from the model. The ruptures occurs when the strain limit, defined in Figure 3.43, is reached. In this model, the rupture starts below the bolt in the horizontal leg, as can be seen inside the black circle drawn in Figure 3.47b, for a displacement of 24 mm. In the experimental test of specimen A5, the rupture did not occur, but cracks near the corner in the horizontal leg started to open, as is shown in Figure 3.33.

3.3.2 Parametric study

The parametric study aimed to obtain force-displacement diagrams for other dimensions of steel angles. A first design solution for the parametric study was the one of specimen A4 because a smaller angle can be used, having a guaranteed good cyclic behaviour by adding a weld along the edge of the leg attached to the base. A second design solution was the one of specimen A5, in order to avoid the use of welding on the construction site, two lines of bolts were used in the horizontal leg. Both design solutions should have a similar

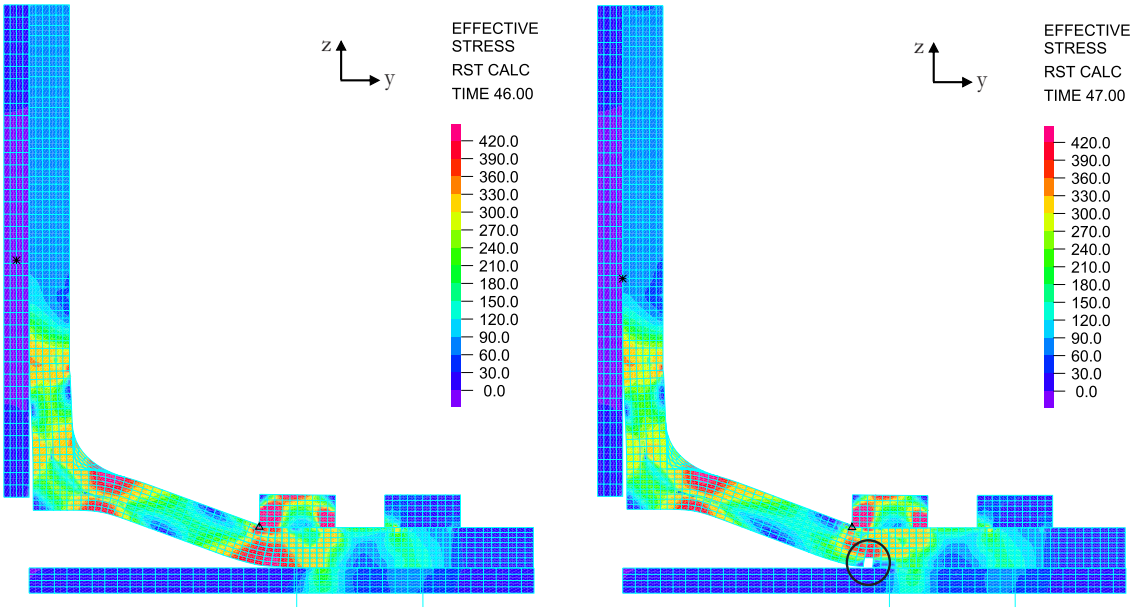

(a) Effective stresses at maximum displacement. **(b)** Effective stresses after failure.

Figure 3.47: Effective stresses, in MPa, for specimen A5.

response. These two design solutions correspond to specimens A4 and A5, being the base numerical model as described in Sections 3.3.1.1 and 3.3.1.2. With the variations in the dimensions some adaptations were made in the number of elements used.

In this study two parameters have been changed: the thickness t and the position g of the bolts in the horizontal leg, as defined in Figures 3.35a and 3.35b. The thicknesses used were 5 mm, 10 mm, 15 mm and 20 mm and the distances g were 60 mm, 70 mm, 80 mm, 90 mm and 100 mm. The steel used was always the same as for specimen A4 and its stress-strain diagram is shown in Figure 3.37.

3.3.2.1 Design solution 1 - welded angle

The numerical model used for this design solution is shown in Figure 3.36. The parametric results are presented in Figures 3.48 and 3.49. For different thicknesses, the scales of the graphs are different because the response forces and displacements showed considerable variations. As referred to above, the displacements corresponding to the failure of the numerical models depend on the mesh used and it cannot be extrapolated to the cyclic actions. Thus the maximum displacement obtained in the models should be seen as an estimation. From the results it can be said that an increase in the thickness of the steel angle has two consequences: an increase in the force and a reduction of the maximum displacement corresponding to failure. The distance g can be associated with the lever arm between the two plastic hinges in the horizontal leg of the steel angles and with

the resulting inclination of the horizontal leg, between plastic hinges. It can be observed that increasing g leads to lower steel angle forces and higher maximum displacements, corresponding to failure.

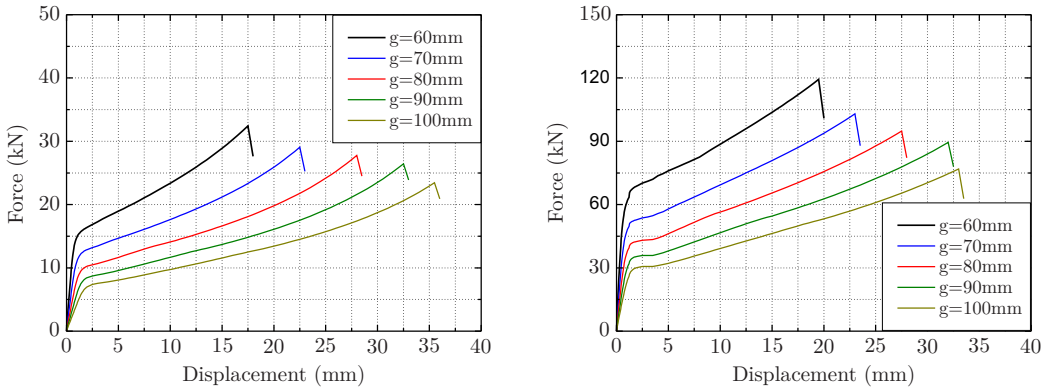

(a) 5mm thickness. **(b)** 10mm thickness.

Figure 3.48: Design solution 1 - parametric study for welded solution with 5 mm and 10 mm thickness.

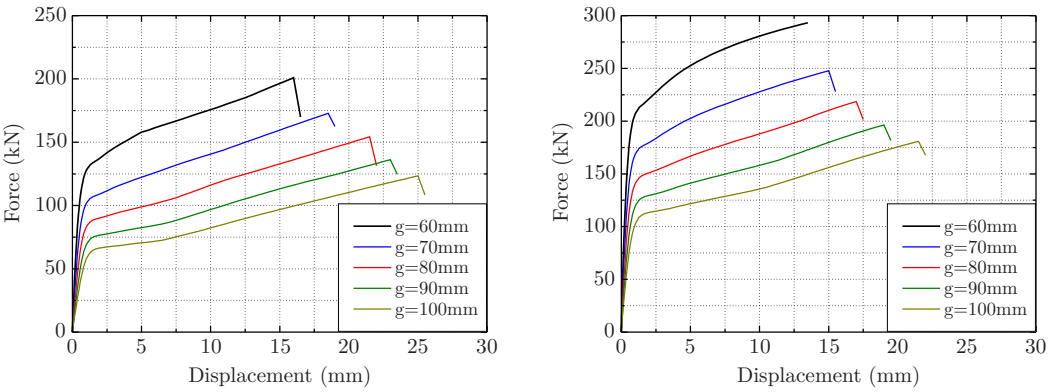

(a) 15mm thickness. **(b)** 20mm thickness.

Figure 3.49: Design solution 1 - parametric study for welded solution with 15 mm and 20 mm thickness.

3.3.2.2 Design solution 2 - two lines of bolts

The numerical model used in the design solution 2 is shown in Figure 3.42. The parametric results are presented in Figures 3.50 and 3.51. From these results, the conclusions are identical to design solution 1.

Comparing the two design solutions, the responses were similar, having small variations without any apparent trends.

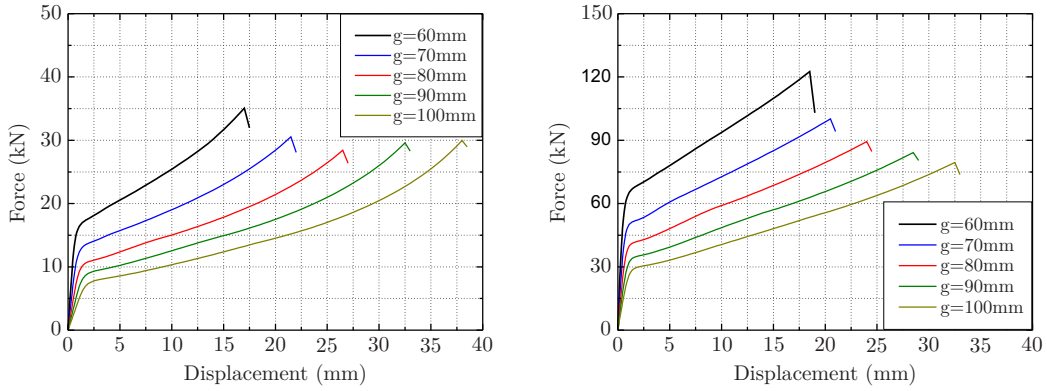

(a) 5mm thickness. **(b)** 10mm thickness.

Figure 3.50: Design solution 2 - parametric study for the two lines of bolts solution with 5 mm and 10 mm thickness.

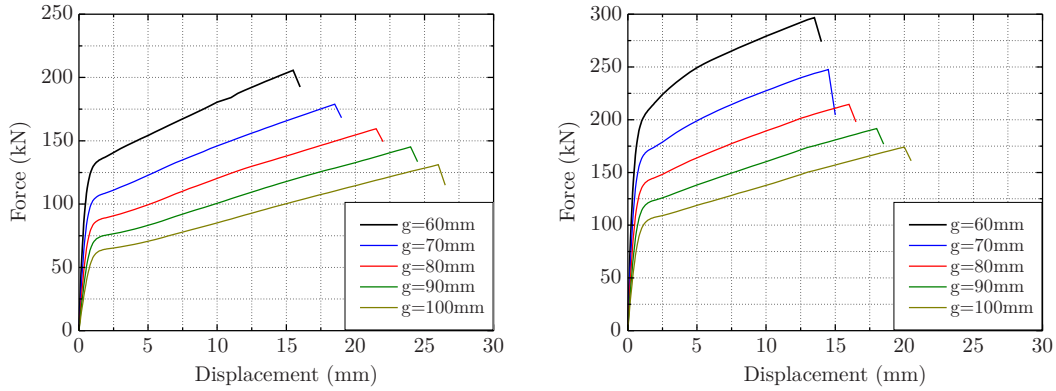

(a) 15mm thickness. **(b)** 20mm thickness.

Figure 3.51: Design solution 2 - parametric study for the two lines of bolts solution with 15 mm and 20 mm thickness.

3.4 Analytical methodology

An analytical method was developed to estimate the response of the angles in the elastic and plastic range. The experimental tests and the numerical analysis showed that four plastic hinges can be formed in sections A, B, C and D as shown in Figure 3.52. Plastic hinges in sections A and B are formed first, followed by the plastic hinge in section C. The plastic hinge in section D may or may not occur for higher displacements.

Sections A and D are not in the centre of the bolt holes, as is shown in Figure 3.29. For calculation purpose it will be assumed that the plastic hinge is formed at $\frac{1}{3}.d_0$ from the bolt holes centre, d_0 being the respective bolt hole diameter. The position of sections B and C are aligned with either side of the fillet.

The distances between plastic hinges, l_{AB} and l_{CD}, in Figure 3.52 are considered to be given by the expression 3.1 and 3.2.

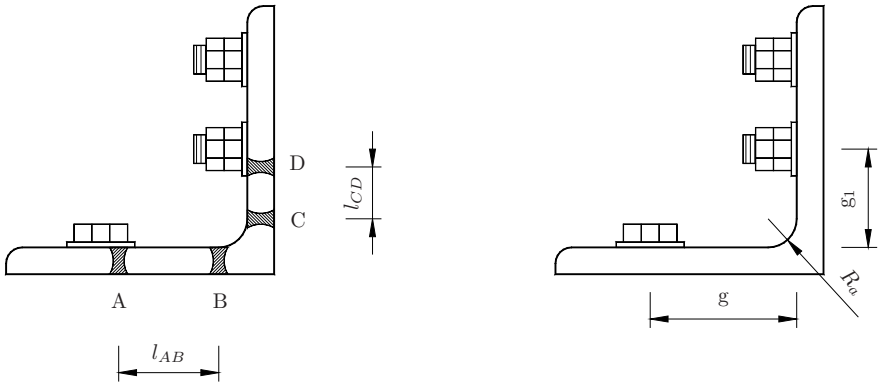

Figure 3.52: Possible plastic hinges in the angles and distances to bolt holes.

$$l_{AB} = g - R_a - \frac{d_0}{3} \tag{3.1}$$

$$l_{CD} = g_1 - R_a - \frac{d_0}{3} \tag{3.2}$$

where,

l_{AB} is the distance between the plastic hinges of sections A and B;
l_{CD} is the distance between the plastic hinges of sections C and D;
R_a is the angle fillet radius;
d_0 is the bolt hole diameter;
g is the distance between the inner face of the vertical leg and the centre of the bolts holes in the horizontal leg;
g_1 is the distance between the upper face of the horizontal leg and the centre of the bolts holes in the vertical leg.

- *Elastic range*

The elastic behaviour of the steel angles goes from the initial load until the first yield strain is reached. It will be assumed that the sections A and B reach the yield strain simultaneously. Based on this assumption, equation 3.3, to estimate the steel angle yielding force F_y, can be written. The yielding of sections A and B occur for a bending moment M_y given by the equation 3.4, assuming pure bending acting in the section with the maximum strain equal to the yield strain ε_y. To estimate the displacement in the elastic range the equation 3.5 is used. The displacement is calculated considering the shear and bending deformation of the horizontal leg between points A and B. An eventual rotation in point A and the axial deformation of the vertical leg are not considered.

$$F_y = \frac{2M_y}{l_{AB}} \tag{3.3}$$

$$M_y = \frac{f_y b t^2}{6} \tag{3.4}$$

$$d_{el} = \frac{F.l_{AB}}{GA_v} + \frac{(2M_A - M_B).{l_{AB}}^2}{6EI} \tag{3.5}$$

where,

F is the steel angle force;
F_y is the steel angle yielding force;
M_A is the bending moment in section A;
M_B is the bending moment in section B;
d_{el} is the angle elastic displacement;
b is the steel angle length;
t is the steel angle thickness;
G is the shear modulus;
A_v is the shear area;
E_s is the steel modulus of elasticity;
I is the second moment of area.

- *Post-yield range*

The estimation of the post-yield response of the angle is obtained by considering the physical and geometrical nonlinearity. The method that will be presented had as a starting point Garlock et al. (2003). A deformed representation of the angle is shown in figure 3.53 considering fixed ends for the horizontal and vertical legs in the bolts closer to the fillet. The fixation forces and the displacements involved are also represented in the axis of the angle. The horizontal displacement d_H will be considered zero, a simplification that is supported by the tests, as can be seen by the deformed positions of the angles in Figures 3.15, 3.18, 3.22, 3.26 and 3.31.

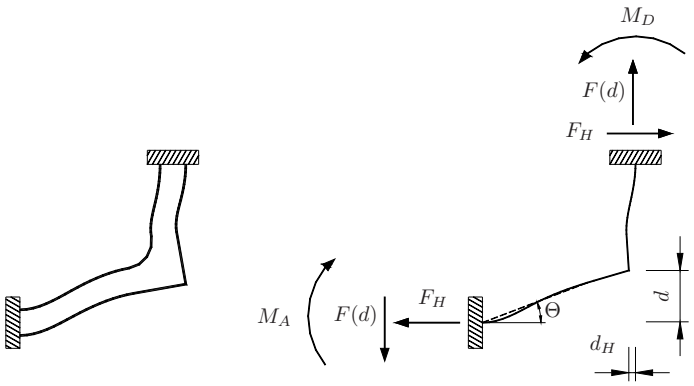

Figure 3.53: Deformed angle and fixation forces.

The basic expression used to estimate the angle force in the post-yield range is similar to the one for the elastic range, but using some corrections. Expression 3.6 gives the angle

force with a correction for the material hardening. This expression calculates the force assuming that the bending moments in sections A and B are equal and are given by the expression 3.7 and has taken into account the material hardening factor, k, given by the expression 3.8. The bending moment is calculated as a function of the yield strain position, c, and results from the equilibrium of the section, as represented in Figure 3.54. To obtain the bending moment no material hardening is considered. The maximum stress needed to calculate k is obtained using the maximum strain in the section and the stress-strain relation of the steel under study.

$$F_{mh} = \frac{2M(c)}{l_{AB}}k \tag{3.6}$$

$$M(c) = f_y b\left[c(t-c) + \frac{(t-2c)^2}{6}\right] \tag{3.7}$$

$$k = \frac{\sigma(\varepsilon_{max})}{f_y} \tag{3.8}$$

where,

F_{mh} is the angle force including material hardening;
$M(c)$ is the bending moment after the yield point;
c is the distance between the yield strain and the maximum strain in the section (see Figure 3.54);
k is the material hardening factor;
$\sigma(\varepsilon_{max})$ is the stress at the fibre with the maximum strain;
f_y is the steel yield strength;
ε_y is the steel yield strain.

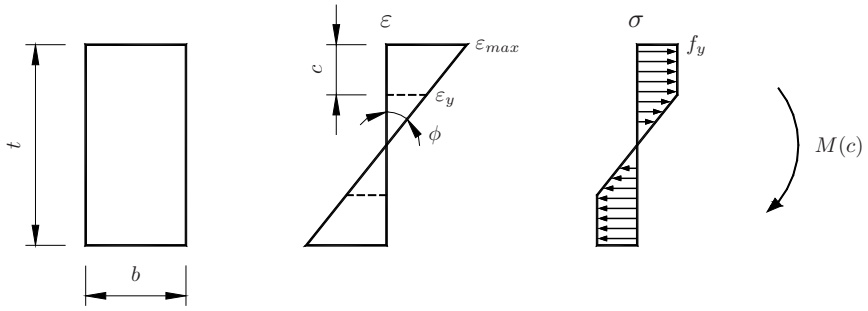

Figure 3.54: Section strains and stresses diagrams.

The geometrically nonlinear behaviour is considered by adding the bending moment applied by the horizontal force F_H in the deformed position represented in the Figure 3.55. The total force is given by expression 3.9, where F_{geom} is obtained by imposing equilibrium with expression 3.10. The horizontal force F_H in the angle can be calculated with the equation 3.11. The equation is the result of equilibrium in the segment CD,

considering that the horizontal displacement between sections C and D do not influence the equilibrium results. Figure 3.55 shows the fixation forces that were considered for the equation. The bending moments in sections C and D are $a.M_P$, being a a number smaller than two, that is the same as saying that the maximum horizontal force F_H is when both sections, C and D reach the plastic bending moment M_P. Using the experimental results, a should be a number between one and two as the plastic hinge in section C was always present.

This equation was obtained by imposing equilibrium on the free body diagram of the segment AB shown in Figure 3.55

$$F(d) = F_{mh} + F_{geom} \tag{3.9}$$

$$F_{geom} = \frac{F_H.d}{l_{AB}} \tag{3.10}$$

$$F_H = \frac{a.M_P}{l_{CD}}, a \leq 2 \tag{3.11}$$

where,

F_{geom} is the geometrically nonlinear angle force;
$F(d)$ is the total angle force;
d is the angle displacement;
M_P is the plastic bending moment;
F_H is the horizontal force in the angle vertical leg;
a is a constant smaller than 2.

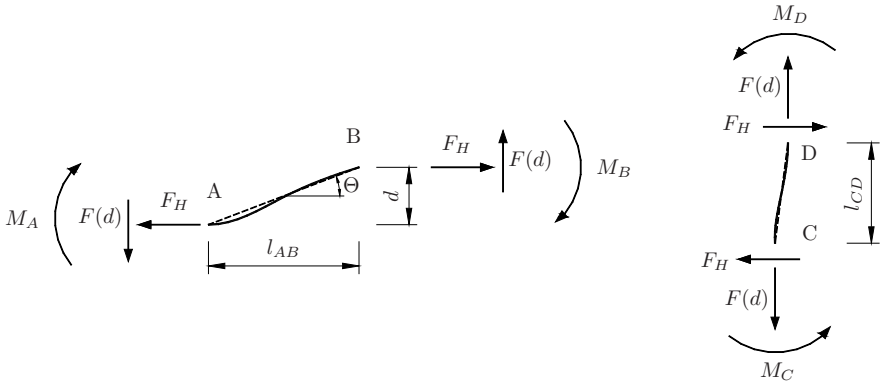

Figure 3.55: Fixation forces in distances AB and CD.

The displacements in the angle are estimated by considering the elastic and plastic contribution of the horizontal leg. The elastic displacement can be calculated using the expression 3.5, being the plastic contribution obtained by considering the rotation of the plastic hinges in section A and B. The total displacement is given by the expression 3.12,

where Θ is the rotation of the plastic hinges obtained by the expression 3.13. To calculate the plastic hinge rotation, the section curvature and the plastic hinge length are needed. The section curvature can be seen in Figure 3.54 and the respective analytic expression is 3.14. The plastic hinge length is a difficult parameter to define. After the plastic hinge is completely formed a length equal to the thickness can generally be assumed to be a good approximation.

It should be highlighted that the elastic displacement depends on the force. However, the force, due to the geometrically nonlinear behaviour, depends on the displacement. This leads to an iterative procedure to obtain the force and the displacement. As a simplification, the elastic displacement can be calculated using only the F_{mh} force, the F_{geom} being obtained from the resulting displacement. As the geometrically nonlinear force involves large displacements and in this case, the rotation of the plastic hinges contributes to the main part of the displacement, this simplification is considered to be satisfactory in most cases.

$$d = d_{el} + \Theta.l_{AB} \tag{3.12}$$

$$\Theta = \phi.l_p \tag{3.13}$$

$$\phi = \frac{2\varepsilon_y}{t - 2c} \tag{3.14}$$

where,

Θ is the angle horizontal leg rotation;
ϕ is the section curvature;
l_p is the plastic hinge length.

As an alternative to the formulation above, after the formation of the two plastic hinges in the horizontal leg equation 3.15 can also be used to estimate the force $F(d)$. This equation was obtained by imposing equilibrium on the free body diagram of the segment AB shown in Figure 3.55. This is useful as it allows the calculation of the force directly from a given displacement.

$$F(d) = \frac{2M_P.k + F_H.d}{l_{AB}} \tag{3.15}$$

- *Application of the analytical method*

To evaluate the validity of the analytical method presented herein, the expressions were used to estimate the response of specimens A4 and A5. The final results are presented in Figures 3.56 and 3.57. The stress-strain relation used for each specimen were presented

respectively in Figures 3.37 and 3.43. This constitutive relations were needed for the f_y and k determination. After the calculation of the yield point, using expression 3.3, the force was controlled by the c in equation 3.7. Due to the difficulty in obtaining the gradual formation of the plastic hinge with the spread of the plastic strains, the first c used was $c = t/4$ and an estimated plastic hinge length of $l_P = t$ was considered. To estimate the displacement in the plastic range, the elastic displacement portion was calculated using only the F_{mh} portion of the force.

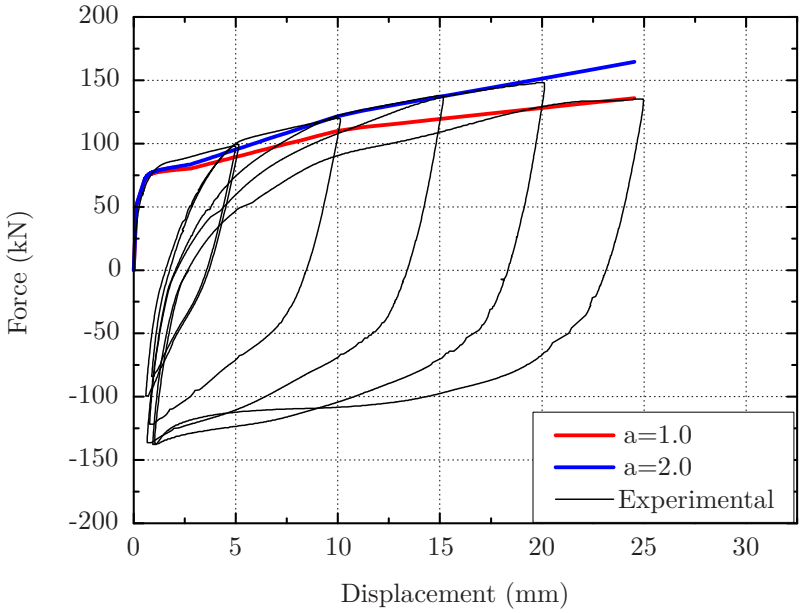

Figure 3.56: Analytical response of specimen A4.

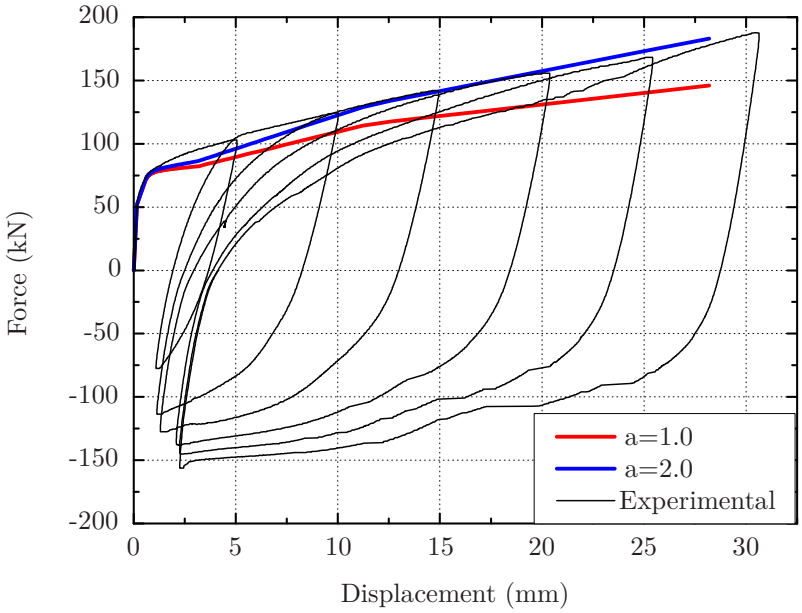

Figure 3.57: Analytical response of specimen A5.

The results are presented for a=1.0 and a=2.0 in the equation 3.11, that are considered to be the minimum and maximum values that the parameter can be considered to be. The results show a good agreement with the experimental tests, especially when a=2.0 for large displacements. This means that the four possible plastic hinges referred to in Figure 3.52 are formed. At the point corresponding to the elastic range limit, using equation 3.3, the force is equal to 51 kN in specimen A4 and 52 kN in specimen A5, the point after which the stiffness gradually decreases. The range of displacements where the good agreement is not so accentuated is after the curve corresponding to the reduction in stiffness.

3.5 Conclusions

In this chapter, the development of steel angles to work as energy dissipaters was studied. Two types of design solutions achieved the desired behaviour, presenting stable cycles with energy dissipation capacity during cyclic actions. The control of the prying action was the main problem and was overcome in these two design solutions by using a weld along the edge of the steel angle and by using a second line of bolts. The first solution allowed the use of a smaller angle while the second is a more flexible design solution to facilitate assembly on construction sites and more ductile. To support the experimental work, a numerical analysis was also developed. The numerical analysis was carried out to model the specimens tested, helping with the understanding of their response and to carry out a parametric study on steel angles with other dimensions. Finally, an analytical model was presented, showing good agreement with the experimental tests, creating the possibility of obtaining an estimation of the nonlinear response of a steel angle using simple equations.

The two solutions that responded with the desired behaviour were designed for the same force. The solution with the welding along the edge had a thickness of 15 mm while the solution with a second line of bolts a thickness of 16 mm. To have similar responses, the thicker angle was designed with smaller gage lengths (the distance between the bolt in the horizontal leg and the heel of the angle). These differences resulted in different maximum displacements. The solution with the welding along the edge reached a displacement of 20 mm while the solution with the second line of bolts reached 30 mm. The welding could also influence the rupture point of the angles, as it has the disadvantage of restraining not only the vertical displacement to the base, but also the horizontal displacements, resulting in higher tensions in the legs. From the tests carried out it should be mentioned that both solutions achieved a similar and good cyclic behaviour, but the maximum displacement is quite different between solutions.

Chapter 4

Post-Tensioned Rocking Wall Systems

4.1 Introduction

The main subject of this research is the behaviour of post-tensioned rocking wall systems under cyclic actions. These structural systems are designed to have a recentring behaviour, resulting in negligible residual displacements. Post-tensioned rocking walls should have an elastic response without residual displacements. When energy dissipation is added to the system it becomes hybrid. In hybrid systems residual displacements can be expected, depending on the balance between the post-tensioning and the energy dissipaters bending moments, but should be negligible.

The experimental testes were carried out in the DEC/FCT/UNL structural laboratory. To evaluate the experimental difficulties and optimise the experimental setup, three post-tensioned rocking walls were tested. After these preliminary tests, two rocking wall hybrid systems were tested using two different steel angle solutions as energy dissipation devices. The development of these steel angle solutions is described in Chapter 3. Finally, a post-tensioned rocking wall was tested using the same precast wall used in the second test on hybrid systems in order to compare the behaviour and results with and without energy dissipaters. This final test was made because the walls tested with energy dissipaters were different from the three previously tested as this last one had stiffening plates on the edges.

4.2 Description of experimental testing

4.2.1 Tests setup

The testing setup is shown in Figure 4.1 and was similar for all the walls. This figure corresponds to specimen RM1.

The base, below the wall, was a rigid reinforced concrete foundation horizontally fixed to the reaction wall by two post-tensioned bars and vertically fixed to the floor by four post-tensioned bars. Two reinforced concrete bases were constructed. One was used for the fist four tests, whilst the other base was used in the final two tests.

The rocking walls were all post-tensioned to the base by two unbonded strands, which allowed the lifting of the wall with the respective stretching of the strands. In specimens RM4 and RM5 the wall was also connected to the base with two steel angles, that were designed to yield. In the first specimen, two displacement blockers were used with no additional material between the wall and the base, in all other specimens the displacement blockers were excluded and grout was used to adjust the wall to the base. For the final two tests, a bracing system was implemented, to keep the wall vertical.

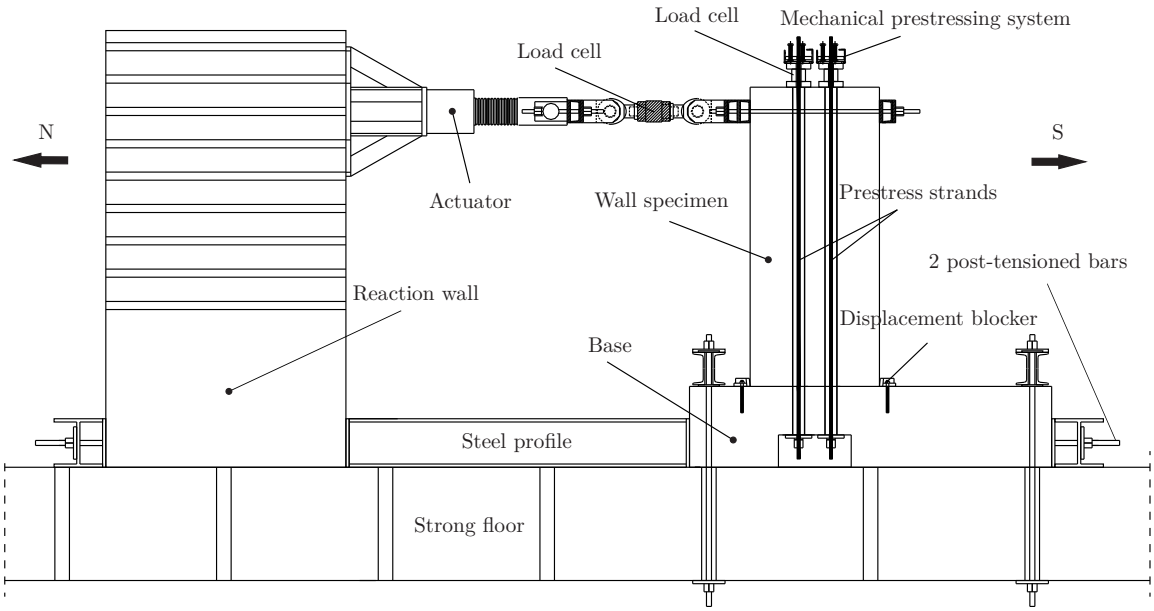

Figure 4.1: Side view of the rocking wall tests setup.

The application of the vertical post-tensioning forces was made using a mechanical prestressing system designed in the FCT/UNL. This system has two steel plates that are separated by screwing the three bolts in the top plate against the bottom plate, being the strand anchored over the top plate. The bottom end of strands was the passive end. In order to assemble and position the anchorage, an opening was made in the base.

The wall specimens were horizontally pushed and pulled against a 2.70 m high reaction wall. The actuator was positioned at a height of 2.20 m, resulting in a 1.70 m lever arm, taking into account the 0.50 m foundation. These values are approximations, more accurate measurements will be presented for each test.

4.2.2 Conventions

The positioning terminology is based on the cardinal compass points of the laboratory and is shown in Figure 4.2. The actuator is aligned in a north-south direction and it was considered that the pushing action was a negative force whilst the pulling action was positive. The counterclockwise rotation about the vertical wall axis was considered positive and these conventions were followed for all forces, displacements and drifts.

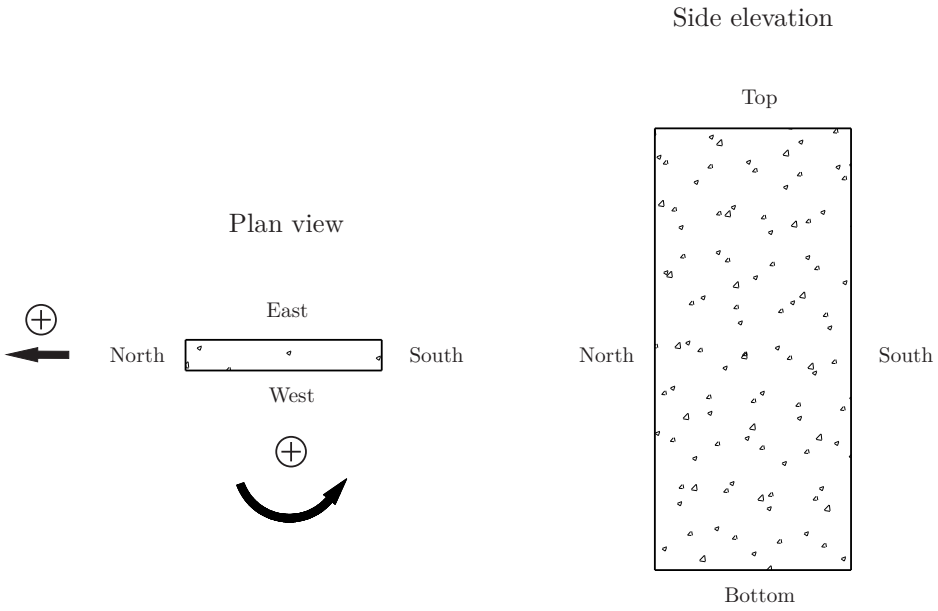

Figure 4.2: Positioning terminology and conventions.

4.3 Preliminary tests on post-tensioned rocking walls

4.3.1 Introduction

The rocking walls experimental program started with three preliminary tests with the aim of gaining knowledge and detecting problems associated with this type of tests. The wall specimens were designated RM1, RM2 and RM3. The second specimen (RM2) was made using the inverted RM1 wall. The walls were designed to rock on the base foundation, concentrating the nonlinear behaviour on that connection. The connection to the foundation was made using two post-tensioned strands, strand N and strand S. The first two

tests were post-tensioned with reduced energy dissipation and the third test was designed to have some energy dissipation by the addition of a new material (epoxy resin and cork) to the northern and southern edges of the horizontal connection.

4.3.2 Specimens

4.3.2.1 Specimen RM1

The first test setup is shown in Figure 4.3. In this test, the wall was placed on top of the foundation without any type of mortar or mechanical connection. An attempt to plane the connecting surfaces of the wall and base, with an angle grinder, was not very successful. This resulted in the wall having a slight inclination in the east-west direction.

In this test procedure the actuator was connected to the wall before applying the post-tensioning. This option was not repeated in the following tests because it led to the introduction of small horizontal forces in the specimen.

4.3.2.2 Specimen RM2

The second test setup is shown in Figure 4.4. After the first test some doubts remained about the effectiveness of the contact between the surfaces of wall and foundation. To overcome this problem, grout was applied between the wall and the foundation. In this specimen, the displacement blockers that had been used on northern and southern sides of the wall were not used. In the first test no visible sliding was noticed and the displacement blockers had the disadvantage of preventing a good assessment of the cracked and spalled concrete cover in those zones. Moreover, the spalled concrete tended to fill the space between the displacement blockers and the wall, creating an eventual additional restriction to the wall rotation.

Before positioning the wall, self-levelling-grout was applied to the foundation, then the wall was lowered into the grout and the vertical and horizontal alignments were verified. Spacers were used between the wall and the base to guarantee that the wall surface was totally supported by grout without touching the base.

4.3.2.3 Specimen RM3

The third test setup is shown in Figure 4.5. This was similar to the specimen RM2 setup, the only difference being the incorporation of wedges made of resin and cork, at the ends of the connecting surface between the wall and the foundation. These wedges were glued to the wall using the S&P resin 220 epoxy adhesive. This new material was developed by

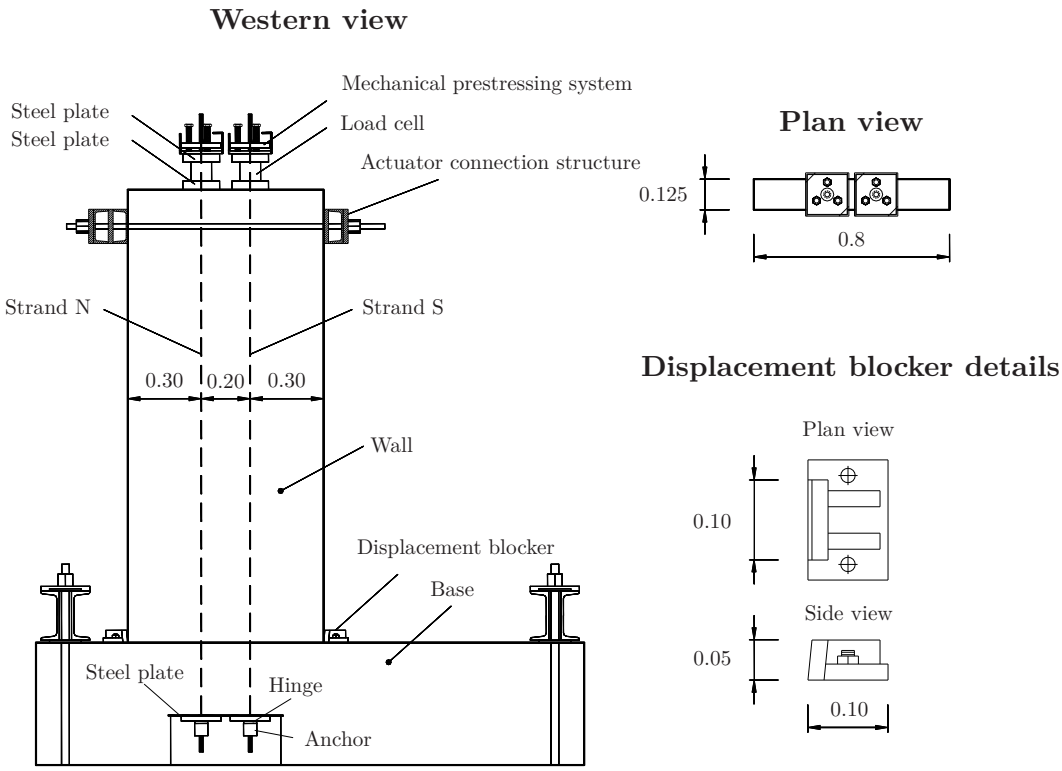

Figure 4.3: Western and plan views of wall specimen RM1 test setup.

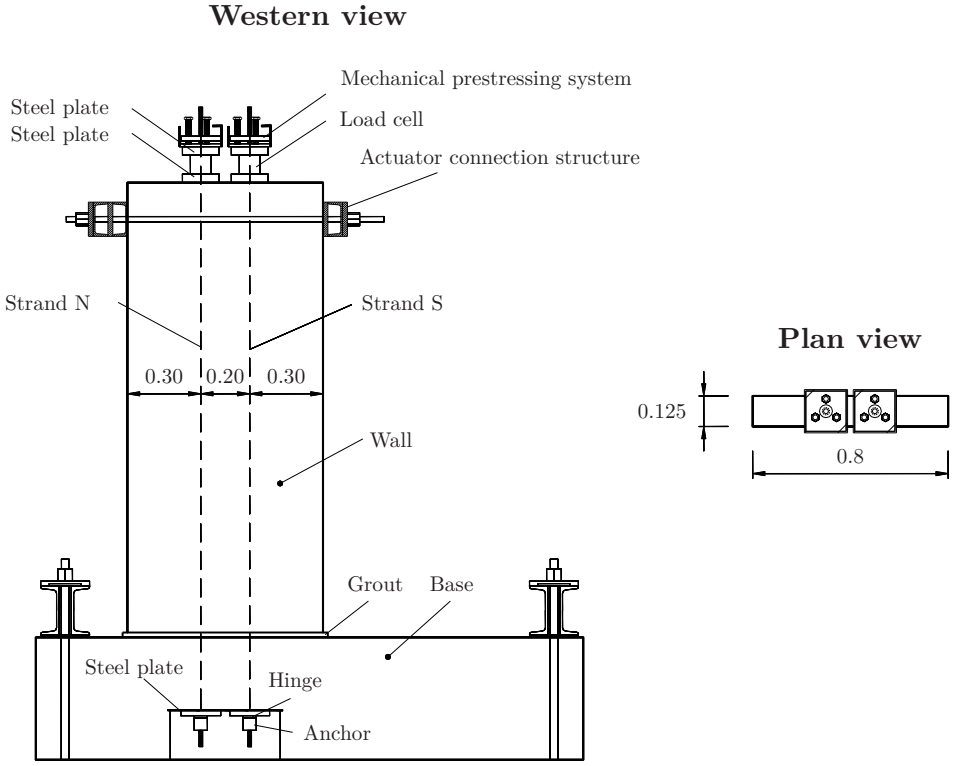

Figure 4.4: Western and plan views of wall specimen RM2 test setup.

another research study at the Civil Engineering Department (Alves (2010), Martins (2010) and Sousa (2010)). This material behaved well under cyclic actions achieving high stresses and deformations in the plastic range with small residual deformation after unloading.

The wall positioning was made using the same procedure as for specimen RM2.

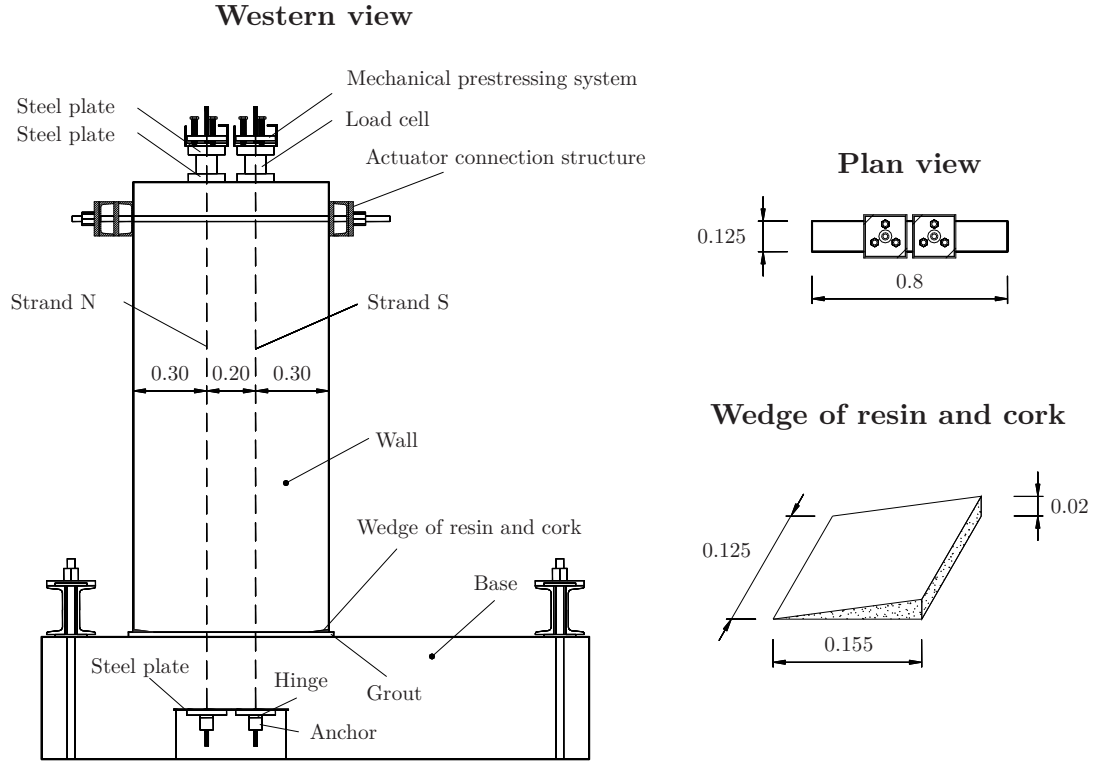

Figure 4.5: Western and plan views of wall specimen RM3 test setup.

4.3.3 Details of specimens

Two reinforced concrete walls and one base were made for the preliminary tests. The reinforced concrete wall used in specimens RM1 and RM2 is detailed in Figure 4.6. The longitudinal reinforcement bars were 8 mm diameter and the transversal bars 6 mm diameter. The transverse reinforcement had 0.10 m spacing in the mid zone and 0.05 m spacing near the top and bottom. The corners of the wall were the zones with the higher density of transverse reinforcement for confinement. The materials used were A500NR steel grade for the bars and C30/37 concrete, with the steel bars having 0.01 m of cover.

The reinforced concrete wall used in specimen RM3 is detailed in Figure 4.7. This wall was chamfered in the bottom corners to accommodate the resin and cork wedges. The steel details were very similar to those of the wall used in specimens RM1 and RM2. The materials specified were the same as for specimens RM1 and RM2.

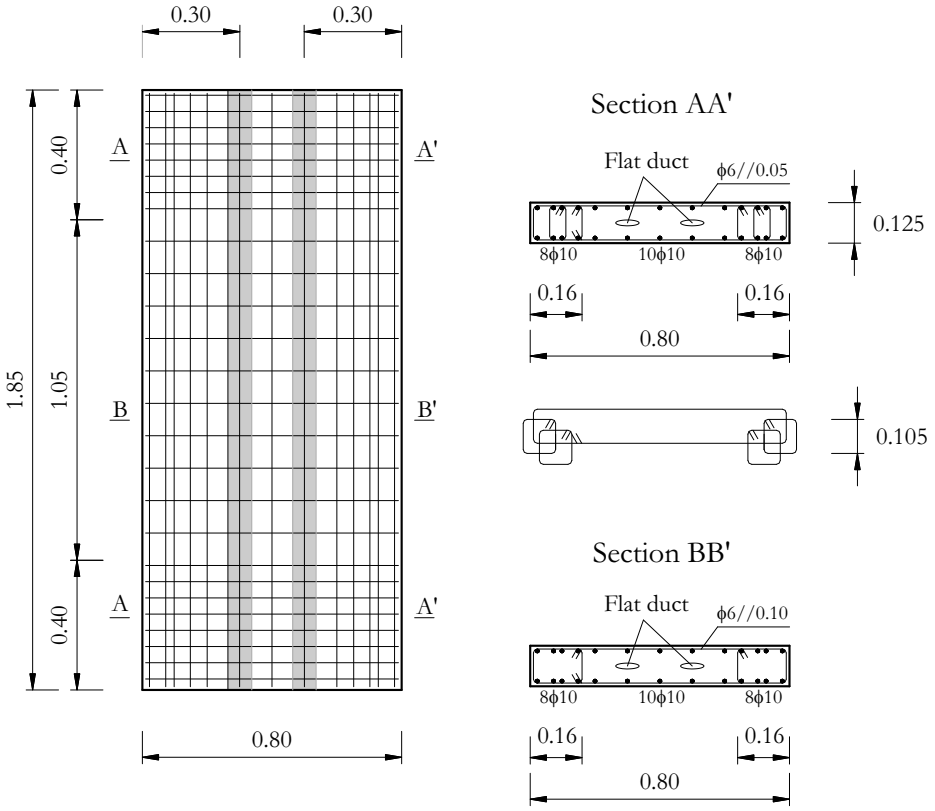

Figure 4.6: Reinforcement details of specimens RM1 and RM2 wall.

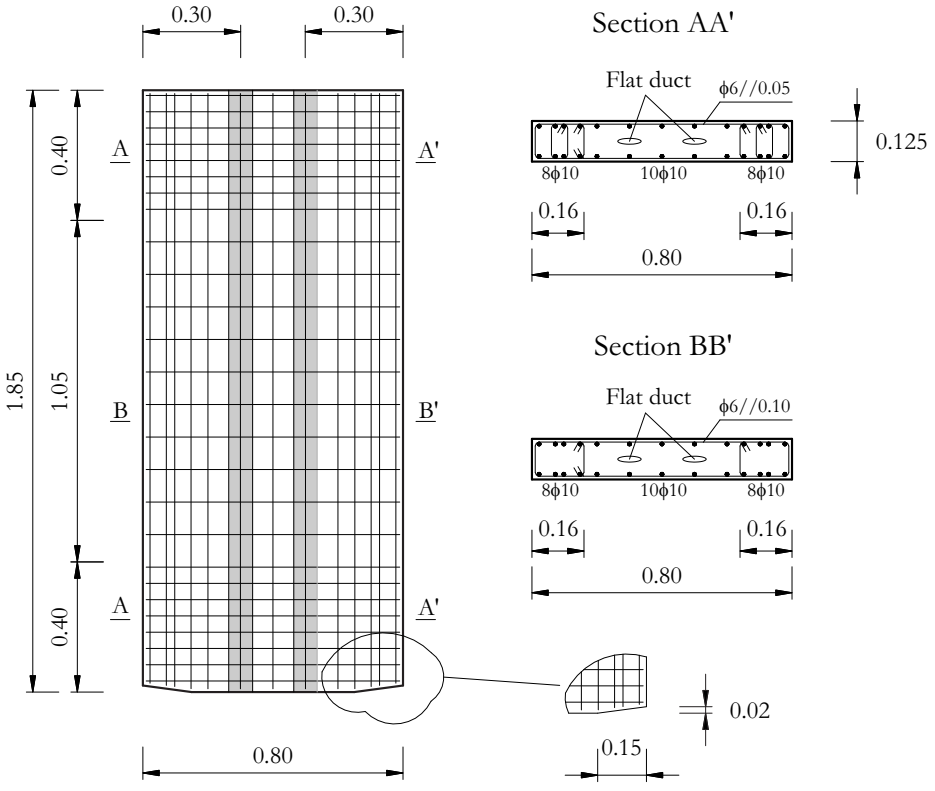

Figure 4.7: Reinforcement details of the specimen RM3 wall.

The reinforced concrete base used in the three preliminary tests and in the fourth test is detailed in Figure 4.8. This block had a 0.5x0.5 m^2 cross section for a 2.0 m span between steel spreader beams. The main longitudinal reinforcement were $6\phi25$ in the top and bottom of the beam and the transverse reinforcement was four leg stirrups of $\phi8//0.075$. To materialise the opening that allowed the access the bottom anchorages, the bottom longitudinal reinforcement had a length of 0.45 m without being embedded by concrete. Two circular ducts were included in the concrete to accommodate the vertical prestress strands. A steel cage made of $\phi8$ bars was used in the zone below the wall-base connection for confinement.

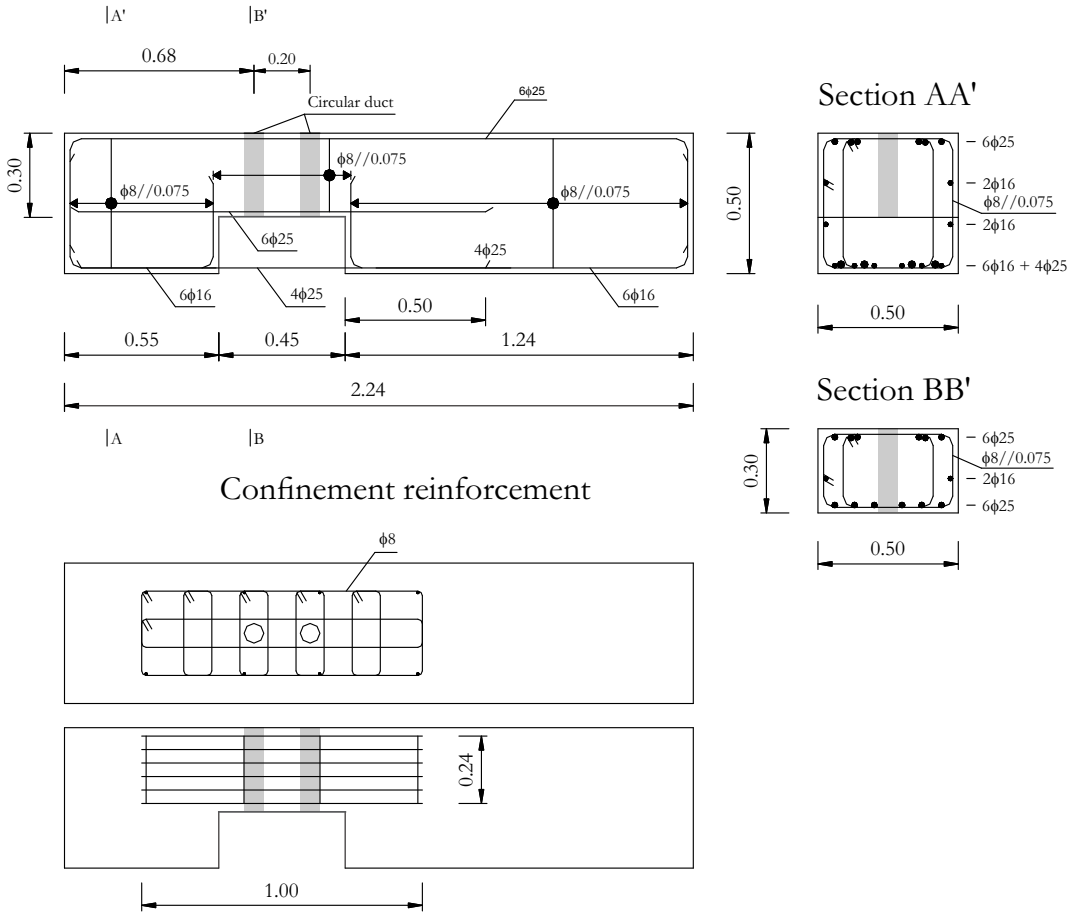

Figure 4.8: Reinforcement details of base used for specimens RM1 to RM4.

4.3.4 Monitoring equipment

4.3.4.1 Specimen RM1

The monitoring of specimen RM1 consisted on recording forces and displacements throughout the test. The forces that were monitored were the horizontal force applied by the actuator and the two vertical strands forces. Load cells with 500 kN and 300 kN measur-

ing capacity were used for the horizontal (actuator) and vertical (post-tensioned strands) forces. Twelve displacement transducers were used to monitor displacements, six for horizontal displacements and six for vertical displacements. The displacement transducers locations are shown in Figure 4.9 and the vertical distance of each transducer to the base is in Table 4.1. The vertical displacement transducers were positioned near the base of the wall and the horizontal displacement transducers along the height. Only the western side of the wall was monitored by displacement transducers due to malfunctions in some of the electric connections. As a result the displacement transducers D2, D4, D6 and D11, that were placed on the eastern face of the wall, were not used.

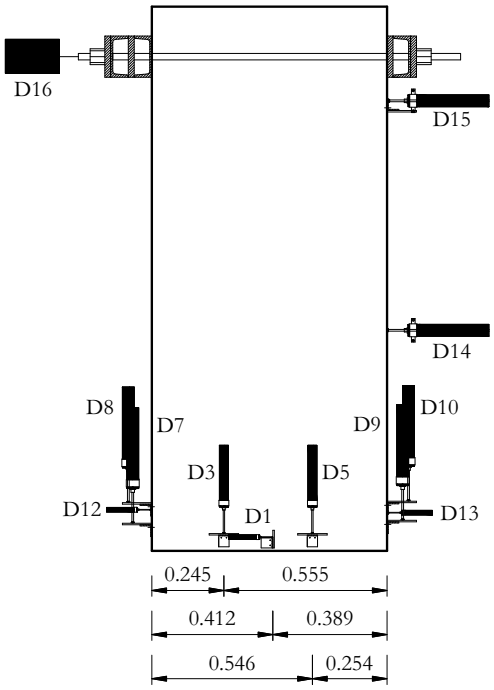

Figure 4.9: Western view of the specimen RM1 displacement transducers.

4.3.4.2 Specimen RM2

The monitoring of specimen RM2 was similar to that in specimen RM1. To monitor displacements, fifteen displacement transducers were used, eight for horizontal displacements and seven for vertical displacements. The problem with the electrical connections that had affected specimen RM1 monitoring was solved and both sides of the wall were monitored. A scheme for each side of the wall is presented in Figure 4.10. The vertical distance of each transducer to the base is in Table 4.2. The wall was supported by the grout and was approximately 10 mm above the base.

Table 4.1: Vertical position of the specimen RM1 displacement transducers.

Transducer	Height (m)	Transducer	Height (m)	Transducer	Height (m)	Transducer	Height (m)
D1	0.047	**D5**	0.045	**D9**	0.090	**D13**	0.130
D2	-	**D6**	-	**D10**	0.155	**D14**	0.750
D3	0.045	**D7**	0.080	**D11**	-	**D15**	1.530
D4	-	**D8**	0.150	**D12**	0.140	**D16**	1.680

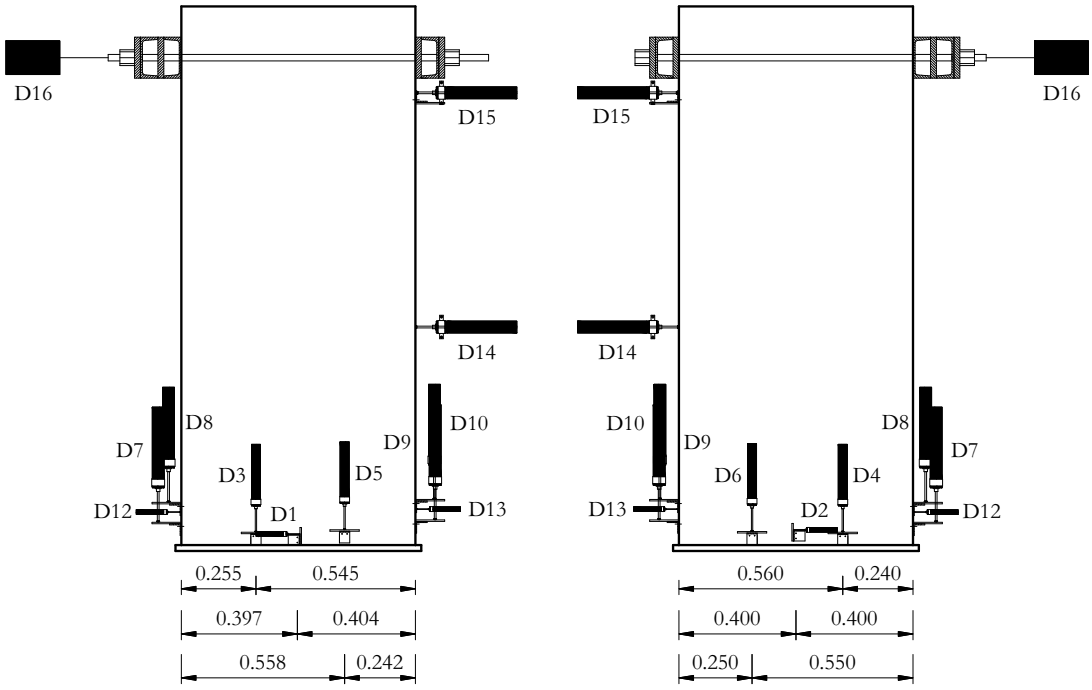

(a) Western side view. **(b)** Eastern side view.

Figure 4.10: Locations of the specimen RM2 displacement transducers.

Table 4.2: Vertical position of the specimen RM2 displacement transducers.

Transducer	Height (m)	Transducer	Height (m)	Transducer	Height (m)	Transducer	Height (m)
D1	0.058	**D5**	0.058	**D9**	0.092	**D13**	0.143
D2	0.072	**D6**	0.052	**D10**	0.162	**D14**	0.765
D3	0.050	**D7**	0.084	**D11**	-	**D15**	1.565
D4	0.050	**D8**	0.152	**D12**	0.133	**D16**	1.685

4.3.4.3 Specimen RM3

The monitoring of specimen RM3 was similar in terms of forces and displacements to that used in specimen RM2, but in this specimen strain gauges were also added to the reinforcing steel bars near the bottom of the wall. The displacement transducers positions are shown in Figure 4.11. The vertical distance of each transducer to the base is in Table 4.3. As in specimen RM2, the wall was approximately 10 mm above the base. The position of the strain gauges used in the transversal confining reinforcing steel bars are shown in Figure 4.12.

4.3.5 Loading protocol

The loading protocol used to test the wall specimens consisted on applying three cycles for each target drift until a maximum 2% drift ratio, as shown in Figure 4.13. The target drift ratio for each set of cycles was 0.25%, 0.50%, 0.75%, 1.00%, 1.50% and 2.00% respectively. In the case of specimens RM2 and RM3, the cycles with 0.75% target drift were not considered. These preliminary tests were prestressed only and had no west-east direction side bracing, thus one of the limitations for the maximum displacement was safety issues due to stability of the wall when reaching a drift ratio of 2.00%.

4.3.6 Materials

Five different materials were used: concrete, ordinary reinforcing steel, prestressing steel, a resin and cork mixture and grout. To characterise the concrete 150x150x150 mm^3 cubes were made for compression tests, according to EN 12390-1 (2000). To characterise the resin and cork and the grout 40x40x160 mm^3 prism specimens were made for bending and compression tests.

These tests were performed according to EN 12390-3 (2001), except that the application of loading was done under displacement control condition with a displacement speed of 0,02 mm/s until failure.

4.3.6.1 Concrete

The two walls and the base were made in two different casts. The specimens were cast at the precast company Concremat - Prefabricação e Obras Gerais, S.A. In both casts, concrete cubes were produced. Using the results from the compression cube tests performed according to EN 12390-3 (2001), an estimation of the strength in cylinders was made using the coefficient 0.8.

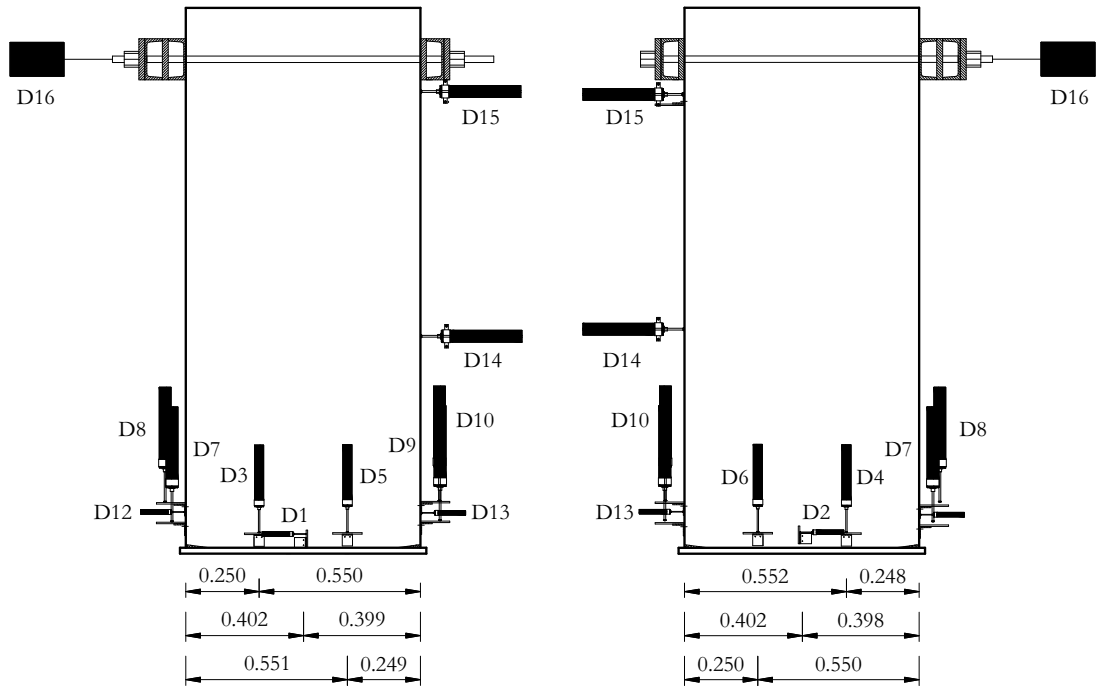

(a) Western side view. **(b)** Eastern side view.

Figure 4.11: Locations of the specimen RM3 displacement transducers.

Table 4.3: Vertical position of the specimen RM3 displacement transducers.

Transducer	Height (m)	Transducer	Height (m)	Transducer	Height (m)	Transducer	Height (m)
D1	0.067	**D5**	0.057	**D9**	0.097	**D13**	0.139
D2	0.073	**D6**	0.058	**D10**	0.164	**D14**	0.741
D3	0.056	**D7**	0.093	**D11**	-	**D15**	1.575
D4	0.057	**D8**	0.160	**D12**	0.142	**D16**	1.685

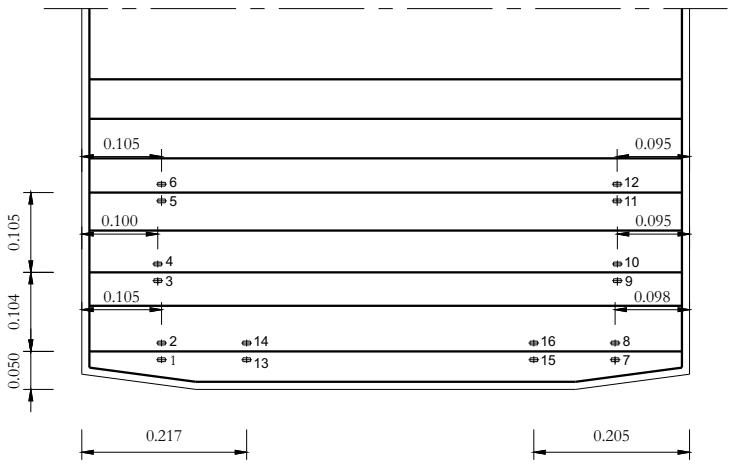

Figure 4.12: Strain gauges locations in specimen RM3.

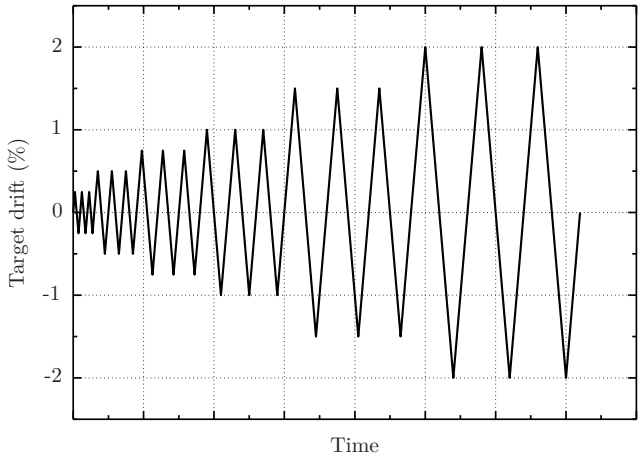

Figure 4.13: Preliminary wall tests protocol.

The base and the first wall were cast in the first batch. The first wall was used in specimens RM1 and RM2. The results for the concrete cube tests are shown in Table 4.4, being the mean compression strength in cylinders at 28 days equal to 22.9 MPa. The concrete cubes were tested with three different ages of 28, 67 and 175 days. The 28 day old specimens were chosen to have the standard concrete resistance, the second of 67 days, to match the specimen RM1 test day and the third, 175 days, to match the specimen RM2 test day.

The second wall, corresponding to specimen RM3 was cast in the second batch. In Table 4.5, the results for the concrete cube tests are shown, being the mean compression strength in cylinders at 28 days equal to 22.4 MPa. The tests were made at the ages of 28 and 202 days. The second tests were made at 202 days to match the specimen RM3 test day.

4.3.6.2 Reinforcing steel

The steel used in all concrete elements was A500NR grade. The steel was not tested as the yielding and rupture points were not expected to be reached in the wall tests.

4.3.6.3 Prestressing steel

Two 7 wire strands of 0.6" with a cross section of 140 mm^2, $f_{p0.1k}$ = 1600 MPa and f_{pk} = 1850 MPa, according to prEN 10138-3 (2004), were used in each test. This prestressing steel was supplied by VSL Sistemas Portugal, S.A.

Table 4.4: Compressive strength of the concrete used in the specimens RM1 and RM2

Cubes	P_{max} [a] (kN)	f_{cmax} [b] (MPa)	$f_{cm,cubes}$ [c] (MPa)	f_{cm} [d] (MPa)
Concrete tests at 28 days				
1	651	28.9	**28.6**	**22.9**
2	633	28.1		
3	659	29.3		
4	658	29.2		
5	599	26.6		
6	665	29.6		
Concrete tests at 67 days - specimen RM1 test day				
1	701	31.2	**29.8**	**23.8**
2	704	31.3		
3	607	27.0		
Concrete tests at 175 days - specimen RM2 test day				
1	735	32.7	**33.1**	**26.5**
2	807	35.9		
3	692	30.8		

[a] Maximum compressive force in each cube

[b] Maximum compressive stress in each cube

[c] Mean compressive strength in cubes

[d] Mean compressive strength in cylinders, obtained using the following expression: $0.8 \times f_{cm,cubes}$

Table 4.5: Compressive strength of the concrete used in specimen RM3

Cubes	P_{max} [a] (kN)	f_{cmax} [b] (MPa)	$f_{cm,cubes}$ [c] (MPa)	f_{cm} [d] (MPa)
Concrete tests at 28 days				
1	644	28.6	**28.0**	**22.4**
2	677	30.1		
3	572	25.4		
Concrete tests at 202 days - specimen RM3 test day				
1	781	34.7	**35.6**	**26.5**
2	809	36.0		
3	815	36.2		

[a] Maximum compressive force in each cube

[b] Maximum compressive stress in each cube

[c] Mean compressive strength in cubes

[d] Mean compressive strength in cylinders, obtained using the following expression: $0.8 \times f_{cm,cubes}$

4.3.6.4 Resin and cork wedges

Epoxy resin and cork wedges were used in the wall specimen RM3. This material has been studied in the Universidade NOVA de Lisboa with promising results. It has a large capacity for deformation without damage. Alves (2010) studied the durability of different compositions in aggressive environments, Sousa (2010) studied the behaviour when subjected to cyclic actions and Martins (2010) studied different compositions and the scale factor effect on the mechanical behaviour.

For the mechanical characterisation of the material, specimens with 160x40x40 mm^3 were made. These specimens were tested by bending and compression. The compression tests were made with the specimens that resulted from the division under bending of the 160x40x40 mm^3 specimens and with a loaded area of 40x40 mm^2.

The epoxy resin used was the MC-DUR1390 VK from MS-Bauchemie and the aggregate was cork powder. To determine the geometrical properties of the cork, a sieving method was used according to NP EN933-1. This test resulted in a maximum aggregate size of 4.76 mm, a minimum aggregate size of 0.075 mm, a fineness modulus of 3.97 and an amount of material finer than No. 200 sieve of 9.74%. The mixture was made with 85% of epoxy resin and 15% of cork by weight. To avoid segregation of the cork, the cast of the mixture was made when a temperature of 50°C was achieved. After 24 hours at room temperature, the specimens were kept for seven days at a constant temperature of 40°C. Only one cast was made for two resin and cork wedges and four 160x40x40 mm^3 specimens were made for the mechanical characterisation.

To estimate the tensile strength, bending tests were performed as shown in Figure 4.14. Four of the resulting pieces of the specimens, one from each original specimen, were then subjected to a compression test with a contact area of 40x40 mm^2, as shown in Figure 4.15. Table 4.6 and Figures 4.16 and 4.17 show the results, where a tensile strength of 16.6 MPa, a compressive strength of 38.6 MPa and a modulus of elasticity of 1226.9 MPa were obtained. The values shown for the compressive strength correspond to the proof compressive stress at 1.5% strain.

4.3.6.5 Grout

Grout (Sika® Grout) was used between the wall and the base in specimens RM2 and RM3. Bending and compression tests on six 40x40x160 mm^3 prisms for each wall specimen, were carried out on the day of the wall specimen tests. The results for the grout flexural and compression tests used in specimens RM2 and RM3 are shown in Tables 4.7 and 4.8, respectively. The tensile and compression strength of the grout were obtained from the 40x40x160 mm^3 specimens and half specimens, according to standard EN 1015-11 (1999).

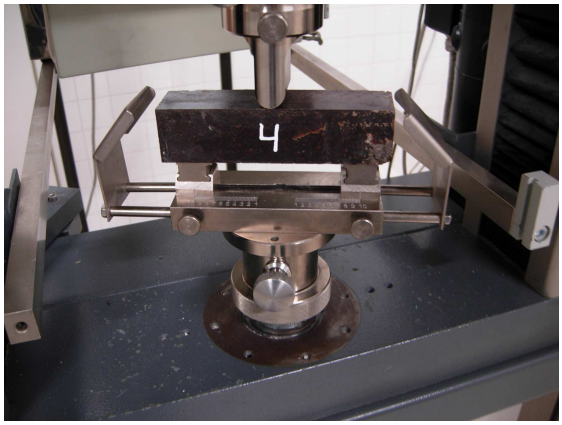

Figure 4.14: Bending test of resin and cork in 40x40x160 mm^3 specimens.

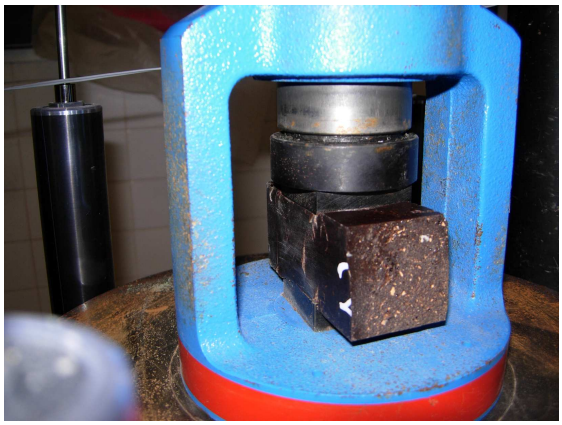

Figure 4.15: Compression test after a flexural test of resin and cork in 40x40x160 mm^3 specimens.

Table 4.6: Tension and compression strength of resin and cork in 40x40x160 mm^3 specimens at specimen RM3 test day.

	Tension		**Compression**			
Specimen	$\sigma_{t,max}$ [a] **(MPa)**	$\sigma_{t,m}$ [b] **(MPa)**	$\sigma_{c1.5}$ [c] **(MPa)**	$\sigma_{cm1.5}$ [d] **(MPa)**	E_r [e] **(MPa)**	$E_{r,m}$ [f] **(MPa)**
1	17.0		42.1		1214.3	
2	15.8	**16.6**	32.4	**38.6**	1144.2	**1226.9**
3	17.1		36.5		1182.7	
4	16.5		43.4		1366.3	

[a] Maximum tensile stress from the bending test

[b] Mean of the maximum tensile stresses from the bending test

[c] 1.5% proof-stress of the resin and cork

[d] Mean value of the 1.5% proof-stress of the resin and cork

[e] Modulus of elasticity corresponding to the tangent of the compression tests diagram at 10 MPa

[f] Mean of the modulus of elasticity corresponding to the tangent of the compression tests diagram at 10 MPa

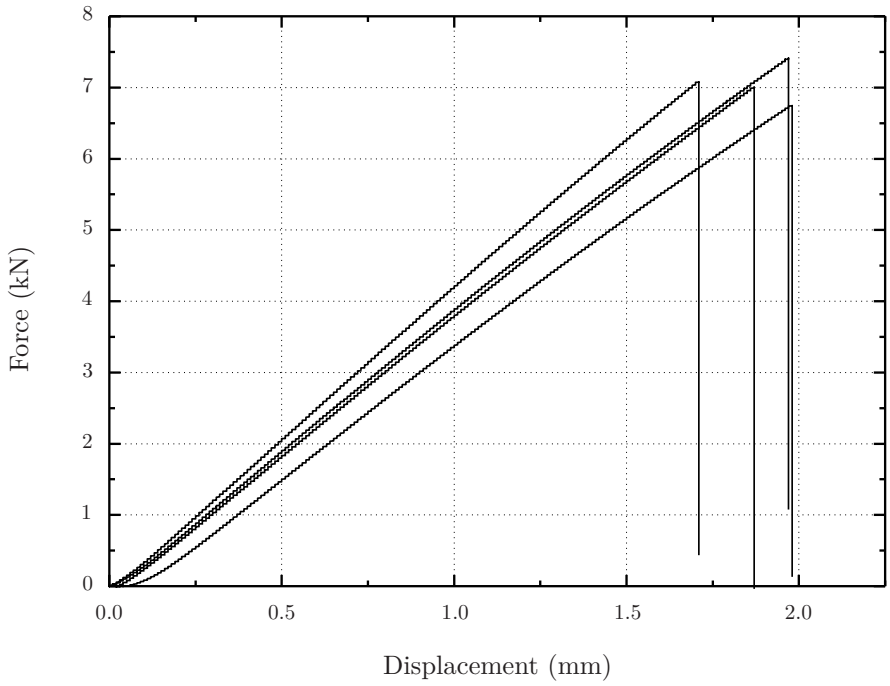

Figure 4.16: Bending test of resin and cork specimens.

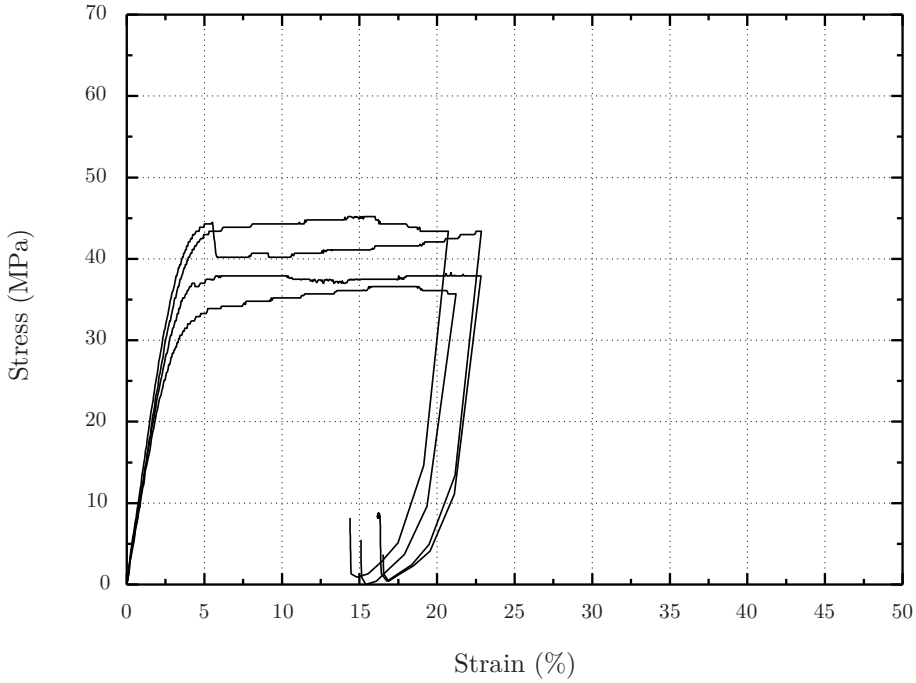

Figure 4.17: Compression test of resin and cork specimens.

Table 4.7: Bending and compression strength for grout used in the wall specimen RM2, 10 days after casting.

Specimen	$\sigma_{t,max}$ (MPa)	$\sigma_{t,m}$ (MPa)	$\sigma_{c,max}$ (MPa)	$\sigma_{c,m}$ (MPa)
1	5.9		56.3	
2	5.7		55.0	
3	6.5	**6.0**	58.8	**55.3**
4	6.5		55.6	
5	5.6		54.4	
6	5.7		51.9	

Table 4.8: Bending and compression strength for grout used in the wall specimen RM3, 8 days after casting.

Specimen	$\sigma_{t,max}$ (MPa)	$\sigma_{t,m}$ (MPa)	$\sigma_{c,max}$ (MPa)	$\sigma_{c,m}$ (MPa)
1	7.2		57.5	
2	7.3		56.3	
3	6.9	**7.2**	58.1	**56.1**
4	7.6		55.0	
5	7.2		55.0	
6	7.0		55.0	

4.4 Tests on hybrid rocking walls

4.4.1 Introduction

The experimental tests that are presented in this section refer to two precast concrete hybrid wall systems (specimen RM4 and RM5). The development of the energy dissipaters included in the hybrid wall systems was described in Chapter 3. The two solutions used in specimens RM4 and RM5 were the ones that achieved the desired cyclic behaviour (see Section 3.2.5). The first solution used steel angles with a weld on the edge of the horizontal leg and the second solution, steel angles with a second line of bolts in the horizontal leg, named as specimens A4 and A5. These experimental tests on the walls were carried out after the preliminary tests described in Section 4.3. To allow the comparison of these two hybrid solutions with a post-tensioned solution with the same characteristics, the wall used in specimens RM5 was tested without the energy dissipaters, and is described in Section 4.5.

4.4.2 Specimens

4.4.2.1 Specimen RM4

Specimen RM4 was a precast concrete hybrid rocking wall and the specimen setup is shown in Figure 4.18. This wall has two post-tensioning strands and energy dissipaters made from steel angles. The steel angles used in this specimen were similar to those in specimen A4.

The connections between the wall and the angles were made with a 15 mm thick steel plate, built into the wall. Two other 20 mm thick plates were added to the base to connect the angles to the base. The horizontal legs of the angles were welded to these plates.

During assembly grout was poured over the base, then the wall was lowered into the grout until the holes in the wall steel plate and the steel angles were aligned and the bolts could be tightened. The vertical and horizontal alignments were verified and some adjustments could be made due to the bolt hole tolerances.

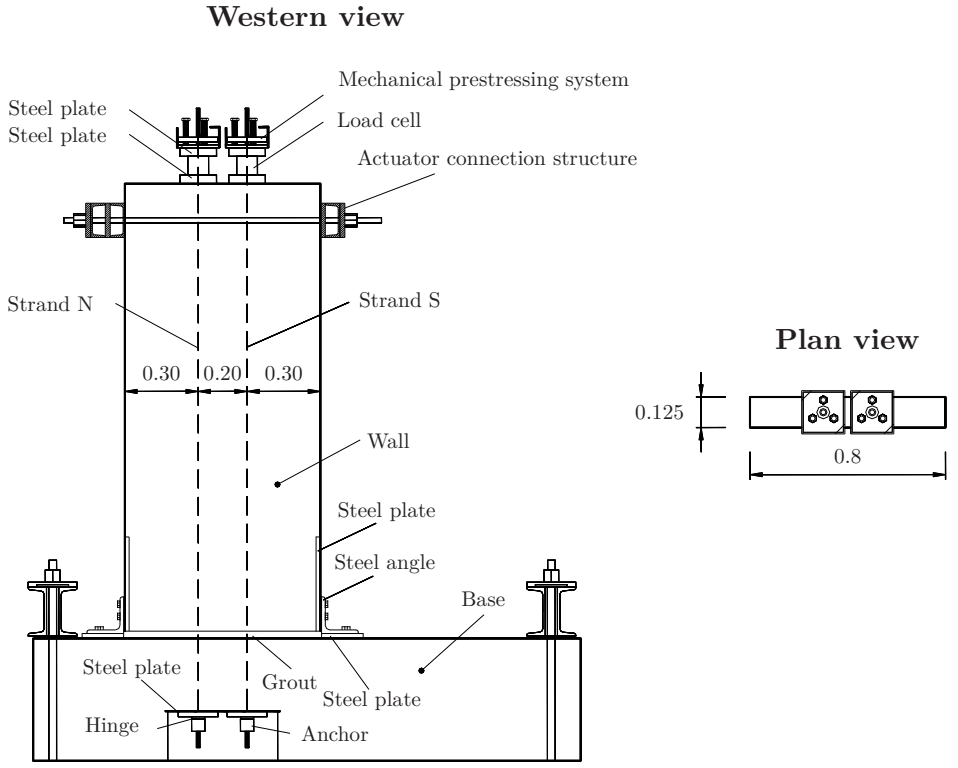

Figure 4.18: Western and plan views of wall specimen RM4 test setup.

4.4.2.2 Specimen RM5

Specimen RM5 setup is shown in Figure 4.19. The steel angles used in this specimen were similar to those in specimen A5. The horizontal legs of the angles had two lines of bolts connecting the steel plate to the base. To control undesired transversal displacements, a bracing system was built with circular hollow tubes. To minimise friction teflon plates were used between the wall and the tubes.

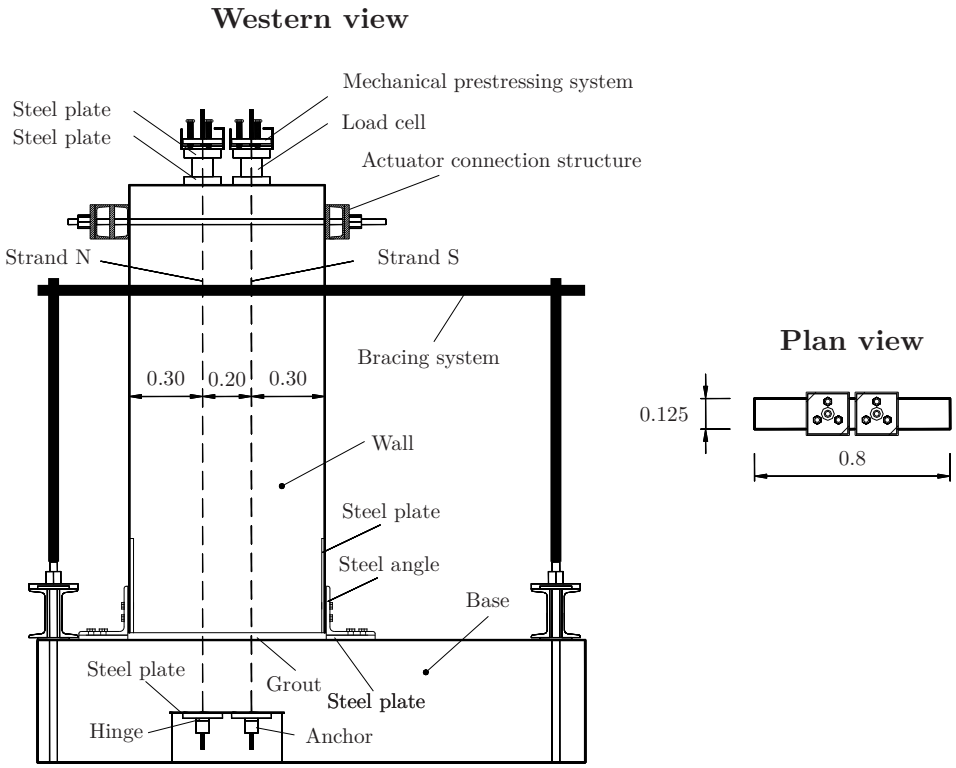

Figure 4.19: Western and plan views of wall specimen RM5 test setup.

4.4.3 Details of specimens

Details of the wall used in specimen RM4 are shown in Figure 4.20. The reinforcement was similar to that in the preliminary tests and the materials prescribed were A500NR steel grade for the bars and C30/37 for the concrete, whilst the steel bars had a 10 mm cover.

The angles were connected to the wall using a 15 mm thick steel plate, previously cast into the wall and secured by twelve 12 mm diameter ordinary steel bars welded to the steel plate (see Figure 4.21). These plates had four protected M16 nuts welded to the inner face to enable the fixation of the angles with M16 bolts. The steel angles were fixed to the base using a similar setup, although the plate was 20 mm thick and there were two M20 nuts and bolts. As the base used for specimen RM4 was the same as for the three

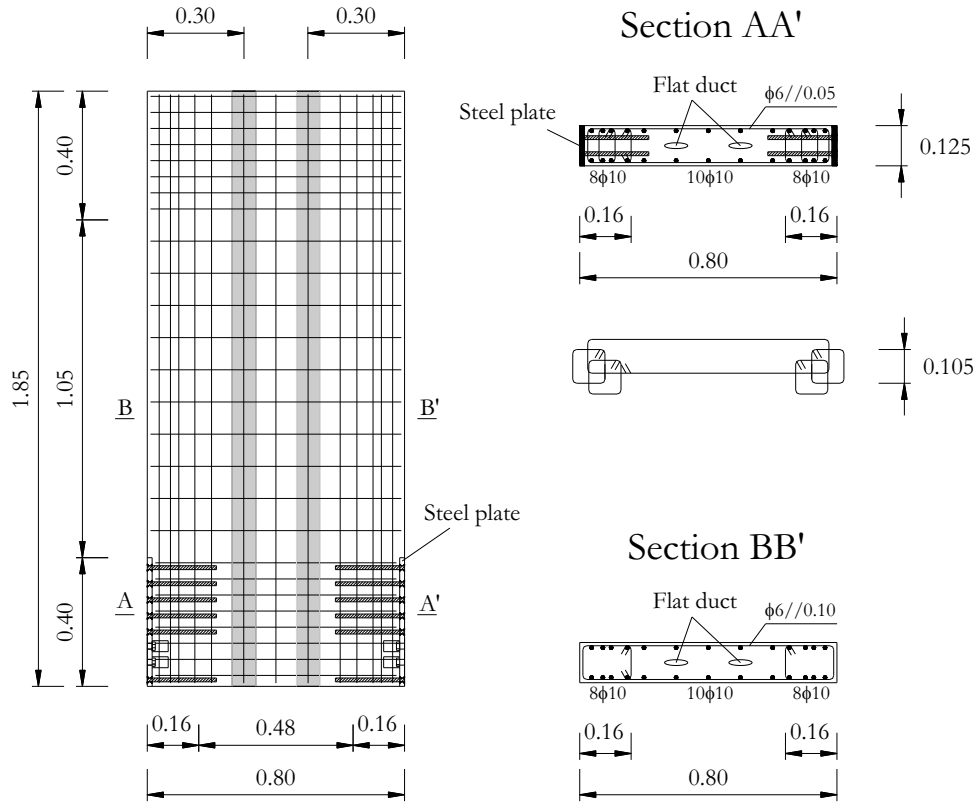

Figure 4.20: Reinforcement details of specimen RM4 wall.

preliminary tests, no steel plate was attached to it as can be seen in Figure 4.8. Holes were drilled in the base and the four 20 mm diameter bars previously welded to the steel plate were sealed with grout. Details of these steel plates are shown in Figure 4.21.

The reinforced concrete wall used in specimen RM5 is detailed in Figure 4.22. This wall was similar to the wall for specimen RM4 with the exception of the steel plates. The prescribed materials were the same as for the previous specimens.

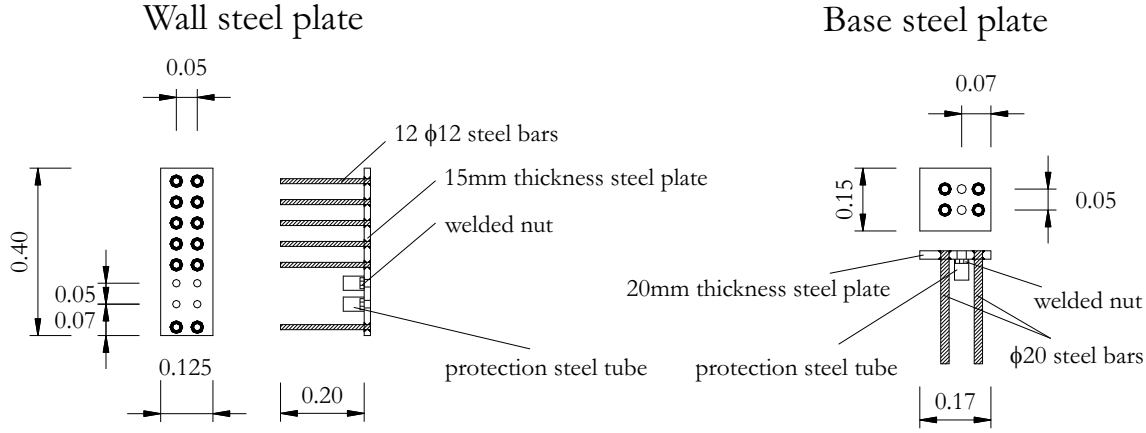

Figure 4.21: Steel plates details used in specimen RM4.

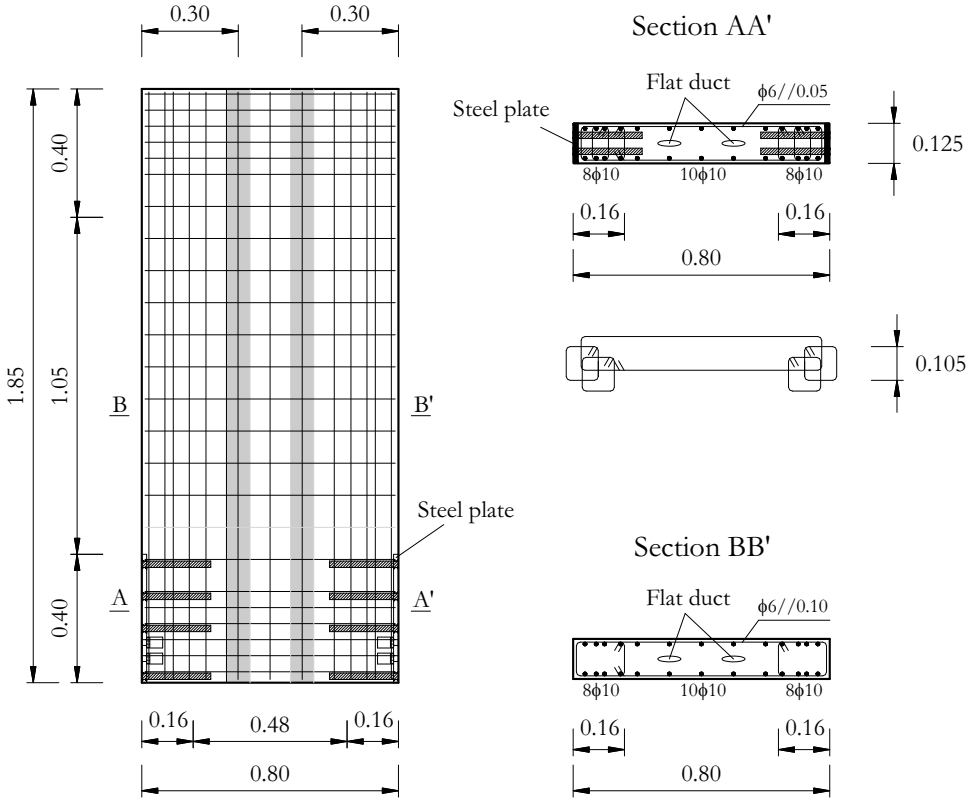

Figure 4.22: Reinforcement details of specimen RM5 wall.

The cast and the execution of the reinforcement for specimen RM4 caused some difficulties. To minimise these problems the plate built into the wall for specimen RM5 was connected to the wall using eight 20 mm diameter steel bars, instead of the 12 bars used in the previous one. These plates had four protected M20 nuts welded at the back side to allow the fixation of the angles with M20 bolts. To connect the angles to the base another plate was used in each side. These 20 mm thick plates had four protected M20 nuts welded to them to allow the fixation of the angle with M20 bolts to the base. Details of the steel plates are shown in Figure 4.23. In the case of these last two specimens (RM5 and RM6), a new base was designed, thus circular cut-offs were left during casting to allow the posterior sealing of the M20 bars with grout.

The reinforced concrete base used in these two tests is detailed in Figure 4.24. This concrete element had a 0.5x0.5 m^2 cross section for a 2.0 m span between steel spreader beams. The main longitudinal reinforcement were 6ϕ20 on the bottom, 6ϕ25 on the top and the transverse reinforcement were four legs stirrups of ϕ8//0.075. To provide access to the prestress bottom anchorages, the bottom longitudinal reinforcement was exterior for 0.45 m length as in the previous designed base. Two circular ducts were included in the concrete to accommodate the vertical prestress strands, and to seal the steel plates, eight cut-offs were left in place during the concrete cast. A steel cage using ϕ8 bars was used in the zone below the wall-base connection for concrete confinement.

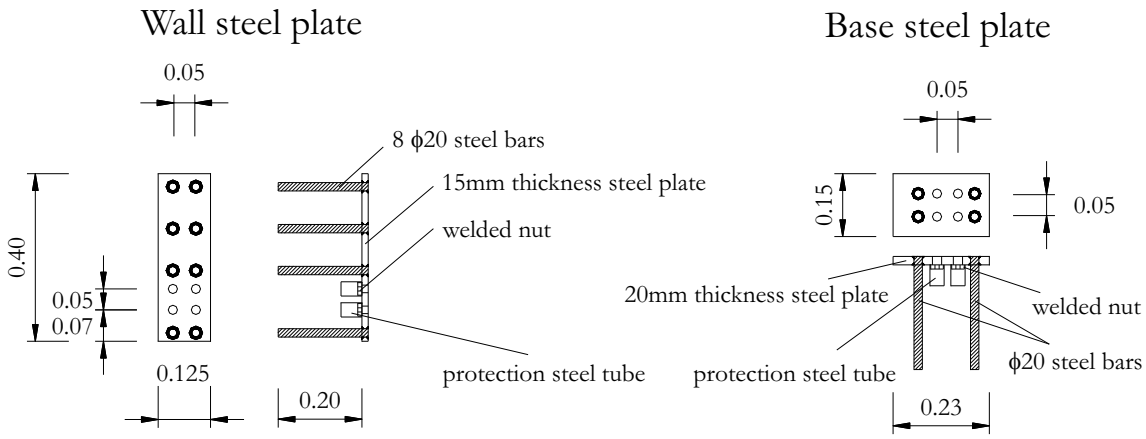

Figure 4.23: Steel plates details used in specimens RM5 and RM6.

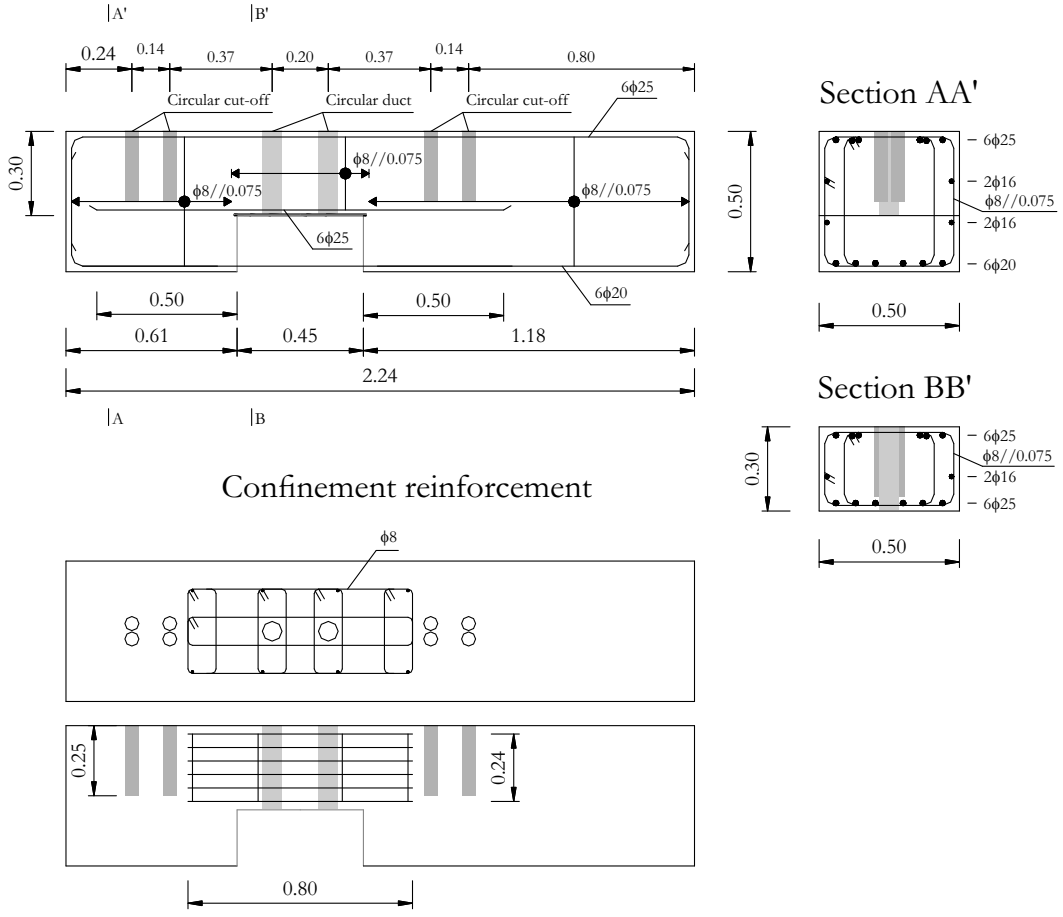

Figure 4.24: Reinforcement details of base used for specimens RM5 to RM6.

4.4.4 Monitoring equipment

4.4.4.1 Specimen RM4

Load cells with 500 kN and 300 kN measuring capacity were used to monitor the horizontal force in the actuator and the vertical force in the post-tensioned strands. Fifteen displacement transducers were used, five for horizontal displacements and ten for vertical displacements. The positions of the displacement transducers are shown in Figure 4.25. The vertical distance of each transducer to the base is in Table 4.9. These vertical distances include the thickness of the steel plate below the steel angles. Two displacement transducers (D15 and D16) were used to measure the relative displacement between the steel plate and the face of the wall. The transducers D7 and D10 were used to measure the elongation of the bolts in the horizontal legs of the angles. The transducers D8 and D11 were used to measure the vertical displacement of the steel angles.

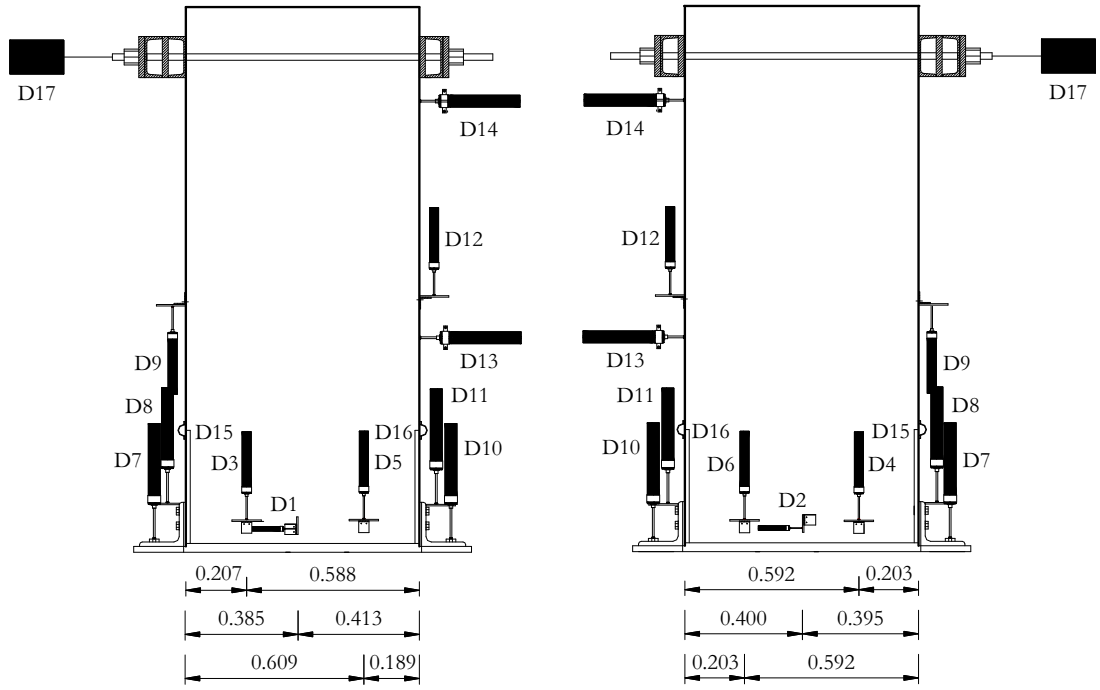

(a) Western side view. **(b)** Eastern side view.

Figure 4.25: Locations of the specimen RM4 displacement transducers.

4.4.4.2 Specimen RM5

In this specimen, sixteen displacement transducers were used, six for horizontal displacements and ten for vertical displacements. The displacement transducers positions are shown in Figure 4.26. The vertical distance of each transducer to the base is in Table 4.10.

Table 4.9: Vertical position of the specimen RM4 displacement transducers.

Transducer	Height (m)	Transducer	Height (m)	Transducer	Height (m)	Transducer	Height (m)
D1	0.082	**D6**	0.109	**D11**	0.163	**D16**	-
D2	0.080	**D7**	-	**D12**	0.859	**D17**	1.680
D3	0.096	**D8**	0.167	**D13**	0.730		
D4	0.107	**D9**	0.850	**D14**	1.535		
D5	0.098	**D10**	-	**D15**	-		

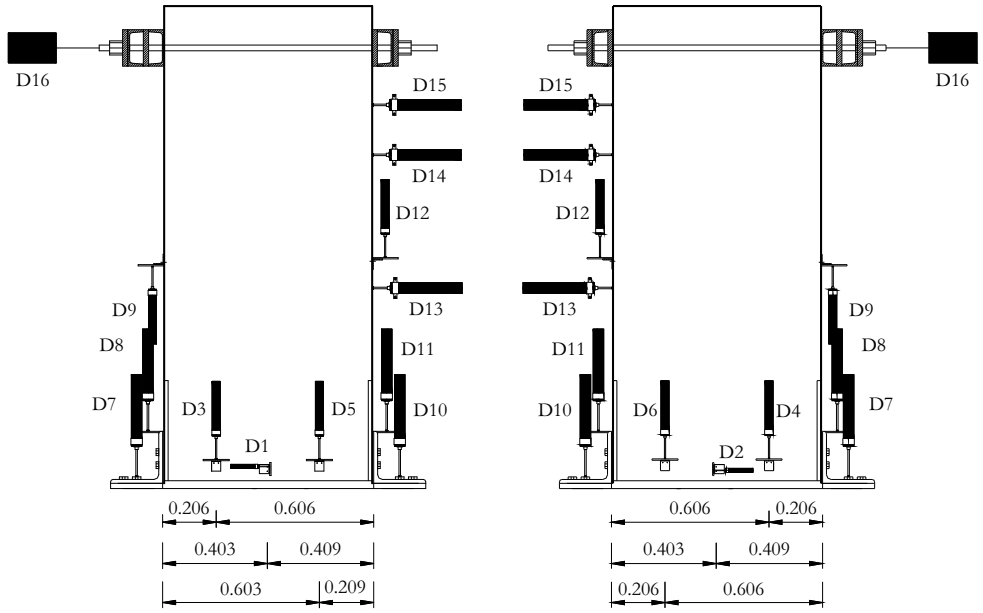

(a) Western side view. **(b)** Eastern side view.

Figure 4.26: Locations of the specimen RM5 displacement transducers.

4.4.5 Loading protocol

The protocol used to test the precast concrete hybrid walls was similar to the one used for the preliminary wall tests. In these tests, the achievement of higher drifts was an objective. The parameters that limited the maximum drift in the preliminary wall tests were the lateral instability of the walls that were without bracing and the short length of the prestress strands. In the hybrid wall systems the lateral instability was mitigated, since the angles increased the rigidity of the connection, improving the lateral stability. Despite that, in wall specimen RM5 a lateral bracing system was used to eliminate the lateral instability problems. For these reasons the protocol used was similar to the preliminary wall tests but with higher maximum target drift ratios, as can be seen in Figure 4.27. The target drift ratio for each set of cycles was 0.25%, 0.50%, 1.00%, 1.50%, 2.00%, 2.50% and 3.00% respectively.

Table 4.10: Vertical position of the specimen RM5 displacement transducers.

Transducer	Height (m)	Transducer	Height (m)	Transducer	Height (m)	Transducer	Height (m)
D1	0.075	**D5**	0.098	**D9**	0.870	**D13**	0.771
D2	0.075	**D6**	0.100	**D10**	-	**D14**	1.283
D3	0.098	**D7**	-	**D11**	0.220	**D15**	1.475
D4	0.100	**D8**	0.215	**D12**	0.874	**D16**	1.694

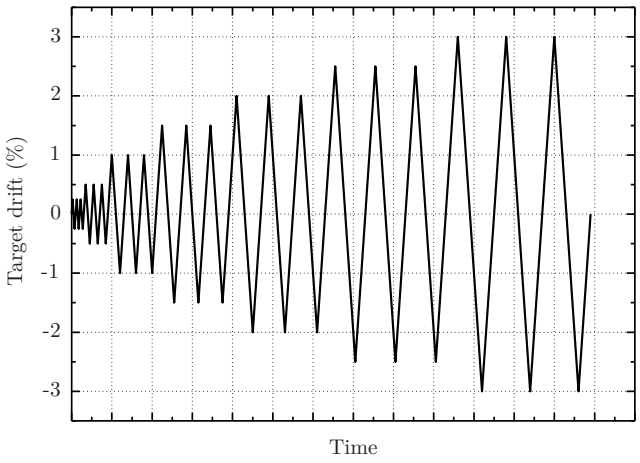

Figure 4.27: Hybrid wall tests protocol.

4.4.6 Materials

Seven different materials were used in the execution of these tests: concrete, reinforcing steel, prestressing steel, grout, steel for the angles, steel for the plates and steel for the bolts.

4.4.6.1 Concrete

Two batches of concrete were prepared, one for wall specimen RM4 and another for the base and the wall used in specimen RM5. The base used for specimen RM4 was the same as the one that was used for specimens RM1, RM2 and RM3.

The results for the compression tests performed, according to EN 12390-3 (2001) for the characterisation of the concrete in the wall specimen RM4, are shown in Table 4.11, being the mean compression strength in cylinders at 28 days equal to 33.4 MPa. The concrete cubes were tested at the ages of 28 and 126 days. The 28 day old specimens were chosen to have the standard concrete resistance and the second of 126 days to match the specimen RM4 test day.

The results for the compression tests made to characterise the concrete in the wall and

the base used in specimen RM5 are shown in Table 4.12. The concrete cubes were tested at the ages of 41 and 92 days. The first age of 41 days was chosen due impossibility of made them at 28 days and the second of 92 days to match the specimen RM5 test day.

Table 4.11: Compressive strength of concrete used in test of the specimen RM4

Cubes	$\mathbf{P}_{max}$ **(kN)**	f_{cmax} **(MPa)**	$f_{cm,cubes}$ **(MPa)**	f_{cm} **(MPa)**
Concrete tests at 28 days				
1	910	40.4		
2	946	42.0	**41.8**	**33.4**
3	965	42.9		
Concrete tests at 126 days - specimen RM4 test day				
1	1035	46.0		
2	999	44.4	**44.8**	**35.8**
3	988	43.9		

Table 4.12: Compressive strength of concrete used in tests of specimens RM5 and RM6

Cubes	$\mathbf{P}_{max}$ **(kN)**	f_{cmax} **(MPa)**	$f_{cm,cubes}$ **(MPa)**	f_{cm} **(MPa)**
Concrete tests at 41 days				
1	1300	57.8		
2	1316	58.5	**59.6**	**47.7**
3	1407	62.5		
Concrete tests at 92 days - specimen RM5 test day				
1	1332	59.2		
2	1479	65.7	**61.5**	**49.2**
3	1340	59.6		

4.4.6.2 Reinforcing steel

The reinforcing steel used in all concrete elements was A500NR grade. The steel was not tested, once the yield and rupture points were no expected to be reached in the wall tests.

4.4.6.3 Prestressing steel

Two 7 wire strands of 0.6" with a cross section of 140 mm^2, $f_{p0.1k}$ = 1600 MPa and f_{pk} = 1850 MPa, according to prEN 10138-3 (2004), were used in each test. This prestressing steel was supplied by VSL Sistemas Portugal, S.A.

4.4.6.4 Grout

Grout (Sika® Grout) was used between the wall and the base. Bending and compression tests were carried out on six 40x40x160 mm^3 prisms for wall specimen on the days of the tests. The results for the flexural and compression grout tests used in specimen RM4 are shown in Table 4.13 and for specimens RM5 in Table 4.14.

Table 4.13: Bending and compression strength for grout used in the wall specimen RM4, 32 days after casting.

Specimen	$\sigma_{t,max}$ **(MPa)**	$\sigma_{t,m}$ **(MPa)**	$\sigma_{c,max}$ **(MPa)**	$\sigma_{c,m}$ **(MPa)**
1	9.2		69.4	
2	8.9		67.0	
3	9.1	**9.5**	71.0	**67.9**
4	10.1		66.1	
5	9.8		66.0	
6	9.9		68.2	

Table 4.14: Bending and compression strength for grout used in the wall specimen RM5, 29 days after casting.

Specimen	$\sigma_{t,max}$ **(MPa)**	$\sigma_{t,m}$ **(MPa)**	$\sigma_{c,max}$ **(MPa)**	$\sigma_{c,m}$ **(MPa)**
1	8.6		54.1	
2	7.8		63.9	
3	7.9	**8.1**	62.9	**61.0**
4	7.8		56.7	
5	8.9		66.1	
6	7.7		62.4	

4.4.6.5 Steel angles, steel plates and steel bolts

The steel angles were made from a S275 steel grade. The steel used in the angles was tested and the results are shown in Chapter 3. All the steel plates were made from a S275 steel grade. The bolts used to attach the steel angles to the wall and base in specimen RM4 were all 10.9 grade. In the specimen RM5, the bolts used to attach the steel angles to the wall were all 8.8 grade and those to the base were 10.9 grade.

4.5 Test on a post-tensioned rocking wall

4.5.1 Introduction

The purpose of the test on the post-tensioned wall specimen RM6 was to observe a specimen similar to RM4 and RM5, but without the steel angle dissipation devices. The main difference to the walls tested in the preliminary wall tests RM1 and RM2 (see Section 4.3) was the inclusion of the 15 mm steel plates along the edges where the steel angles were attached. These steel plates have an influence on the compression zone between the wall and the base and replace the concrete cover in the location where it would be subject to higher compressive stresses.

4.5.2 Specimen

Specimen RM6 was a post-tensioned precast concrete rocking wall and the specimen setup is shown in Figure 4.28. The concrete wall used in this test was the same as for wall specimen RM5, but without the energy dissipaters. From this test it was possible to evaluate the energy dissipation without specific dissipaters. The test setup and assemblage procedure were similar to specimen RM5. In this test, the bracing system to prevent transversal undesired displacements was important and fulfilled the objective.

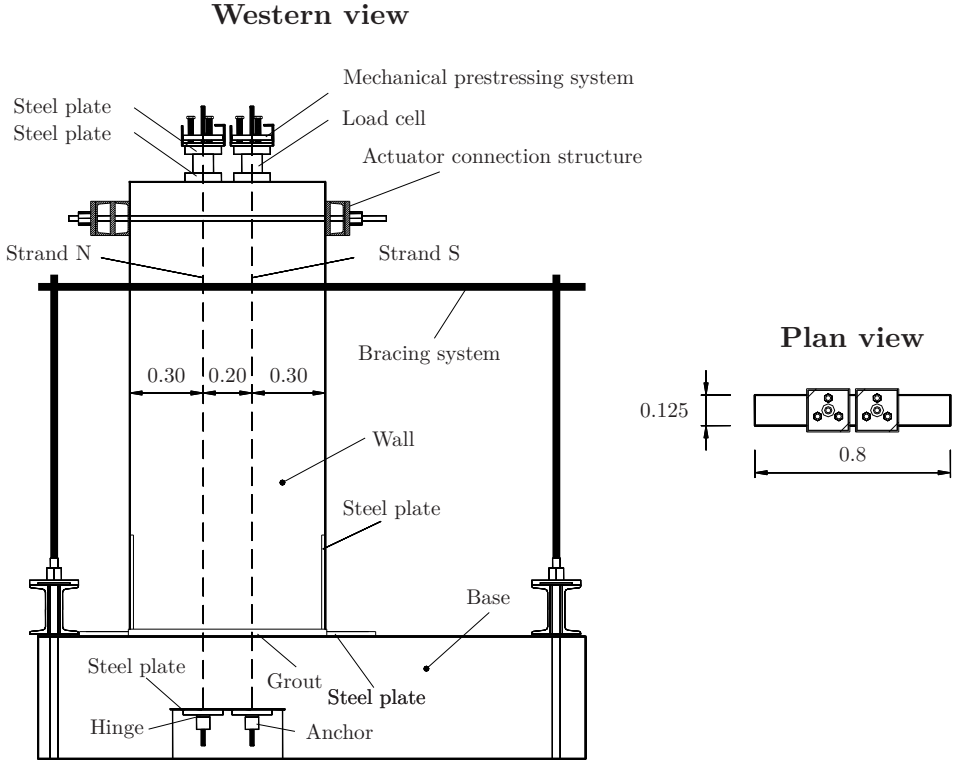

Figure 4.28: Western and plan views of wall specimen RM6 test setup.

4.5.3 Details of specimen

The concrete wall and base that were used were the same as for specimen RM5. The details are described in Section 4.4.3 and the wall steel details are shown in Figure 4.22, the steel plate details in Figure 4.23 and the base steel details in Figure 4.24.

4.5.4 Monitoring equipment

4.5.4.1 Specimen RM6

To monitor displacements in the specimen RM6, fourteen displacement transducers were used, eight for horizontal displacements and six for vertical displacements. In this wall specimen, more horizontal displacement transducers were used in order to record the displacements in both sides of the wall. The displacement transducers positions are shown in Figure 4.29. The vertical distance of each transducer to the base is in Table 4.15. These vertical distances include the thickness of the steel plate below the steel angles.

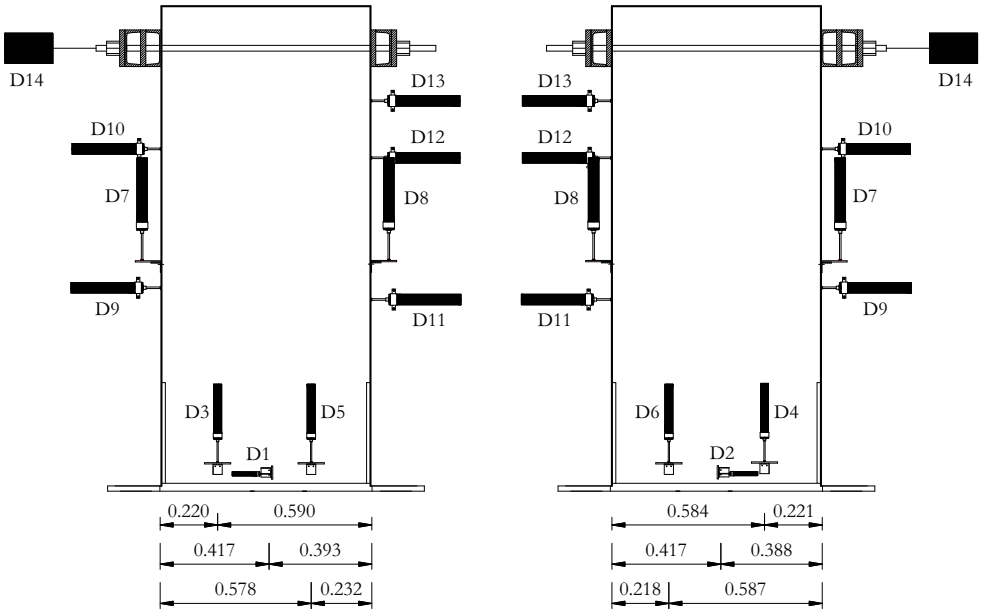

(a) Western side view. **(b)** Eastern side view.

Figure 4.29: Locations of the specimen RM6 displacement transducers.

4.5.5 Loading protocol

The protocol used to test the precast concrete post-tensioned wall was the same as for the specimen RM5 and is shown in Figure 4.30. The target drift ratio for each set of cycles was 0.25%, 0.50%, 1.00%, 1.50%, 2.00%, 2.50% and 3.00% respectively.

Table 4.15: Vertical position of the specimen RM6 displacement transducers.

Transducer	Height (m)	Transducer	Height (m)	Transducer	Height (m)	Transducer	Height (m)
D1	0.071	**D5**	0.095	**D9**	0.778	**D13**	1.493
D2	0.072	**D6**	0.095	**D10**	1.309	**D14**	1.694
D3	0.095	**D7**	0.867	**D11**	0.733		
D4	0.098	**D8**	0.868	**D12**	1.275		

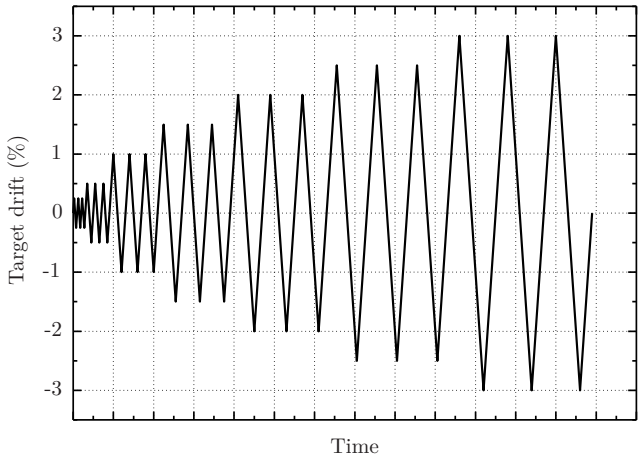

Figure 4.30: Post-tensioned only wall test protocol.

4.5.6 Materials

Four different materials were used in the execution of these tests: concrete, reinforcing steel, prestressing steel and grout.

4.5.6.1 Concrete

The wall and the base used in this test were the same as for the specimen RM5 test, thus the results for the compression tests made on the concrete are shown in Table 4.12. There were no more concrete specimens to test at specimen RM6 test day, but it was not considered important due to the small variations in the properties of the materials after a period of 41 days or 92 days.

4.5.6.2 Reinforcing steel

The reinforcing steel used was A500NR grade. It was not considered necessary to test the steel as the yield and rupture points were not expected to be reached during the wall test.

4.5.6.3 Prestressing steel

Two 7 wire strands of 0.6" with a cross section of 140 mm^2, $f_{p0.1k}$ = 1600 MPa and f_{pk} = 1850 MPa, according to prEN 10138-3 (2004), were used in each test. This prestressing steel was supplied by VSL Sistemas Portugal, S.A.

4.5.6.4 Grout

Grout (Sika® Grout) was used between the wall and the base. Bending and compression tests were carried out at the wall specimen test day in six 40x40x160 mm^3 prisms. The results for the flexural and compression grout tests used in specimen RM6 are shown in Table 4.16.

Table 4.16: Bending and compression strength for grout used in the wall specimen RM6, 29 days after casting.

Specimen	$\sigma_{t,max}$ **(MPa)**	$\sigma_{t,m}$ **(MPa)**	$\sigma_{c,max}$ **(MPa)**	$\sigma_{c,m}$ **(MPa)**
1	9.2		61.4	
2	10.1		63.8	
3	8.9	**9.2**	60.1	**61.5**
4	9.1		62.0	
5	9.0		59.8	
6	9.1		62.1	

4.6 Experimental results

In this section the experimental results of the tested specimens are presented and some important parameters of the behaviour are quantified.

4.6.1 Analysis parameters

The main parameters that will be analysed with the experimental results are the reached drift ratio, the equivalent viscous damping ratio, the rotation of the wall about a vertical axis, the neutral axis depth of the bottom section of the wall, the base shear force and the post-tensioning forces history.

- *Drift ratio*

The drift ratios of the walls were determined using the top displacement at the actuator level divided by the actuator's height from the wall bottom, as shown in equation 4.1. The

top displacement was obtained in two different ways, first using directly the displacement transducer associated to the actuator and second by using the bottom rotation, added to an estimation of the wall elastic displacement, as shown in equation 4.2. The bottom rotation was calculated using the measures of the four vertical displacement transducers placed near the wall bottom, D3, D4, D5 and D6 (equation 4.3). The elastic top displacement was estimated taking into account the bending and shear deformation, as can be seen in equation 4.4. After the decompression of the bottom section, this elastic displacement is an approximation and the associated error increases with the drift ratio. This error is acceptable as the elastic displacement is small when compared to the displacement due to the bottom rotation for high drifts. The concrete parameters needed to calculate the elastic displacements were the ones estimated in EN 1992-1-1 (2004) for the used concrete. Due to the lateral, west-east, displacements in the wall specimens, specially in the post-tensioned specimens without steel angles, the drift based on the bottom rotation was the main choice, used in the results of all specimens except wall specimen RM1. In specimen RM1, only the western side of the wall had displacement transducers, as a result it was not possible to have reliable results.

$$Drift\ ratio = \frac{Top\ displacement}{Actuator's\ heigh} \tag{4.1}$$

$$Top\ displacement = Bottom\ rotation\ \times\ Actuator's\ height + Elastic\ top\ displacement \tag{4.2}$$

$$Bottom\ rotation = \left[\frac{\delta_{D5} - \delta_{D3}}{d_{D3D5}} + \frac{\delta_{D6} - \delta_{D4}}{d_{D4D6}}\right]/2 \tag{4.3}$$

$$Elastic\ top\ displacement = \frac{VH^3}{3E_{cm}I} + \frac{VH}{GA_v} \tag{4.4}$$

where,

δ_{Dx} is the displacement measured by displacement transducer Dx;
d_{DxDy} is the absolute distance between displacement transducers Dx and Dy;
V is the base shear;
H is the horizontal actuator's height;
E_{cm} is the secant modulus of elasticity of concrete between $\sigma_c = 0$ and $0.4\sigma_c = f_{cm}$;
I is the second moment of area;
G is the shear modulus;
A_v is the shear area.

- *Residual drift ratio*

A residual drift ratio for each set of cycles in the results of each specimen will be presented. This value corresponds to the drift after each set of cycles when the base shear

reaches zero. The sign of this value respects the general convention, positive corresponding to a wall with a residual displacement towards north. In Figure 4.31, the residual displacements are marked, Δ_{r1} is the residual displacement after a half cycle in positive displacements and Δ_{r1} in negative displacements. The residual drift after each cycle corresponds to the Δ_{r1} as the tests started with the wall being pushed in the southern direction (negative direction).

- *Equivalent viscous damping ratio*

A parameter that will be obtained for all the specimens as a function of the drift ratio is the equivalent viscous damping ξ_{eq}. Hose and Seible (1999) defined the ξ_{eq} for asymmetric hysteresis loops, separating the diagram by positive and negative displacements, as presented in Figure 4.31. equation 4.5 gives the ξ_{eq} for asymmetric hysteresis loops as the sum of the ξ_{eq} obtained for positive and negative displacements.

$$\xi_{eq} = \frac{1}{4\pi}\left(\frac{E_{d1}}{E_{s1}} + \frac{E_{d2}}{E_{s2}}\right) \tag{4.5}$$

where,

ξ_{eq} is the equivalent viscous damping ratio;
E_{d1} is the energy dissipated for positive displacements;
E_{s1} is the elastic strain energy for positive displacements;
E_{d2} is the energy dissipated for negative displacements;
E_{s2} is the elastic strain energy for negative displacements.

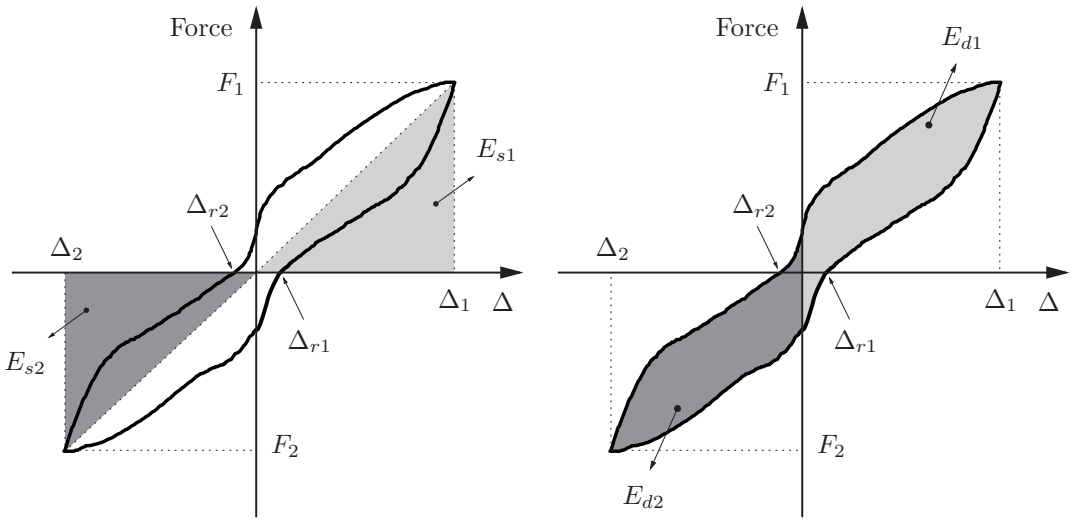

Figure 4.31: Hysteretic diagram of a typical cyclic action (adapted from Hose and Seible (1999)).

- *Wall rotation about the vertical axis*

Due to the lack of transversal bracing, not only transversal top displacement was expected but also rotation of the wall about the vertical axis. These rotation can be

calculated using the following equation 4.6. The transducers D1 and D2 used to calculate this rotation were located at about 50 mm from the bottom, thus the rotation calculation is not exactly in the bottom of the wall, but is close enough to make a qualitative analysis of the wall rotation.

$$Rotation = arctan\left(\frac{\delta_{D2} - \delta_{D1}}{d_{12}}\right) \tag{4.6}$$

where,

d_{12} is the absolute distance between displacement transducers D1 and D2 showed in Table 4.17 for each specimen.

Table 4.17: Distance between the transducers D1 and D2.

$\boldsymbol{d_{12}}$ (m)					
RM1	RM2	RM3	RM4	RM5	RM6
-	0.265	0.283	0.270	0.242	0.286

- Neutral axis depth from displacement transducers

To estimate the neutral axis depth x, four vertical displacement transducers placed near the bottom of the wall were used. Figure 4.32 illustrates the wall rotation on the bottom from a western side view, where the neutral axis position is the transition from the zone where the wall is in contact with the base and the zone where the wall lifts from the base can be seen. This drawing includes two of the displacement transducers used for the calculations and is valid for the situation when the wall has positive drifts. Two expressions were developed, equation 4.7a and equation 4.7b for positive and negative drift ratios.

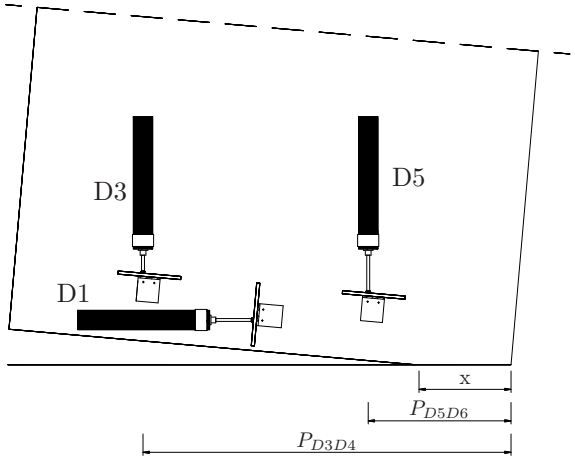

Figure 4.32: Neutral axis.

$$x = P_{D3D4} + \delta_{D1D2} - \delta_{D3D4}\left(\frac{P_{D3D4} - P_{D5D6}}{\delta_{D3D4} - \delta_{D5D6}}\right) \tag{4.7a}$$

$$x = l_w - \left(P_{D3D4} + \delta_{D1D2} - \delta_{D3D4} \left(\frac{P_{D3D4} - P_{D5D6}}{\delta_{D3D4} - \delta_{D5D6}} \right) \right) \tag{4.7b}$$

where,

P_{DxDy} is the average position of the displacement transducers Dx and Dy relatively to the southern corner;
δ_{DxDy} is the average displacement measured by the displacement transducers Dx and Dy;
l_w is the wall length.

- *Forces*

The post-tensioning force in strands and the base shear force, that will be presented, were directly measured by the load cells.

4.6.2 Preliminary tests on post-tensioned rocking walls

4.6.2.1 Wall specimen RM1

After having everything prepared to start the test, the first step was to apply the post-tensioning forces to the strands. The forces were applied gradually and alternately to the strands using the mechanical devices shown in Figure 4.33. Each one of these devices have three bolts that, when tightened, separate the two plates and elongate the strand. This procedure was carried out until each strand force reached 130 kN.

Figure 4.33: Mechanical device for the application of the post-tensioning force.

The wall specimen RM1 was submitted to a cyclic displacement control protocol as described above. Figure 4.34 shows a general view of the test setup. In Figure 4.35 the displacements that were applied to the wall are shown, where it can be seen that, for each target drift ratio, three cycles were applied. The desired target cycles were not strictly achieved, in Table 4.18 the actual drift ratios are shown. The difference between the planned and reached drifts was due to the need to continuously adjust the target displacement inserted in the system. The direction of movement of the actuator was changed by the use of two backstop plates that send the information to reverse to the system. However, this change is not instantaneous and depends on the stiffness of the system and the inertia of the actuator.

This specimen had an initial transversal inclination (Section 4.3.2.1) and being post-tensioned without any bracing system, made it instable. This instability resulted in transversal displacements and a picture of the wall with transversal inclination is shown in Figure 4.36. The displacement transducer that was assigned to be the reference was D15 (Figure 4.9), but due to these transversal displacements the results of this transducer were not reliable and alternatively the displacement transducer D16, associated directly to the actuator, was used (Figure 4.37). The measurements obtained from this transducer included the clearances of the connection system between the actuator and the wall. In the subsequent experimental test analyses, this problem was overcome by using the displacement transducers near the bottom of the wall as described in Section 4.6.1.

Figure 4.34: Picture of RM1 wall general southwest view.

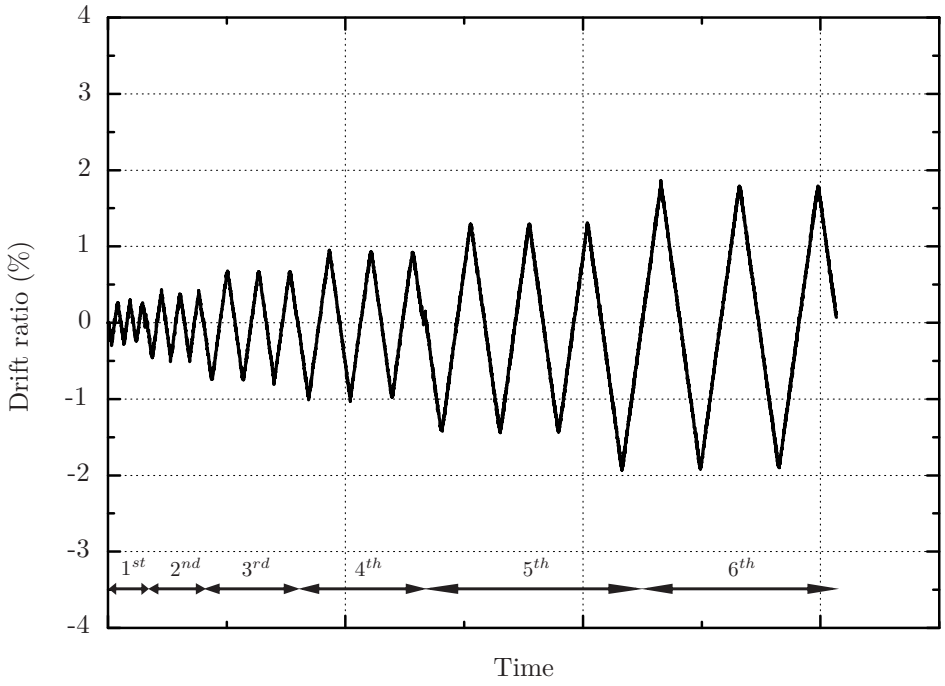

Figure 4.35: Test RM1 history of drift ratio.

Table 4.18: RM1 summary of results for base shear and drift ratio, for each set of cycles.

	Base shear force (kN)		**Drift ratio (%)**		
	Max	**Min**	**Max**	**Min**	**Residual**
1^{st} Cycles	61.1	-58.2	0.30	-0.30	0.03
2^{nd} Cycles	61.3	-64.0	0.43	-0.51	0.09
3^{rd} Cycles	64.1	-65.7	0.68	-0.81	0.08
4^{th} Cycles	66.9	-64.3	0.95	-1.03	0.08
5^{th} Cycles	69.4	-70.0	1.31	-1.44	0.08
6^{th} Cycles	73.1	-74.5	1.86	-1.93	0.07

Figure 4.36: Picture of RM1 wall transversal inclination.

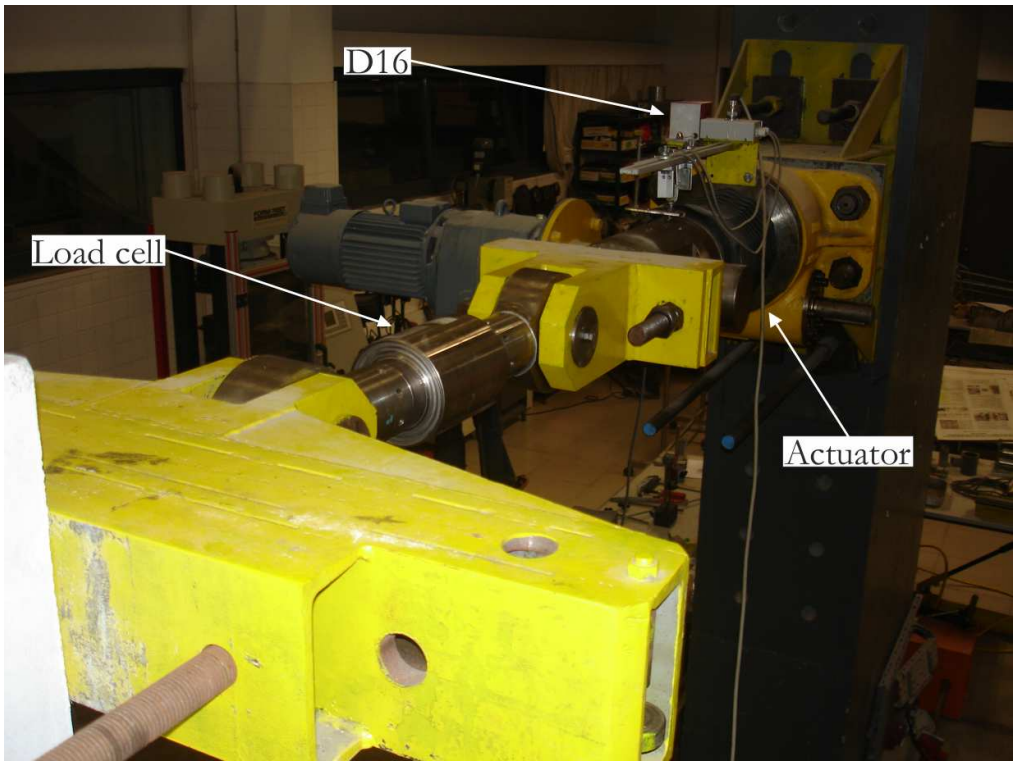

Figure 4.37: Picture of the actuator in specimen RM1.

The base shear force applied to the wall was the force of the actuator. The base shear response is shown in Figure 4.38 and should be analysed taking into account the drift ratios in Figure 4.35. It can be seen that the maximum shear base in each cycle did not change significantly with the growing drift ratios targets. In fact, the diagram shows an initial stiffness that reduces close to the base shear value of 50 kN, leading to an almost bi-linear response. This transition was due to the propagation of the gap opening length, thus it was a geometric softening. It can also be seen that this transition occurred for a force higher than 50 kN at the beginning of the test and smaller than 50 kN in the final cycles. This reduction was due to the loss of post-tensioning force, which is clear in Figures 4.39 and 4.40 and is quantified in Table 4.19, reaching 20% at the end. The post-tensioning affects directly the equilibrium of the wall and the transition zone (softening). It can be said that the main problem that led to these high values of post-tensioning losses was the short length of the strands. The full length of the strands was approximately 2.30 m, meaning that a small adjustment of 1 mm corresponded to a loss of 9% of the 130 kN initial post-tensioning force. Nevertheless, the strands were always in the elastic range ($f_{p0.1k}$ = 224kN). Finally, some degradation in the concrete was observed in the northern and southern corners of the wall, as can be seen in Figures 4.41 and 4.42. In the subsequent wall specimen experimental tests, a pre-loading, higher than the working initial post-tensioning force, was applied to the strands to reduce the effects of the adjustments of the anchorage wedges.

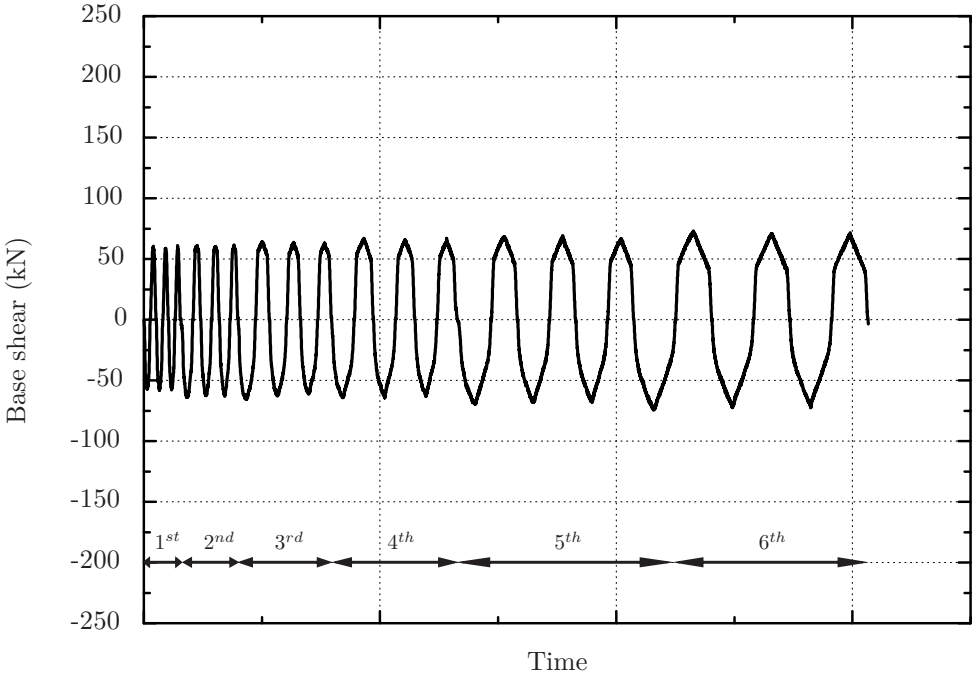

Figure 4.38: Test RM1 history of base shear force.

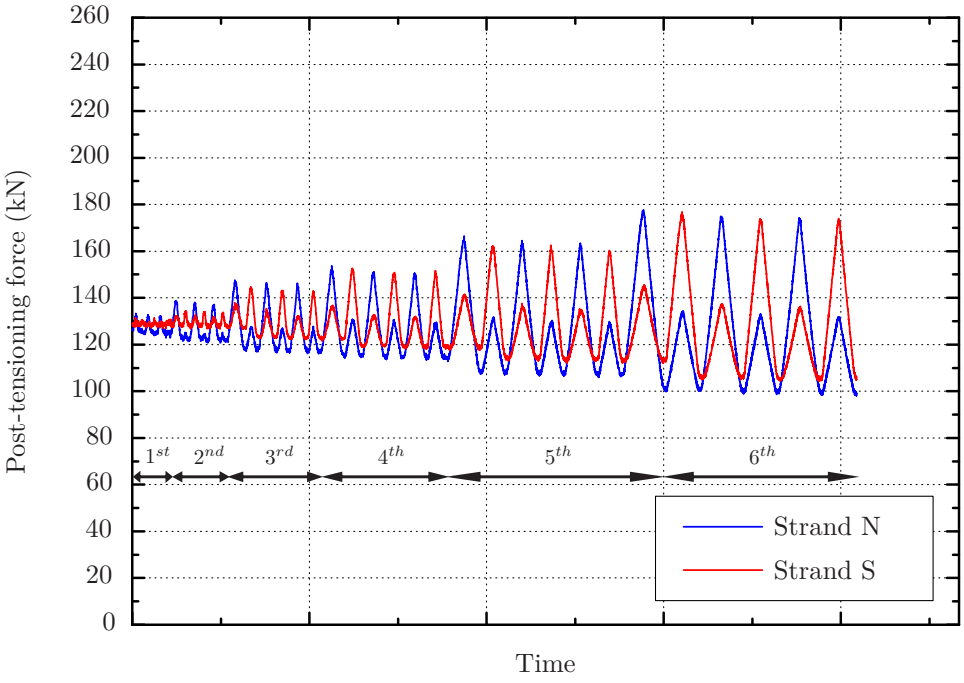

Figure 4.39: Test RM1 post-tensioning force vs time.

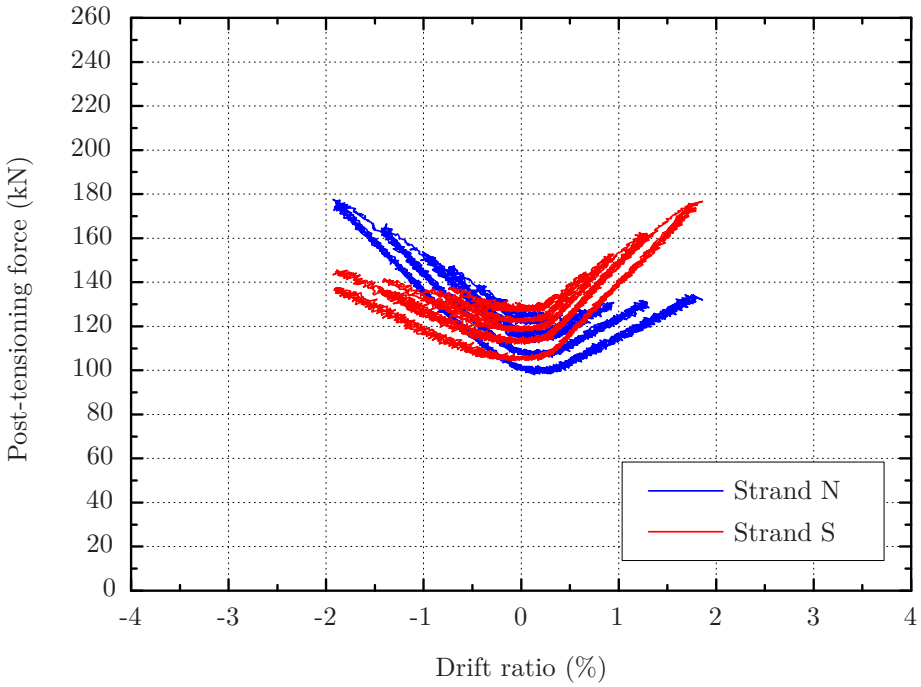

Figure 4.40: Test RM1 post-tensioning force vs drift ratio.

Table 4.19: RM1 test summary of post-tensioning force for each set of cycles

	Final post-tensioning force				**Maximum post-tensioning force**			
	Strand N		**Strand S**		**Strand N**		**Strand S**	
	F_N (kN)	**Δ**	**F_S (kN)**	**Δ**	**F_N (kN)**	**Δ**	**F_S (kN)**	**Δ**
Initial	126.4		129.1					
1^{st} Cycles	124.8	-1%	128.3	-1%	133.4	6%	131.6	2%
2^{nd} Cycles	122.6	-3%	128.7	0%	138.7	10%	134.3	4%
3^{rd} Cycles	117.0	-7%	123.4	-4%	147.5	17%	144.6	12%
4^{th} Cycles	114.4	-10%	118.8	-8%	153.7	22%	152.7	18%
5^{th} Cycles	107.0	-15%	112.3	-13%	166.6	32%	162.5	26%
6^{th} Cycles	99.1	-22%	105.1	-19%	177.6	41%	176.6	37%

Figure 4.41: Picture of RM1 wall southern corner after test.

Figure 4.42: Picture of RM1 wall southern corner after cover cleaning.

To analyse the global behaviour of the specimen, the hysteretic response diagram is shown in Figure 4.43. This diagram shows the referred bi-linear response and that the residual displacements were negligible (see also Table 4.18), as the wall recentred after every cycle. In an ideal response, all the cycles should be overlapping, without distinction between them, but the losses in prestress and some wall degradation led to a progressive reduction of the base shear force of the softening zone. The evolution of the equivalent viscous damping ratio ξ_{eq}, is shown in Figure 4.44 and the values presented reveal that the specimen had an essential elastic response, with very small dissipation energy.

Finally, two displacement blockers were used to restrain the wall, preventing any resulting sliding. During the test no sliding tendency was observed, leading to the conclusion that the blockers were not needed. Moreover, their location made it difficult to observe the southern and northern corners of the wall and created an uncertainty about the point of rotation of the wall, as the wall could be indirectly rocking on the blockers. For these reasons, their use are not recommended.

4.6.2.2 Wall specimen RM2

In the wall specimen RM2, the grout used in the wall-base connection allowed the correct vertical positioning of the wall. The application of the post-tensioning was made by pulling the strands to a higher pre-loading to reduce the system adjustments during test.

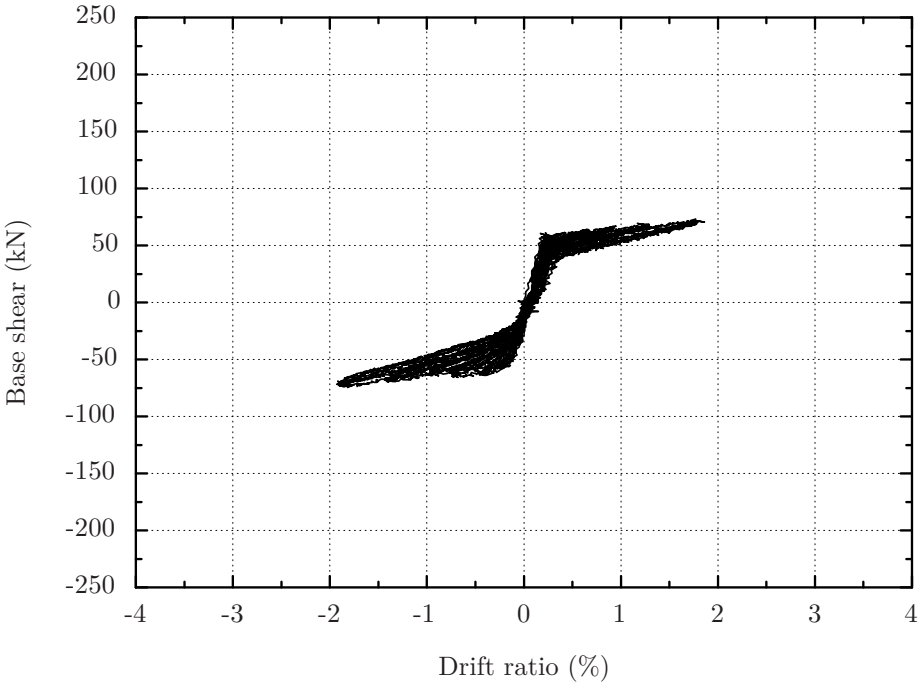

Figure 4.43: Test RM1 base shear vs drift ratio.

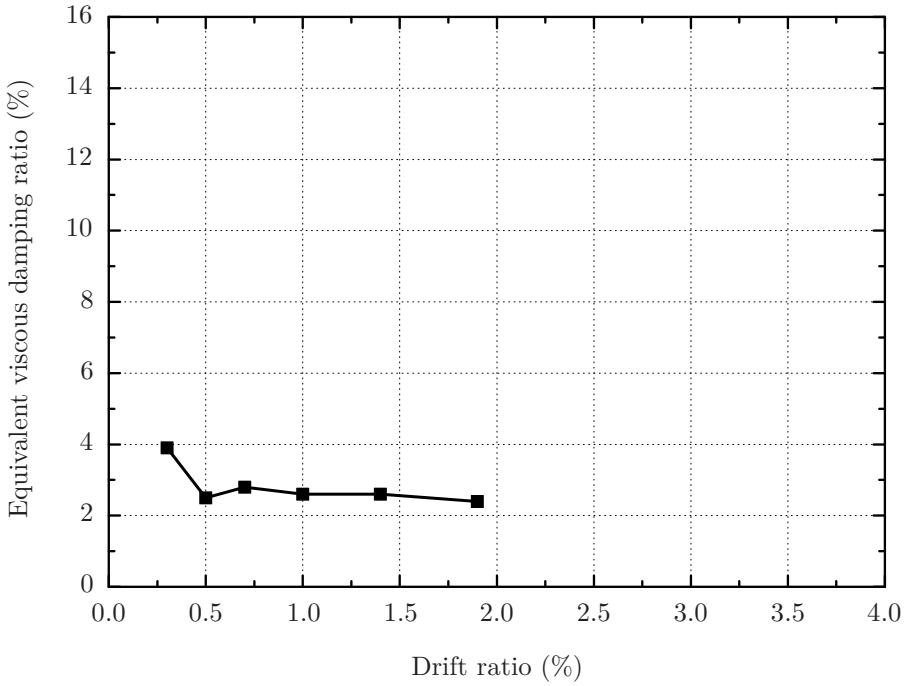

Figure 4.44: Test RM1 equivalent viscous damping ratio.

The strands were tensioned slowly until they reached 170 kN each then, when the forces were stabilised, they were reduced to 130 kN in each strand. For this wall specimen, the problems that led to a reduction of the number of displacement transducers in specimen RM1 were solved and the drift ratio was calculated using the bottom rotation, as explained in Section 4.6.1.

The imposed drift ratio had similar problems as in specimen RM1. The diagram in Figure 4.45 and Table 4.20 shows that the cycles are slightly asymmetric, specially the first two sets of cycles. Table 4.20 also shows that the residual displacements were negligible.

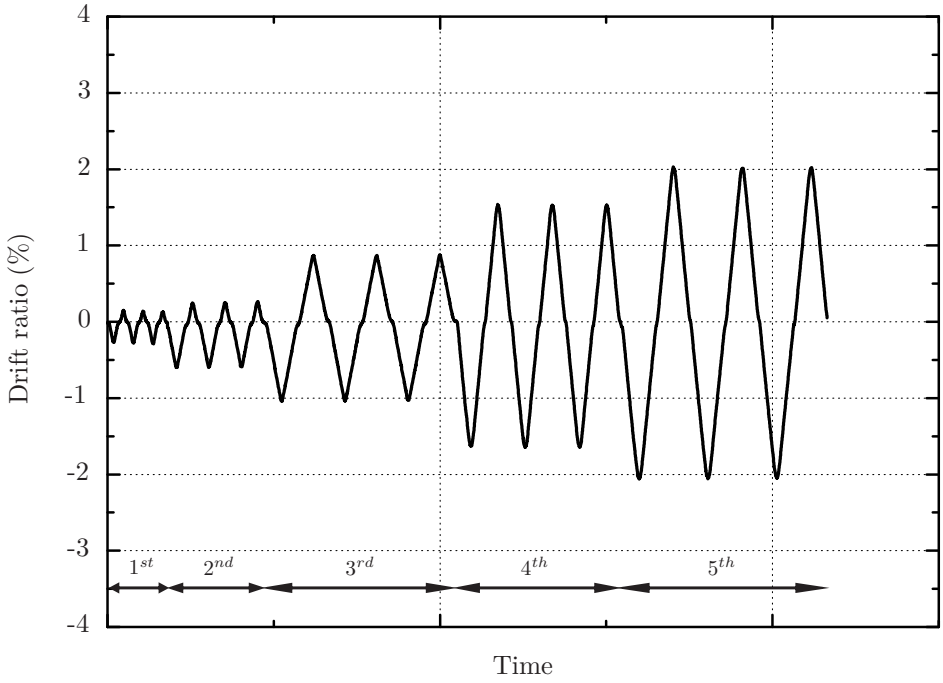

Figure 4.45: Test RM2 history of drift ratio.

Table 4.20: RM2 summary of results for base shear and drift ratio, for each set of cycles.

	Base shear force (kN)		**Drift ratio (%)**		
	Max	**Min**	**Max**	**Min**	**Residual**
1^{st} Cycles	63.1	-60.8	0.15	-0.29	-0.01
2^{nd} Cycles	67.9	-71.9	0.26	-0.60	-0.01
3^{rd} Cycles	80.2	-74.5	0.88	-1.04	0.01
4^{th} Cycles	85.2	-80.9	1.54	-1.64	0.02
5^{th} Cycles	86.3	-73.6	2.03	-2.06	0.05

The response of the specimen RM2 in terms of base shear force is shown in Figure 4.46 and Table 4.20. It can be seen that this wall reached higher shear base forces than the specimen RM1, mostly due to the better post-tensioning behaviour. In this specimen the described procedure to apply the post-tensioning resulted in no force losses until 170 kN was reached in the strands, which corresponds to the pre-loading applied before the test.

Figures 4.47 and 4.48 and Table 4.21 show that for 1% drift ratio the maximum post-tensioning force was 170 kN ($3^r d$ cycles), meaning that in the following cycles, with higher drift ratio targets, forces higher than the pre-loading value of 170 kN were reached and losses were a consequence. The final post-tensioning losses achieved 20% as in specimen RM1. Despite these losses, the maximum post-tensioning force was 194.0 kN, corresponding to an increment of 45% for 2% drift ratio, in comparison with the initial force of 133.4 kN. This high increment is also very clear in the diagram shown in Figure 4.48 and is due to the short length of the strands.

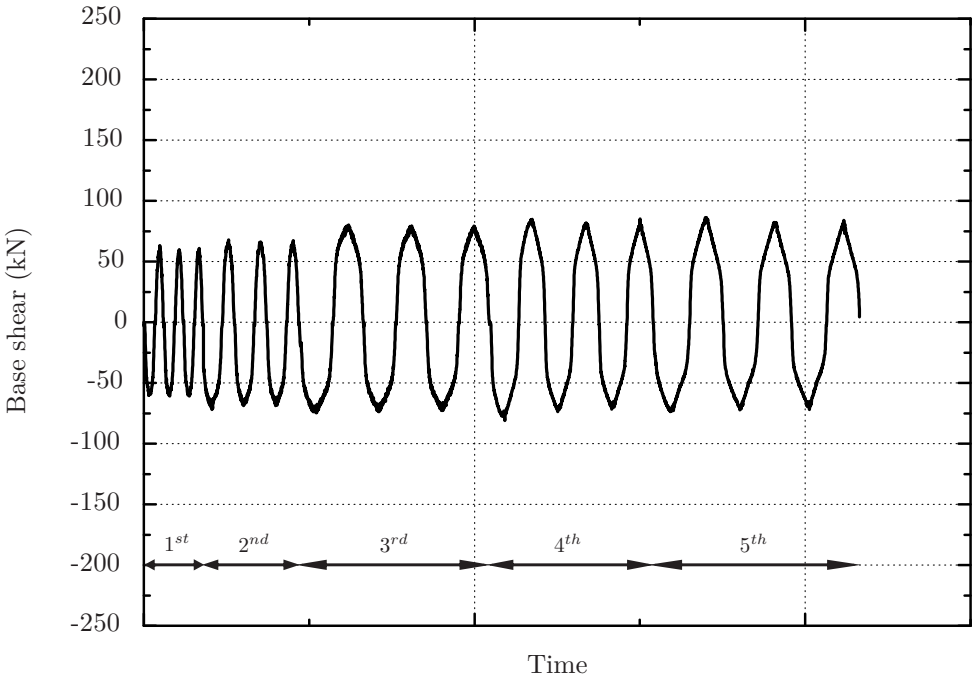

Figure 4.46: Test RM2 history of base shear force.

Table 4.21: RM2 test summary of post-tensioning force for each set of cycles

	Final post-tensioning force				**Maximum post-tensioning force**			
	Strand N		**Strand S**		**Strand N**		**Strand S**	
	$\mathbf{F_N}$ **(kN)**	**Δ**	$\mathbf{F_S}$ **(kN)**	**Δ**	$\mathbf{F_N}$ **(kN)**	**Δ**	$\mathbf{F_S}$ **(kN)**	**Δ**
Initial	134.1		133.4					
1^{st} Cycles	133.7	0%	133.8	0%	142.1	6%	137.5	3%
2^{nd} Cycles	133.5	0%	133.7	0%	155.9	16%	143.2	7%
3^{rd} Cycles	132.3	-1%	132.7	-1%	171.8	28%	169.4	27%
4^{th} Cycles	115.8	-14%	115.1	-14%	184.9	38%	185.3	39%
5^{th} Cycles	107.5	-20%	103.9	-22%	191.6	43%	194.0	45%

Table 4.22 shows the position of the neutral axis, measured from the nearest face, south or north, for each set of cycles. These values were obtained using the displacement transducers near the bottom of the wall and the methodology presented in Section 4.6.1. Each set of cycles had three maximum and minimum displacements and the neutral axis

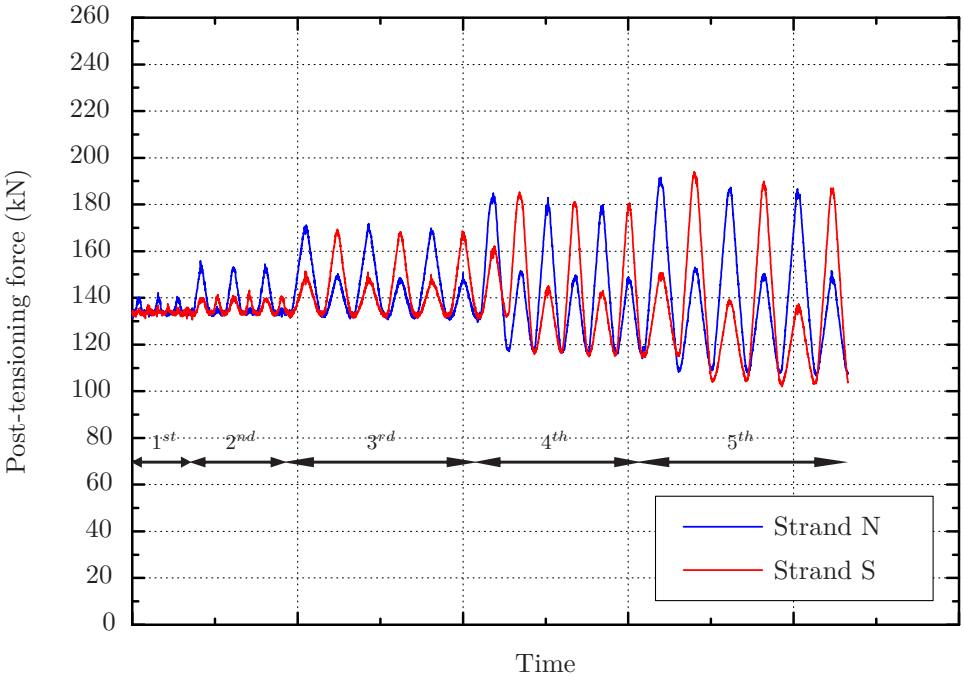

Figure 4.47: Test RM2 post-tensioning force vs time.

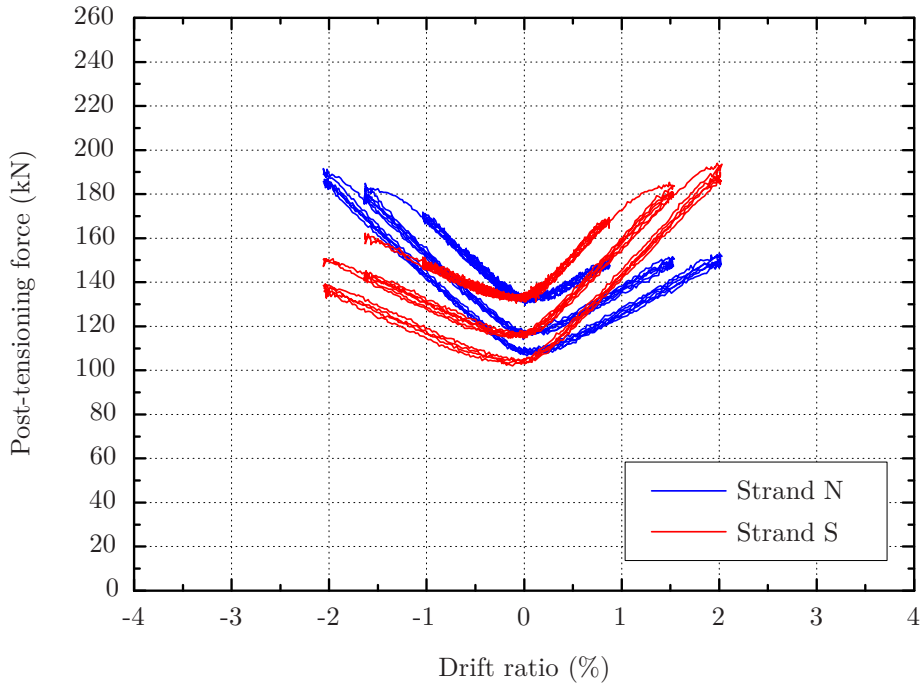

Figure 4.48: Test RM2 post-tensioning force vs drift ratio.

is the average neutral axis obtained for those three peaks. The dimension of the neutral axis decreased with the increase of the drift ratio target and for the last three sets of cycles there was a tendency to stabilise near 100 mm.

Table 4.22: Specimen RM2 neutral axis at maximum displacements (mm).

Sign	1^{st} Cycles	2^{nd} Cycles	3^{rd} Cycles	4^{th} Cycles	5^{th} Cycles
Negative	177.6	131.9	109.2	96.4	96.4
Positive	197.8	158.7	108.3	100.0	104.0

The global response of the specimen can be seen in the hysteretic diagram in Figure 4.49. This diagram shows a bi-linear response with negligible residual displacements (see also Table 4.20), where the wall recentred after every cycle. In an ideal response, all the cycles should be overlapping, but the losses in post-tensioning force and some wall degradation led to a small reduction of the base shear force correspondent to the softening zone. The equivalent viscous damping ratio ξ_{eq} evolution, is shown in Figure 4.50 and the values presented reveal that the specimen had basically an elastic response, with very small energy dissipation. The first point of the ξ_{eq} diagram is not consistent with the results of the other post-tensioned wall tests, as the others started with a higher value. The pictures in Figures 4.51 and 4.52 show that the degradation of the wall was confined to a small area of the concrete cover in the northern and southern corners of the wall.

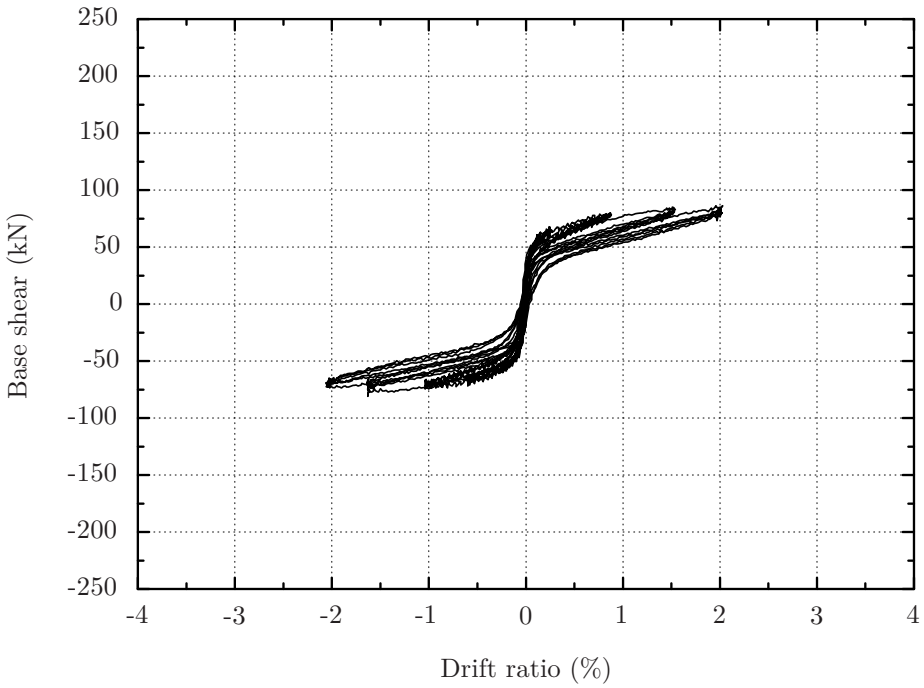

Figure 4.49: Test RM2 base shear vs drift ratio.

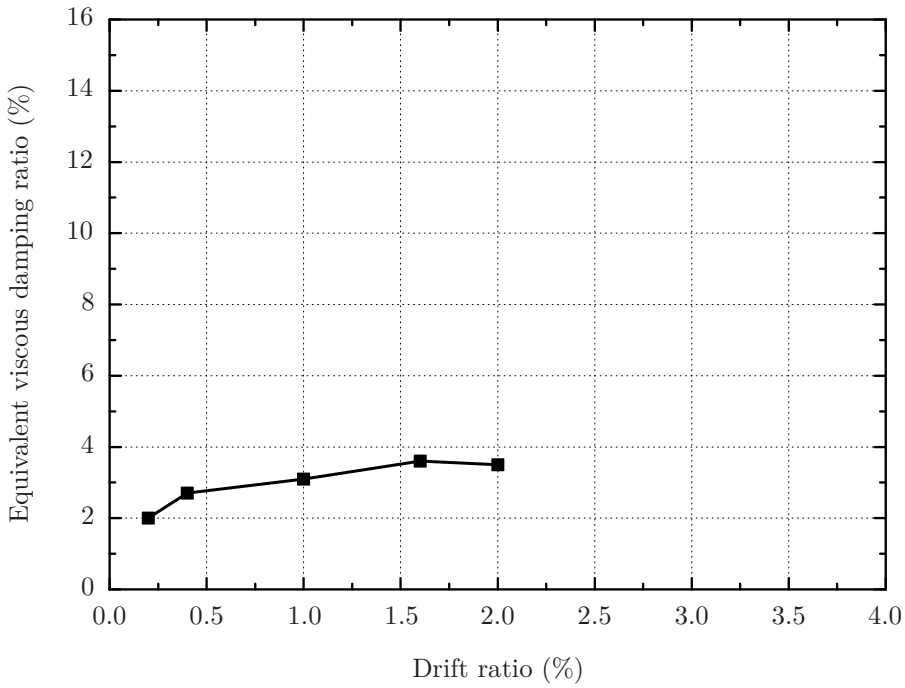

Figure 4.50: Test RM2 equivalent viscous damping ratio.

Figure 4.51: View of the western side of RM2 wall test.

Figure 4.52: View of the eastern side of RM2 wall test.

The wall rotation about the vertical axis is shown in Figure 4.53 as a function of time. The rotations were small and grew with the increase of the drift ratio target. In the fourth and fifth sets of cycles it is clear that the wall had residual rotations between the cycles.

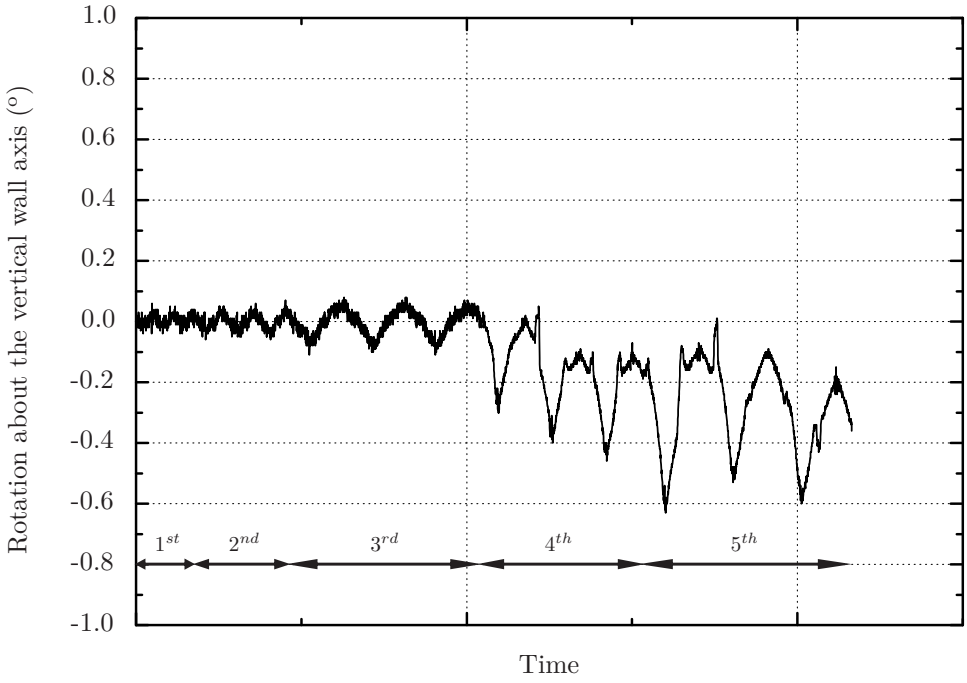

Figure 4.53: Test RM2: rotation about the vertical wall axis.

4.6.2.3 Wall specimen RM3

During specimen RM3 assembly grout was applied between the wall and the base, as in the previous test and wedges of resin and cork were included, as shown in Figure 4.54. The wedges of resin and cork were made from a material under development in FCT/UNL and was described in Section 4.3.6. When the wall was designed, the information available about the resin and cork material pointed to a proof stress of 20 MPa, much lower than the concrete compressive strength, and with a very high ultimate strain. These wedges were designed to work beyond 5% strain to be able to dissipate energy. In fact the proof stress of the resin is near 40 MPa, as may be seen in Table 4.6, and the function of the wedges of resin and cork was compromised.

Figure 4.54: View of a resin and cork wedge glued to the edge of the wall.

The application of the post-tensioning force was made following a procedure similar to the one for specimen RM2. Taking into consideration the losses of post-tensioning in specimen RM2, the applied pre-loading was higher and equal to 180 kN. The strand forces were then reduced to 130 kN in each strand.

The drift ratio was obtained using the bottom rotation, as explained in Section 4.6.1, and its time history is shown in Figure 4.55. In this specimen the wall rotation about the north-south axis was not negligible, as can be seen in Figure 4.56. As a result of this rotation, which was also present in the first two specimens, the top displacement transducer measures were not considered reliable. The maximum and minimum values of the drift ratio reached did not comply with the desired target drifts as is shown in

Table 4.23. The cause of this difference was explained for specimen RM2 and is essentially due to the inertia and clearances of the system and actuator. The first set of cycles was the one where the difference was bigger. Following this set of cycles the differences between the observed drift ratio and the desired results were still not negligible, but much smaller.

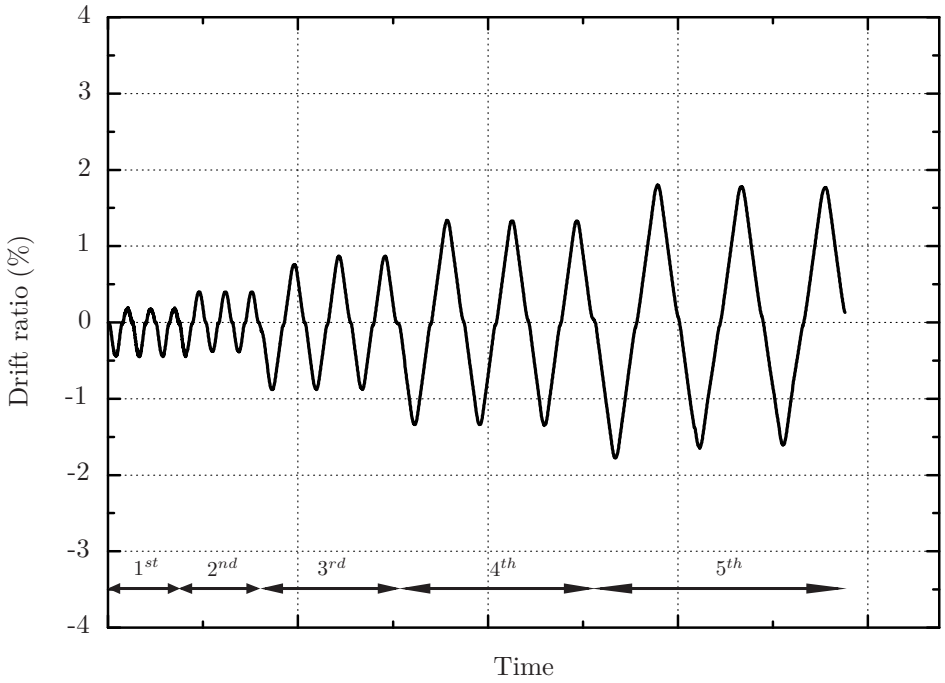

Figure 4.55: Test RM3 history of drift ratio.

(a) Top displacement transducer. **(b)** Horizontal load cell.

Figure 4.56: Wall specimen RM3 inclination.

Table 4.23: RM3 summary of results for base shear and drift ratio, for each set of cycles.

	Base shear force (kN)		Drift ratio (%)		
	Max	**Min**	**Max**	**Min**	**Residual**
1^{st} Cycles	61.4	-64.0	0.19	-0.45	0.03
2^{nd} Cycles	64.4	-65.0	0.40	-0.45	0.01
3^{rd} Cycles	74.2	-73.9	0.87	-0.88	0.01
4^{th} Cycles	84.5	-76.3	1.34	-1.35	0.04
5^{th} Cycles	81.9	-77.6	1.80	-1.78	0.00

The base shear force response of the specimen RM3 is shown in Figure 4.57 and Table 4.23. The force increases with the increment of the target drift ratio until the final set of cycles, where the maximum values of base shear force do not change significantly compared with the behaviour of the previous set.

Associated with the behaviour of the base shear force is the post-tensioning force that did not have the losses observed in tests of the previous specimens, as is shown in Figures 4.58 and 4.59 and Table 4.24. The force exceeded the pre-loading value of 180 kN without losses. The post-tensioning force had a maximum of 198.3 kN, corresponding to an increment of 52% from the starting force. With no losses in the post-tensioning forces, the base shear should continue to increase during the last set of cycles, as the drift ratio clearly increased, but that did not happen. The likely explanation for this fact is an increase in the neutral axis value from the fourth set of cycles to the fifth, as shown in Table 4.25, which was due to the degradation in the wedge-wall connection, resulting in the wedge becoming detached during the fourth set of cycles, as illustrated in Figure 4.60. The neutral axis calculation was explained in Section 4.6.1. The values obtained for this specimen can be related to two scenarios: first, the wedge remains fixed to the wall and lifts from the base; second, the wedge remains in contact with the base whilst the wall separates from the wedge. In this last option, the value is an approximation of the horizontal position where the wall lifts from the wedge.

Table 4.24: RM3 test summary of post-tensioning force for each set of cycles

	Final post-tensioning force				Maximum post-tensioning force			
	Strand N		Strand S		Strand N		Strand S	
	F_N (kN)	**Δ**	**F_S (kN)**	**Δ**	**F_N (kN)**	**Δ**	**F_S (kN)**	**Δ**
Initial	130.9		130.6					
1^{st} Cycles	131.7	1%	131.9	1%	146.5	12%	138.7	6%
2^{nd} Cycles	131.6	1%	131.1	0%	146.3	12%	145.0	11%
3^{rd} Cycles	132.0	1%	131.7	1%	165.6	27%	165.9	27%
4^{th} Cycles	130.7	0%	132.3	1%	183.6	40%	185.2	42%
5^{th} Cycles	128.1	-2%	129.2	-1%	194.6	49%	198.3	52%

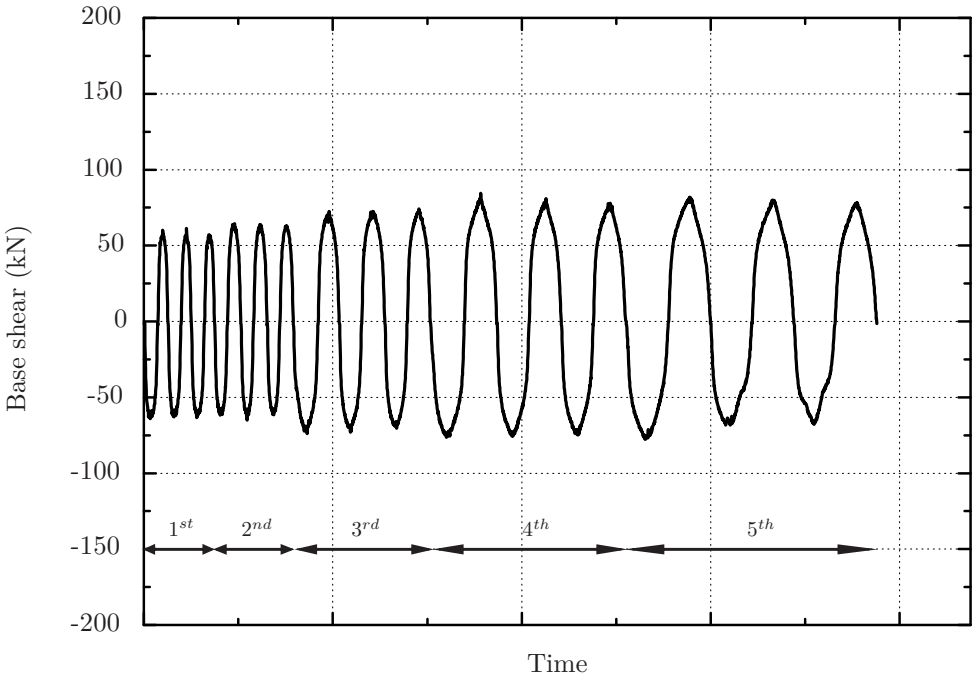

Figure 4.57: Test RM3 history of base shear force.

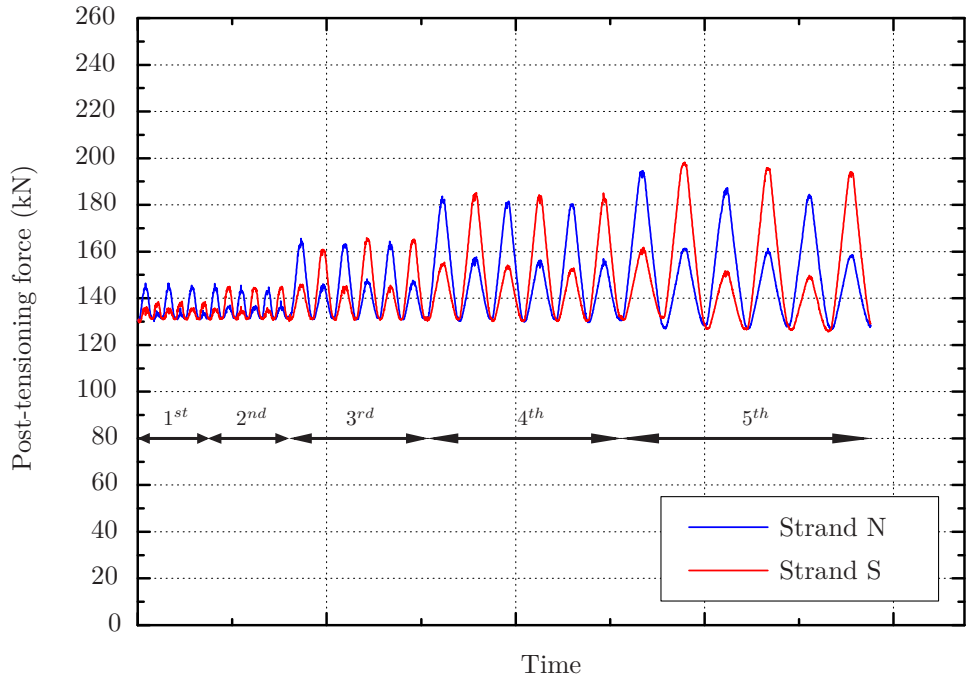

Figure 4.58: Test RM3 post-tensioning force vs time.

Table 4.25: Specimen RM3 neutral axis at maximum displacements (mm).

Sign	1^{st} Cycles	2^{nd} Cycles	3^{rd} Cycles	4^{th} Cycles	5^{th} Cycles
Negative	187.2	169.5	131.3	119.9	126.7
Positive	132.7	149.5	115.6	110.4	114.7

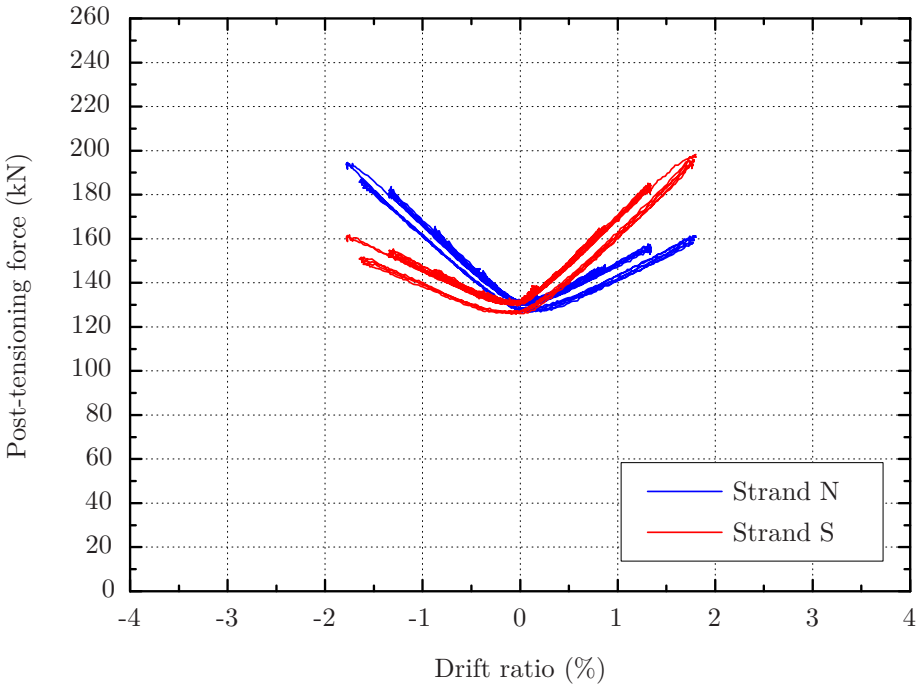

Figure 4.59: Test RM3 post-tensioning force vs drift ratio.

Figure 4.60: Detail of the southern corner with the detached wedge and damaged concrete.

The global response of the specimen is presented in the hysteretic diagram in Figure 4.61. This diagram shows a bi-linear response and negligible residual displacements (see also Table 4.23), where the wall recentred after each cycle. The equivalent viscous damping ratio ξ_{eq}, is shown in Figure 4.62 and the values presented reveal that the specimen had basically an elastic response, with very little energy dissipation. The last point of the ξ_{eq} diagram shows a large increase compared with the previous ones, and the probable cause was the degradation associated with the detachment of the wedge and, eventually, the plastic nonlinear response of the resin and cork. Figure 4.63 shows that the degradation of the wall was confined to the area of concrete cover in the northern and southern corners.

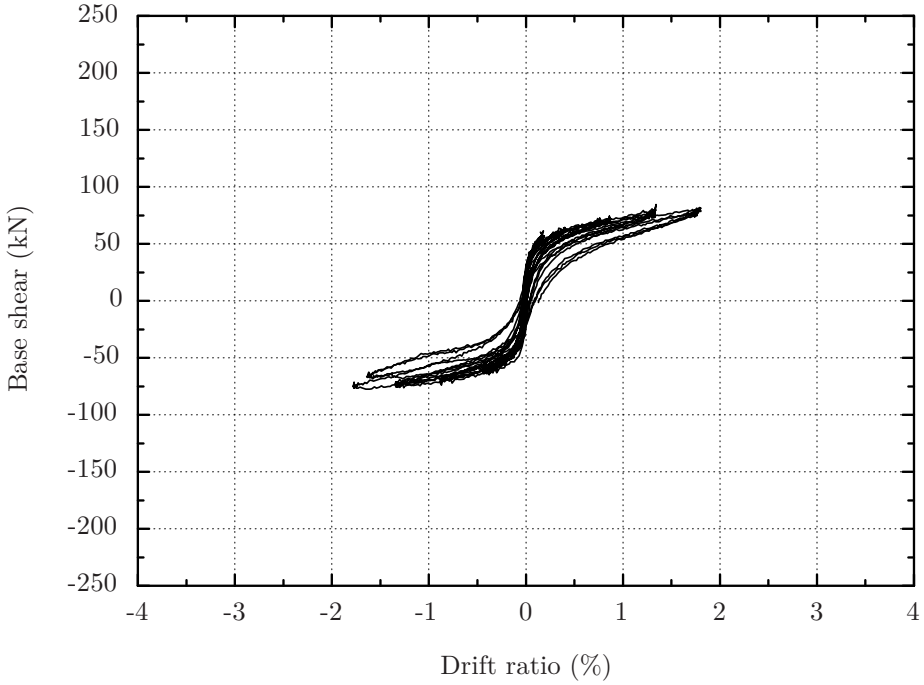

Figure 4.61: Test RM3 base shear vs drift ratio.

The wall rotation evolution about the vertical axis along time is shown in Figure 4.64. The rotations were minimal and increased as the drift ratio grew, specially in the final two sets of cycles. In the final set of cycles the wall had residual positive rotations between cycles.

The strains measured from the strain gauges glued to the steel bars were not considered relevant. The maximum stresses obtained were 100 MPa in the positive direction and 30 MPa in the negative one. The qualitative values were as expected, higher strains near the bottom and lower strains in the upper bars, with relatively low values.

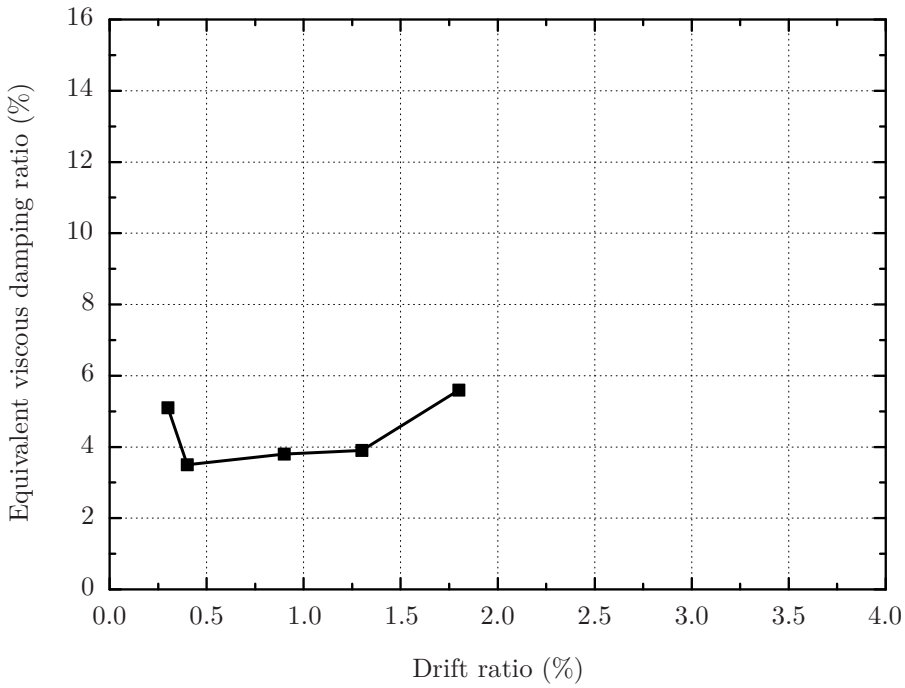

Figure 4.62: Test RM3 equivalent viscous damping ratio.

Figure 4.63: Picture of RM3 wall after testing.

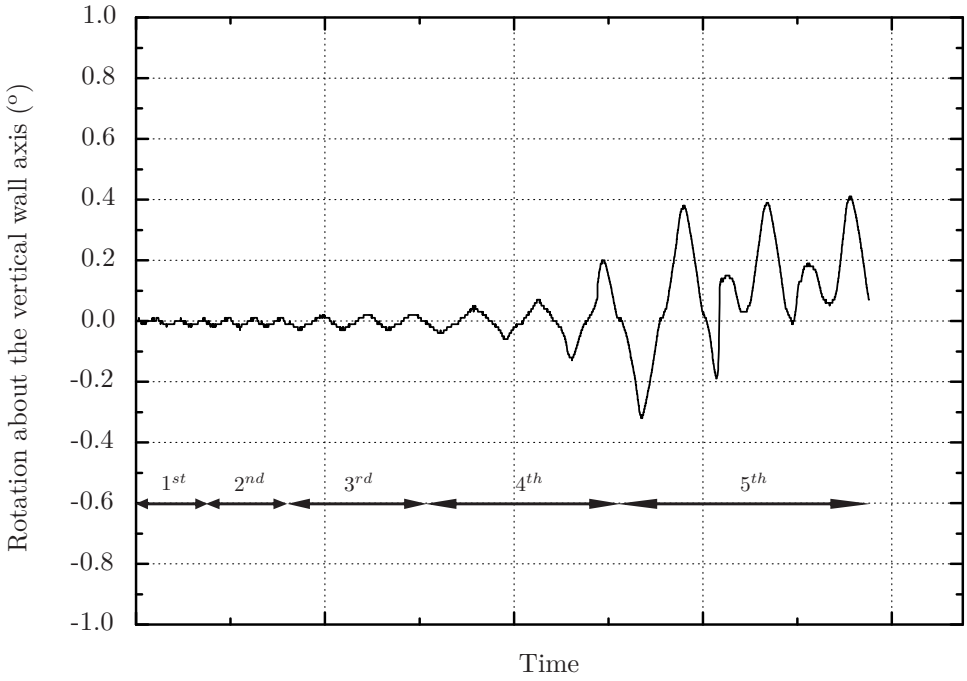

Figure 4.64: Test RM3: rotation about the vertical wall axis.

4.6.3 Tests on hybrid rocking walls

4.6.3.1 Wall specimen RM4

The wall test specimen RM4 was a precast concrete hybrid solution and the results reflect a recentring behaviour with energy dissipation. The maximum drift ratio reached was around 2.7% and the displacement history is shown in Figure 4.65. From this graphic, and also from Table 4.26, a difference between the prescribed displacement history (Figure 4.27) and the test can be observed. This difference, as already mentioned in the preliminary tests, was due to the difference between the reading of the transducer that controlled the displacement and the actual displacement of the specimen. The presented drift ratios were obtained based on the four vertical displacements near the bottom of the wall, as described in Section 4.6.1.

Figure 4.66 shows the history of the base shear and Table 4.26 presents the maximum values for each set of cycles. It can be seen that most of the force increment occurs in the first set of cycles for a target drift of 0.25%. This initial high force increment reduces with the spreading of the gap opening in the bottom section and the yielding of the steel angles. The yielding of the steel angles can be estimated from Figure 3.28 and would be around 1 mm, which means that it is possible that the angles have reached the yielding displacement in the first set of cycles (Figure 4.67).

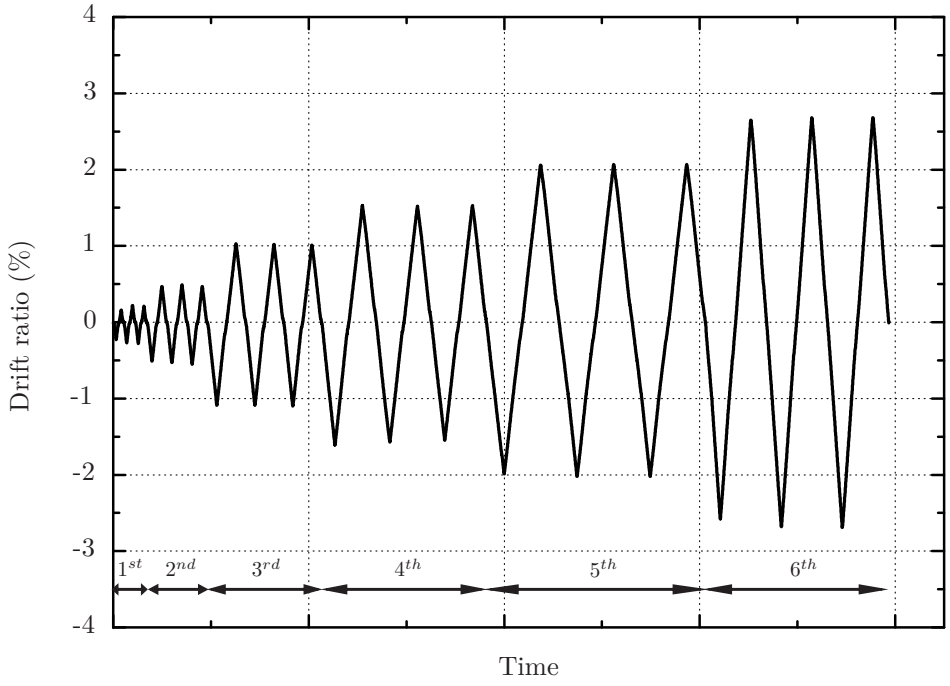

Figure 4.65: Test RM4 history of drift ratio.

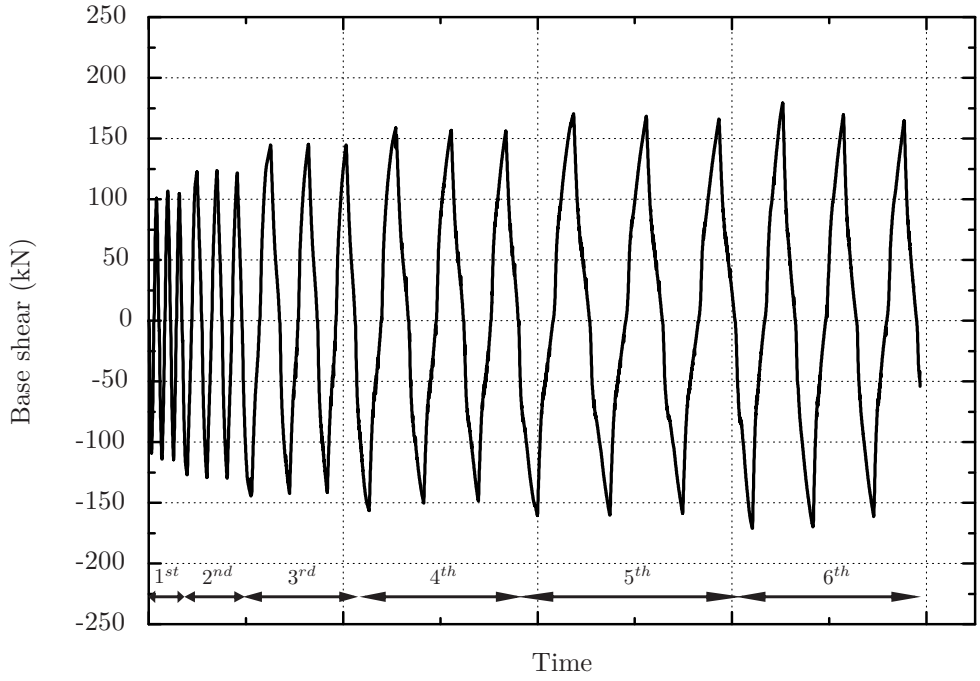

Figure 4.66: Test RM4 history of base shear force.

Table 4.26: RM4 summary of results for base shear and drift ratio, for each set of cycles.

	Base shear force (kN)		Drift ratio (%)		
	Max	**Min**	**Max**	**Min**	**Residual**
1^{st} Cycles	106.8	-114.8	0.22	-0.28	0.00
2^{nd} Cycles	123.7	-129.8	0.49	-0.55	0.00
3^{rd} Cycles	145.2	-144.3	1.03	-1.10	0.04
4^{th} Cycles	158.8	-156.5	1.53	-1.61	0.14
5^{th} Cycles	170.5	-160.5	2.07	-2.02	0.25
6^{th} Cycles	179.3	-171.2	2.68	-2.69	0.51

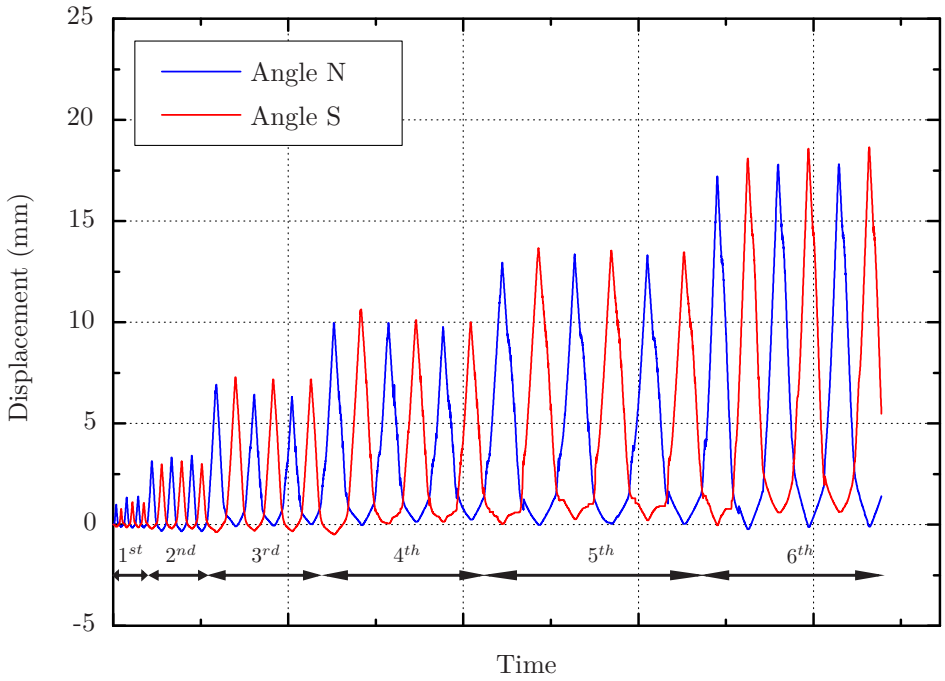

Figure 4.67: Test RM4 angles displacement vs time.

The post-tensioning is very important in the whole system behaviour. The application of the post-tensioning force was carried out in a procedure similar to the one for the previous specimen. The force applied to each strand before the test started was 180 kN and then reduced to 130 kN.

Figures 4.68 and 4.69 show the evolution of the post-tensioning forces throughout the cyclic test. During the test there were losses in the post-tensioning forces that started after the force in the strands went beyond the maximum initial force of 180 kN. The values of the post-tensioning forces at the end of each set of cycles are presented in Table 4.27. During the test two of the plates in the post-tensioning force application system yielded. This yielding promoted a shortening in the strands, being considered as an important cause of the final losses of post-tensioning forces. The post-tensioning force increased up to high values during the test.This is not the ideal response and do not represent a real

situation. This could be explained by the short length of the strands, which led to to high strains for low displacements. A real wall would be constructed with significantly longer strands which would result in lower force increments.

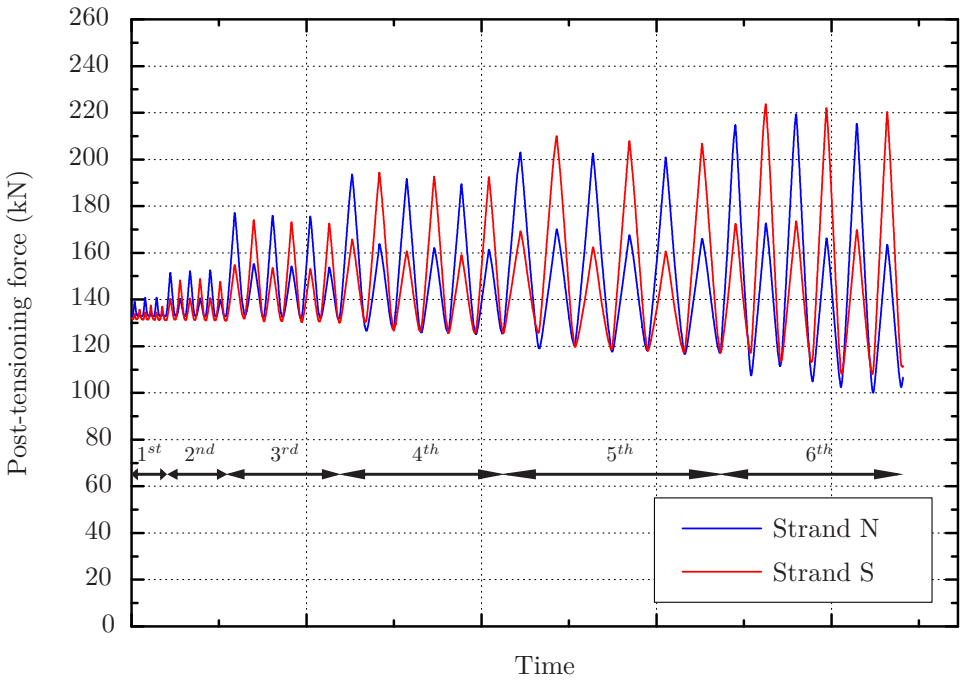

Figure 4.68: Test RM4 post-tensioning force vs time.

Table 4.27: RM4 test summary of post-tensioning force for each set of cycles.

	Final post-tensioning force				**Maximum post-tensioning force**			
	Strand N		**Strand S**		**Strand N**		**Strand S**	
	F_N (kN)	**Δ**	**F_S (kN)**	**Δ**	**F_N (kN)**	**Δ**	**F_S (kN)**	**Δ**
Initial	133.0		131.9					
1^{st} Cycles	132.8	0%	131.4	0%	140.8	6%	137.4	4%
2^{nd} Cycles	132.8	0%	131.3	0%	152.5	15%	148.7	13%
3^{rd} Cycles	132.0	-1%	131.6	0%	177.1	33%	174.1	32%
4^{th} Cycles	126.6	-5%	129.9	-2%	193.5	46%	194.3	47%
5^{th} Cycles	119.4	-10%	124.0	-6%	203.0	53%	210.0	59%
6^{th} Cycles	106.4	-20%	120.8	-8%	219.4	65%	223.7	70%

The two steel angles energy dissipaters used in the experimental test presented a good global behaviour. The deformed shape of an angle is shown in Figure 4.70. The angle setup is similar to the one used in Chapter 3 and the expected response is shown in Section 3.2. The evolution with time of the relative displacement between the angles vertical legs and the base is shown in Figure 4.67.

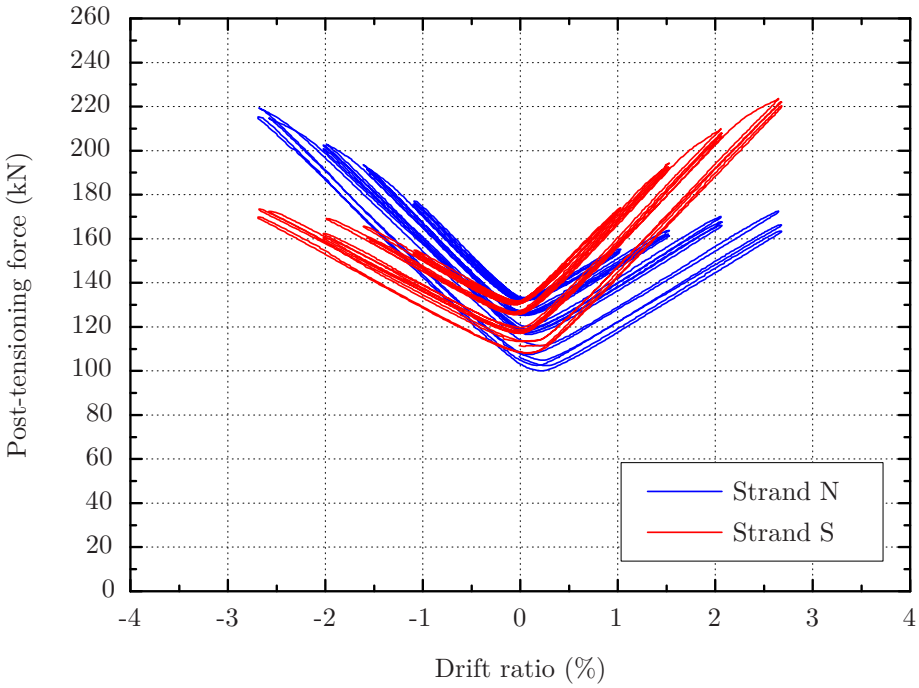

Figure 4.69: Test RM4 post-tensioning force vs drift ratio.

Figure 4.70: Picture of the deformed angle.

A small slippage between the angles and the steel plates was observed, it was noticed that until a drift ratio of 1% was reacher the slippage was essentially in the steel angle device in the northern corner of the wall. Above this value, both angles had this relative displacement. The origin of this slippage was the bending of the bolts in the plate holes and the 1 mm tolerance of the bolt holes in the steel angles. There was estimated to be a maximum of 2 mm slippage. Figure 4.71 shows the displacement of the angles as a function of drift ratio and the slippage is evident. An ideal response would have no slippage and all the curves would all be overlapping.

Figure 4.72 shows the vertical relative displacement between the vertical steel plates embedded in the concrete wall and the concrete. The time scale used is equal to the other time scales related to specimen RM4, and it can be seen that the transducers stopped reading at the beginning of the fifth set of cycles, corresponding to the target drift ratio of 2.0%. This was a result of the transducer connection becoming detached from the concrete due to spalling, as illustrated in Figure 4.73. This spalling was a consequence of the relative displacement of the plates. The maximum relative displacement measured was about 1 mm and the reason for this displacement was identified as the lack of welding between the plates and the steel bars that connect the plates to the concrete. The vertical steel plates were connected to the wall using steel bars that were welded to the plate only in one side (outside) of the plate hole instead of both sides (see Figure 4.21). As a result, the steel bars could bend in the zone of the 1 mm bolt hole tolerance between the plates and the steel bar.

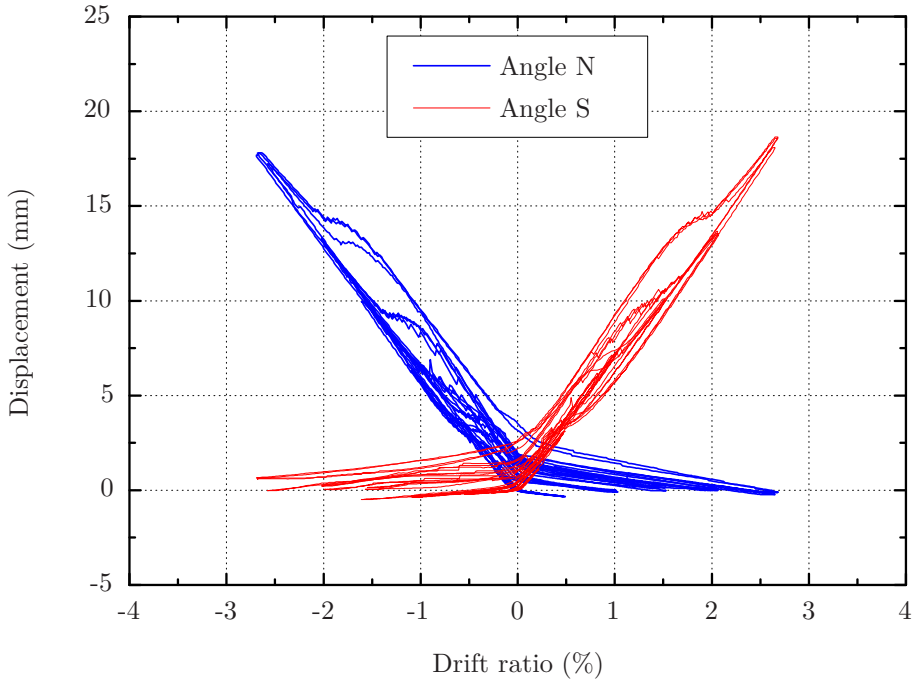

Figure 4.71: Test RM4 angles displacement vs drift.

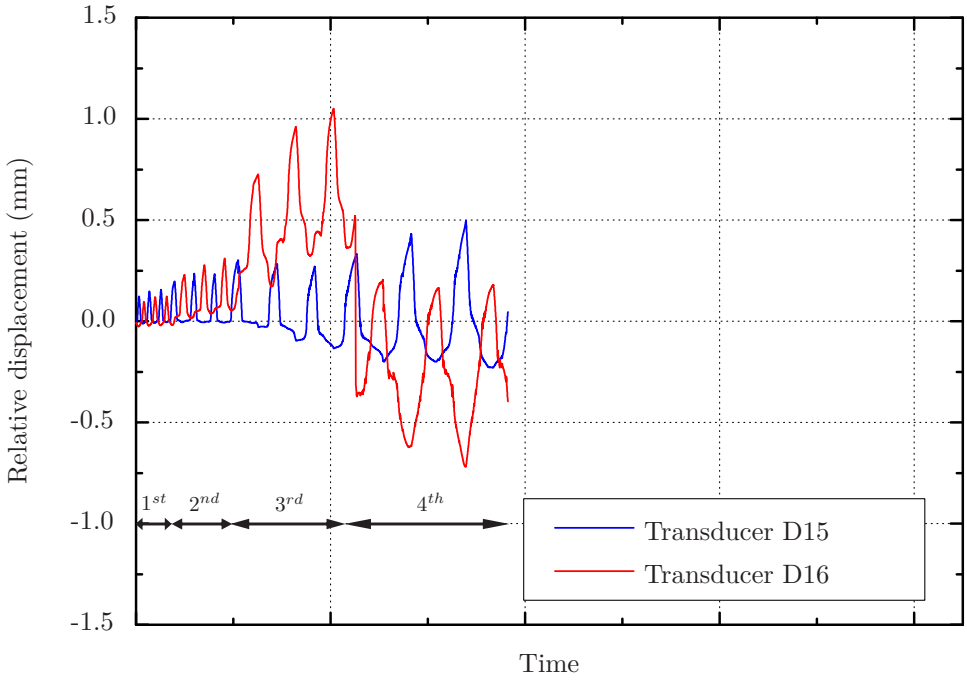

Figure 4.72: Test RM4 vertical relative displacement between connection plates and concrete.

Figure 4.73: Picture of the relative displacement transducer and concrete spalling.

In the final set of cycles, both angles reached rupture, as illustrated in Figure 4.74. The rupture was in the horizontal leg between the bolts, as observed in the angles tested in Chapter 3, as shown in Figure 3.29. Figure 4.67 shows that the maximum displacement in the angle in the southern corner of the wall was approximately 17.5 mm, which is approximately the displacement value reached in the experimental tests carried out on the steel angles, where the final stable cycle was for 20 mm displacement.

Figure 4.74: Specimen RM4 picture of the angle rupture.

The hysteretic response diagram, where base shear as a function of drift ratio is shown in Figure 4.76 and in Figure 4.75 for each set of cycles separately. The response was stable until 2% drift ratio, presenting residual displacements of 0.25% drift ratio (Table 4.26) due to losses in the post-tensioning forces, that increased after the first cycle of 2% target drift ratio. The failure started at the set of cycles of 2.5% target drift ratio due to the increased losses of post-tensioning forces and cracks opening in the steel angles. Figure 4.77 shows the equivalent viscous damping ratio as a function of drift ratio. From these results, a value of around 12.5% equivalent viscous damping ratio can be used for design drift ratios between 1.5% and 2.0%. The behaviour of the steel angles was as desired until the final cycles, when rupture was achieved.

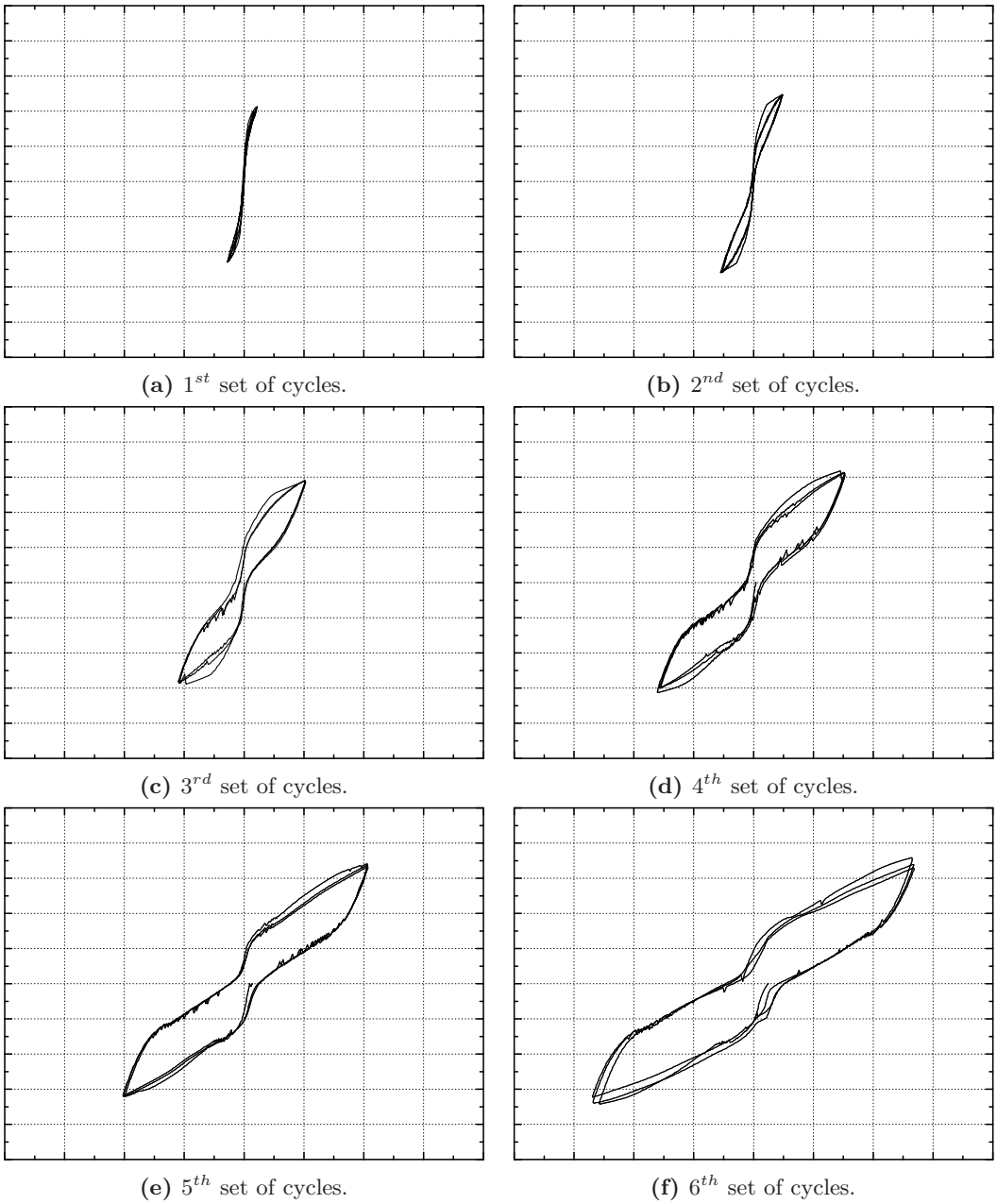

(a) 1^{st} set of cycles.

(b) 2^{nd} set of cycles.

(c) 3^{rd} set of cycles.

(d) 4^{th} set of cycles.

(e) 5^{th} set of cycles.

(f) 6^{th} set of cycles.

Figure 4.75: Test RM4 base shear vs drift ratio for each set of cycles.

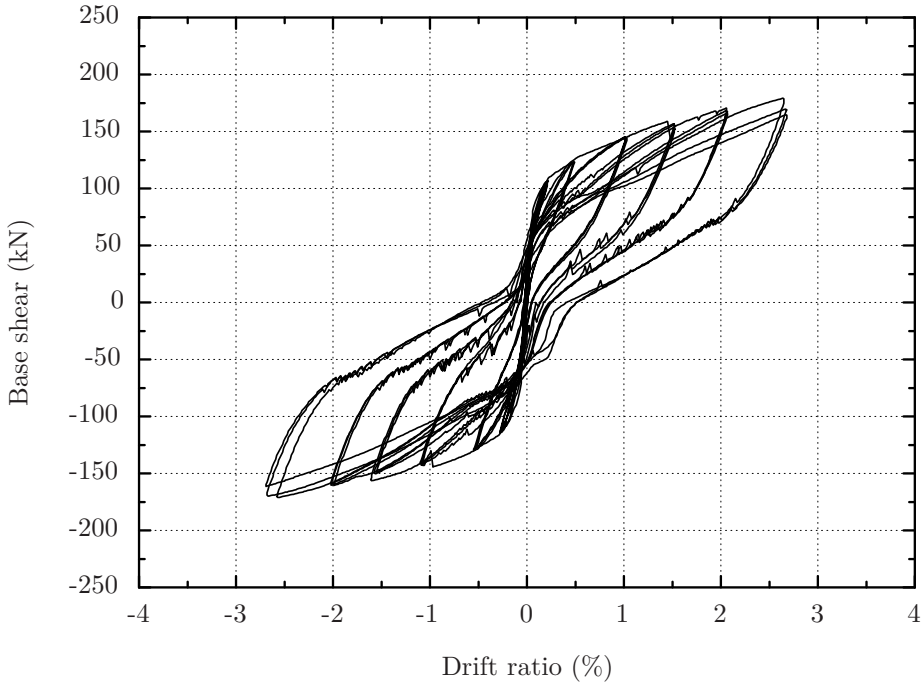

Figure 4.76: Test RM4 base shear vs drift ratio.

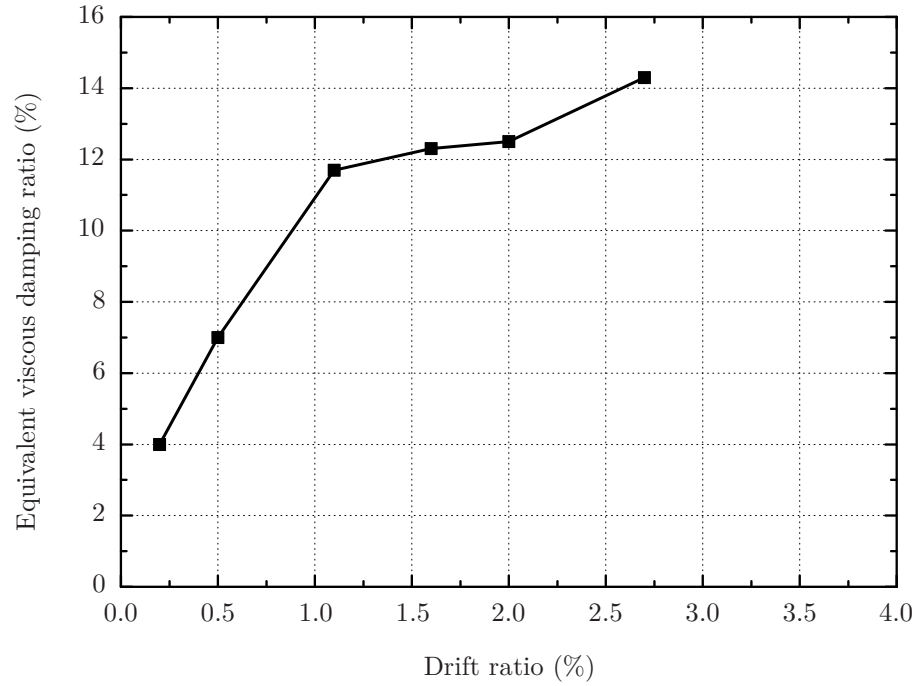

Figure 4.77: Test RM4 equivalent viscous damping ratio.

The wall rotation about the vertical axis is shown in Figure 4.78 as a function of time. The rotations were small and grew with the increase of the drift ratio target, specially in the last three sets of cycles, where the wall had residual positive rotations between cycles. These rotations were not expected in this specimen as the angles should make the connection stiffer, helping to control the undesired rotations and displacements. The conclusion was that when the angles achieve the yielding point, the hardening stiffness was not enough to restrain those rotations and displacements. Consequently the following experimental tests on wall specimens included a lateral bracing system.

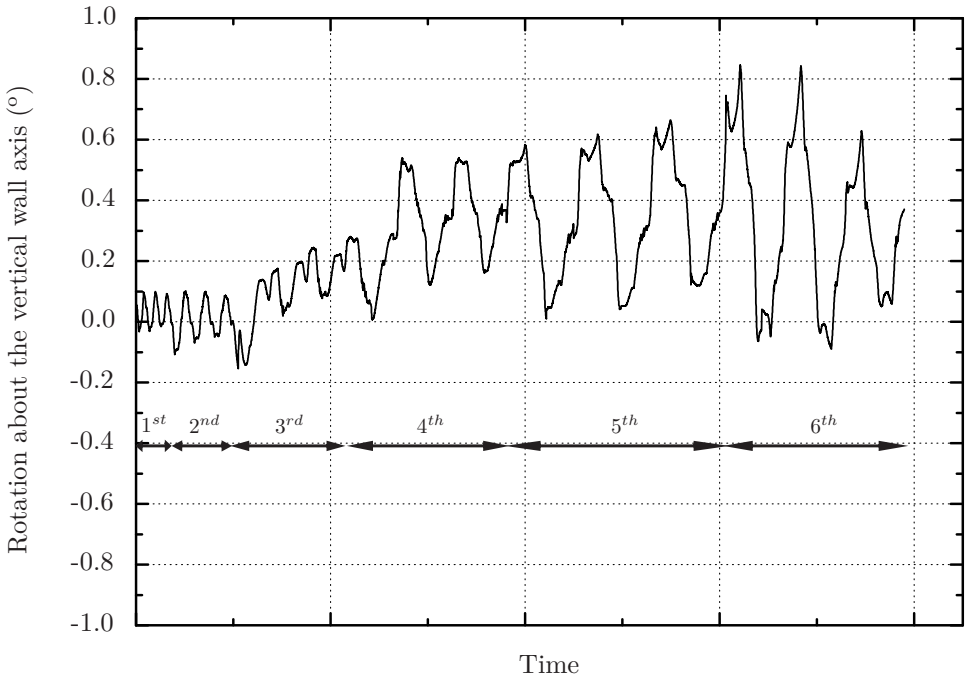

Figure 4.78: Test RM4: rotation about the vertical wall axis.

4.6.3.2 Wall specimen RM5

Wall specimen RM5 was considered the final and best solution. The energy dissipaters used were the steel angles tested in Chapter 3 designated as specimen A5. In this test a bracing system was included. The bracing system was fabricated from steel scaffolding tubes, clamped and welded together and to the base as shown in Figure 4.79. With the bracing system, the rotations about the north-south axis were negligible and the measured response was considered more reliable. Furthermore the limit target drift ratio was raised to 3.0% and was conditioned by the high post-tensioning forces reached. The design drift for the specimens was 2.0% and the goal was a good response up to a drift ratio of 2% and a stable and predictable behaviour beyond that point. The global response of this specimen was very good.

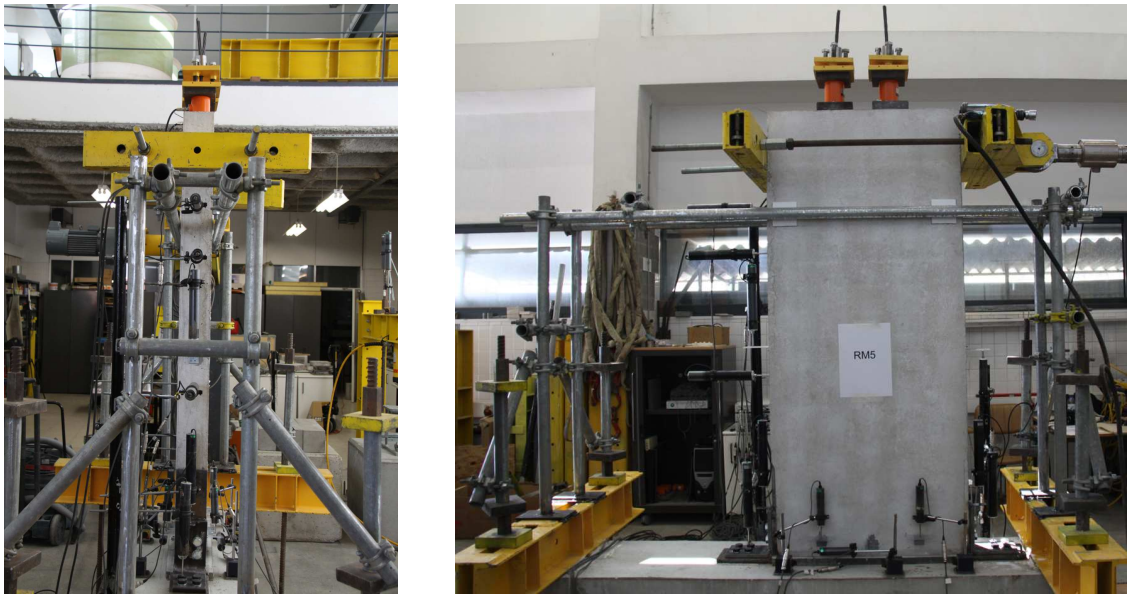

(a) Southern view. **(b)** Eastern view.

Figure 4.79: Pictures of specimen RM5 bracing system.

The history of drift ratio is plotted in Figure 4.80 and the extreme values are in Table 4.28. As previously stated, the maximum target drift ratio was 3.0%. The drift ratio results for every set of cycles were close to targets as seen in Figure 4.27. The energy dissipater made the system more stable and the actuator response to the reverse command more rapid. The bracing system also allowed a better control of the drift ratio.

Table 4.28: RM5 summary of results for base shear and drift ratio, for each set of cycles.

	Base shear force (kN)		**Drift ratio (%)**		
	Max	**Min**	**Max**	**Min**	**Residual**
1^{st} Cycles	102.3	-116.5	0.17	-0.22	0.03
2^{nd} Cycles	124.8	-133.0	0.45	-0.50	0.05
3^{rd} Cycles	145.7	-149.9	0.97	-1.02	0.10
4^{th} Cycles	161.4	-162.0	1.56	-1.51	0.16
5^{th} Cycles	174.1	-172.8	2.07	-1.98	0.26
6^{th} Cycles	185.1	-178.7	2.62	-2.47	0.45
7^{th} Cycles	194.3	-184.5	3.14	-2.93	0.20

Figure 4.81 shows the history of the base shear force. An initial higher increase in the force was observed for reasons that were already explained for specimen RM4. During each set of cycles the maximum base shear force had small variations and the maximum values for each set are registered in Table 4.28.

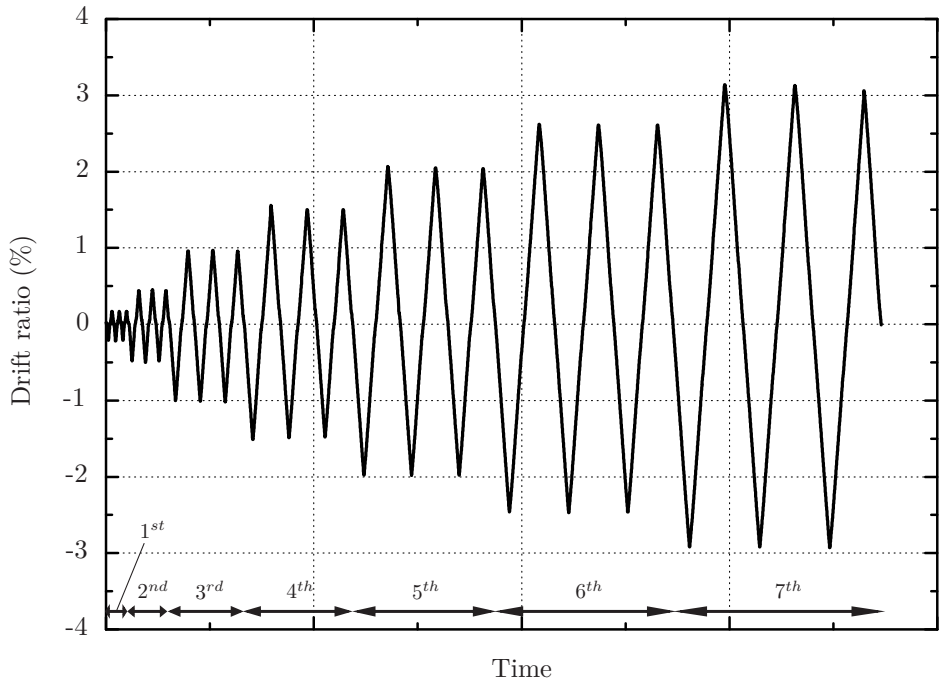

Figure 4.80: Test RM5 history of drift ratio.

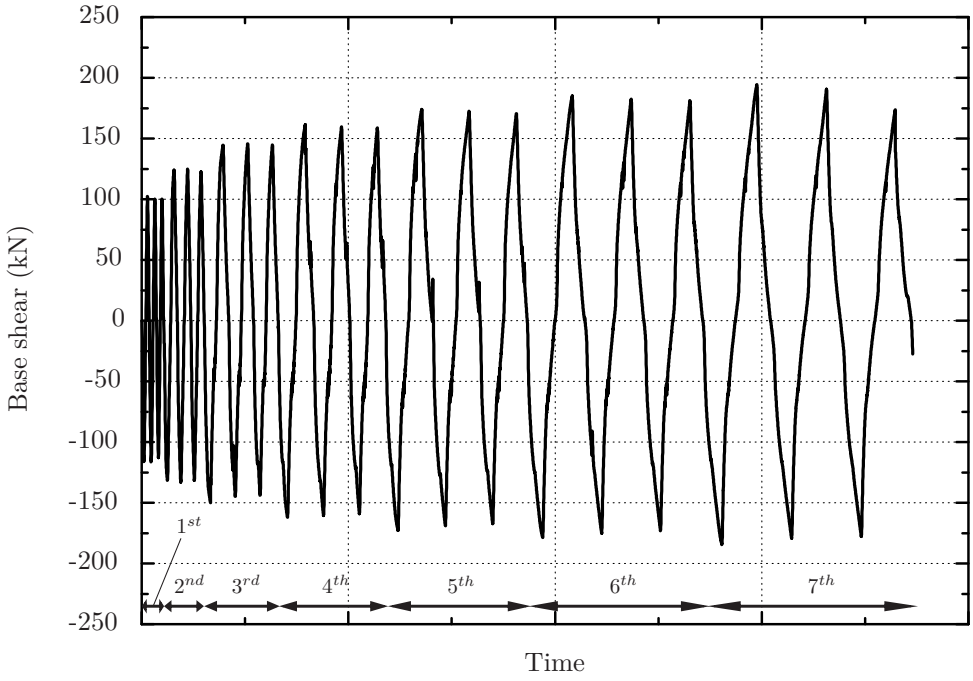

Figure 4.81: Test RM5 history of base shear force.

The post-tensioning forces were responsible for the elastic component of the hybrid system and were relevant in the whole response. The application of the post-tensioning force was made in a procedure similar to the one in the previous specimen. Once the adjustments and the respective force losses were associated with the maximum pre-loading applied, it was decided to increase the pre-loading in relation to the previous specimen. The applied pre-loading was 200 kN and then reduced to 130 kN in each strand.

Figures 4.82 and 4.83 show the evolution of the post-tensioning forces during the cyclic test. The post-tensioning forces reached very high values, reaching the characteristic 0.1% proof-stress of prestressing steel $f_{p0.1k}$, as shown in Table 4.29. Theoretically the force corresponding to that limit is $F_{p0.1k}$ =224 kN and for the sets of cycles with target drift ratios higher than 2%, that force was exceeded. When this limit is exceeded losses in the corresponding post-tensioning forces are expected, thus this was one of the reasons for the decrease of the post-tensioning forces in the final sets of cycles. Furthermore, the losses in the post-tensioning forces started when the maximum 200 kN forces was exceeded, as expected. The losses reached 27% and the maximum force was 241.6 kN, far beyond $F_{p0.1k}$, but also far away from rupture.

Table 4.29: RM5 test summary of post-tensioning force for each set of cycles.

	Final post-tensioning force				**Maximum post-tensioning force**			
	Strand N		**Strand S**		**Strand N**		**Strand S**	
	$\mathbf{F_N}$ **(kN)**	**Δ**	$\mathbf{F_S}$ **(kN)**	**Δ**	$\mathbf{F_N}$ **(kN)**	**Δ**	$\mathbf{F_S}$ **(kN)**	**Δ**
Initial	130.2		131.3					
1^{st} Cycles	130.1	0%	131.5	0%	138.4	6%	135.8	3%
2^{nd} Cycles	130.2	0%	131.8	0%	151.6	16%	148.4	13%
3^{rd} Cycles	130.5	0%	133.0	1%	177.5	36%	173.0	32%
4^{th} Cycles	130.2	0%	133.9	2%	200.6	54%	201.3	53%
5^{th} Cycles	122.8	-6%	126.6	-4%	216.6	66%	218.4	66%
6^{th} Cycles	115.1	-12%	120.9	-8%	228.6	76%	232.1	77%
7^{th} Cycles	98.2	-25%	96.0	-27%	237.7	83%	241.6	84%

The energy dissipaters used had a good global behaviour. The deformed shape of an angle is shown in Figure 4.84. The angle setup is similar to the one tested in Chapter 3 and the expected response was presented in Section 3.2. The readings of the displacement transducers used to monitor the relative displacement between the angles vertical legs and the base are shown in Figure 4.85.

There was some slippage between the angles and the steel plates, mainly in the angle in the northern corner, after that both angles had that relative displacement. As explained above, the slippage had two origins; the 1 mm tolerance of the bolt holes and the bending of the bolts in the 1 mm plate holes. There was a maximum estimated of 2 mm slippage if all the elements were perfectly built and aligned. Figure 4.86 shows the displacement of

the angles as a function of drift ratio and, as for the specimen RM4. The slippage is also evident in this diagram.

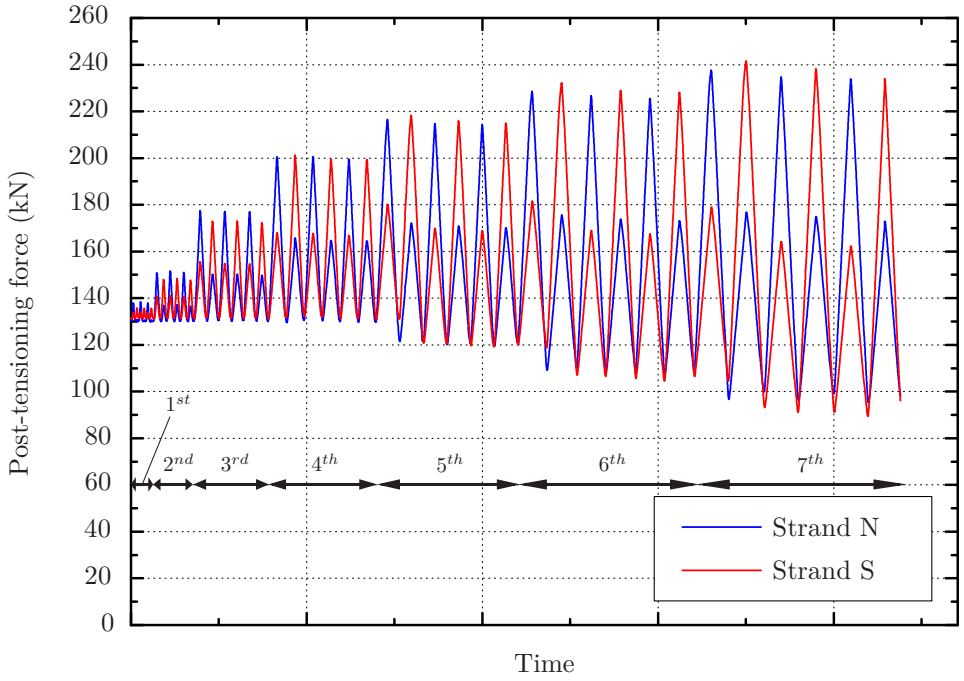

Figure 4.82: Test RM5 post-tensioning force vs time.

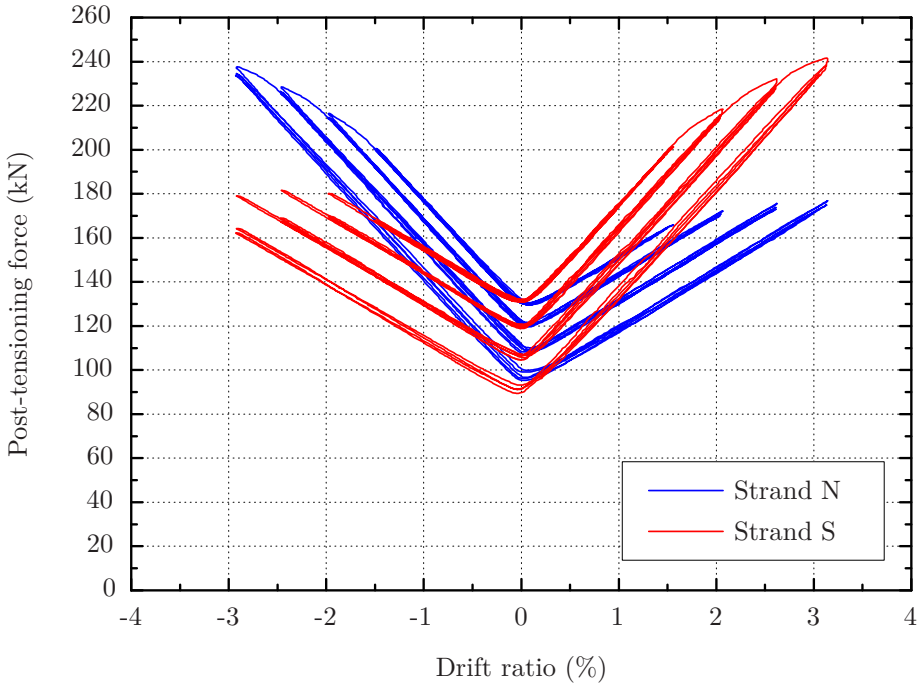

Figure 4.83: Test RM5 post-tensioning force vs drift ratio.

Figure 4.84: Picture of the angle deformation in specimen RM5.

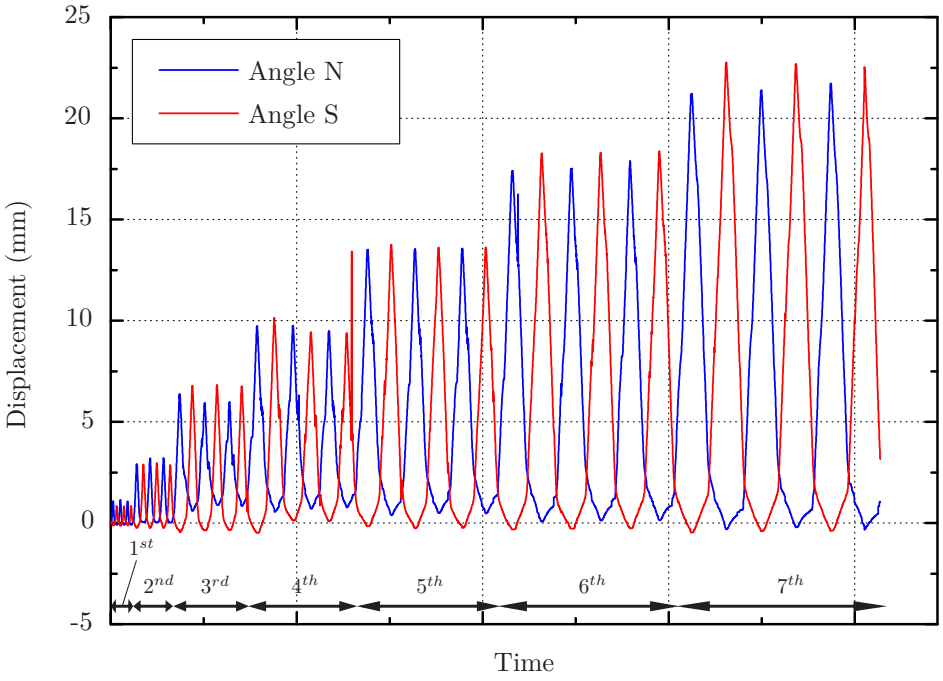

Figure 4.85: Test RM5 angles displacement vs time.

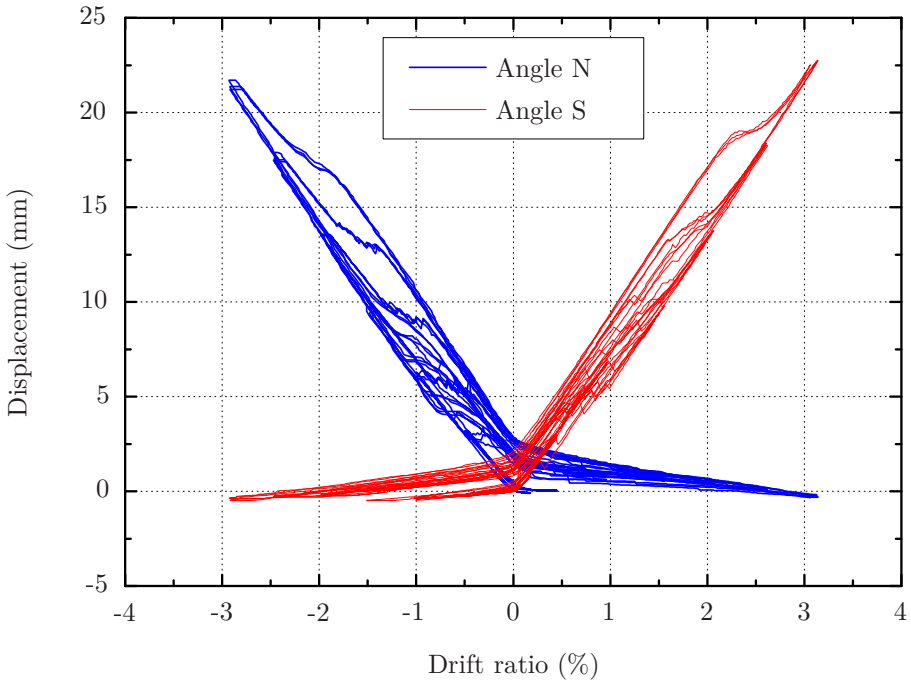

Figure 4.86: Test RM5 angles displacement vs drift.

The plates that made the connection between the angles and the concrete were welded properly to the bars embedded into the concrete and no visible slippage of the plate was observed. No concrete spalling was visible above the plate and the plate-concrete connections worked as desired.

During the last set of cycles the angles in the southern corner reached rupture, as can be seen in Figure 4.87. The rupture was in the fillet of the angle, similar to the cracks observed in the angles tested in Chapter 3, as shown in Figure 3.33. In the same angle a crack was forming along the first line of bolts. Figure 4.85 shows that the maximum displacement in the in the southern angle was about 22.5 mm, which is smaller than the displacements reached in the tests on the angles, where serious cracks where forming at 30 mm displacement. This difference could be due to the loading protocol or/and the displacement direction. The loading protocol applied to the angles had only one cycle per target rather than the three cycles used in the wall specimens. The displacement direction with which the angles were tested applied a perfect vertical displacement although in the wall specimen besides the vertical displacement there was also a rotation that induced the angle to "open" and "close" slightly.

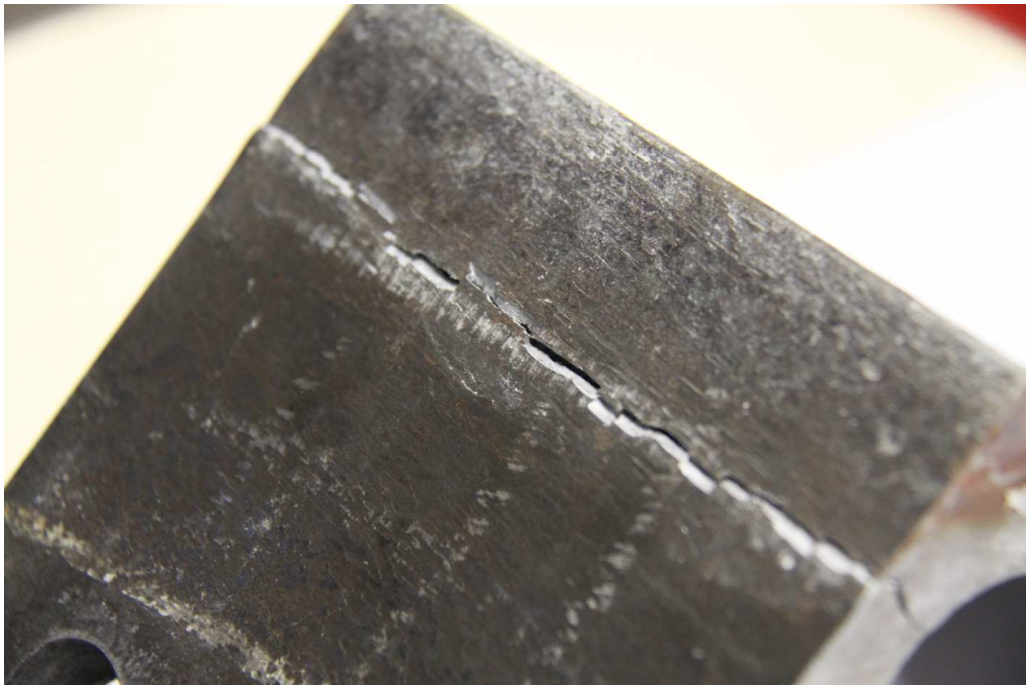

Figure 4.87: Specimen RM5 picture of the southern angle rupture.

The global response can be observed in the hysteretic diagram, shown in Figure 4.89 and in Figure 4.88 for each set of cycles separately. The response was stable until 2% drift ratio, presenting residual displacements of 0.26% (Table 4.28) after the 2% drift ratio set of cycles. In the set of cycles of 3.0% drift ratio the response started to fail due to the loss of post-tensioning forces and the cracks opening in the steel angles, as shown in Figure 4.87. The hysteretic diagram also shows the slippage between the angles and the vertical steel plate, that are visible as instantaneous losses in the base shear. Figure 4.90 shows the equivalent viscous damping ratio as a function of drift ratio. In this case, for design drift ratios between 1.5% and 2% a value around 13.5% equivalent viscous damping ratio can be obtained. The behaviour of the steel angles was the desired (Figure 4.84) until the last cycles, when the rupture was achieved. Figure 4.91 shows a picture taken during disassembly, showing that the wall had no visible damage.

The wall rotation about the vertical axis is shown in Figure 4.92 as a function of time. The rotations were negligible and the bracing system and the angles were essential to eliminate the undesired rotations and displacements that were present in other specimens.

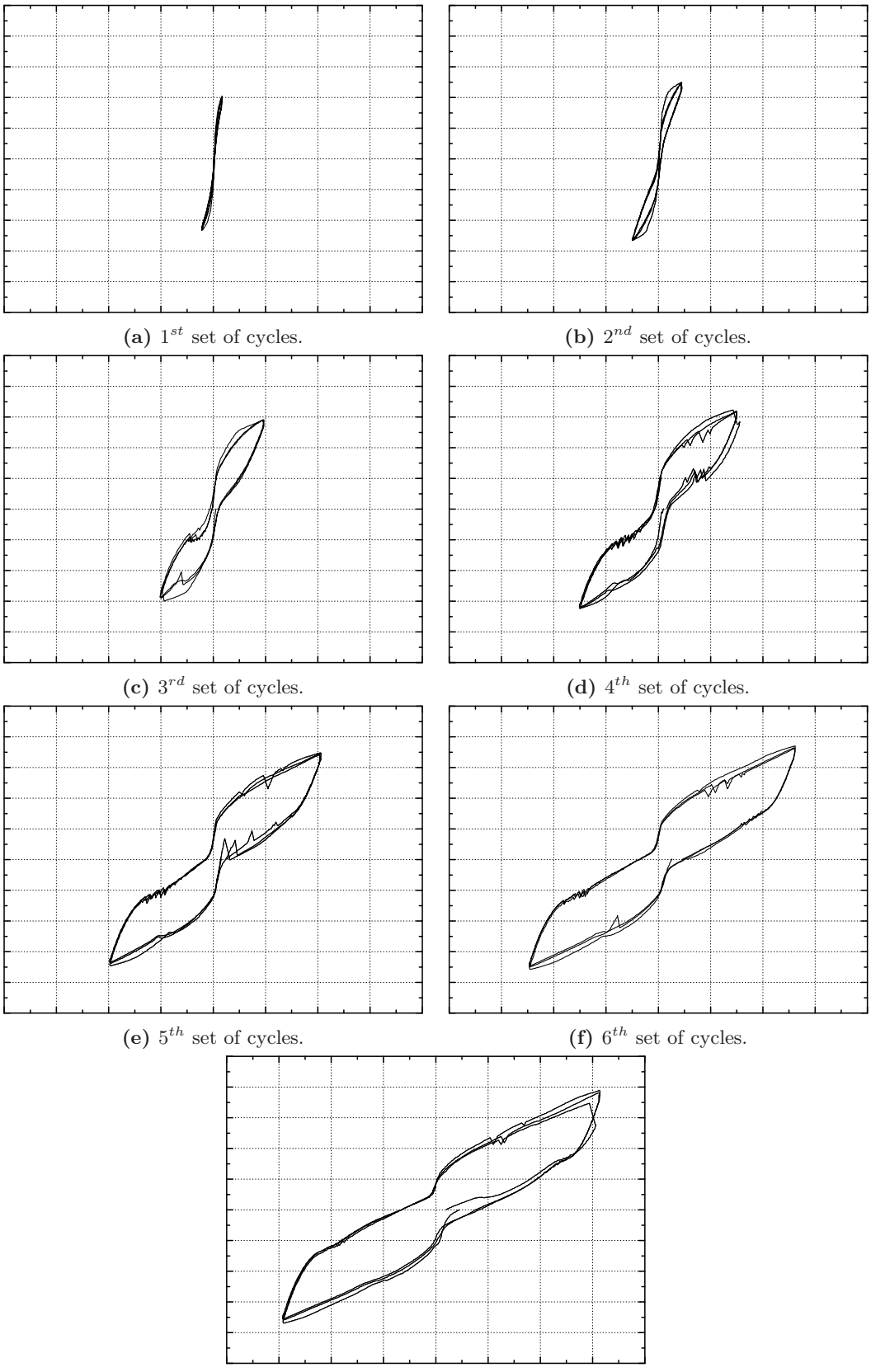

(a) 1^{st} set of cycles.

(b) 2^{nd} set of cycles.

(c) 3^{rd} set of cycles.

(d) 4^{th} set of cycles.

(e) 5^{th} set of cycles.

(f) 6^{th} set of cycles.

(g) 7^{th} set of cycles.

Figure 4.88: Test RM5 base shear vs drift ratio for each set of cycles.

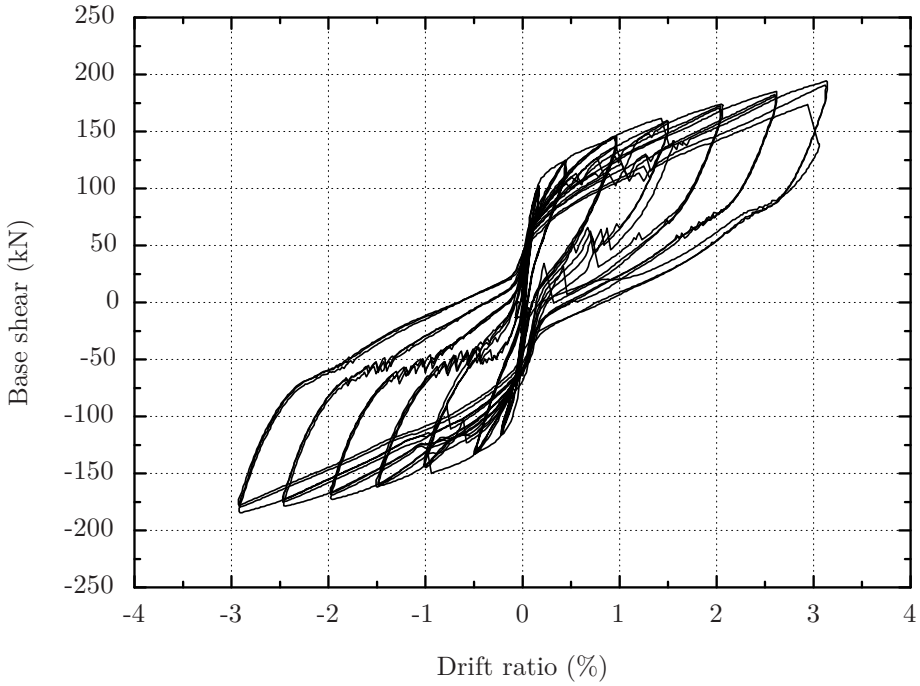

Figure 4.89: Test RM5 base shear vs drift ratio.

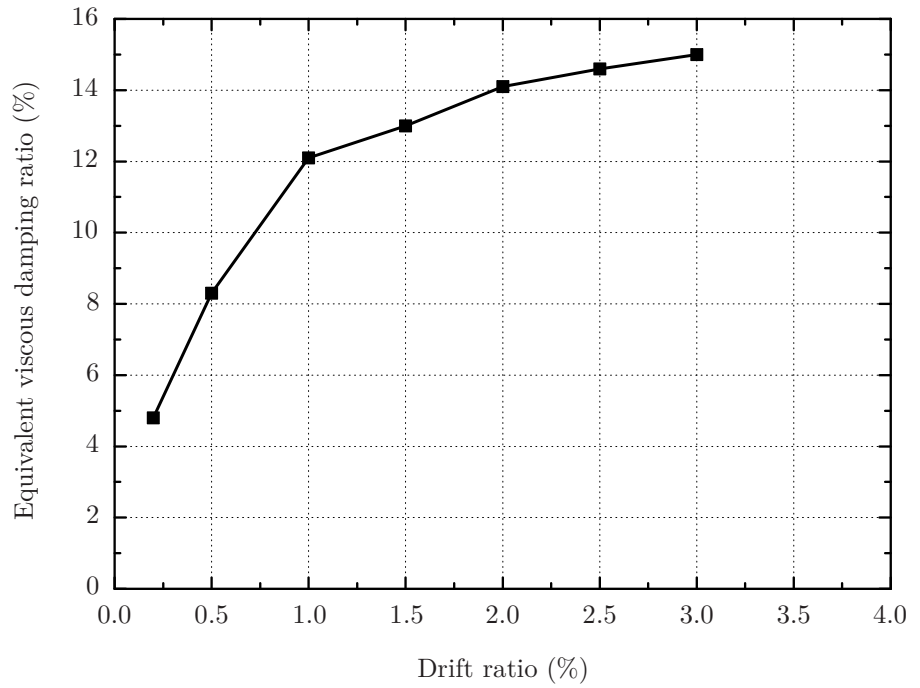

Figure 4.90: Test RM5 equivalent viscous damping ratio.

Figure 4.91: Picture of the specimen RM5 western side after test.

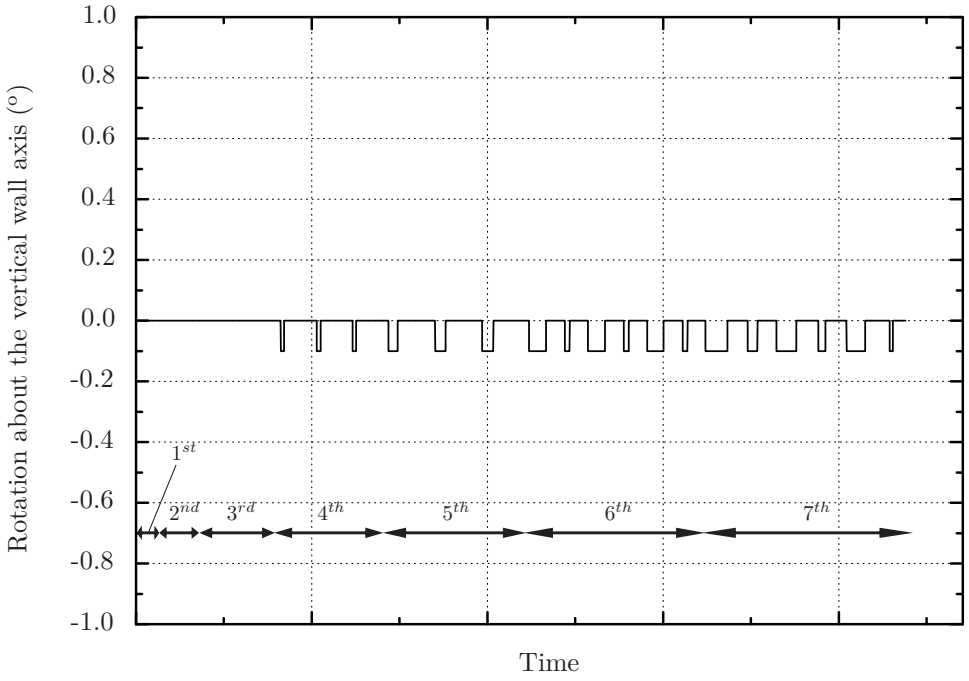

Figure 4.92: Test RM5: rotation about the vertical wall axis.

4.6.4 Test on a post-tensioned rocking wall

The wall specimen RM6 was a post-tensioned rocking wall. The reinforced concrete wall tested was the same as for specimen RM5, and the objective was to evaluate the wall specimen without energy dissipaters. The southern corner of the wall specimen is shown in Figure 4.93, where the vertical steel plate is visible, which can change the wall response in relation to the typical reinforced concrete wall, as in specimens RM1 and RM2. The test setup included the same bracing system as in specimen RM5 with the previously referred to advantages. In this test, the drift ratio target reached 3.0%. The test was ended because very high post-tensioning forces were reached making it unsafe to go further. As referred to in the previous specimen, the design drift for the tested specimens was 2.0%, which means that the objective was a perfect response until 2.0% drift ratio and a stable and predictable behaviour beyond that point.

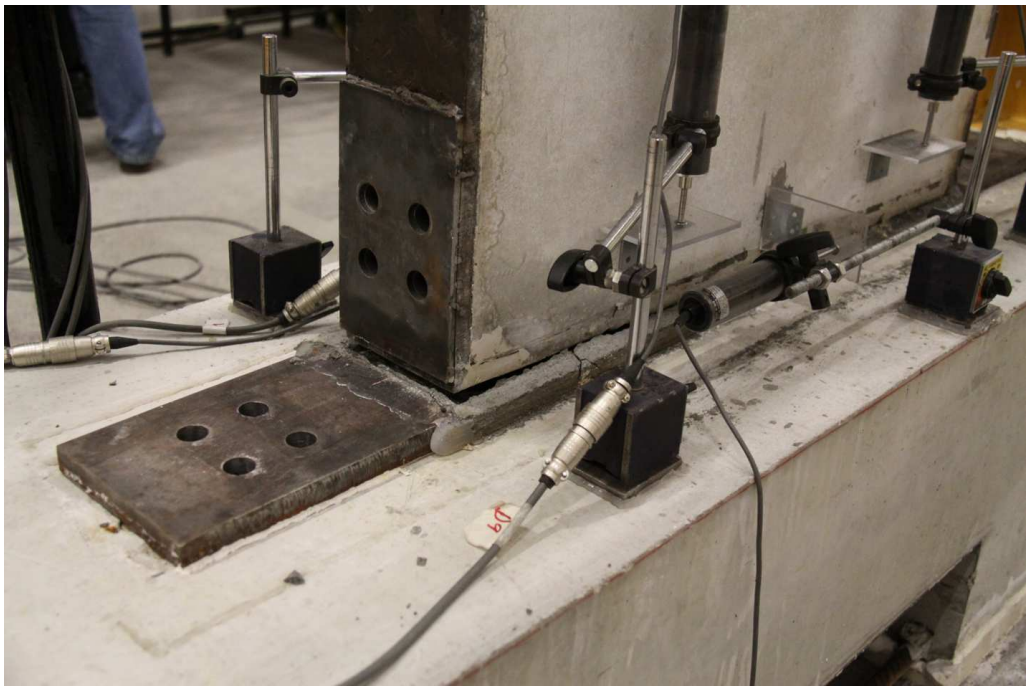

Figure 4.93: Picture of the specimen RM6 southern corner.

The drift ratio as a function of time is plotted in Figure 4.94 and the extreme values are presented in Table 4.30. As was previously referred to, the maximum target drift ratio was 3.0%, being the actual drift ratios different from the desired ones and showed in Figure 4.27. Most of the actual drift ratios were higher than the target ones (see Figure 4.27). The reason for these differences was, as already mentioned in other specimens, the difference from the control displacement transducer to the actual wall displacement.

The base shear in specimen RM6 as a function of time is shown in Figure 4.95. There is initially a more rapid increase of the base shear force that has been already referred to

and the origin is the lifting of the wall. The maximum values for each set of cycles are shown in Table 4.30.

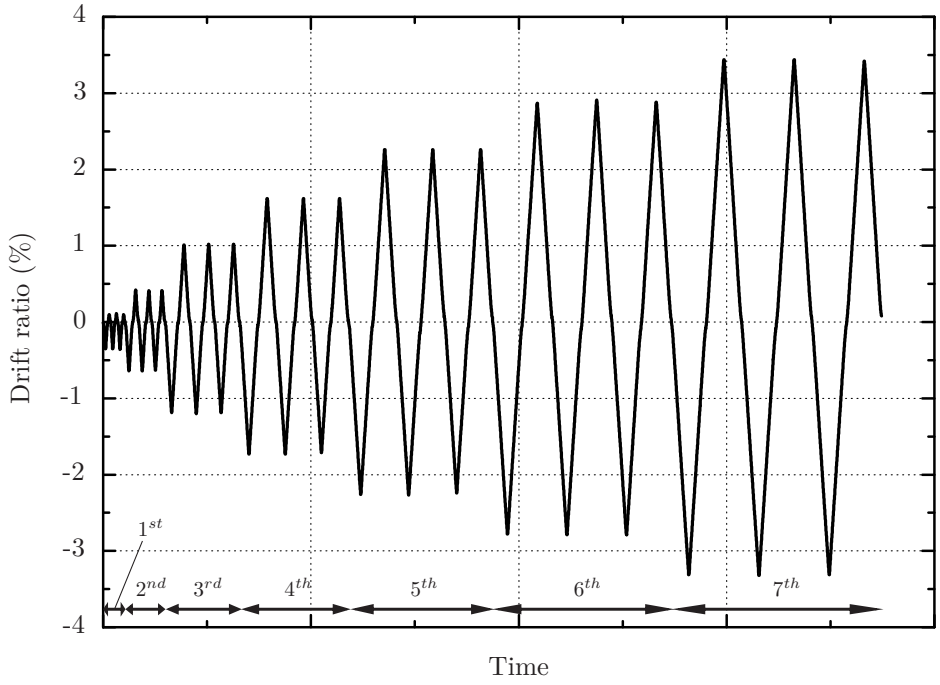

Figure 4.94: Test RM6 history of drift ratio.

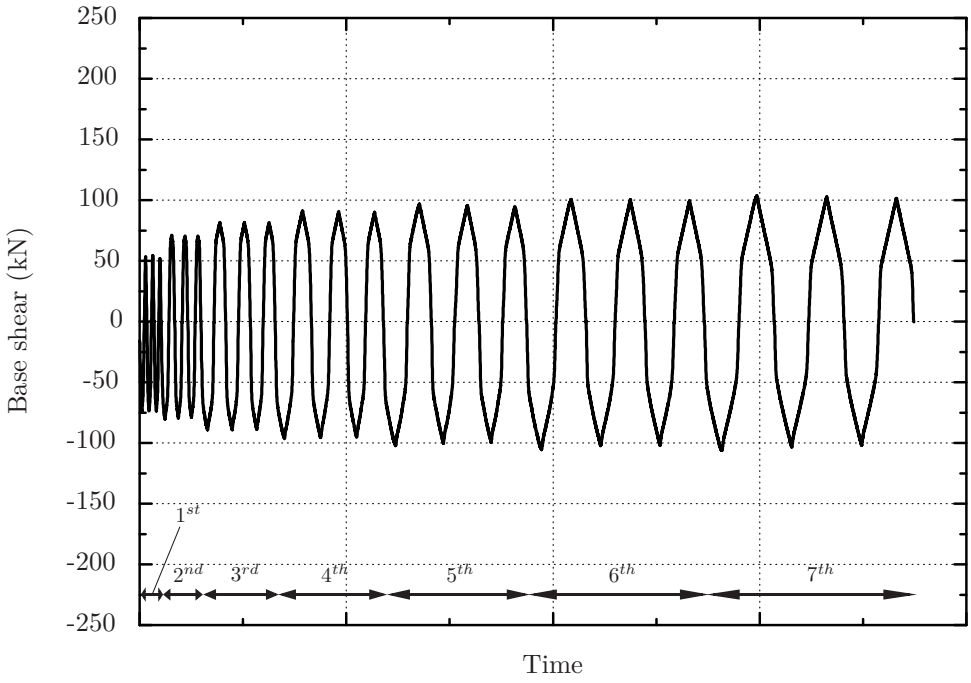

Figure 4.95: Test RM6 history of base shear force.

Table 4.30: RM6 summary of results for base shear and drift ratio, for each set of cycles.

	Base shear force (kN)		Drift ratio (%)		
	Max	**Min**	**Max**	**Min**	**Residual**
1^{st} Cycles	54.4	-74.5	0.11	-0.36	0.01
2^{nd} Cycles	71.2	-80.3	0.42	-0.64	0.01
3^{rd} Cycles	81.6	-89.2	1.02	-1.20	0.01
4^{th} Cycles	91.2	-96.5	1.62	-1.73	0.02
5^{th} Cycles	96.9	-102.2	2.26	-2.27	0.07
6^{th} Cycles	100.6	-105.6	2.91	-2.79	0.05
7^{th} Cycles	103.8	-106.2	3.44	-3.32	0.08

The post-tensioning, in the case of this specimen, was the only connection of the wall to the base and the only source of strength. The application of the post-tensioning force was made in a procedure similar to the one in the previous specimens. Due to some problems in the mechanical post-tensioning force application system, the maximum pre-loading applied was only 190 kN in each strand, which was reduced to 130 kN at the beginning of the test.

The response of the post-tensioning was very similar to specimen RM5. Figures 4.96 and 4.97 show the evolution of the post-tensioning forces during the cyclic test. For the set of cycles with the target drift of 2.0% the maximum force, from Table 4.31, was 217.7 kN, near the theoretical limit $F_{p0.1k}$ =224 kN. For the last two sets of cycles the force reached values higher than $F_{p0.1k}$. The losses in the post-tensioning forces started when the 190 kN force was reached in each strand, for the same reasons as explained for the other experimental wall tests. The losses achieved 35% and the maximum force was 239.7 kN, far beyond $F_{p0.1k}$, but also far away from rupture.

Table 4.31: RM6 test summary of post-tensioning force for each set of cycles.

	Final post-tensioning force				Maximum post-tensioning force			
	Strand N		Strand S		Strand N		Strand S	
	F_N (kN)	**Δ**	**F_S (kN)**	**Δ**	**F_N (kN)**	**Δ**	**F_S (kN)**	**Δ**
Initial	133.5		131.2					
1^{st} Cycles	133.4	0%	131.3	0%	145.6	9%	136.6	4%
2^{nd} Cycles	133.3	0%	131.3	0%	158.5	19%	147.0	12%
3^{rd} Cycles	133.3	0%	131.3	0%	184.1	38%	174.3	33%
4^{th} Cycles	126.7	-5%	128.7	-2%	203.5	52%	200.0	52%
5^{th} Cycles	116.9	-12%	118.4	-10%	217.7	63%	217.0	65%
6^{th} Cycles	102.5	-23%	103.7	-21%	229.9	72%	230.2	75%
7^{th} Cycles	86.6	-35%	87.7	-33%	238.6	79%	239.7	83%

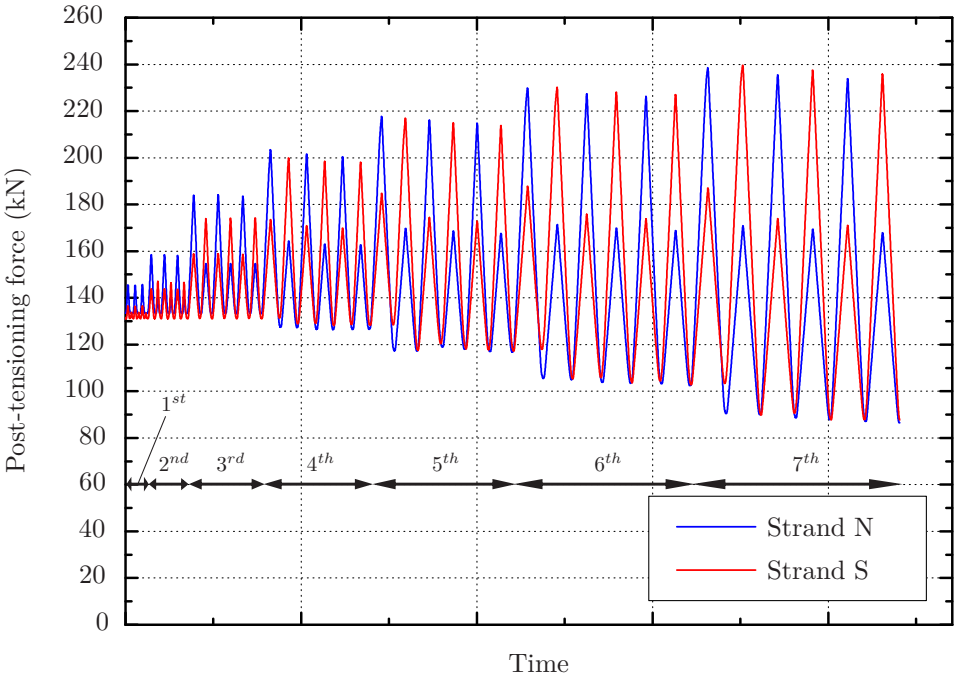

Figure 4.96: Test RM6 post-tensioning force vs time.

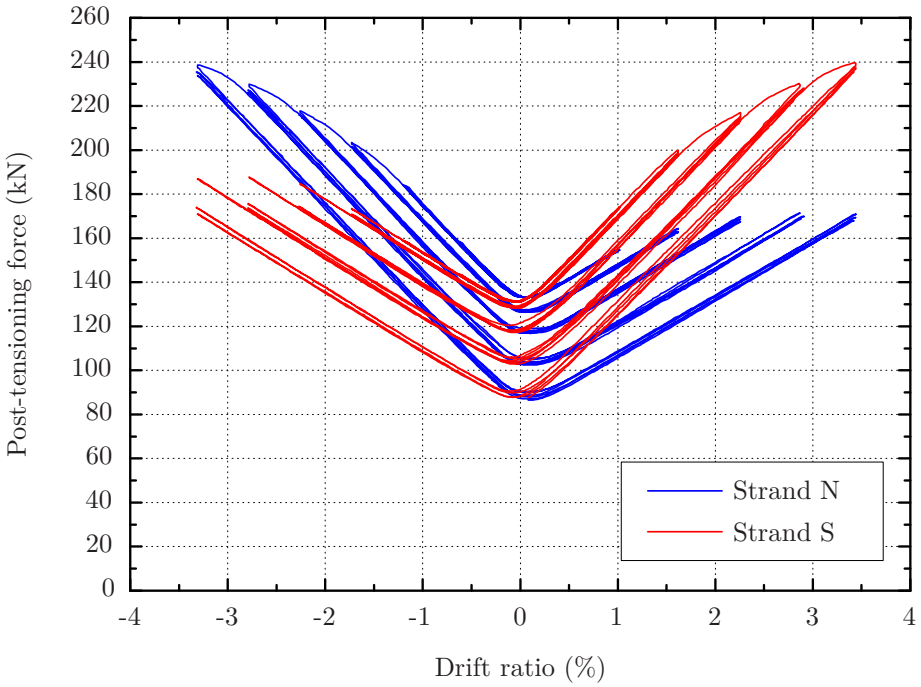

Figure 4.97: Test RM6 post-tensioning force vs drift.

The global response can be observed in the hysteretic diagram, shown in Figure 4.98 and in Figure 4.99 for each set of cycles separately. This figure shows the bi-linear response with the softening zone for drift ratios smaller than 0.5% and an elastic response that always resulted in a very small residual drift ratio, as shown in Table 4.30. In the response diagram the sets of cycles should be overlapping, but the losses in the post-tensioning forces made the cycles slightly different. The response was essentially elastic and consequently, the equivalent viscous damping ratio was small, near 2.0% for drift ratios higher than 0.5%, as shown in Figure 4.100. Figure 4.102 shows a picture taken during disassembly, showing almost no damage to the wall with only small cover spalling zones.

The wall rotation about the vertical axis is shown in Figure 4.101. This specimen with no energy dissipaters had small rotations that increased throughout the test. After the third set of cycles, a negative residual rotation was increasing and accumulating. This rotation was minimal and had little influence on the test results.

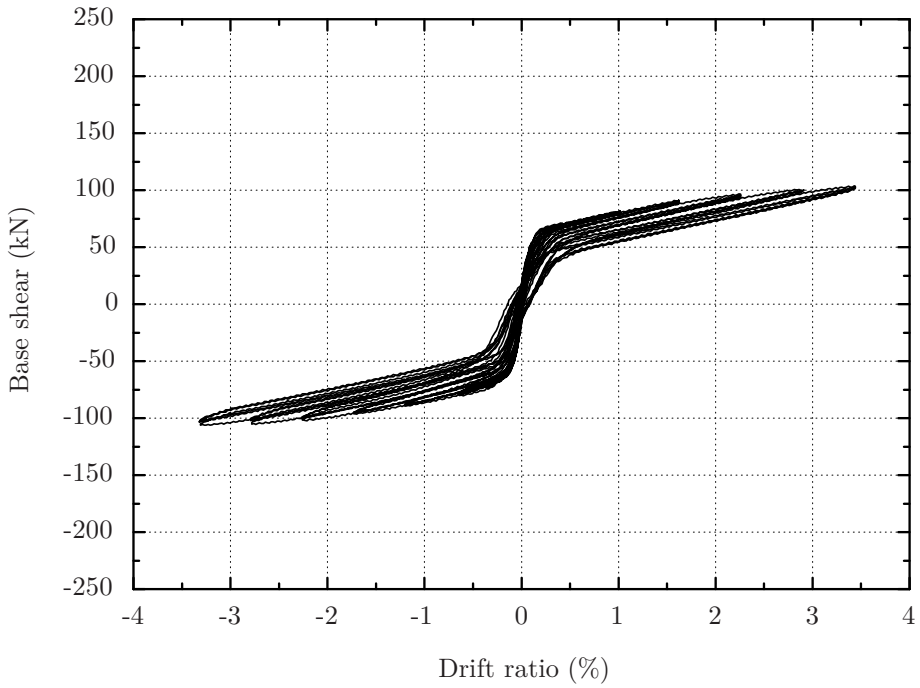

Figure 4.98: Test RM6 base shear vs drift ratio.

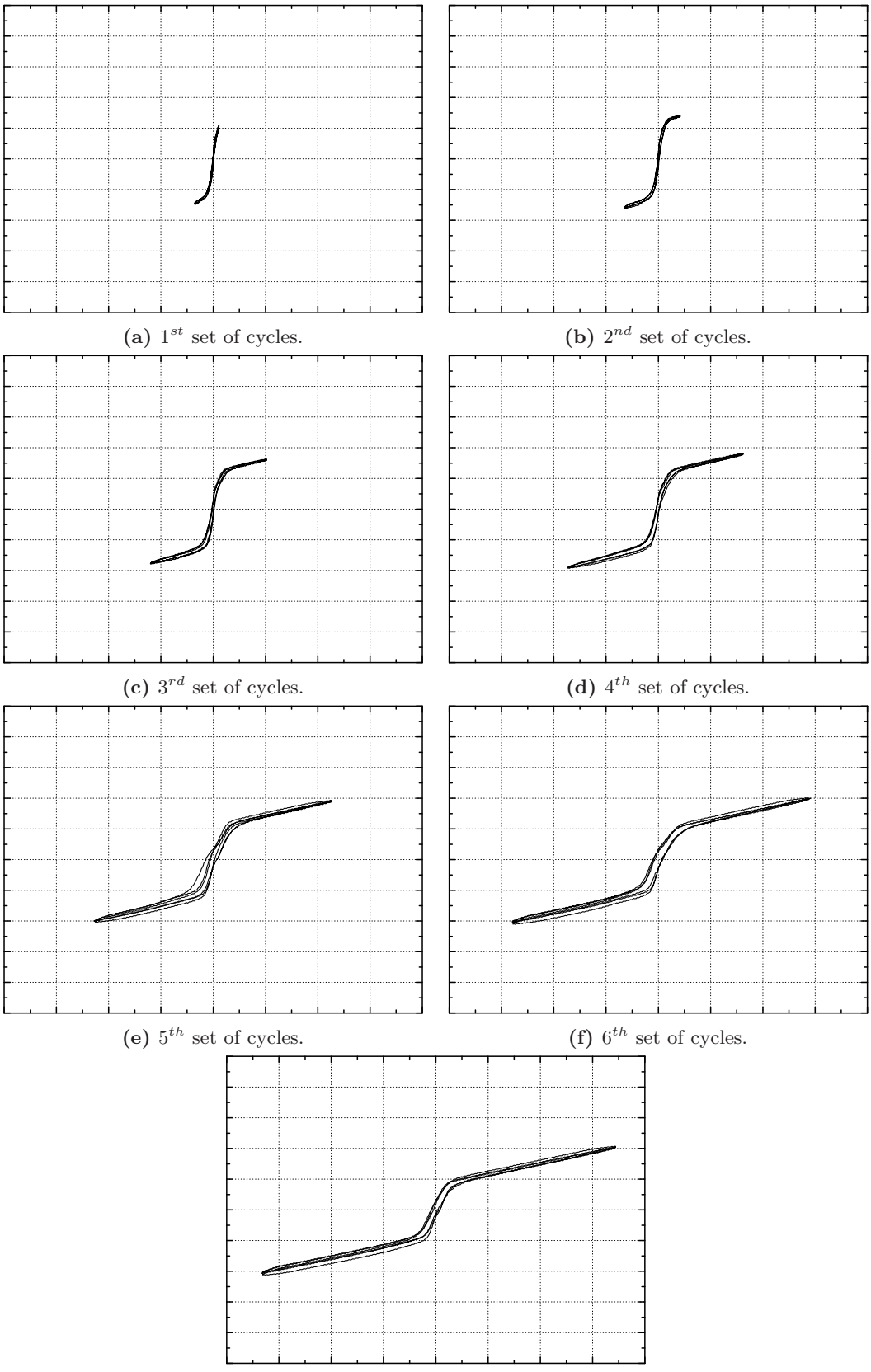

(a) 1^{st} set of cycles.

(b) 2^{nd} set of cycles.

(c) 3^{rd} set of cycles.

(d) 4^{th} set of cycles.

(e) 5^{th} set of cycles.

(f) 6^{th} set of cycles.

(g) 7^{th} set of cycles.

Figure 4.99: Test RM6 base shear vs drift ratio for each set of cycles.

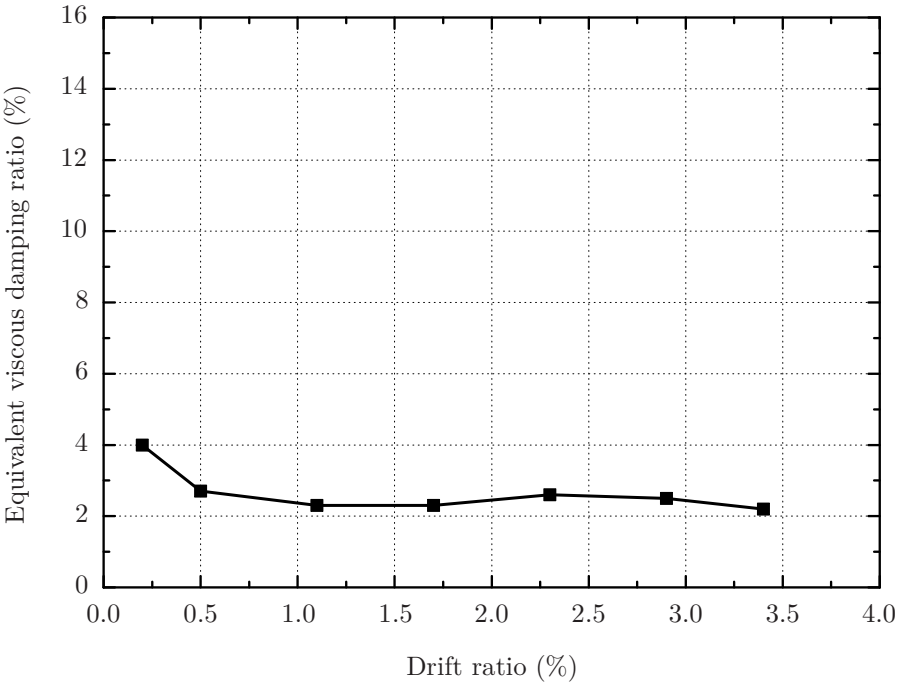

Figure 4.100: Test RM6 equivalent viscous damping ratio.

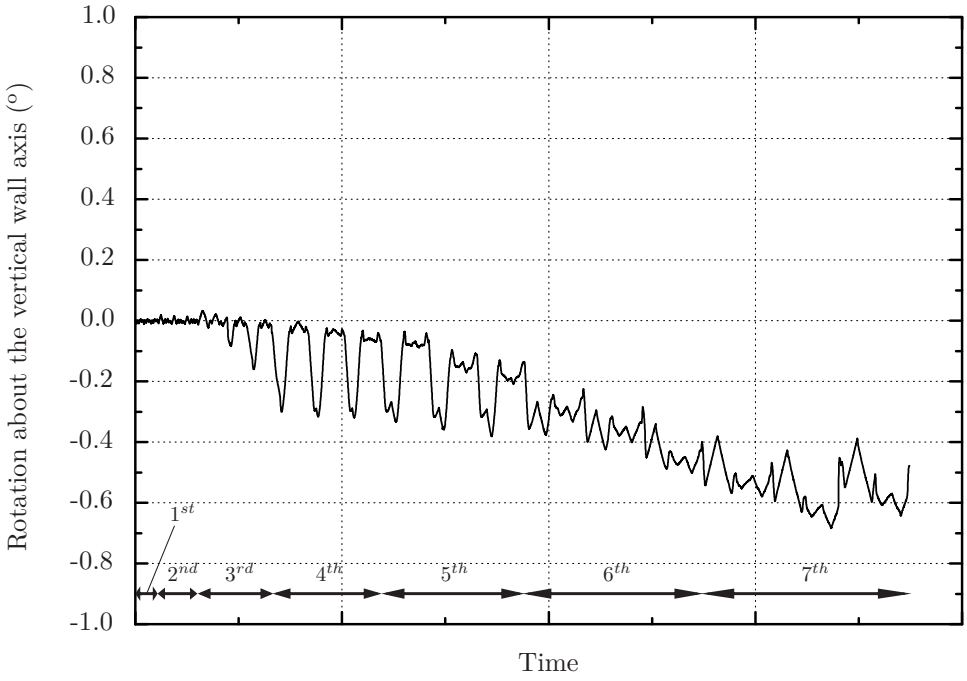

Figure 4.101: Test RM6: rotation about the vertical wall axis.

Figure 4.102: Picture of the specimen RM6 eastern side after test.

4.7 Numerical models for tested wall specimens

4.7.1 Compatibility condition for wall-base joint

In reinforced concrete rocking wall systems the rocking movements cause a gap to open between the wall and the base. As one side of the wall lifts, the compressive forces are concentrated in the side of the wall remaining in contact with the base. This results in a curvature in the compression zone and a plane surface in the zone where the gap opens, creating a compatibility problem. When an approximate method is used, like a rectangular stress block or a parabola-rectangle stress distribution, without a check on the maximum compressive strain this problem can be bypassed. When the concrete compressive strain is needed, this problem has to be solved.

To overcome this problem, Pampanin et al. (2001) developed a procedure named Monolithic Beam Analogy (MBA) where a theoretical curvature is defined by comparing the system to an equivalent monolithic solution (Figure 4.103). Based on the work of Pampanin et al. (2001), Palermo (2004) presented a solution distinguishing the following three cases:

Case 1. $0 \leq \Delta \leq \Delta_{dec}$

The first case corresponds to the situation before the decompression point is reached. Within this range all the section is compressed and the displacement of the real element

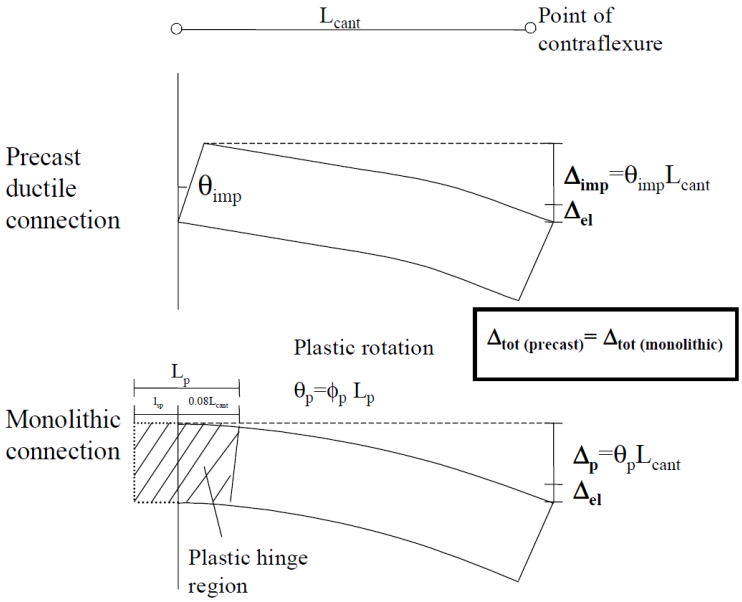

Figure 4.103: Monolithic beam analogy for reinforced concrete elements (extracted from Pampanin et al. (2001)).

and the monolithic equivalent is given by the equation 4.8. Within this range, there was no need to use a special procedure, since the curvature of the section can be calculated by $\phi = M/(EI)$, being M the section bending moment and EI the bending stiffness of the gross area.

$$\Delta = \Delta_{mon} = \phi \frac{L_{cant}^2}{3} \tag{4.8}$$

where,

Δ is the displacement of the real element;
Δ_{mon} is the displacement of the equivalent monolithic element;
ϕ is the theoretical curvature;
l_{cant} is the length until the point of contraflexure (cantilever length).

Case 2. $\Delta_{dec} \leq \Delta \leq \Delta_y$

After the decompression point, the wall lifts and a gap opens. The theoretical curvature of the equivalent monolithic element is given by the equation 4.9. For this case, the rotation limits are presented in the inequations 4.10.When the equivalent monolithic element can reach a yielding point, that point corresponds to the limit range for this second case. These formulas do not take into consideration the wall deformation after the decompression, and the displacement results from the elastic displacement at the decompression point plus the

displacement due to the bottom rotation.

$$\phi = 3\frac{\theta}{l_{cant}} + \phi_{dec} \tag{4.9}$$

$$0 \leq \theta \leq (\phi_y - \phi_{dec})\frac{l_{cant}}{3} \tag{4.10}$$

where,

θ is the rotation of the bottom of the real element;
ϕ_{dec} is the curvature at the decompression point;
ϕ_y is the curvature at the yield point.

Case 3. $\Delta_y \leq \Delta \leq \Delta_u$

The third case is after the development of a plastic hinge in the monolithic element. The theoretical curvature of the equivalent monolithic element is given by the equation 4.11. The range in rotation of this case is presented in inequations 4.12 and it lies between the moment of the plastic hinge formation till the maximum rotation capacity of the plastic hinge.

$$\phi = \frac{3\frac{\theta}{l_{cant}} - (\phi_y - \phi_{dec})}{\frac{3l_p}{l_{cant}}\left(1 - \frac{l_p}{2l_{cant}}\right)} + \phi_y \tag{4.11}$$

$$(\phi_y - \phi_{dec})\frac{l_{cant}}{3} \leq \theta \leq (\phi_u - \phi_y)l_p\left(1 - \frac{l_p}{2l_{cant}}\right) + (\phi_y - \phi_{dec})\frac{l_{cant}}{3} \tag{4.12}$$

where,

ϕ_u is the ultimate curvature;
l_p is the length of the plastic hinge in the equivalent monolithic element.

4.7.2 Numerical procedure for shear base-drift ratio analysis

To calculate the base shear as a function of the drift ratio, the prime task was the quantification of the moment-rotation in the bottom section. The rotation was estimated from zero to the point where the strands reached the characteristic 0.1% proof stress of $f_{p0.1k}$=1600 MPa. The rotation is zero until the decompression point is reached. With the bottom rotation, the drift ratio was obtained by calculating the top displacement and dividing it by the height of the wall. The shear base was obtained by dividing the bending moment in the bottom section by the height of the wall.

- *Moment-rotation*

Adapting the procedure from Pampanin et al. (2001), seven steps may be considered to obtain the bending moment for a given rotation:

1. Fix the rotation, θ;
2. Consider an initial neutral axis depth;
3. Evaluate the displacements at post-tensioned strands and steel angle positions;
4. Estimate the compression strains in the concrete, end plates and steel angles;
5. Equilibrate the forces in the bottom section and obtain a new value of neutral axis depth;
6. Consider the new neutral axis depth and go to step 3 until converge;
7. Evaluate bending moment capacity.

To complement the listed steps, Figure 4.104 shows a deformed wall with the forces in the bottom section of the wall. The shown vertical forces are the post-tensioning forces F_{pns} and F_{pss}, the tension force acting in the northern steel angle F_{ta} (considered to be concentrated in the first line of bolts), the compressive force in the concrete F_{cc}, the compressive force in the plate on the edge of the wall F_{cp} and compressive force in the compressed steel angle F_{ca} (considered to be acting in the centre of the vertical leg). The post-tensioning forces were considered to be always acting vertically. The compressive stresses in the concrete were calculated using the EC2 stress-strain relation for nonlinear structural analysis in equation 4.13. The stress in the steel plate was calculated using the strain in its centre, being the stress limited by the grout strength located under the plate. The compressive stress in the compressed angle was calculated for the strain estimated in the centre of the vertical leg.

$$\frac{\sigma_c}{f_{cm}} = \frac{k\eta - \eta^2}{1 + (k-2)\eta} \tag{4.13}$$

where,

σ_c is the concrete stress;
ε_c is the concrete compressive strain;
$\eta = \varepsilon_c/\varepsilon_{c1}$;
$k = 1.05E_{cm} \times |\varepsilon_{c1}|/f_{cm}$.

Table 4.32 summarises the general information needed for the numerical model. The concrete is a C30/37 and the mean values for the modulus of elasticity E_{cm} and compressive strength f_{cm} as well as the strains corresponding to the compressive strength ε_{c1} and to the ultimate compressive strain ε_{cu1} are shown. In wall information, the cross section dimensions, the height of the horizontal H load and the concrete cover cc are shown. The post-tensioned was composed by two strands, being their unbonded length l_{ub} measured

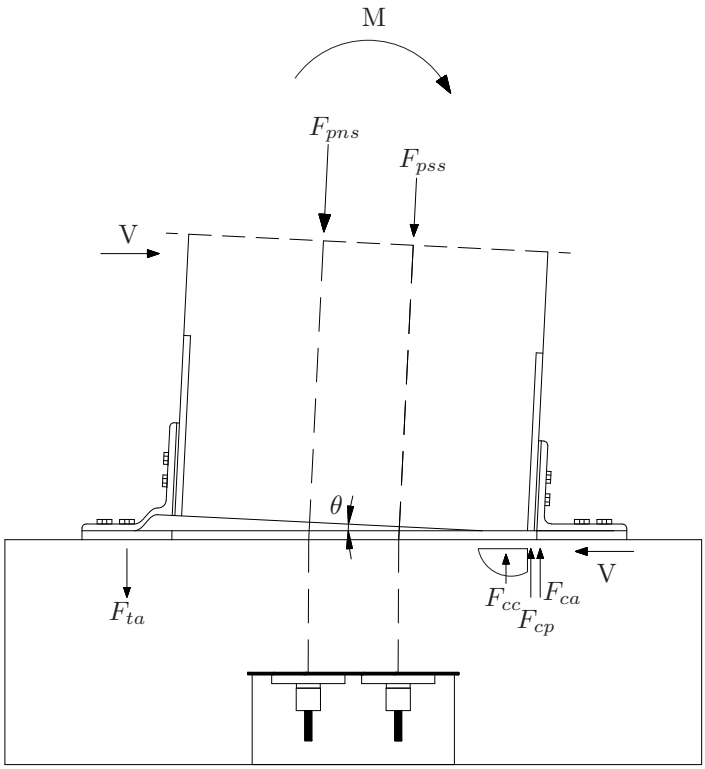

Figure 4.104: Forces in the base section of a deformed wall.

from the bottom anchorages to the top anchorages. The initial post-tensioning force was considered to be equal in all cases and the initial stress used was $f_{p0} = 930\ MPa$, that corresponds to a post-tensioning force of 130 kN.

Table 4.32: Values used in the numerical model for concrete, geometric and post-tensioning steel.

Concrete		**Wall geometry**		**Post-tensioning**	
E_{cm} **(GPa)**	33	l_w **(m)**	0.8	f_{pk} **(MPa)**	1860
f_{cm} **(MPa)**	38	b_w **(m)**	0.125	$f_{p0.1k}$ **(MPa)**	1600
ε_{c1} **(‰)**	2.2	**H (m)**	1.58	E_p **(GPa)**	195
ε_{cu1} **(‰)**	3.5	**cc (m)**	0.01	l_{ub} **(m)**	2.36
				A_p**/strand (mm^2)**	140
				f_{p0} **(MPa)**	930

4.7.3 Post-tensioned wall

The post-tensioned wall analysed with this numerical model was specimen RM6. The forces involved in this analysis were the ones listed above and shown in Figure 4.104, excluding the forces acting in the steel angles. To solve the bottom section compatibility problem, as no yield could be reached, the *Case 3* was not used. The force acting on steel plate on the edge of the wall inside the compression area was limited to take into account

the grout below. This stresses transmitted from the plate to the grout were limited to the compressive strength of the grout, that was tested and resulted in a strength about 60 MPa, thus the maximum force allowed was $60 \times (15 \times 125)/1000 = 112.5$ kN.

Figure 4.105 shows the force-displacement diagram for specimen RM6, compared with the experimental test results. The simulation was stopped when the stress in the most tensioned strand reached $f_{p0.1k}$. From the figure it can be observed that a good agreement was achieved. At 2.0% drift ratio, the numerical simulation ended and the experimental test showed a tendency to deviate from the numerical due to losses in the post-tensioning force, as reported in Section 4.6.4. The post-tensioning forces are shown in Figure 4.106, where can be seen the experimental values and the numerical values. The losses in the post-tensioning forces can be seen by comparing the several values corresponding to a drift ratio of zero. The numerical values correspond to the ideal response and should be said that the experimental tests would have ended for lower drift ratios if there were no losses in the post-tensioning forces.

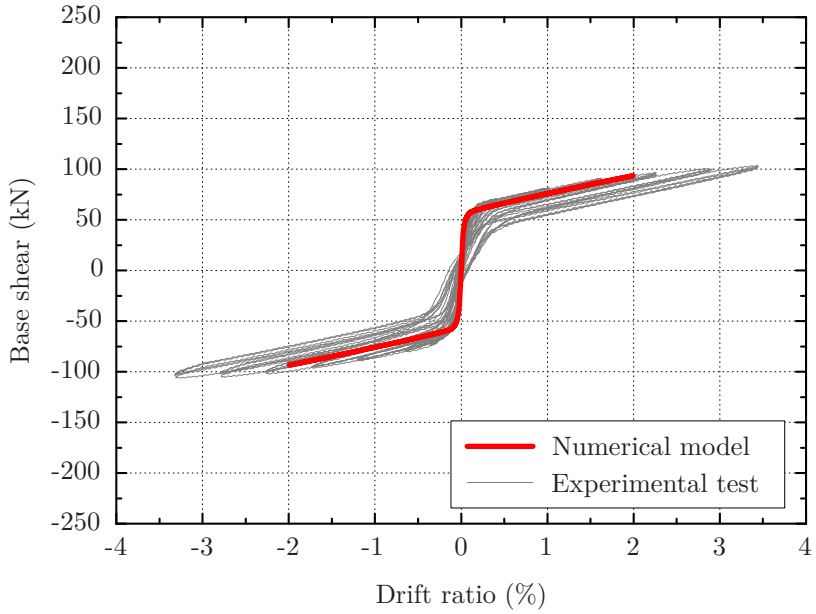

Figure 4.105: Numerical model of the specimen RM6.

4.7.4 Hybrid rocking wall

The hybrid solutions tested were specimens RM4 and RM5. The forces involved were shown and explained above. To solve the bottom section compatibility problem, the *Case 3* was not considered. This was an approximation that resulted in minor differences in the neutral axis position, thus the response is reliable. This simplification was made after some numerical parametric studies and as was difficult to estimate the yielding point and the response was little affected, the option was not to consider *Case 3*. As was explained

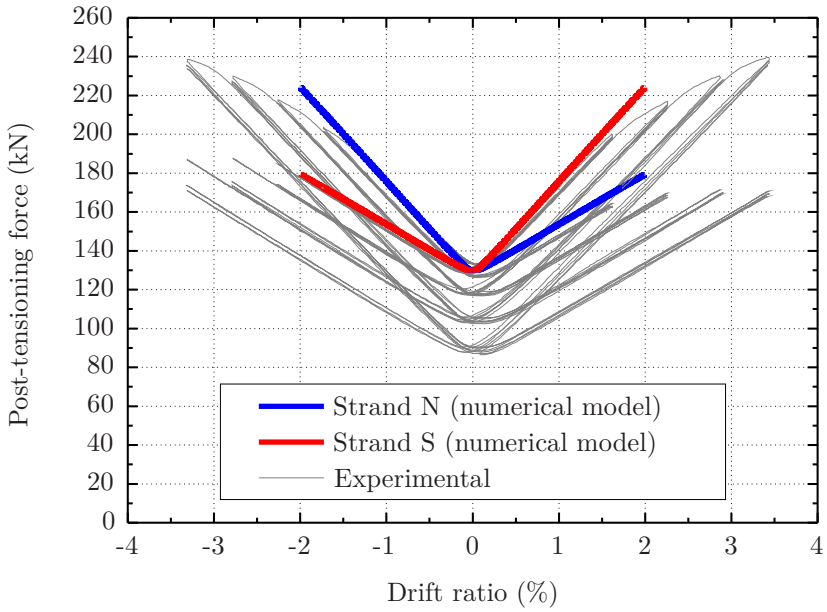

Figure 4.106: Numerical model of RM6 post-tensioning force vs drift.

above for the post-tensioned wall, the compressive stress between the steel plate and the grout was limited by the grout strength.

To obtain these numerical simulations the parameters used were the prescribed ones, not taking directly into consideration the experimental tests for the steel angles or for the walls. Taking this into account, simplified bi-linear idealisations for the steel angles response were used, calibrated from the analytical model presented in Section 3.4. These models are shown in Figures 4.107 and 4.108.

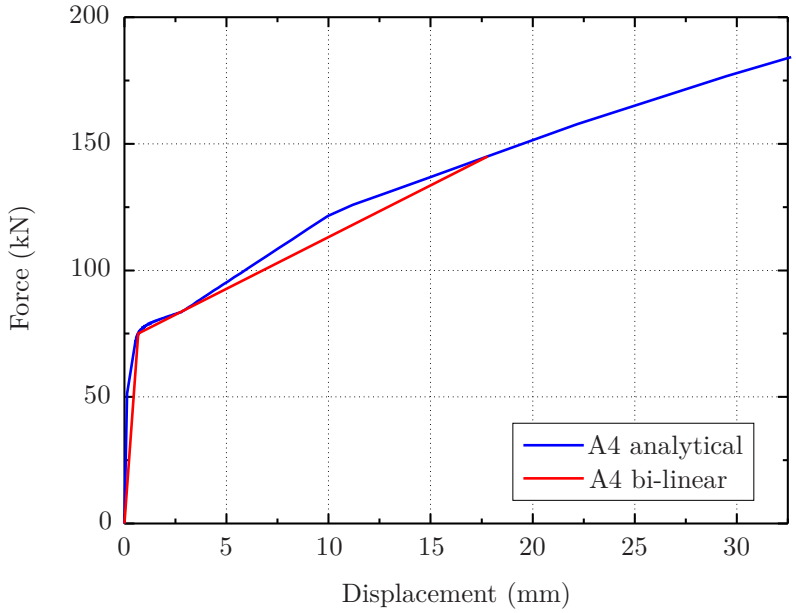

Figure 4.107: Bi-linear idealisation of the specimen A4 analytical response.

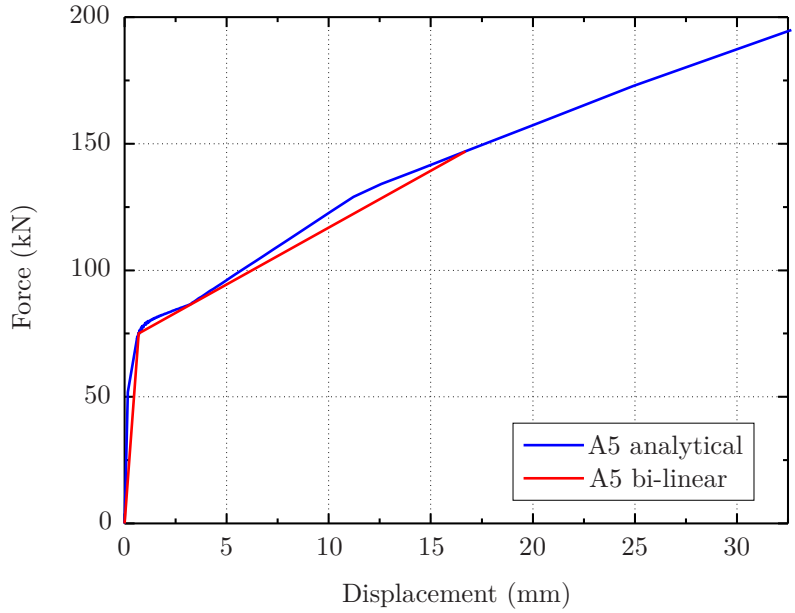

Figure 4.108: Bi-linear idealisation of the specimen A5 analytical response.

The parameter a needed for the analytical models, referred in Section 3.4, was considered equal to 2. These bi-linear idealisations can give an overall good approximation. When compared with the experimental tests, the analytical model presents an error in the displacement range between 1 mm and 8 mm that reaches about 10% as can be seen in Figures 3.56 and 3.57 for specimen A4 and A5, respectively.

The force-displacement diagrams for the numerical simulations of specimens RM4 and RM5 are shown in Figures 4.109 and 4.110, along with the experimental tests results.

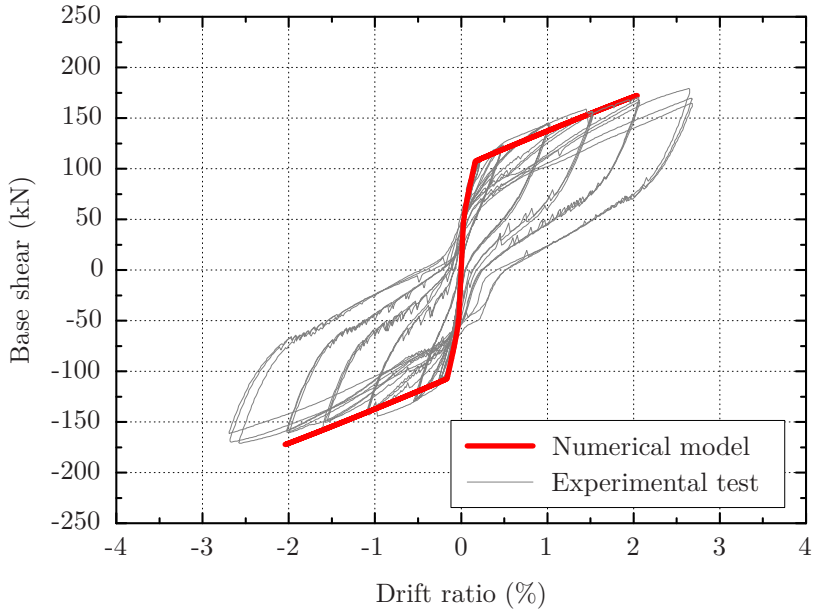

Figure 4.109: Numerical model of the specimen RM4 base shear vs drift.

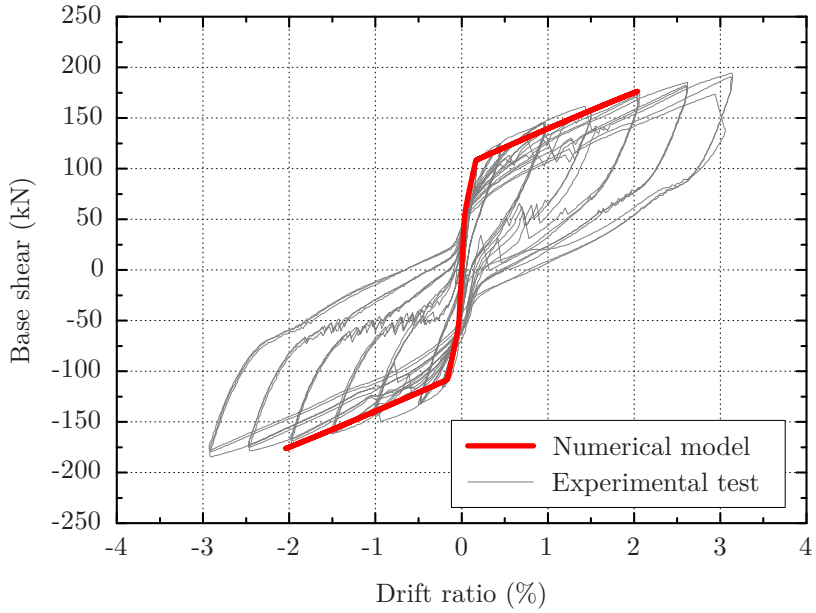

Figure 4.110: Numerical model of the specimen RM5 base shear vs drift.

As for specimen RM6, the simulation was stopped when the stress in the most tensioned strand reached $f_{p0.1k}$. The agreement between the numerical and the experimental results is good. The differences were attributed mainly to the bi-linear force-displacement idealisation considered for the steel angles. Another simplification that may lead to differences is the bending of the vertical leg in the compressed steel angle. This bending to accommodate the wall rotation could make a small increment to the horizontal force.

The post-tensioning forces are shown in Figures 4.111 and 4.112.

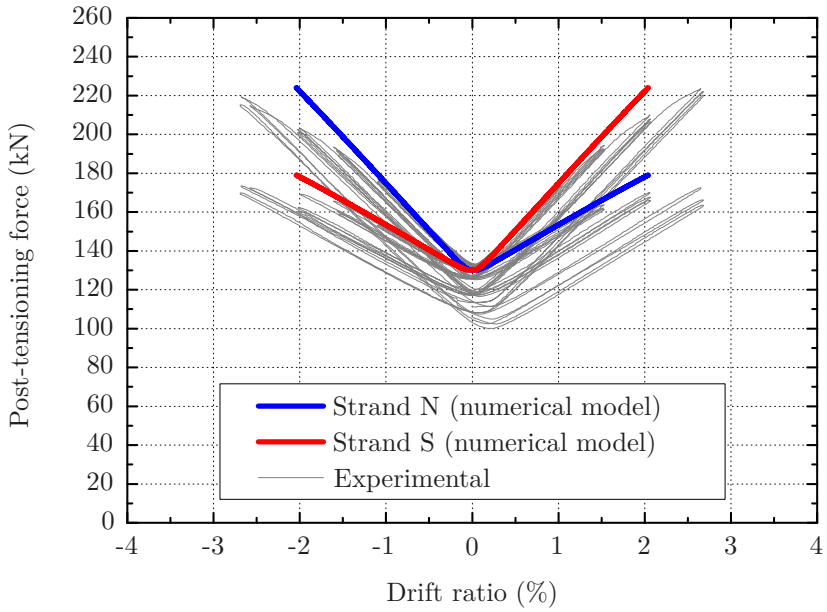

Figure 4.111: Numerical model of RM4 post-tensioning force vs drift.

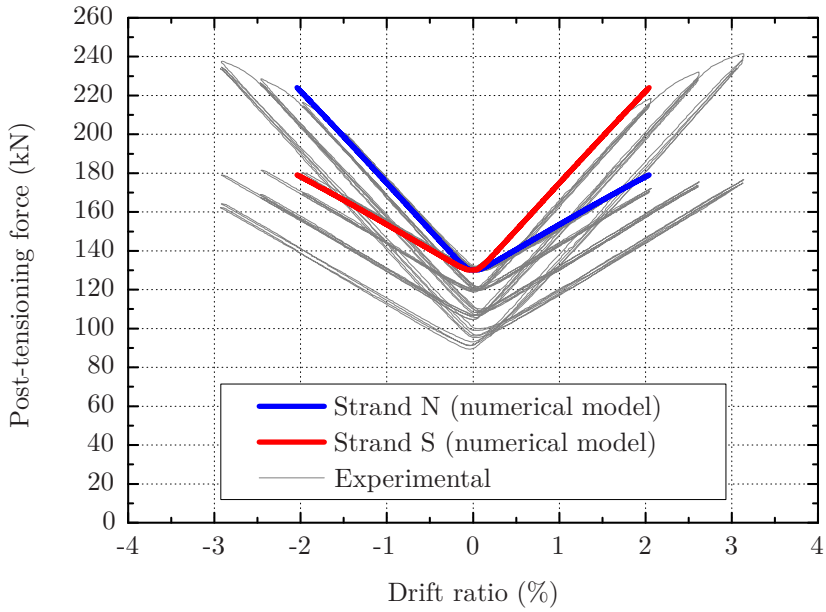

Figure 4.112: Numerical model of RM5 post-tensioning force vs drift.

The losses in the post-tensioning forces can be seen by comparing the several values corresponding to a drift ratio of zero. The numerical values correspond to the ideal response with no losses in the post-tensioning forces.

Figures 4.113 and 4.114 show the response of the steel angles in the numerical models and compared to the experimental tests.

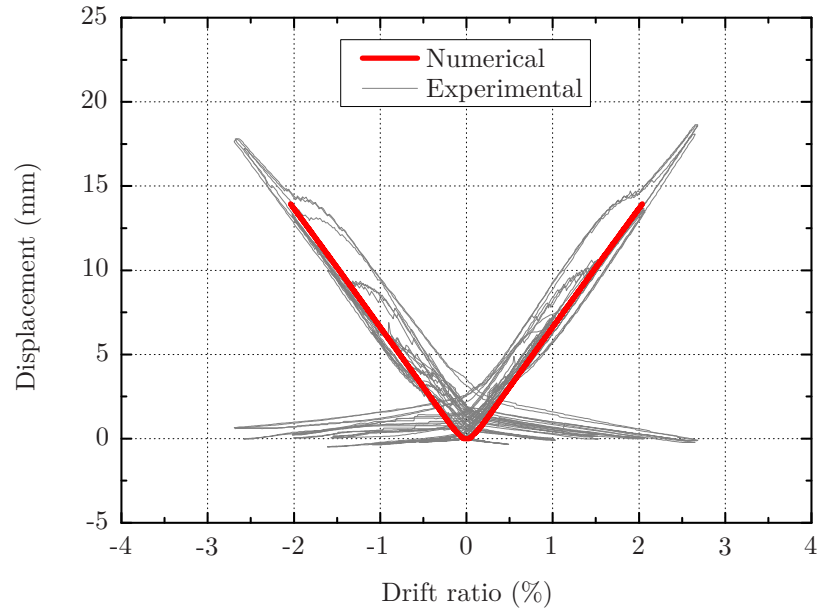

Figure 4.113: Numerical model of RM4 angles displacement vs drift.

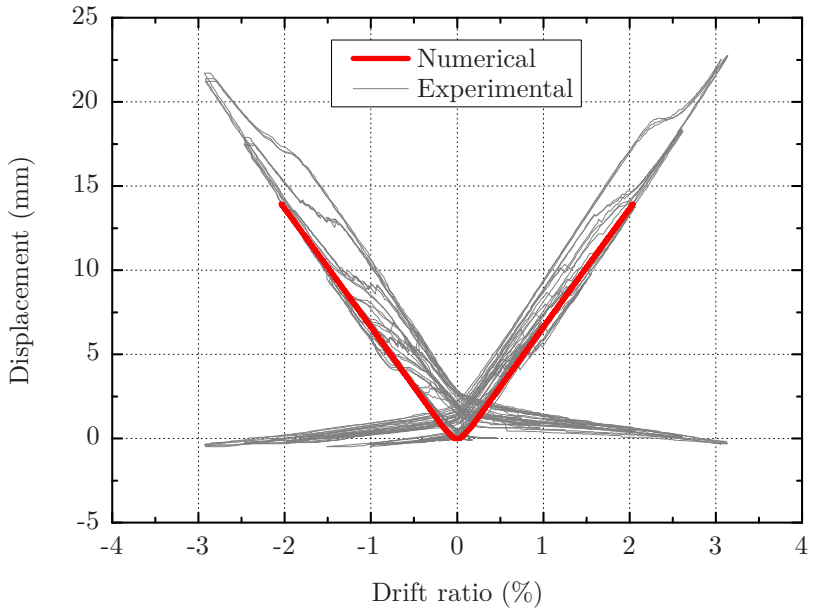

Figure 4.114: Numerical model of RM5 angles displacement vs drift.

In the tests, the steel angles slipped in relation to the wall and that is visible in the figures. This is the main cause for the difference between the numerical model and the experimental tests. In the tests, the angles slipped when they were pushed and pulled, so along time there are some instances where the numerical and experimental values overlap.

The differences between the bi-linear idealisation and the experimental tests have already been mentioned, but one other simplification can also have a small influence in the response. This simplification is the vertical displacement applied during the experimental tests on the steel angles, instead of a vertical displacement with a small rotation as in the experimental tests on the walls.

For these numerical wall specimen simulations, a perfect connection between the wall and the steel angles was assumed. The slippage between the angle and the steel plate built into the wall was assumed to be zero as well as the deformation of the bolts that connect the steel angles to the same plate. A perfect connection was also assumed between the built into steel plate and the concrete.

4.8 Conclusions

The study of post-tensioned precast concrete rocking walls with or without energy dissipaters included experimental and numerical work. The experimental work showed the effectiveness of these systems for cyclic actions and a good behaviour of the steel angle dissipation devices. The numerical work showed a good agreement with the experimental work.

Six precast concrete wall specimens were tested, three preliminary post-tensioned walls, two hybrid wall systems and a final post-tensioned wall. The walls were designed for a drift ratio of 2%. This implies that the post-tensioning has to be within the elastic range at that drift ratio, otherwise losses in the initial post-tensioning force would be expected, which means that, in the case of the hybrid systems, the ratio between the post-tensioning recentring forces and the forces of the dissipation devices would be changed and the recentring behaviour of the system would be at risk.

The three preliminary tests (wall specimens RM1, RM2 and RM3) were made with the purpose of testing and optimising the laboratory setup. Throughout these tests, the construction method for the joint between the wall and the base was developed, as some problems were detected in the first wall. It was believed that the wall could slip and two displacement blockers were used in the first test, but it was concluded that they were not necessary and could even cause problems in the analysis of the wall behaviour. The main problem that was detected, and solved only in the following tests, was the lack of bracing of the wall in the transversal direction. The first two walls tested (RM1 and RM2) were post-tensioned and had an elastic behaviour, having no significative energy dissipation. The third wall tested (RM3) was a post-tensioned wall including two resin and cork wedges in the bottom with the purpose of dissipating energy. Due to a scaling problem, the resin and cork did not respond as expected and there was no significative energy dissipation.

The two hybrid wall systems were post-tensioned walls with steel angles as energy dissipaters. The steel angle solutions used were similar to the ones identified as A4 and A5 in Chapter 3. The first was a steel angle with welding along the edge and was used in wall specimen RM4. The second was a steel angle with a second line of bolts and was used in wall specimen RM5.

The hybrid systems, specimens RM4 and RM5, presented energy dissipation and equivalent viscous damping ratios of 12.5% for RM4 and 14% for RM5 at a drift ratio of 2%, which are usual values for a hybrid solution. The final post-tensioned rocking wall solution, specimen RM6, resulted in equivalent viscous damping ratios of approximately 3%, which can be considered as an elastic response.

The main problem that was faced in these experimental tests was the loss of post-

tensioning forces. This was not desired, but should not be given too much significance, as it was mainly caused by the short length of the strands, a situation that would not normally be found in a real structure. In the southern strand, for a drift ratio of 2%, the post-tensioning force losses were 6%, 4% and 2% for the specimens RM4, RM5 and RM6, respectively. In the northern strand, for a drift ratio of 2%, the post-tensioning force losses were 10%, 6% and 5% for the specimens RM4, RM5 and RM6, respectively.

The maximum drifts that were reached in the final three walls were 2.5%, 3.0% and 3.5% for specimens RM4, RM5 and RM6, respectively. High values for the post-tensioning forces were reached as a consequence of the short length of the strands, with maximum values of 223.7 kN, 241.6 kN and 239.7 kN for specimens RM4, RM5 and RM6, respectively. The steel angles used in specimens RM4 and RM5 cracked for the maximum drifts, as can be seen in Figures 4.74 and 4.87, having reached maximum displacements of about 17.5 mm and 22.5 mm in specimens RM4 and RM5, respectively.

In all the wall specimens the maximum reached drift ratio was at least 2%, with the end of the tests being caused by the lack of transversal bracing, excessive stresses in the strands or the rupture of the angles. A bracing system was used in tests RM5 and RM6 allowing the strand stress to influence the maximum drift ratio. This drift ratio would have been even higher if the strands had been longer.

Chapter 5

Case study

5.1 Introduction

To complement the experimental work, a seismic case study was carried out to illustrate the rocking wall post-tensioned solutions proposed and tested experimentally. Direct displacement-based design (DDBD) methodology was used in determining design forces since it was considered more suitable for estimating structural response. In this methodology the structure was designed for the design drift. The design drift can be prescribed by code or material strain limits. The seismic action considered had a return period of 475 years as defined by EN 1998-1 (2004).

5.2 Direct displacement-based design procedure

In this section, the main steps for the DDBD procedure that were applied in this chapter are presented. Some specific steps for each structural system are explained in the respective calculation section. The DDBD concepts were mainly based on Priestley (1998), Priestley (2002), Priestley (2003), Priestley et al. (2007) and NZCS (2010). The basic concepts of DDBD are explained in Section 2.5.1.

To begin the DDBD procedure, a multi degree of freedom (MDOF) structure is converted into an equivalent single degree of freedom (SDOF) system, as illustrated in Figure 5.1. For this conversion, it is necessary to assume an inelastic deformed shape for the MDOF structure, that depends on the type of structure and is defined for each specific structural solution.

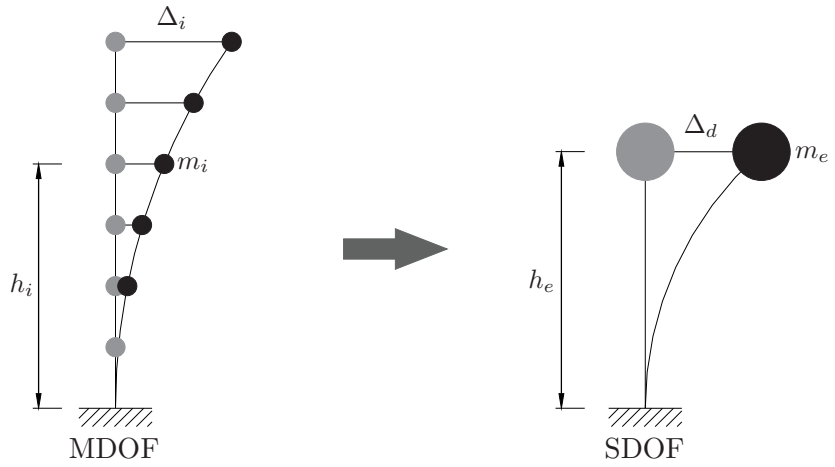

Figure 5.1: Conversion of MDOF to SDOF system (adapted from NZCS (2010).

Knowing the displacement profile for the MDOF structure, the SDOF structure design displacement Δ_d is calculated with equation 5.1, where m_i is the mass at the floor i.

$$\Delta_d = \frac{\sum_{i=1}^{n}(m_i \Delta_i^2)}{\sum_{i=1}^{n}(m_i \Delta_i)} \tag{5.1}$$

To complete the definition of the SDOF structure, the structure effective mass m_e and the structure effective height h_e are obtained with equations 5.2 and 5.3, where h_i is the height of floor.

$$m_e = \frac{\sum_{i=1}^{n}(m_i \Delta_i)}{\Delta_d} \tag{5.2}$$

$$h_e = \frac{\sum_{i=1}^{n}(m_i \Delta_i h_i)}{\sum_{i=1}^{n}(m_i \Delta_i)} \tag{5.3}$$

With the equivalent SDOF system defined, the equivalent viscous damping ratio needs to be estimated. The damping is a parameter that depends on the type of structure and on the expected demand ductility and is estimated for each structural solution. With the equivalent viscous damping ratio, the displacement response spectrum corresponding to the structure location is built. Having the spectrum and the design displacement Δ_d, the effective period of vibration T_e of the SDOF system at the design displacement is obtained. The effective stiffness k_e of the SDOF system at the design displacement is then calculated with expression 5.4.

$$k_e = 4\pi^2 \frac{m_e}{T_e^2} \tag{5.4}$$

As illustrated in Figure 5.2, with Δ_d and k_e, the total base shear V_B results from equation 5.5. In Figure 5.2, k_{cr} is the stiffness of the structure with cracked sections, V_{By} the base shear at yield and Δ_y the displacement at yield.

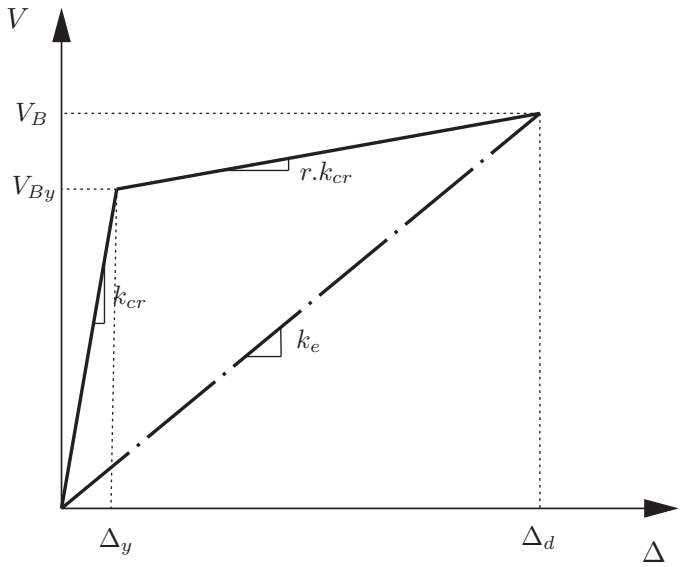

Figure 5.2: Effective stiffness of the SDOF system at the design displacement.

$$V_B = k_e \Delta_d \tag{5.5}$$

The next step is to distribute the total base shear force between the floors. In Figure 5.3 the distribution of the forces for each floor of the MDOF system is illustrated. These forces are calculated with equation 5.6, where F_i is the horizontal force at floor i.

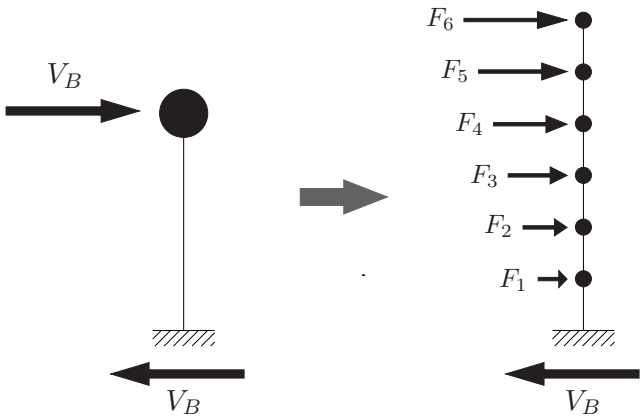

Figure 5.3: Distribution of base shear in MDOF system.

$$F_i = V_B \frac{m_i \Delta_i h_i}{\sum_{i=1}^{n} (m_i \Delta_i)} \tag{5.6}$$

5.3 Case study structure

The structure considered for this case study was a regular 6 storey precast concrete residential building. The plan dimensions are shown in Figure 5.4. Hollowcore slabs with a span of 7 m were considered with a thickness of 0.15 m plus a 0.05 m topping layer of concrete. As illustrated in Figure 5.5, the structure has 6 floors with 3 m intervals. The dimensions of the cross sections were defined for each system and are shown in the respective section. For simplification, the building stairs and lift shafts are not represented or taken into account in the design. It is assumed that their location do not change the centre of mass of the slabs, not having significant influence in the design.

The lateral seismic resisting systems were two frames in the longitudinal direction and two walls in the transverse direction. An emulation of a monolithic solution and a post-tensioned hybrid solution were analysed.

The two frames in the transverse direction were designed to carry only gravity loads and resist the demand lateral seismic displacements.

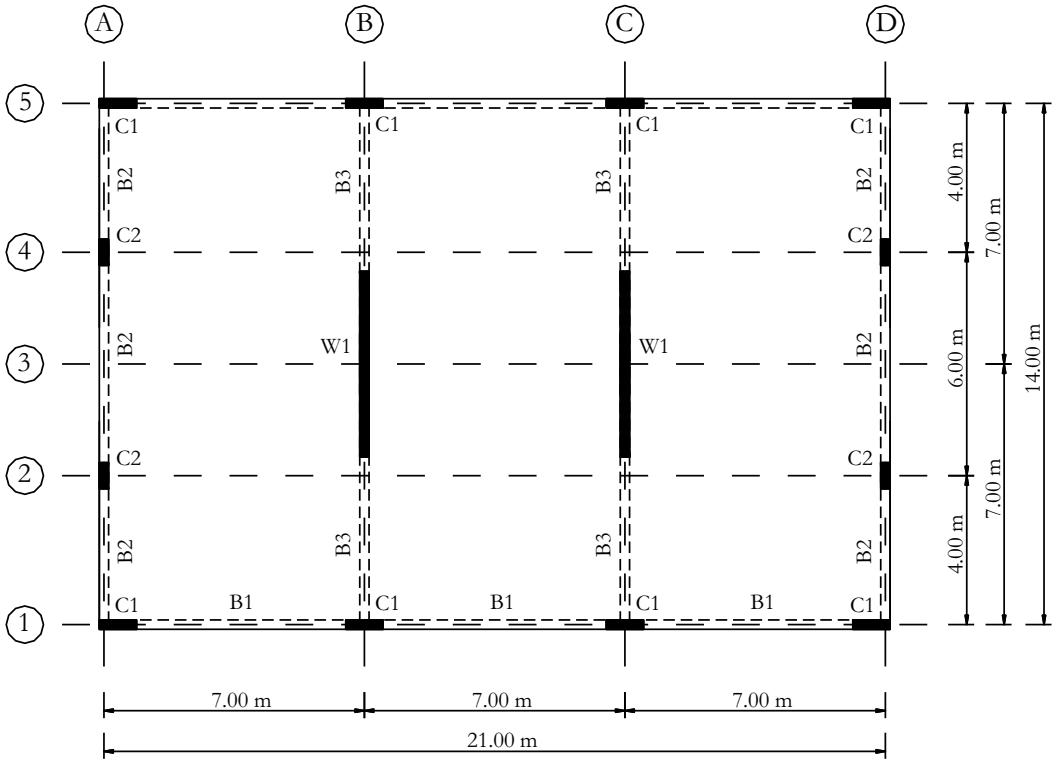

Figure 5.4: Case study structure floor plan.

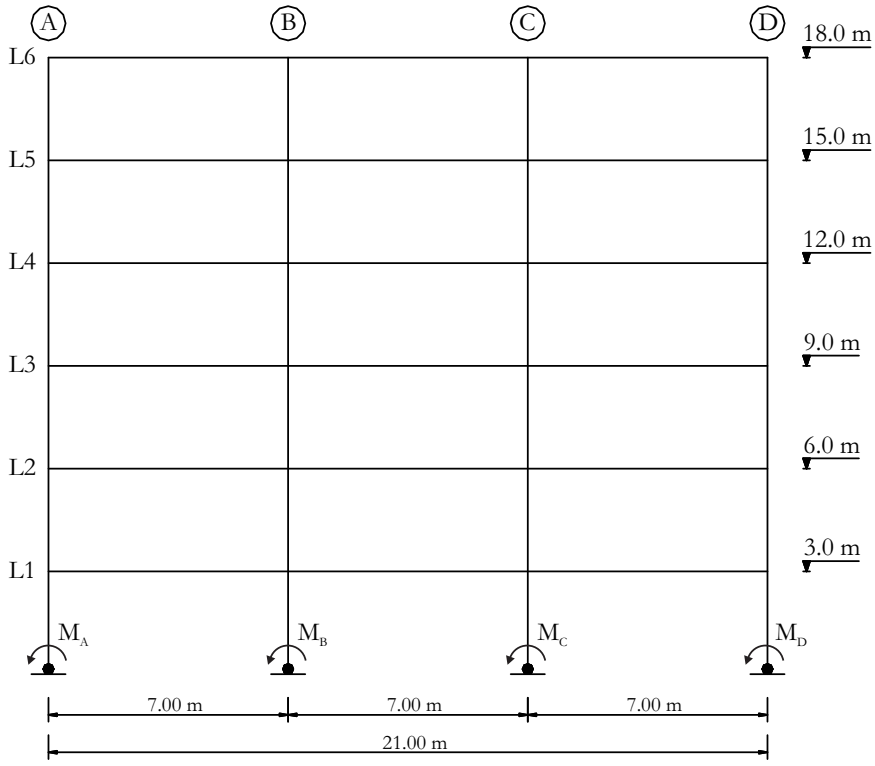

Figure 5.5: Case study structure frame elevation.

5.4 Materials

The case study was a reinforced concrete structure. Three types of steel were used, reinforcing steel for the longitudinal and transversal reinforcing bars, prestressing steel for the post-tensioning bars and steel for the angles used in the hybrid solution. The specified concrete was C30/37. Depending on the confinement, it was considered to have different stress-strain relations. Three different relationships were considered: unconfined concrete; concrete confined by transverse reinforcement and concrete confined by transverse reinforcement with an external protective steel cover plate.

5.4.1 Steel for reinforcing bars

The reinforcing steel used for the design was grade A500NR, according to EC2 (EN 1992-1-1, 2004). The characteristic yield stress value of the steel used is $f_{yk} = 500$ MPa. The EC2 maximum characteristic stress can be obtained with Kf_{yk}, being K a value between 1.15 and 1.35 for a steel ductility class C. For this study, the value of $K = 1.25$ was used. The characteristic strain at maximum force was assumed to be equal to $\varepsilon_{uk} = 7.5\%$, that corresponded to the minimum value for a steel ductility class C. Considering the referred values and a modulus of elasticity of $E_s = 200$ GPa, the stress-strain relation

with characteristic values was built and is shown Figure 5.6. When needed, an estimation of mean values using a factor of 1.1 was used.

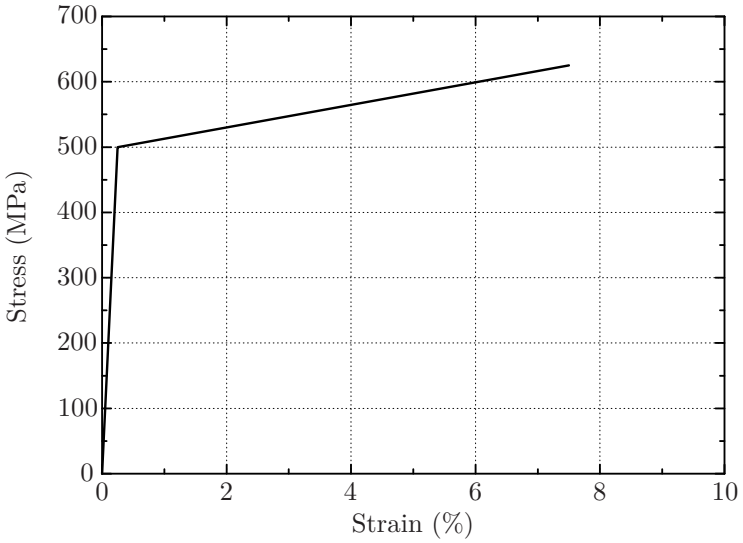

Strain (%)	Stress (MPa)
0.00	0.0
0.25	500.0
7.50	625.0

Figure 5.6: Stress-strain characteristic values relation for A500NR reinforcing steel.

5.4.2 Steel for angles

The steel used for the angles in the case study was grade S355. According to EC2 (EN 1993-1-1, 2005) and EN 10025-2 (2004), the considered nominal yield strength was $f_y = 355$ MPa and the nominal ultimate tensile strength $f_t = 510$ MPa, values that could be considered for nominal thicknesses up to 40 mm. The elastic modulus was $E_s = 210\ GPa$ (EN 1993-1-1, 2005) and the elongation at failure $\varepsilon_{su} = 22\%$ (EN 10025-2, 2004). The stress-strain relation with nominal values was built and is shown Figure 5.7. The nominal values were considered as mean values when needed.

5.4.3 Prestressing steel

To design the post-tensioned hybrid system, post-tensioning Dywidag bars with a diameter of 57 mm were used. These bars have a characteristic 0.1% proof-stress of $f_{p0.1k} = 835$ MPa, a characteristic tensile strength of $f_{pk} = 1035$ MPa and a modulus of elasticity of $E_p = 205$ GPa.

5.4.4 Concrete

The concrete used for this case study structure was C30/37. Depending on the wall section zone and detailing solution, unconfined and confined concrete was considered. For

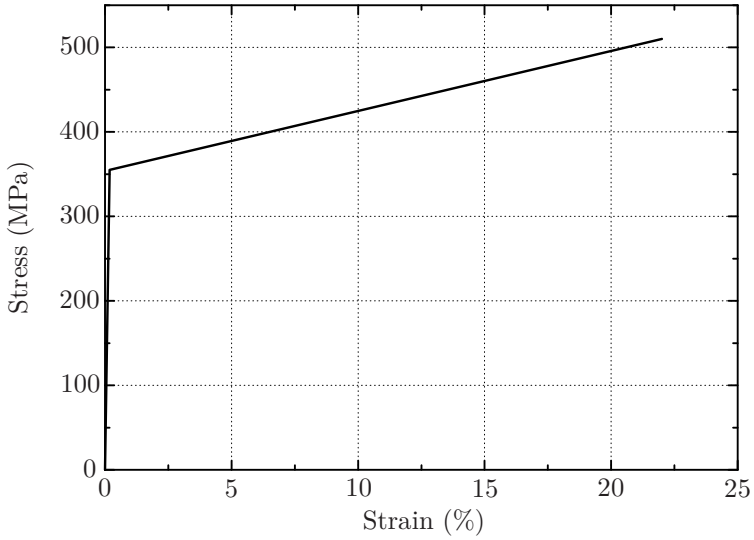

Strain (%)	Stress (MPa)
0.00	0.0
0.17	355.0
22.00	510.0

Figure 5.7: Stress-strain nominal values relation for S355 steel.

the unconfined concrete, the EC2 stress-strain relation for nonlinear structural analysis was used. For the confined stress-strain relation, Mander's model (Mander et al., 1988) was used. For the case where the confinement was due to transverse reinforcement and external protective steel cover, an adaptation of Mander's model developed by Marriott (2009) was used.

EC2 stress-strain relation for nonlinear structural analysis

For unconfined concrete, the model presented by EC2 was used. The stress-strain relation for unconfined concrete prescribed by EC2 is given in equation 5.7. Taking into consideration the C30/37 concrete and the respective EC2 parameters, the obtained stress-strain curve is shown in Figure 5.8. The values used for the parameters were the strain corresponding to unconfined concrete compressive strength of $\varepsilon_{c1} = 2.2‰$, the ultimate compressive strain in the concrete of $\varepsilon_{cu1} = 3.5‰$, the mean value of concrete cylinder compressive strength of $f_{cm} = 38$ MPa and the secant modulus of elasticity of concrete of $E_{cm} = 33\ GPa$.

$$\frac{\sigma_c}{f_{cm}} = \frac{k\eta - \eta^2}{1 + (k-2)\eta} \tag{5.7}$$

where,

σ_c is the concrete stress;
ε_c is the concrete compressive strain;
$\eta = \varepsilon_c/\varepsilon_{c1}$;
$k = 1.05E_{cm} \times |\varepsilon_{c1}|/f_{cm}$.

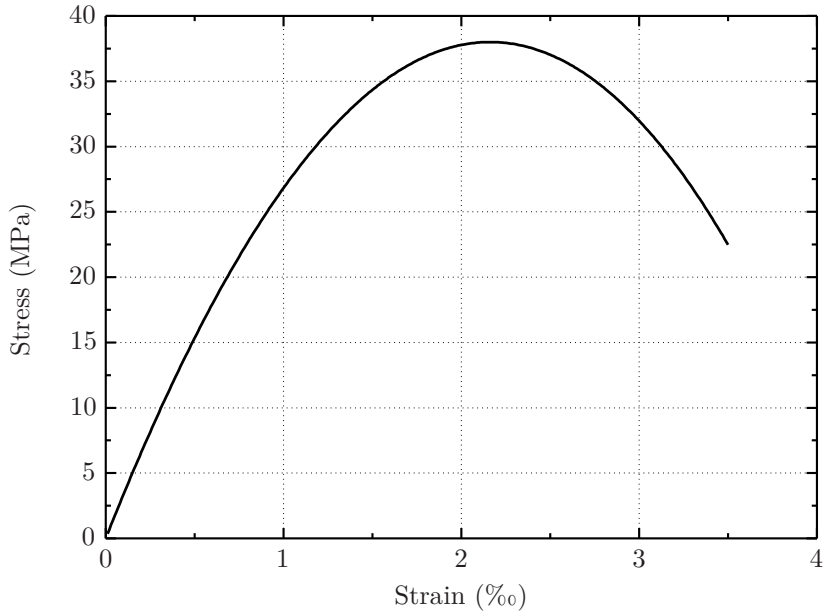

Figure 5.8: C30/37 stress-strain relation for nonlinear structural analysis.

Mander's model for confined concrete (Mander et al., 1988)

For confined concrete, where the confinement was given by transverse reinforcement, the model presented by Mander et al. (1988) was used. The stress-strain model presented by Mander et al. (1988) was based on an equation presented by Popovics (1973). The stress of the confined concrete σ_{cc} was calculated using equation 5.8, depending on the compressive strength of confined concrete $f_{cm,c}$ and two parameters x and r.

$$\sigma_{cc} = \frac{f_{cm,c} x r}{r - 1 + x^r} \tag{5.8}$$

where,

$$x = \frac{\varepsilon_c}{\varepsilon_{cc}} \tag{5.9}$$

$$r = \frac{E_c}{E_c - E_{sec}} \tag{5.10}$$

Equation 5.11 gives the concrete tangent modulus of elasticity at the origin E_c. The concrete secant modulus of elasticity E_{sec} was calculated by equation 5.12.

$$E_c = 5000\sqrt{f_{cm}} \tag{5.11}$$

$$E_{sec} = \frac{f_{cm,c}}{\varepsilon_{cc}} \tag{5.12}$$

The strain corresponding to confined concrete compressive strength ε_{cc} was obtained by equation 5.13, as suggested by Richart et al. (1928). For parameters corresponding to unconfined concrete, EC2 values were assumed, thus the strain corresponding to the compressive strength of unconfined concrete was $\varepsilon_{c1} = 2.2‰$and the compressive strength of unconfined concrete $f_{cm} = 38$ MPa.

$$\varepsilon_{cc} = \varepsilon_{co}\left[1 + 5\left(\frac{f_{cm,c}}{f_{cm}} - 1\right)\right] \tag{5.13}$$

For rectangular cross sections, Mander et al. (1988) use a confinement chart to estimate the concrete strength enhancement factor k_c. Equations 5.14, 5.15 and 5.16 were suggested by Wang and Restrepo (2001) as an alternative to the referred chart and were adopted for this study as being easier to compute. In the expressions, f_1 and f_2 are the maximum and minimum effective lateral confining pressures from the confining pressures f_{ly} and f_{lz}.

$$\frac{f_{cm,c}}{f_{cm}} = k_c = \alpha_1\alpha_2 \tag{5.14}$$

$$\alpha_1 = 1.25\left(1.8\sqrt{1 + 7.94\frac{f_1}{f_{cm}}} - 1.6\frac{f_1}{f_{cm}} - 1\right) \tag{5.15}$$

$$\alpha_2 = \left[1.4\frac{f_2}{f_1} - 0.6\left(\frac{f_2}{f_1}\right)^2 - 0.8\right]\sqrt{\frac{f_1}{f_{cm}}} + 1 \tag{5.16}$$

The effective lateral confining pressure in each direction, f_{ly} and f_{lz}, were calculated using equations 5.17 and 5.18. These equations take into account the lateral pressure mobilised by the transverse reinforcement, $\rho_y f_{sh}$ and $\rho_z f_{sh}$, with a correction factor to take into account the difference between the confined core A_{cc} and the effectively confined core A_e. This correction was made with the confinement effectiveness coefficient k_e defined in equation 5.19. The transverse reinforcement stress f_{sh} was considered equal to the yield stress f_{yh}, as defined by Mander et al. (1988). In Figure 5.9a the effectively confined core, as well as the ineffectively confined core and the unconfined concrete are shown and in Figure 5.9b the smeared model used for the calculations (Mander et al., 1988).

$$f_{ly} = k_e\rho_y f_{sh} \tag{5.17}$$

$$f_{lz} = k_e\rho_z f_{sh} \tag{5.18}$$

$$k_e = \frac{A_e}{A_{cc}} = \frac{\left(1 - \sum_{i=1}^{n}\frac{(w_i')^2}{6b_y b_z}\right)\left(1 - \frac{s'}{2b_y}\right)\left(1 - \frac{s'}{2b_z}\right)}{(1 - \rho_{cc})} \tag{5.19}$$

where,

ρ_y is the ratio between the transverse reinforcement area and the section core area in the y direction, $\rho_y = A_{shy}/(b_z s)$;

ρ_z is the ratio between the transverse reinforcement area and the section core area in the z direction, $\rho_z = A_{shz}/(b_y s)$;

ρ_{cc} is the ratio between the longitudinal reinforcement area and the section core area;

b_y is the concrete core dimension to centre line of transverse reinforcement in the y direction;

b_z is the concrete core dimension to centre line of transverse reinforcement in the z direction;

s' is the clear longitudinal spacing between transverse reinforcement;

w'_i is the i^{th} clear transversal spacing between longitudinal reinforcement.

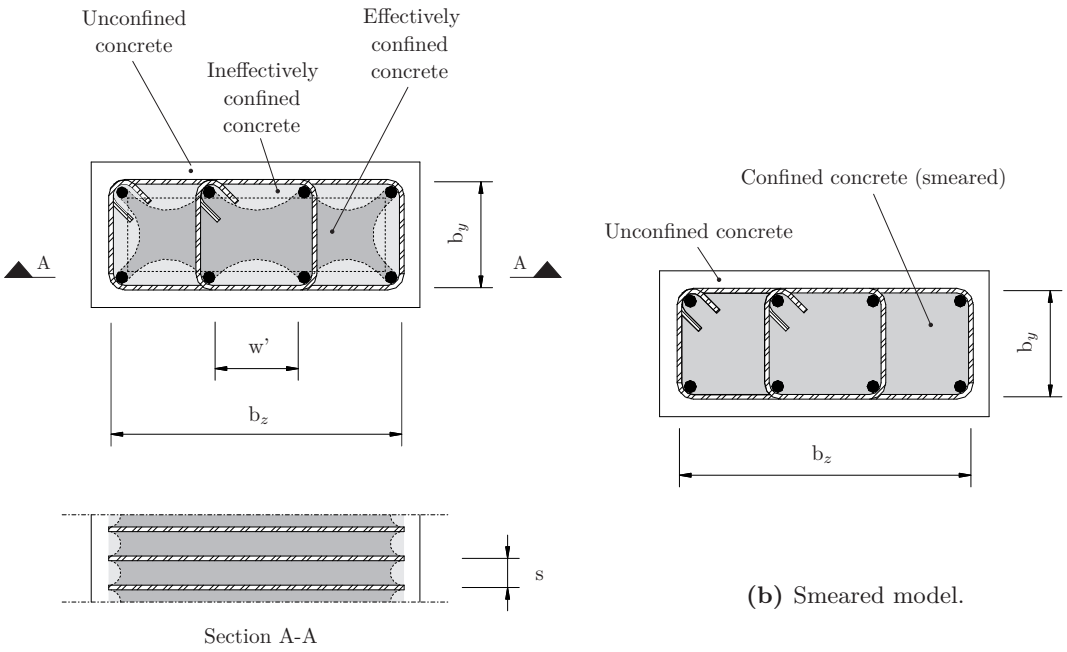

(a) Effectively confined core.

(b) Smeared model.

Figure 5.9: Confinement zones for rectangular hoop reinforcement (Mander et al., 1988).

To determine the ultimate confined concrete compressive strain $\varepsilon_{cu,c}$, Scott et al. (1982) suggested that this stage corresponds to the first rupture of the transverse reinforcement. Following this principle, Mander et al. (1988) developed equations for the energy balance approach at the rupture of the transverse reinforcement. According to the research quoted, Priestley et al. (1996) published equation 5.20 that was used in this case study, which Priestley et al. (1996) considered as being very conservative.

$$\varepsilon_{cu,c} = 0.004 + \frac{1.4\rho_v f_{yh}\varepsilon_{su}}{f_{cm,c}} \tag{5.20}$$

The ratio between the transverse reinforcement area and the section core area ρ_v was calculated using equation 5.21, where s is the longitudinal spacing between transverse reinforcement.

$$\rho_v = \rho_y + \rho_z \tag{5.21}$$

where,

s is the longitudinal spacing between transverse reinforcement;
A_{shy} is the total area of transverse reinforcement in the y direction;
A_{shz} is the total area of transverse reinforcement in the z direction.

Confinement with concrete cover protection

When a column or a wall concrete section has an external protection cover, the concrete will have more confinement than the solution with only transverse reinforcement. This protection can be a steel plate or a fiber reinforced polymer (FRP). The additional confinement supplied by the protection depends on its characteristics and on the detailing of the connections between the protection and the concrete. Marriott (2009) suggested three simple methods to estimate the confinement for these cases. The first method consisted in ignoring the contribution of the protection, considering only the confinement due to the transverse reinforcement. The second method consisted in expanding the ineffectively confined area in the confined core to the area outside the transverse reinforcement. The third method consisted in considering the concrete, that in the Figure 5.9a is identified as ineffectively confined, as moderately confined concrete and the cover concrete as ineffectively confined.

From the three methods mentioned above, the second one was adopted for this study. To use this method, a modification to the equation 5.19, corresponding to the confinement effectiveness coefficient k_e was made, leading to equation 5.22. This modification was to calculate the coefficient using the section gross area instead of the area of the confined core.

$$k_e = \frac{A_e}{A_g} = \frac{\left(1 - \sum_{i=1}^{n} \frac{(w_i')^2}{6 b_y b_z}\right)\left(1 - \frac{s'}{2b_y}\right)\left(1 - \frac{s'}{2b_z}\right)}{(1 - \rho_{cc})} \times \frac{A_{cc}}{A_g} \tag{5.22}$$

where,

A_g is the section gross area.

5.5 Definition of seismic action

The building structure was assumed to be located in Lagos, a town in the South West of Portugal. The seismic action was defined according to EN 1998-1 (2004) (EC8) and the respective Portuguese National Annex. The building was classified with an importance class II. The National Annex defines two types of seismic actions: type 1 and type 2. In this study only type 1 seismic action was considered, as this leads to higher seismic displacements. The building location corresponds to zone 1 for type 1 seismic action. A ground type C was assumed in the design.

The EN 1998-1 (2004) design response spectrum for Ultimate Limit States (ULS) has a 475 year return period, corresponding to 10% probability of being exceeded in 50 years. The response spectrum is defined in equations 5.23. The presented equations give the mass acceleration for a single degree of freedom system function of the system period. The spectrum has three straight lines and a final curve. The period limit defined in the main part of the code is 4 s, but it is possible to define beyond that period using a code annex. The ground acceleration a_g depends on the reference acceleration a_{gR} and the importance class ($a_g = \gamma_I.a_{gR}$), where γ_I is the importance factor that depends on the building use.

$$0 \leq T \leq T_B : S_e(T) = a_g\, S \left[1 + \frac{T}{T_B}(\eta\, 2.5 - 1)\right] \tag{5.23a}$$

$$T_B \leq T \leq T_C : S_e(T) = a_g\, S\, \eta\, 2.5 \tag{5.23b}$$

$$T_C \leq T \leq T_D : S_e(T) = a_g\, S\, \eta\, 2.5 \left[\frac{T_C}{T}\right] \tag{5.23c}$$

$$T_D \leq T \leq 4s : S_e(T) = a_g\, S\, \eta\, 2.5 \left[\frac{T_C\, T_D}{T^2}\right] \tag{5.23d}$$

where,

$S_e(T)$ is the elastic acceleration response spectrum;
T is the vibration period of a linear single-degree-of-freedom system;
a_g is the design ground acceleration on type A ground ($a_g = \gamma_I.a_{gR}$);
T_B is the lower limit of the period of the constant spectral acceleration branch of the spectrum;
T_C is the upper limit of the period of the constant spectral acceleration branch of the spectrum;
T_D is the value defining the beginning of the constant displacement response range of the spectrum;
S is the soil factor;
η is the damping correction factor with a reference value of $\eta = 1$ for 5% viscous damping;

a_{gR} is the reference peak ground acceleration.

When the structural damping to be considered is different from 5%, a correction factor can be calculated from equation 5.24.

$$\eta = \sqrt{\frac{10}{5+\xi}} \geq 0.55 \tag{5.24}$$

where ξ is the viscous damping ratio of the structure, expressed as a percentage.

To obtain the displacement spectrum, equation 5.25 can be used.

$$S_{De}(T) = S_e(T) \left[\frac{T}{2\pi}\right]^2 \tag{5.25}$$

where S_{De} is the elastic displacement response spectrum.

The values for the parameters needed to complete the equations were defined by the Portuguese National Annex and, for this case study, are shown in Table 5.1. In Figure 5.10, displacement spectra for this case are shown taking into consideration different viscous damping ratio values.

Table 5.1: EC8 spectrum parameters.

a_{gR} (m/s^2)	γ_I -	S -	T_B (s)	T_C (s)	T_D (s)
2.5	1.0	1.3	0.1	0.6	2.0

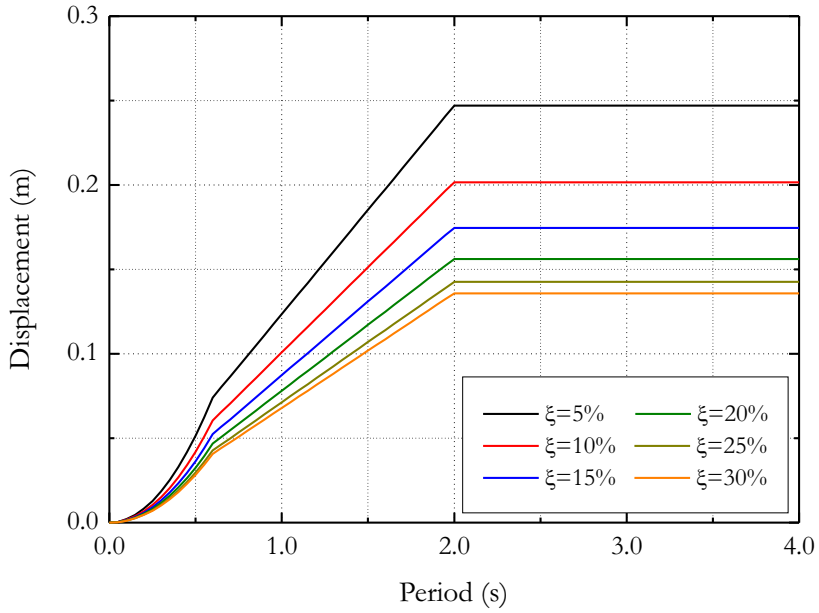

Figure 5.10: Displacement spectra for 475 year return period for Lagos, Portugal.

5.6 Gravity loads

The gravity loads for the seismic load combination was a quasi-permanent vertical load. A slab with a self-weight of 3.95 kN/m^2 and super-imposed loads of 3.50 kN/m^2 were considered. From EN 1991-1-1 (2002) (EC1), the live load for the residential building was 2.00 kN/m^2 with the respective quasi-permanent factor ψ_2 of 0.3. From these loads, the quasi-permanent gravity load resulted in 8.05 kN/m^2. The loads were assumed equal for all the floors.

5.7 Equivalent monolithic system

The equivalent monolithic system is the most common solution for precast concrete moment resisting frame. The design procedure can be the same as for the usual cast in place system, but the detailing has to take into account the assembly method. The dimensions of the cross sections of the precast concrete elements are shown in Table 5.2 (see also Figure 5.4).

Table 5.2: Cross sections of the reinforced concrete elements.

		$Section(m^2)$
Vertical elements	**C1**	1.00 x 0.25
	C2	0.25 x 0.70
	W1	0.25 x 4.00
Beams	**B1**	0.25 x 0.70
	B2	0.25 x 0.70
	B3	0.25 x 0.70

To determine the forces in the walls, the DDBD procedure, as explained in Section 5.2, was used. After obtaining the forces acting in the walls, the base cross section was designed and submitted to a design verification procedure. The design was the traditional design used for monolithic structures with the safety factors specified by the codes for the materials stress-strain relations. The design verification was carried out to check the cross section response at the design drift. To obtain a realistic response for the structure, mean values were used for the stress-strain relations and a final global safety factor was calculated.

5.7.1 Wall direction (transverse direction)

To implement the DDBD procedure in the wall direction, the equivalent SDOF system was determined. For a monolithic reinforced concrete wall, the displacement profile given

by equation 5.26 was assumed (Priestley et al., 2007). This shape was obtained assuming a linear curvature distribution along the height of the wall, until the achievement of the yield curvature at the wall base section, and a rigid body rotation about the base plastic hinge after yielding. In the displacement profile equation, the yield curvature ϕ_y was assumed equal to $2.0\varepsilon_y/l_w$ (Priestley et al., 2007), where l_w is the length of the wall cross section. When a wall dominates the displacement profile of the structure, the maximum drift θ_{yn} is expected to be at roof level and equal to $\varepsilon_y h_n/l_w$, where h_n is the height of the roof level.

Having the displacement profile, it was possible to obtain the design displacement, the effective mass and the effective height from equations 5.1, 5.2 and 5.3 (auxiliary calculations are presented in Table 5.3). These parameter values are shown in Table 5.4. With the basic SDOF system parameters determined, the design drift ratio obtained was 1.92%. This design drift was conditioned by the maximum spectral displacement, corresponding to a period of 2.0 seconds.

$$\Delta_i = \Delta_{yi} + (\theta_d - \theta_{yn})h_i = \frac{\varepsilon_y}{l_w}h_i^2\left(1 - \frac{h_i}{3h_n}\right) + \left(\theta_d - \frac{\varepsilon_y h_n}{l_w}\right)h_i \tag{5.26}$$

Table 5.3: Wall direction DDBD calculations for the equivalent monolithic system.

Floor	h_i (m)	m_i (ton)	Δ_i (m)	Δ_i^2 (m^2)	$\Delta_i \times m_i$ $(m \times ton)$	$\Delta_i^2 \times m_i$ $(m^2 \times ton)$	$\Delta_i \times m_i \times h_i$ $(m^2 \times ton)$
1	3	305.6	0.026	0.0007	8.0	0.21	24.1
2	6	305.6	0.063	0.0040	19.2	1.21	115.4
3	9	305.6	0.108	0.0116	33.0	3.55	296.6
4	12	305.6	0.159	0.0252	48.6	7.72	582.7
5	15	305.6	0.214	0.0458	65.4	14.01	981.3
6	18	291.4	0.271	0.0736	79.1	21.46	1423.4
Sum		1819.3			253.3	48.16	3423.5

Table 5.4: SDOF parameters for the equivalent monolithic system in the wall direction.

θ_d (%)	Δ_d (m)	m_e (ton)	h_e (m)
1.92	0.190	1332.2	13.5

5.7.1.1 Yield displacement and damping

To calculate the equivalent viscous damping ratio, the displacement ductility, which is a function of the yield displacement, was determined. Equation 5.27 gives the displacement profile at yield and was used to obtain the yield displacement, for $h_i = h_e$. The yield strain of the steel was obtained assuming the yield stress of the reinforcing steel $\sigma_y = 500$ MPa,

multiplied by 1.1 in order to estimate the mean value, as recommended by Priestley et al. (2007). These values are shown in Table 5.5.

For the monolithic reinforced concrete wall, the equivalent viscous damping ratio was estimated by expression 5.28 (Priestley et al., 2007), where the displacement ductility μ_δ was obtained from expression 5.29. Table 5.5 contains the calculations for the equivalent viscous damping ratio. The obtained value was 12.1%.

$$\Delta_{yi} = \frac{\varepsilon_y}{l_w} h_i^2 \left(1 - \frac{h_i}{3h_n}\right) \tag{5.27}$$

$$\xi_{eq} = 0.05 + 0.444 \left(\frac{\mu_\delta - 1}{\mu_\delta \pi}\right) \tag{5.28}$$

$$\mu_\delta = \frac{\Delta_d}{\Delta_y} \tag{5.29}$$

where,

h_n is the height of the roof level;
Δ_{yi} is the displacement of floor i at yield.

Table 5.5: Wall direction yield parameters and ξ_{eq} calculation for the equivalent monolithic system.

h_e	e_y	Δ_y	Δ_d	μ_δ	ξ_{eq}
(m)	-	(m)	(m)	(m)	(%)
13.5	0.0028	0.094	0.190	2.02	12.1

5.7.1.2 Base shear and forces distribution

To obtain the SDOF effective period, the spectra in Figure 5.10 was used, with the equivalent viscous damping ratio of Table 5.5. The effective stiffness was calculated with equation 5.4 and the base shear with equation 5.5, giving the results shown in Table 5.6. To distribute the base shear in the MDOF structure, equation 5.6 was used, resulting in the forces F_i shown in Table 5.7. From the forces acting on each floor, the internal demand forces were calculated.

Table 5.6: Wall base shear for the equivalent monolithic system.

T_e	K_e	V_B
(s)	(kN/m)	(kN)
2.00	13148.5	2499.8

Table 5.7: Wall forces distribution for the equivalent monolithic system.

Floor	h_i (m)	m_i (ton)	Δ_i (m)	$\Delta_i \times m_i$ $(m \times ton)$	F_i (kN)
1	3	305.6	0.026	8.0	79.4
2	6	305.6	0.063	19.2	189.9
3	9	305.6	0.108	33.0	325.2
4	12	305.6	0.159	48.6	479.2
5	15	305.6	0.214	65.4	645.7
6	18	291.4	0.271	79.1	780.5
Sum		1819.3		253.3	2499.8

5.7.1.3 Internal forces

Assuming that the walls resist the total seismic action, they were considered cantilever structures with forces applied at the floor levels. The internal forces corresponding to the shear forces and bending moments are shown in Figures 5.11a and 5.11b. It was assumed that the influence of the beams, that converge on the walls, was negligible for the calculation of these internal forces. The resulting base reactions were a base shear V_w=1249.9 kN and a bending moment M_w=16894.5 kNm in each wall.

To calculate the axial load at the base, the slab loads and the slab, beams and wall self-weights were taken into account. The slab loads were obtained with the estimation of the wall tributary area shown in Figure 5.12. The beams that converge in the wall were both type B3 (see Figure 5.4 and Table 5.16). The value estimated for the axial load at the base was N_w=3750.9 kN.

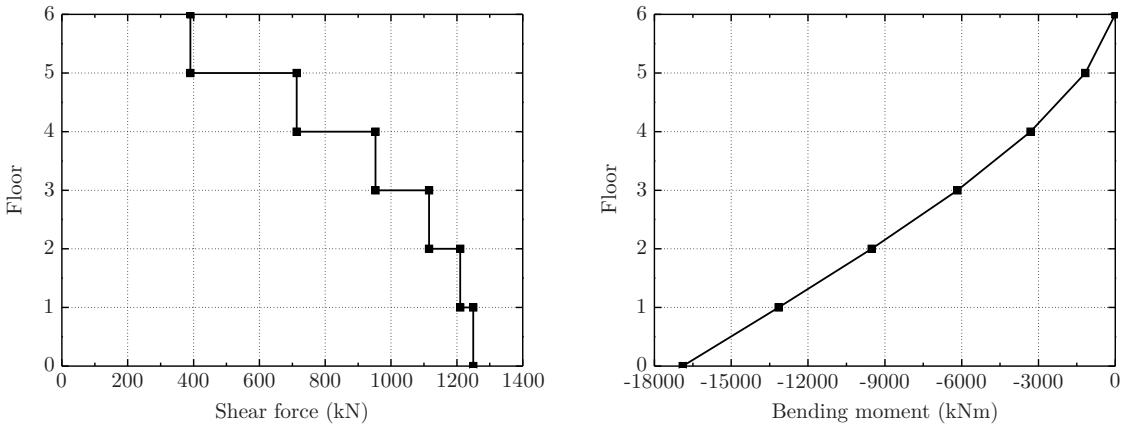

(a) Storey shear forces. **(b)** Overturning bending moments.

Figure 5.11: Internal forces of the walls for the equivalent monolithic system in each wall.

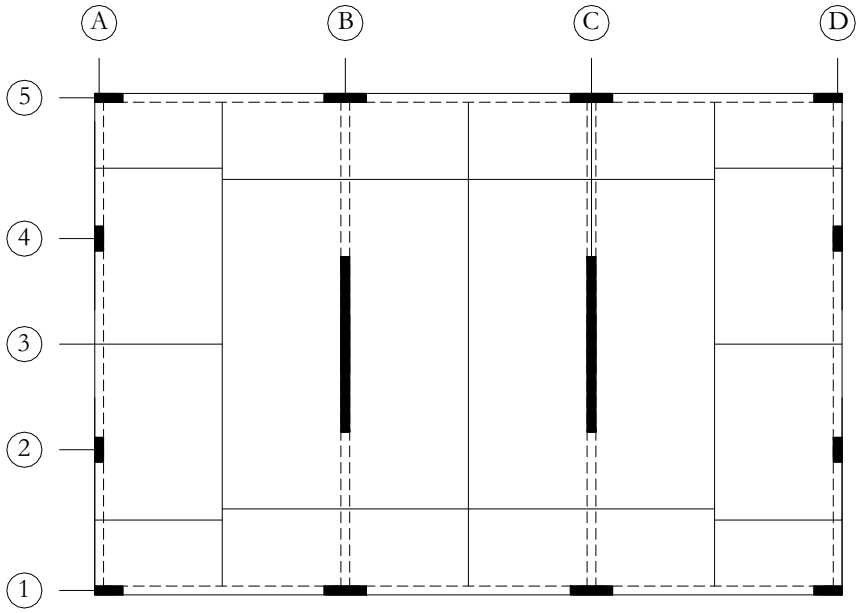

Figure 5.12: Tributary areas of vertical elements.

5.7.1.4 Cross section design

The design and detailing of the wall was made for the maximum bending moment at the wall base section. Having the base bending moment and axial load, equation 5.30 was used to estimate the tensile force in the reinforcing steel and equation 5.31 to obtain the steel area. Table 5.8 shows the results for the longitudinal reinforcing steel. The steel area required for the combined bending moment and axial load was 0.00679 m^2. The chosen solution was to concentrate 14 bars with a diameter of 25 mm at each end and 28 bars with a diameter of 16 mm at 0.20 m intervals along the wall, as detailed in Figure 5.13.

$$F_s \simeq \frac{M}{z} + \frac{N}{2} \tag{5.30}$$

$$A_s = \frac{F_s}{f_{yd}} \tag{5.31}$$

where,

F_s is the demand tensile force in the reinforcing steel;
z is the lever arm between the tensile and compressive forces;
f_{yd} is the design yield strength of the reinforcing steel $f_{yd} = f_{yk}/1.15$;
A_s is the area of the reinforcing steel under tension.

Table 5.8: Longitudinal reinforcement steel calculation for the equivalent monolithic system.

N (kN)	M (kNm)	z (m)	F_s (kN)	f_{yd} (MPa)	A_s (m^2)
-3750.9	16894.5	3.50	2951.6	435	0.00679

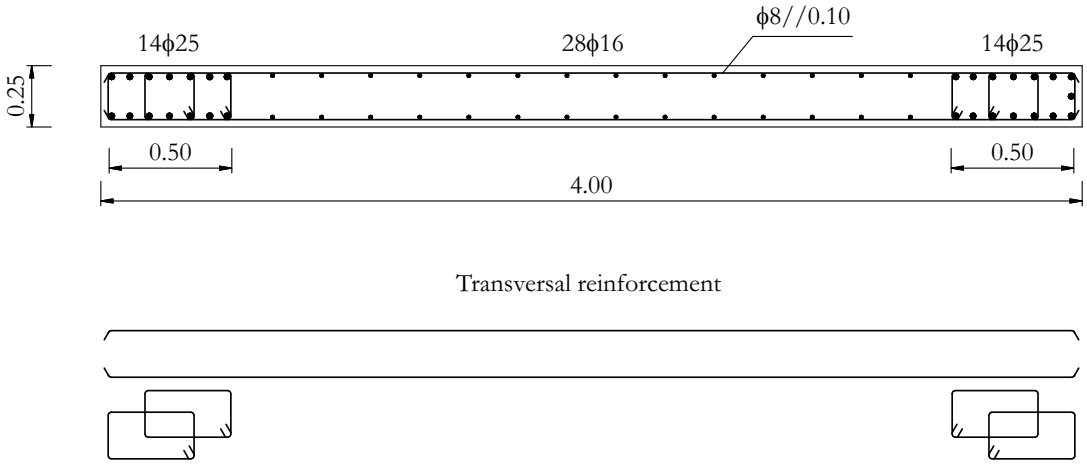

Figure 5.13: Wall base section detail for the equivalent monolithic system (dimensions in metres).

5.7.1.5 Cross section design verification

The design forces were calculated for the design drift, thus the structure response was checked in the deformed position at the design drift ratio. To check the design, the maximum curvature corresponding to the design drift was calculated, then the concrete and reinforcement steel forces were obtained to calculate the bending moment. This analysis should be as close to the real response as possible, thus mean values were used for the materials stress-strain relations.

Curvature

The section curvature ϕ was determined using equation 5.32.

$$\phi = \phi_y + \phi_p \tag{5.32}$$

where,

ϕ_y is the section elastic curvature at yield;
ϕ_p is the section plastic curvature resulting from the rotation of the wall base plastic hinge.

The yield curvature was calculated using equation 5.33 (Priestley, 2003).

$$\phi_y = 2.0\varepsilon_y / l_w \tag{5.33}$$

The plastic hinge rotation was estimated as the plastic curvature integration along the plastic hinge length. Assuming a constant curvature along the length, the plastic curvature was obtained from equation 5.34.

$$\phi_p = \frac{\theta_p}{l_p} \tag{5.34}$$

where,

θ_p is the plastic hinge rotation;
l_p is the plastic hinge length.

To calculate the plastic hinge length, equation 5.35 (Priestley et al., 2007) was adopted. This equation takes into account steel strain hardening, tension shift effects and strain penetration length.

$$l_p = kh_e + 0.1l_w + l_{sp} \tag{5.35}$$

where,

k is a parameter taken as $0.2(f_t/f_y - 1) \leq 0.08$;
l_{sp} is the strain penetration length taken as $0.022 f_y d_{bl}$ (m);
f_y is the yield stress of the reinforcement (MPa);
f_t is the ultimate tensile strength of the reinforcement (MPa);
d_{bl} is the diameter of the reinforcing bar (m).

As the plastic displacement depends on the plastic curvature, the wall length, the plastic hinge length and the strain penetration length, the plastic hinge rotation θ_p was obtained using equation 5.36 (Priestley et al., 2007).

$$\theta_p = \frac{\Delta_p}{h_e - (0.5l_p - l_{sp})} \tag{5.36}$$

Finally, the plastic displacement Δ_p was obtained from the design displacement and the yield displacement with equation 5.37.

$$\Delta_p = \Delta_d - \Delta_y \tag{5.37}$$

The results for the plastic hinge length, assuming $f_t/f_y = 1.25$, are presented in Table 5.9. Intermediate values computed in the determination of the total curvature is shown in Table 5.10.

Table 5.9: Wall plastic hinge length for the equivalent monolithic system at design drift.

k	d_{bl}	h_e	l_w	l_{sp}	l_p
-	(m)	(m)	(m)	(m)	(m)
0.05	0.025	13.5	4	0.275	1.351

Table 5.10: Curvature calculation for the equivalent monolithic system at design drift.

Δ_d	Δ_y	Δ_p	θ_p	ϕ_y	ϕ_p	ϕ
(m)	(m)	(m)	-	-	-	-
0.190	0.094	0.096	0.0073	0.0014	0.0054	0.0068

Cross section bending moment

To calculate the bending moment, the procedure consisted on predicting an initial neutral axis depth, calculating all the forces and checking the section equilibrium. The neutral axis depth was changed until the required equilibrium was achieved. The procedure can be resumed in the following steps:

1. Estimate neutral axis depth, x;
2. Calculate the concrete compression forces;
3. Calculate the bar tension and compression forces;
4. Compare the sum of all forces with the axial load and return to first step until they converge;
5. Evaluate the moment capacity.

As illustrated in Figure 5.14, the conventions for the wall axis followed the EC2 (EN 1992-1-1, 2004), being the wall section in the plan yz. It can also be seen that the length of the compression zone was defined as x. The compression zone was divided into n fibres and x_i was the distance from the neutral axis to the centre of each fibre.

After the iterative procedure was concluded, the final neutral axis depth that corresponded to equilibrium was x=0.854m. The values that will be presented were determined for this final cycle.

Table 5.11 shows the forces for each concrete fibre. As can be seen in the section detail in Figure 5.13, the concrete at both ends of the wall had transverse reinforcement along a length of 0.50 m and was considered confined, whilst the remainder was considered

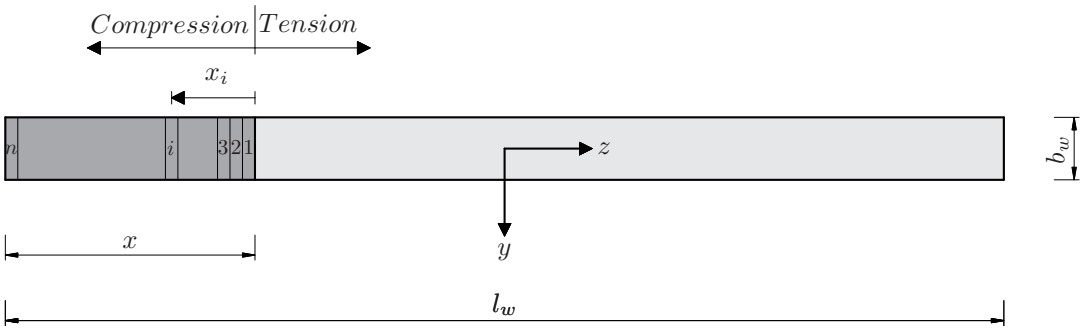

Figure 5.14: Wall local axis convention and concrete compressed fibres.

unconfined. The A_i is the area of fibre i and the ε_{ci} the strain of fibre i determined using equation 5.38.

$$\varepsilon_{ci} = \phi.x_i \tag{5.38}$$

The fibres could have unconfined concrete or confined and unconfined concrete. The stress of the confined part of the fibres σ_{cci} was obtained using Mander's model (Mander et al., 1988) with the equation 5.8, as explained previously in this chapter. The concrete strength enhancement factor was k_c=1.41. The stress of the unconfined part of the fibres σ_{ci}, was determined using EC2 stress-strain relation. With these stresses, the force in each fibre F_{ci} was determined. It can be seen in Table 5.11 that the total concrete reaction was 6636.8 kN.

Tables 5.12 and 5.13 summarise the forces acting on the longitudinal bars in the confined zone and outside that zone (see Figure 5.13). The tables have the following content:

1. the bar position coordinate in z axis z_j;
2. the area of the bars in position j A_{sj};
3. steel bars strain in position j $\varepsilon_{sj} = \phi.z_j$;
4. steel bars stress in position j σ_{sj};
5. steel bars compressive force in position j F_{scj};
6. steel bars tensile force in position j F_{stj};
7. bending moments due to each tension bar $M_{stj} = F_{stj}.[z_j - (x_{cg} - l_w/2)]$.

Table 5.14 summarises the total forces in the wall cross section. The forces presented are the axial load demand N_w, the concrete compressive force F_c, the sum of all compressive forces in the steel bars F_{sc} and the sum of all tensile forces in the steel bars F_{st}. From these values it was verified that the obtained solution was correct.

The bending moment for this equivalent monolithic system could be determined at any point of the section, as long as the axial load force is taken into account. In this

Table 5.11: Concrete compressive forces for the equivalent monolithic system at design drift.

	$Fibre$ i	A_i (m^2)	x_i (m)	ε_{ci} -	σ_{cci} (MPa)	σ_{ci} (MPa)	F_{ci} (kN)
Unconfined	1	0.0069	0.014	-0.0001	0.0	-0.1	-0.5
	2	0.0069	0.041	-0.0003	0.0	-0.8	-5.5
	3	0.0069	0.069	-0.0005	0.0	-2.6	-17.9
	4	0.0069	0.096	-0.0007	0.0	-5.9	-40.2
	5	0.0069	0.124	-0.0008	0.0	-10.7	-73.5
	6	0.0069	0.151	-0.0010	0.0	-16.8	-115.5
	7	0.0069	0.179	-0.0012	0.0	-23.3	-160.1
	8	0.0069	0.206	-0.0014	0.0	-29.1	-199.9
	9	0.0069	0.234	-0.0016	0.0	-33.5	-229.8
	10	0.0069	0.261	-0.0018	0.0	-36.2	-248.7
	11	0.0069	0.288	-0.0020	0.0	-37.6	-258.2
	12	0.0069	0.316	-0.0021	0.0	-38.0	-261.0
Confined plus side cover	13	0.0069	0.343	-0.0023	-41.2	-37.8	-277.3
	14	0.0069	0.371	-0.0025	-42.8	-37.2	-284.6
	15	0.0069	0.398	-0.0027	-44.2	-36.5	-290.8
	16	0.0069	0.426	-0.0029	-45.5	-35.7	-296.1
	17	0.0069	0.453	-0.0031	-46.6	-34.8	-300.6
	18	0.0069	0.481	-0.0033	-47.6	-34.0	-304.4
	19	0.0069	0.508	-0.0035	-48.5	-33.2	-307.8
	20	0.0069	0.536	-0.0036	-49.2	0.0	-257.1
	21	0.0069	0.563	-0.0038	-49.9	0.0	-260.6
	22	0.0069	0.591	-0.0040	-50.5	0.0	-263.8
	23	0.0069	0.618	-0.0042	-51.1	0.0	-266.5
	24	0.0069	0.646	-0.0044	-51.5	0.0	-268.9
	25	0.0069	0.673	-0.0046	-51.9	0.0	-271.0
	26	0.0069	0.701	-0.0048	-52.2	0.0	-272.8
	27	0.0069	0.728	-0.0049	-52.5	0.0	-274.3
	28	0.0069	0.756	-0.0051	-52.8	0.0	-275.5
	29	0.0069	0.783	-0.0053	-53.0	0.0	-276.6
	30	0.0069	0.811	-0.0055	-53.1	0.0	-277.4
End cover	31	0.0002	0.852	-0.0058	-	0.0	0.0
	32	0.0002	0.853	-0.0058	-	0.0	0.0
	33	0.0002	0.854	-0.0058	-	0.0	0.0
Sum							**-6636.8**

Table 5.12: Calculations for the contribution of the end bars to the bending moment.

Bar j	z_j (m)	A_{sj} (m^2)	ε_{sj} -	σ_{sj} (MPa)	F_{scj} (kN)	F_{stj} (kN)	M_{stj} (kNm)
1	-1.96	0.0010	-0.0055	-554.8	-544.8	0.0	0.0
2	-1.89	0.0010	-0.0050	-553.9	-543.9	0.0	0.0
3	-1.81	0.0010	-0.0045	-553.0	-543.1	0.0	0.0
4	-1.71	0.0010	-0.0038	-551.9	-541.9	0.0	0.0
5	-1.61	0.0010	-0.0032	-550.7	-540.8	0.0	0.0
6	-1.54	0.0010	-0.0026	-528.7	-519.2	0.0	0.0
7	-1.46	0.0010	-0.0021	-426.9	-419.2	0.0	0.0
8	1.46	0.0010	0.0177	575.8	0.0	565.4	1767.7
9	1.54	0.0010	0.0182	576.6	0.0	566.3	1812.9
10	1.61	0.0010	0.0187	577.5	0.0	567.1	1858.2
11	1.71	0.0010	0.0194	578.7	0.0	568.3	1918.8
12	1.81	0.0010	0.0201	579.9	0.0	569.4	1979.6
13	1.89	0.0010	0.0206	580.7	0.0	570.3	2025.3
14	1.96	0.0010	0.0211	581.6	0.0	571.2	2071.2
Sum					**-3652.9**	**3978.0**	**13433.6**

Table 5.13: Calculations for the contribution of the middle bars to the bending moment.

Bar j	z_j (m)	A_{sj} (m^2)	ε_{sj} -	σ_{sj} (MPa)	F_{scj} (kN)	F_{stj} (kN)	M_{stj} (kNm)
15	-1.3	0.0004	-0.0010	-209.5	-84.2	0.0	0.0
16	-1.1	0.0004	0.0003	62.1	0.0	25.0	14.1
17	-0.9	0.0004	0.0017	333.7	0.0	134.2	102.8
18	-0.7	0.0004	0.0030	550.5	0.0	221.3	213.9
19	-0.5	0.0004	0.0044	552.8	0.0	222.2	259.2
20	-0.3	0.0004	0.0057	555.2	0.0	223.2	305.0
21	-0.1	0.0004	0.0071	557.5	0.0	224.1	351.1
22	0.1	0.0004	0.0085	559.8	0.0	225.1	397.5
23	0.3	0.0004	0.0098	562.2	0.0	226.0	444.4
24	0.5	0.0004	0.0112	564.5	0.0	226.9	491.6
25	0.7	0.0004	0.0125	566.9	0.0	227.9	539.3
26	0.9	0.0004	0.0139	569.2	0.0	228.8	587.3
27	1.1	0.0004	0.0153	571.6	0.0	229.8	635.6
28	1.3	0.0004	0.0166	573.9	0.0	230.7	684.4
Sum					**-84.2**	**2645.1**	**5026.2**

Table 5.14: Summary of the equivalent monolithic system wall forces.

N_w (kN)	F_c (kN)	F_{sc} (kN)	F_{st} (kN)	Sum (kN)
3750.9	-6636.8	-3737.2	6623.1	0.0

case, the bending moment was determined for the point corresponding to the resultant compressive force location. This meant, it was necessary to calculate the position of this point. Equation 5.39 was used to determine the distance from the resultant compressive force location to the most compressed concrete fibre, resulting in x_{cg}=0.334 m.

$$x_{cg} = \frac{\sum_{j=1}^{n} F_{scj}.d_{sj} + \sum_{i=1}^{m} F_{ci}.d_{ci}}{\sum_{j=1}^{n} F_{scj} + \sum_{i=1}^{m} F_{ci}} \tag{5.39}$$

where,

x_{cg} is the distance from the resultant compressive force to the compressed wall end;
F_{scj} is the compressive force on the bar j;
d_{sj} is the distance from the compressed bar j to the compressed wall end, $d_{sj} = |l_w/2 + z_j|$;
F_{ci} is the compressive force on the concrete fibre i;
d_{ci} is the distance from the concrete fibre i to the compressed wall end, $d_{ci} = |x - x_i|$.

Finally, the bending moment was calculated with equation 5.40, being the results summarised in Table 5.15. The bending moment resulted in M_t=24710.5 kNm, obtained using mean values, without safety factors. Comparing this value with the bending moment demand M_w=16894.5 kNm, a ratio M_t/M_w=1.46 was obtained, thus it can be said that the section has an global safety factor of 1.46. **?**, based on König et al. (1997), adopted an global safety factor for nonlinear analysis of 1.27, thus the obtained value was considered an adequate safety factor.

$$M_t = M_s + M_N = \sum_{j=1}^{n} F_{stj}.\left[z_j - \left(x_{cg} - \frac{l_w}{2}\right)\right] + N\left(\frac{l_w}{2} - x_{cg}\right) \tag{5.40}$$

where,

M_t is the total section bending moment;
M_s is the contribution of the steel bars to the bending moment;
M_N is the contribution of the axial load to the bending moment.

Table 5.15: Summary of the equivalent monolithic system wall bending moments.

M_S (kNm)	M_N (kNm)	M_t (kNm)	M_w (kNm)	M_t/M_w $-$
18459.8	6250.7	24710.5	16894.5	1.46

5.8 Post-Tensioned Hybrid system

The hybrid system has a prestressing force (and/or axial load) that allows the recentring of the wall and energy dissipaters that add moment and shear capacity to the wall, as well as structural damping. The energy dissipaters that were adopted for this solution were developed in Chapter 3 and in the hybrid wall system RM5 in Chapter 4. This system should be designed to have negligible residual displacements, which can be achieved by taking advantage of the recentring characteristics of the axial load due to gravity loads and to post-tensioning forces. The cross sections of all elements illustrated in Figure 5.4 are listed in Table 5.16.

Table 5.16: Concrete elements cross sections of the hybrid system.

		$\boldsymbol{Section(m^2)}$
Vertical elements	**C1**	1.00 x 0.25
	C2	0.25 x 0.70
	W1	0.25 x 4.00
Beams	**B1**	0.25 x 0.70
	B2	0.25 x 0.70
	B3	0.25 x 0.70

As for the equivalent monolithic system, the forces were calculated using a DDBD procedure. After obtaining the forces acting in the walls, the base cross section was designed and submitted to a design verification procedure. The design verification was carried out to check the wall base section response at design drift. To have a realistic response for the structure, mean values were used for the stress-strain relations and a final global safety factor was achieved.

5.8.1 Wall direction (transverse direction)

To implement the DDBD procedure in the wall direction, the equivalent SDOF system was determined. In wall hybrid systems, the wall is expected to remain elastic at the design drift and the displacements are mostly due to the rocking base rotation. As a result, at the design drift, a linear displacement profile was considered adequate, as was also considered in NZCS (2010). Equation 5.41 was used to calculate the displacements of the structure.

$$\Delta_i = \theta_d h_i \tag{5.41}$$

The design displacement, the effective mass and the effective height were obtained using equations 5.1, 5.2 and 5.3 (auxiliary calculations are presented in Table 5.17). These values are shown in Table 5.18.

With the basic SDOF system parameters, the design drift ratio was defined as 1.20% and was imposed taking into account the maximum displacements of the energy dissipaters selected for the system.

Table 5.17: DDBD calculations for the hybrid system in the wall direction.

Floor i	h_i (m)	m_i (ton)	Δ_i (m)	Δ_i^2 (m^2)	$\Delta_i \times m_i$ $(m \times ton)$	$\Delta_i^2 \times m_i$ $(m^2 \times ton)$	$\Delta_i \times m_i \times h_i$ $(m^2 \times ton)$
1	3	305.6	0.036	0.0013	11.0	0.40	33.0
2	6	305.6	0.072	0.0052	22.0	1.58	132.0
3	9	305.6	0.108	0.0117	33.0	3.56	297.0
4	12	305.6	0.144	0.0207	44.0	6.34	528.0
5	15	305.6	0.180	0.0324	55.0	9.90	825.1
6	18	291.4	0.216	0.0467	62.9	13.60	1133.1
Sum		1819.3			228.0	35.38	2948.2

Table 5.18: SDOF parameters for the hybrid system in the wall direction.

θ_d (%)	Δ_d (m)	m_e (ton)	h_e (m)
1.20	0.155	1468.9	12.9

5.8.1.1 Yield displacement and damping

For this system, the linear displacement profile assumed at the design drift, equation 5.41, cannot be used at yield, because at this point only a small rocking base rotation can be expected and the displacements are mostly due to the wall elastic deformation. Therefore another equivalent SDOF system was determined at yield to calculate the yield displacement. The displacement profile considered at yield was the same as the one used in the monolithic wall system. In (NZCS, 2010), this procedure was used for hybrid systems using reinforcement steel bars with unbonded lengths, and as the steel angles have a similar response, the same procedure was used in this case. There are two major differences in the behaviour of the hybrid and the monolithic systems. Firstly, in the hybrid systems, in order to reach the yield point, a base rotation is needed, resulting in a bigger yield displacement. Secondly, the prestressing forces of the hybrid systems makes the structure stiffer and consequently a smaller displacement is needed in order to reach the same yield point. In light of this, it seems appropriate that we should be able to use the same procedure as the one used in the monolithic wall systems. However, this should be evaluated in future research.

To calculate the equivalent viscous damping ratio, the displacement ductility was needed so the yield displacement was estimated. To calculate the yield displacement, referred to above, a similar procedure to the one used for the design displacement was

followed at yield. The displacements at yield, shown in Table 5.19, were calculated using the equation 5.27 for monolithic walls. The intermediate values computed in the determination of the yield displacement are also in the same table. Using equations 5.1, 5.3 and 5.29, the yield displacement, the effective height and ductility were obtained. The yield strain of the steel was obtained using the nominal yield stress of the steel angle material, $\sigma_y = 355$ MPa, as defined in Section 5.4. These values are shown in Table 5.20.

For the hybrid concrete wall, the equivalent viscous damping ratio was estimated with equation 5.42 (NZCS, 2010), where the parameter λ was the target recentring ratio that was chosen to equal 1.25. This parameter was calculated using equation 5.43, where M_N, M_p and M_a are the contributions of the axial load, post-tensioning and steel angles to the bending moment. Table 5.20 contains the data for the equivalent viscous damping ratio calculation (equation 5.42).

Table 5.19: DDBD calculations for the hybrid frame system at yielding in the wall direction.

Floor	h_i (m)	m_i (ton)	Δ_{yi} (m)	Δ_{yi}^2 (m^2)	$\Delta_{yi} \times m_i$ $(m \times ton)$	$\Delta_{yi}^2 \times m_i$ $(m^2 \times ton)$	$\Delta_{yi} \times m_i \times h_i$ $(m^2 \times ton)$
1	3	305.6	0.004	0.0000	1.1	0.00	3.3
2	6	305.6	0.014	0.0002	4.1	0.06	24.8
3	9	305.6	0.029	0.0008	8.7	0.25	78.5
4	12	305.6	0.047	0.0022	14.5	0.68	173.6
5	15	305.6	0.069	0.0047	21.0	1.44	314.8
6	18	291.4	0.091	0.0083	26.6	2.43	478.9
Sum		1819.3			76.0	4.86	1073.8

$$\xi_{eq} = 0.05 + 0.30\frac{\left(1 - \frac{1}{\sqrt{\mu}}\right)}{(\lambda + 1)} \tag{5.42}$$

$$\lambda = \frac{M_N + M_p}{M_a} \tag{5.43}$$

Table 5.20: Yield parameters and ξ_{eq} calculation for the hybrid system in the wall direction.

h_e (m)	e_y -	Δ_y (m)	Δ_d (m)	μ_δ (m)	ξ_{eq} (%)
14.1	0.0017	0.062	0.155	2.49	9.9

5.8.1.2 Base shear and forces distribution

To obtain the SDOF period, the response spectrum of Figure 5.10 was used, with the equivalent viscous damping ratio of Table 5.20. The effective stiffness was calculated with

equation 5.4 and the base shear with equation 5.5, the results being shown in Table 5.21. To return to the MDOF structure, the base shear was distributed between the floors according to equation 5.6 resulting in the forces F_i shown in Table 5.22. With the forces acting on each floor, the internal forces were calculated.

Table 5.21: Wall base shear for the hybrid system.

T_e (s)	K_e (kN/m)	V_B (kN)
1.52	25098.7	3895.2

Table 5.22: Wall forces distribution for the hybrid system.

Floor	h_i (m)	m_i (ton)	Δ_i (m)	$\Delta_i \times m_i$ $(m \times ton)$	F_i (kN)
1	3	305.6	0.036	11.0	188.0
2	6	305.6	0.072	22.0	375.9
3	9	305.6	0.108	33.0	563.9
4	12	305.6	0.144	44.0	751.9
5	15	305.6	0.18	55.0	939.9
6	18	291.4	0.216	62.9	1075.6
Sum		1819.3		228.0	3895.2

5.8.1.3 Internal forces

As for the equivalent monolithic system, it was assumed that the seismic action was resisted by the walls alone, being considered as cantilever structures with the forces applied at the floor levels. The shear forces and bending moments are shown in Figures 5.15a and 5.15b. The resulting base reactions were V_w=1947.6 kN for the base shear and M_w=25188.4 kNm for the bending moment in each wall.

The calculations for the axial load at the base were presented for the equivalent monolithic system. The resulting value was N_w=3750.9 kN.

5.8.1.4 Cross section design

The total bending moment of 25188.4 kNm was estimated taking into account the assumption of a recentring ratio equal to $\lambda = 1.25$. According to NZS3101 (2006), λ should not be less than 1.15 and a value of 1.25 was used in the design example included in NZCS (2010). To be able to fulfill that purpose, the moment ratio parameters from equations 5.45 and 5.44 (NZCS, 2010) should be satisfied. For a recentring ratio of $\lambda = 1.25$, the parameters result in $\alpha_{OTM} = 0.56$ and $\beta_{OTM} = 0.44$. Using these parameters, the bending

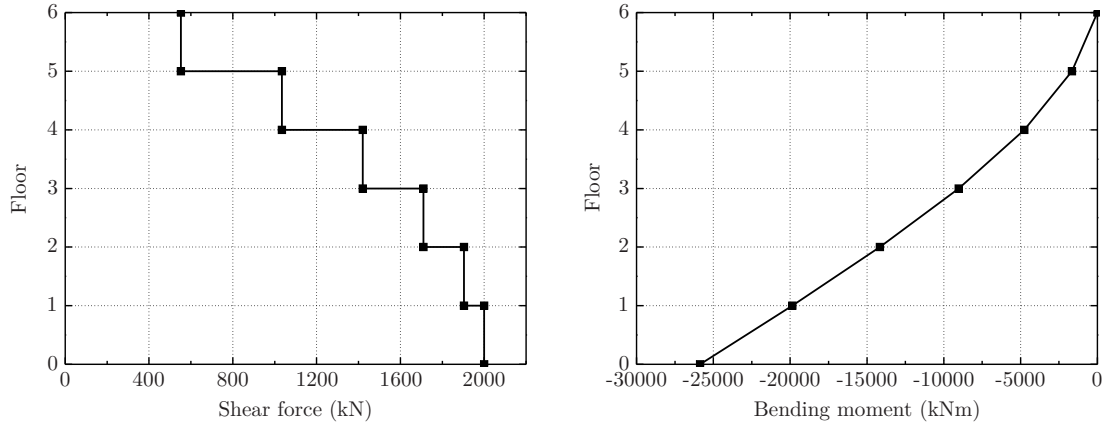

(a) Storey shear forces. **(b)** Overturning bending moments.

Figure 5.15: Wall internal forces for the hybrid system in each wall.

moment was divided into two parts, one for the unbonded post-tensioning with axial load ($M_p + M_N$) and the other for the energy dissipaters (M_a). The moments for each part were $M_p + M_N = 13993.6\ kNm$ and $M_a = 11194.9\ kNm$

$$\alpha_{OTM} = \frac{M_p + M_N}{M_w} = \frac{\lambda}{\lambda + 1} \tag{5.44}$$

$$\beta_{OTM} = \frac{M_a}{M_w} = \frac{1}{\lambda + 1} \tag{5.45}$$

For the design of the cross section, some assumptions were made. The compression zone was considered to be along a length of $x = 0.25 l_w = 1\ m$ and the the lever arm between tensile and compressive forces to equal $z_a = 0.85 d_a$, being d_a the distance between the centroid of the steel angles and the most compressed concrete fibre. These assumptions should be verified as the response of the section strongly depend on them. This verification is in Section 5.8.1.6. This design not only needs to guarantee the structural safety, but also the recentring ratio to ensure the desired response behaviour.

Design of the steel angles

To estimate the demand force in the steel angles, a mean displacement was calculated and the force in all angles was assumed to be equal. The design was made by fixing the position and length of the angles and then choosing the angle design detail for the demand force. The Figure 5.17 shows that a 1.25 m line of 10 steel angles may be fixed on both sides of the of the wall ends. Each steel angle was connected to a plate anchored in the wall by four M20 class 8.8 bolts. The steel angles were fixed to the foundations with another set of four M20 class 8.8 bolts for each one. The option to have several smaller steel angle instead of one was to have a more redundant system. Having several angles

minimises the risk of a local rupture, in the maximum displacement zone, to spread to the other angles with smaller displacements. Table 5.23 shows the total tensile demand force in the angles considering the referred assumptions, where the force was obtained with the equation 5.46.

$$F_a = M_a / z_a \tag{5.46}$$

Table 5.23: Steel angles total tensile force demand.

$\boldsymbol{d_a(m)}$	3.375
$\boldsymbol{z(m)}$	2.869
$\boldsymbol{M_a(kNm)}$	11194.9
$\boldsymbol{F_a(kN)}$	3902.3
$\boldsymbol{F_a/angle(kN)}$	195.1

To evaluate the force in the angles, a displacement estimation was needed, as the force of the angles strongly depend on this displacement. To estimate this displacement, besides the referred assumptions, the base rotation θ was assumed equal to the structure rotation, therefore $\theta = \theta_d$. Using equation 5.47, the mean angle displacement d was calculated and the results are presented in Table 5.24.

$$d = \theta \times (d_a - x) \tag{5.47}$$

Table 5.24: Steel angles mean demand displacement.

$\boldsymbol{x(m)}$	1
$\boldsymbol{\theta}(\%)$	1.20
$\boldsymbol{d(m)}$	0.0285

The choice of an adequate angle for the design had to take into account the angle profiles and the grades of steel that can be found in the market. The expected failure displacement and the strength force also had to be considered. The option was for an angle L250x250x23 detailed in Figure 5.16. The procedure to find the correct angle was keeping the dimensions of angle constant and changing distance g until the force for the displacement d_a corresponded to the desired one. The angles response force was calculated using equation 3.15 obtained in Chapter 3 and the result is shown in Table 5.25. The steel grade of the angle was S355 and the nominal values were used (Figure 5.7).

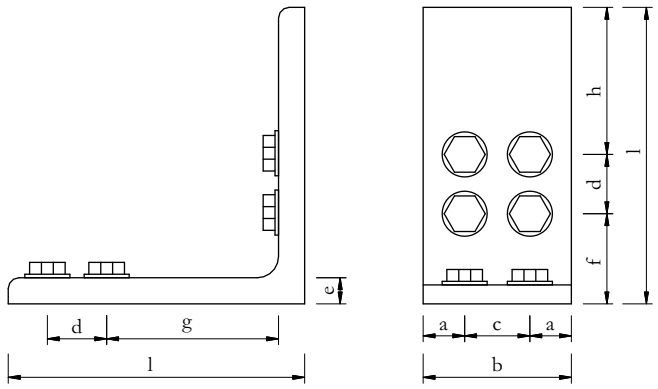

Distance	Value (m)
a	0.035
b	0.125
c	0.055
d	0.050
e	0.023
f	0.076
g	0.145
h	0.124
l	0.250

Figure 5.16: Steel angle detail for the hybrid system.

Table 5.25: Steel angle mean demand force.

d_a	ε_{max}	$\sigma(\varepsilon_{max})$	α	a	F_H	F_d
(m)	-	(MPa)	-	-	(kN)	(kN)
0.0285	0.117	436.8	1.23	2	395.6	214.9

Design of the post-tensioning steel

To estimate the post-tensioning bar forces, a mean displacement was calculated and the force in all bars was assumed equal. Figure 5.17 shows the position of the bars, centred in the middle of the wall cross section.

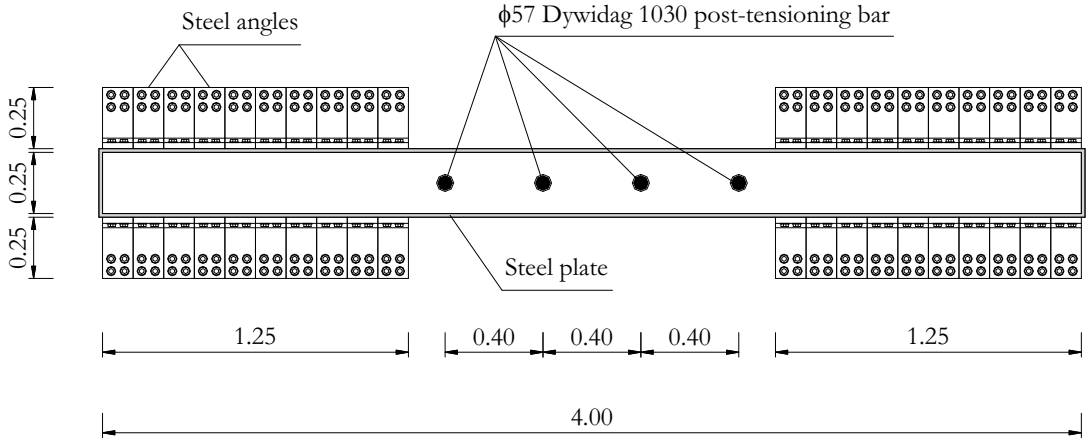

Figure 5.17: Wall base section detail for the hybrid system. (Dimensions in metres)

Table 5.26 shows the total tensile demand force in the post-tensioning bars, where the force was obtained with the equation 5.48. The post-tensioning force lever arm was calculated with equation 5.49. This lever arm was obtained from the lever arm of forces acting on the steel angles z_a.

Table 5.26: Demand force in the post-tensioning bars.

$\boldsymbol{d_p(m)}$	2
$\boldsymbol{z_p(m)}$	1.494
$\boldsymbol{M_p(kNm)}$	13993.6
$\boldsymbol{N(kN)}$	3750.9
$\boldsymbol{Fp(kN)}$	5617.1

$$F_p = M_p/z_p - N \tag{5.48}$$

$$z_p = z_a - (d_a - d_p) \tag{5.49}$$

From the calculated post-tensioning force, the chosen solution was to use 4 Dywidag 1030 bars with a diameter of 57 mm. These bars present a characteristic 0.1% proof-stress of 835 MPa and a modulus of elasticity of 205 GPa.

To obtain the mean displacement in the post-tensioning bars, equation 5.50 was used.

$$d = \theta \times (d_p - x) \tag{5.50}$$

The elongation of the bars can be obtained by calculating the wall displacement at their position, thus the stress increment in the bars was calculated by equation 5.51, resulting in a force increment obtained from equation 5.52.

$$\Delta\sigma_p = \frac{d}{l_{ub}} E_p \tag{5.51}$$

$$\Delta F_p = \Delta\sigma_p A_p \tag{5.52}$$

Knowing the total demand force and the increment during rotation, the initial post-tensioning force was estimated from equation 5.53.

$$F_{pi} = F_p - \Delta F_p \tag{5.53}$$

Table 5.27 summarises the results from the referred equations to make it possible to define an initial post-tensioning force. According to the calculations, the initial force should be 49.5% of the characteristic 0.1% proof-force. To control the recentring behaviour of the wall accounting for the overstrength of the chosen steel angles solution

Table 5.27: Demand post-tensioning force for in the post-tensioning bars.

$\boldsymbol{\theta}(\%)$	1.20
$\boldsymbol{d(m)}$	0.012
$\boldsymbol{l_{ub}(m)}$	18.0
$\boldsymbol{E_p(GPa)}$	205.0
$\boldsymbol{\Delta\sigma_p(MPa)}$	136.7
$\boldsymbol{Number\ of\ bars}$	4
$\boldsymbol{A_p/bar(m^2)}$	0.00255
$\boldsymbol{\Delta F_p(kN)}$	1395.0
$\boldsymbol{F_{pi}(kN)}$	4222.2
$\boldsymbol{F_{pi}/F_{p0.1k}}(\%)$	49.5

(overstrength=(214.9-195.1)/195.1x100=10.1%), a higher initial post-tensioning force should be applied and 55% of the characteristic 0.1% proof-force was adopted.

With an initial force equal to 55% of the characteristic 0.1% proof-force, the final expected force should be verified. The maximum allowed force, according to NZS3101 (2006), should be 90% of the characteristic 0.1% proof-force. Table 5.28 shows the results for the calculation of the final force at design displacement. These results correspond to the sum of all the forces in the post-tensioning bars, thus the tension force in the most tensioned bar should be calculated and compared with 90% of the characteristic 0.1% proof-force. This calculation was made in the cross section design verification process (see Section 5.8.1.6).

Table 5.28: Final force in post-tensioning bars.

$\boldsymbol{Number\ of\ bars}$	4
$\boldsymbol{A_p/bar(m^2)}$	0.00255
$\boldsymbol{f_{p0.1k}(MPa)}$	835
$\boldsymbol{F_{p0.1k}}(kN)$	8522.9
$\boldsymbol{F_{pi}/F_{p0.1k}}(\%)$	55
$\boldsymbol{F_p}(kN)$	6082.5

5.8.1.5 Cross section above the base

The detailing of the post-tensioned reinforced concrete cross section above the base was made taking into account the steel angles in the base section. The 10 steel angles on each side of the wall were in a 1.25 m long row width and a total force of 20x214.9=4298.0 kN. To provide continuity to this force, 34 A500NR steel bars with 20 mm diameter were distributed along the 1.25 m length, corresponding to a total design strength of 4646.4 kN. This section detailing is shown in Figure 5.18.

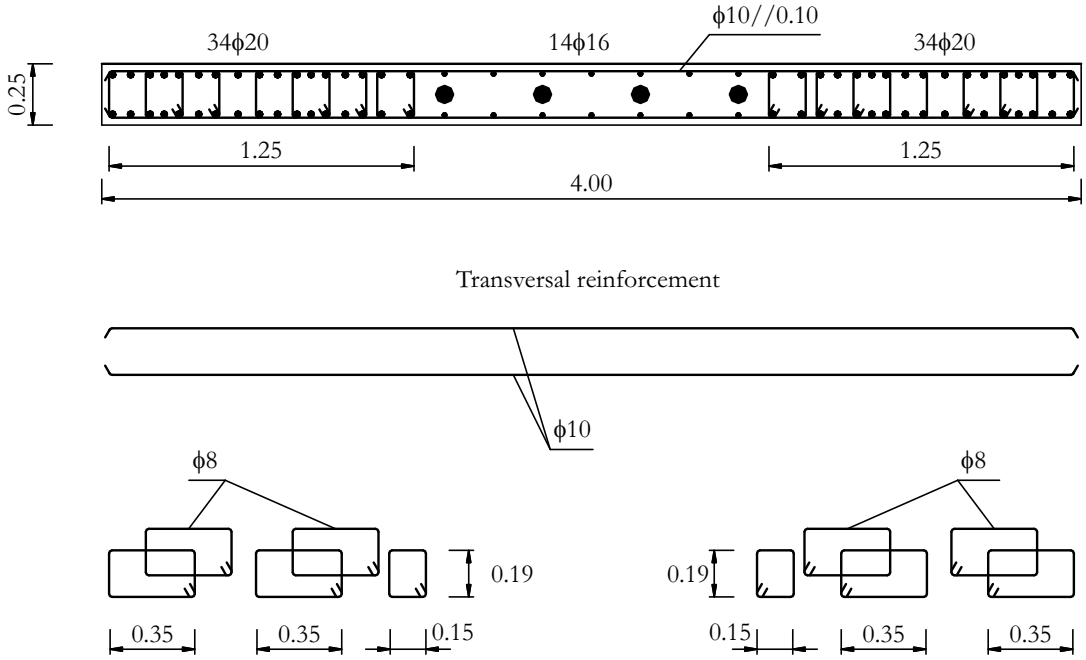

Figure 5.18: Wall section detailing above the base section for the hybrid system.

5.8.1.6 Cross section design verification

To carry out the verification of the cross section design, the opening gap was determined and the forces acting in each angle were obtained, as well as the compressive forces in the concrete. For the stress-strain relations, mean values were used for the concrete and nominal values were used for the steel of the angles.

Base rotation / opening gap

To estimate the opening gap between the wall and the foundation, the elastic displacements should be subtracted from the design drift displacements. The opening gap results from the rotation after yielding. Table 5.29 shows the plastic displacements, the results of the difference between the displacements for the design drift (Table 5.17) and the displacements at yield (Table 5.19). Taking into account the plastic displacements, the opening gap was calculated from the drift of the first floor, resulting in a base rotation of 1.08%.

Cross section bending moment

As done for the equivalent monolithic system to quantify the resistant bending moment, an initial neutral axis depth was estimated before all the forces are determined and then the section equilibrium was established. The neutral axis depth was adjusted until the equilibrium was achieved.

Table 5.29: Design wall rotation for the hybrid system.

Floor i	Design displacements, Δ_i (m)	Yield displacements, Δ_{yi} (m)	Plastic displacements, Δ_{pi} (m)	Gap opening, θ
1	0.036	0.004	0.032	1.08%
2	0.072	0.014	0.058	
3	0.108	0.029	0.079	
4	0.144	0.047	0.097	
5	0.180	0.069	0.111	
6	0.216	0.091	0.125	

After the iterative procedure, the final neutral axis depth was x=0.872 m.

To compute the compressive strains in the concrete, a theoretical curvature was considered based on the studies of Pampanin et al. (2001) and Palermo (2004), as mentioned in Chapter 4. Equation 5.54 was used to determine the curvature, where θ_{imp} is the base rotation and ϕ_y was estimated with equation 5.33. The l_{cant} is the effective height, that was estimated and showed in Table 5.30. The plastic hinge length was estimated with equation 5.35.

$$\phi = \frac{3\dfrac{\theta_{imp}}{l_{cant}} - (\phi_y - \phi_{dec})}{\dfrac{3l_p}{l_{cant}}\left(1 - \dfrac{l_p}{2l_{cant}}\right)} + \phi_y \tag{5.54}$$

The decompression curvature was calculated with equation 5.55. Table 5.30 shows the theoretical curvature calculation for the hybrid system.

$$\phi_{dec} = \frac{2(N_w + F_{pi})}{E_c A_g l_w} \tag{5.55}$$

Table 5.30: Theoretical curvature calculation for the hybrid system

θ_{imp} (%)	l_{cant} (m)	l_p (m)	ϕ_y	ϕ_{dec}	ϕ
1.08	12.9	1.432	0.00089	0.00013	0.00646

Table 5.31 shows the forces for each concrete fibre. The A_i is the area of fibre i and the ε_{ci} the strain of fibre i determined using equation 5.38. All the concrete in the cross section was considered to be confined, using the method described in Section 5.4 for confinement with concrete cover protection, to determine the stress in each fibre σ_{cci}. With the stress and the fibre area, the force in each fibre F_{ci} was determined.

To determine the compressive stress-strain relation for the concrete, the base section detailing in Figures 5.17 and 5.18 was considered. As the transversal steel reinforcement was similar along the 1.25 m and the obtained compression zone length was x=0.872 m, the compressive stress-strain relation was considered to be equal in the whole compression zone. From the confinement method referred to herein a concrete strength enhancement factor of k_c=1.30 was obtained. Finally, a total concrete reaction of 8559.8 kN was obtained.

Table 5.31: Concrete compressive forces for the hybrid system at design drift.

Fibre ***i***	A_i (m^2)	x_i (m)	ε_{ci} -	σ_{cci} (MPa)	F_{ci} (kN)
1	0.0073	0.015	-0.0001	-3.1	-22.2
2	0.0073	0.044	-0.0003	-8.9	-64.7
3	0.0073	0.073	-0.0005	-14.3	-103.8
4	0.0073	0.102	-0.0007	-19.1	-139.1
5	0.0073	0.131	-0.0008	-23.5	-170.5
6	0.0073	0.160	-0.0010	-27.3	-198.2
7	0.0073	0.189	-0.0012	-30.6	-222.5
8	0.0073	0.218	-0.0014	-33.5	-243.6
9	0.0073	0.247	-0.0016	-36.0	-262.0
10	0.0073	0.276	-0.0018	-38.2	-277.9
11	0.0073	0.305	-0.0020	-40.1	-291.5
12	0.0073	0.334	-0.0022	-41.7	-303.3
13	0.0073	0.363	-0.0023	-43.1	-313.3
14	0.0073	0.392	-0.0025	-44.3	-321.9
15	0.0073	0.422	-0.0027	-45.3	-329.2
16	0.0073	0.451	-0.0029	-46.1	-335.3
17	0.0073	0.480	-0.0031	-46.8	-340.5
18	0.0073	0.509	-0.0033	-47.4	-344.8
19	0.0073	0.538	-0.0035	-47.9	-348.3
20	0.0073	0.567	-0.0037	-48.3	-351.2
21	0.0073	0.596	-0.0038	-48.6	-353.6
22	0.0073	0.625	-0.0040	-48.9	-355.4
23	0.0073	0.654	-0.0042	-49.1	-356.8
24	0.0073	0.683	-0.0044	-49.2	-357.8
25	0.0073	0.712	-0.0046	-49.3	-358.5
26	0.0073	0.741	-0.0048	-49.4	-358.9
27	0.0073	0.770	-0.0050	-49.4	-359.1
28	0.0073	0.799	-0.0052	-49.4	-359.0
29	0.0073	0.829	-0.0054	-49.4	-358.7
30	0.0073	0.858	-0.0055	-49.3	-358.3
Sum					**-8559.8**

The forces acting in the steel angles are shown in Table 5.32 as well as their bending moments contribution. There were steel angles under tension and others under compression. To estimate the steel angles under tension, equation 3.15 was used, considering the parameter a to be equal to 2. The value for the horizontal force F_H was 395.6 kN, as each angle had a length of 0.125 m. The tensile force F_{atj} in the table corresponds to two angles, one on each side of the wall. To calculate the steel maximum stress σ_{max} the stress-strain relation defined in Section 5.4 was used using nominal values the steel S355 grade. To estimate the compression forces in the angles located in the compression zone, F_{acj}, the strain in the vertical legs was assumed equal to the adjacent concrete strain. With the compressive strain in the angle, the force was calculated considering the vertical leg under compression with the maximum value limited by the shear strength of the bolts. Each angle was designed with four M20 class 8.8 bolts, corresponding to a nominal shear yield strength of 470.4 kN.

Table 5.32: Contribution of the steel angles to the bending moment.

Angle j	z_j (m)	d (m)	ε_{max}	σ_{max} (MPa)	α	F_{atj} (kN)	ε_{acj}	F_{acj} (kN)	M_{atj} (kNm)
1	1.938	0.033	0.1350	449.6	1.27	467.4	-	-	830.9
2	1.813	0.032	0.1297	445.9	1.26	456.4	-	-	782.9
3	1.688	0.030	0.1244	442.1	1.25	445.4	-	-	736.2
4	1.563	0.029	0.1191	438.4	1.23	434.4	-	-	690.8
5	1.438	0.028	0.1138	434.6	1.22	423.3	-	-	646.8
6	1.313	0.026	0.1084	430.8	1.21	412.3	-	-	604.2
7	1.188	0.025	0.1030	426.9	1.20	401.3	-	-	562.9
8	1.063	0.024	0.0976	423.1	1.19	390.2	-	-	523.0
9	0.938	0.022	0.0921	419.2	1.18	379.1	-	-	484.5
10	0.813	0.021	0.0867	415.3	1.17	368.1	-	-	447.4
11	-0.813	0.003	0.0142	363.9	1.03	223.6	-	-	90.1
12	-0.938	0.002	0.0086	359.9	1.01	212.5	-	-	72.3
13	-1.063	0.001	0.0029	355.9	1.00	201.3	-	-	56.0
14	-1.188	-0.001	-	-	-	-	0.0004	-465.0	-
15	-1.313	-0.002	-	-	-	-	0.0012	-940.8	-
16	-1.438	-0.003	-	-	-	-	0.0020	-940.8	-
17	-1.563	-0.005	-	-	-	-	0.0028	-940.8	-
18	-1.688	-0.006	-	-	-	-	0.0036	-940.8	-
19	-1.813	-0.007	-	-	-	-	0.0044	-940.8	-
20	-1.938	-0.009	-	-	-	-	0.0052	-940.8	-
Sum						**4815.1**		**-6109.8**	**6528.0**

To calculate the final prestressing force in each bar, it was necessary to calculate the displacement d corresponding to the elongation of each one. Having the base rotation, the neutral axis depth and the bar position, the displacement was calculated with equation 5.50. With the elongation and assuming the length of the bars length to be equal to

the wall height, $h_n = 18\ m$, the strain increment was calculated as well as the force increment ΔF_p. Adding the force increment to the initial post-tensioning force F_{pi}, the installed force F_p was obtained for the design drift (equation 5.56). Finally, verification was made to evaluate if the installed force did not exceed the desired limit of $0.9F_{p0.1k}$. Table 5.33 presents the prestressing forces and the total force of 6103.6 kN was achieved with a maximum bar force reaching 89.4% of $0.9F_{p0.1k}$. In this table, the contribution of each bar for the bending moment was also included, as will be explained later.

$$F_p = F_{pi} + \Delta F_p = F_{pi} + \frac{d}{h_n} E_p A_p \tag{5.56}$$

Table 5.33: Calculations for the post-tensioning forces in the bars.

Bar	$\boldsymbol{x}$ $(\boldsymbol{m})$	$\boldsymbol{d}$ $(\boldsymbol{m})$	$\boldsymbol{F_{pi}}$ $(\boldsymbol{kN})$	$\boldsymbol{\Delta F_p}$ $(\boldsymbol{kN})$	$\boldsymbol{F_p}$ $(\boldsymbol{kN})$	$\boldsymbol{F_p/0.9F_{p0.1k}}$ (%)	$\boldsymbol{M_p}$ $(\boldsymbol{kNm})$
1	0.60	0.006	1171.9	165.7	1337.6	69.8	1362.1
2	0.20	0.010	1171.9	291.2	1463.1	76.3	2075.2
3	-0.20	0.014	1171.9	416.8	1588.7	82.8	2888.7
4	-0.60	0.019	1171.9	542.3	1714.2	89.4	3802.7
Sum			**4687.6**		**6103.6**		**10128.8**

Table 5.34 summarises the total forces in the wall cross section. The forces presented are the axial load demand N_w, the concrete compressive force F_c, the sum of all compressive forces in the steel angles F_{ac}, the sum of all tensile forces in the steel angles F_{at} and the sum of the bars post-tensioning forces $\boldsymbol{F_p}$. From these forces it can be seen that the obtained solution is correct.

Table 5.34: Summary of the hybrid system wall forces.

$\boldsymbol{N_w}$ $(\boldsymbol{kN})$	$\boldsymbol{F_c}$ $(\boldsymbol{kN})$	$\boldsymbol{F_{ac}}$ $(\boldsymbol{kN})$	$\boldsymbol{F_{at}}$ $(\boldsymbol{kN})$	$\boldsymbol{F_p}$ $(\boldsymbol{kN})$	$\boldsymbol{Sum}$ $(\boldsymbol{kN})$
3750.9	-8559.8	-6109.8	4815.1	6103.6	0.0

As in the equivalent monolithic system, the bending moment was determined for the point corresponding to the resultant compressive force, thus it was necessary to calculate the position of this point. Equation 5.57 was used to determine the distance from the resultant compressive force to the compressed wall end, resulting in x_{cg}=0.382 m.

$$x_{cg} = \frac{\sum_{j=1}^{n} F_{acj}.d_{aj} + \sum_{i=1}^{m} F_{ci}.d_{ci}}{\sum_{j=1}^{n} F_{acj} + \sum_{i=1}^{m} F_{ci}} \tag{5.57}$$

where,

x_{cg} is the distance from the resultant compressive force to the compressed wall end;
F_{acj} is the compressive force on the steel angles j;
d_{aj} is the distance from the compressed steel angle j to the compressed wall end, $d_{aj} = |l_w/2 + z_j|$;
F_{ci} is the compressive force on the concrete fibre i;
d_{ci} is the distance from the concrete fibre i to the compressed wall end, $d_{ci} = |x - x_i|$.

Finally, the bending moment was calculated with the equation 5.58, the results being summarised in Table 5.35. The bending moment resulted in M_t=28998.5 kNm, obtained using nominal values for the steel angles and mean values for the concrete. Comparing this value with the bending moment demand M_w=25188.4 kNm, a ratio M_t/M_w=1.15 was obtained, thus it can be said that the section has an global safety factor of 1.15. According to EC3 (EN 1993-1-1, 2005) the safety factors of the steel angles should be 1.0. The concrete has a safety factor of 1.5 but has little influence on the bending moment value. Therefore, 1.15 was considered to be an adequate global safety factor for the system.

$$M_t = M_a + M_N + M_p \tag{5.58}$$

being :

$$M_a = \sum_{j=1}^{n} F_{atj}. \left[z_j - \left(x_{cg} - \frac{l_w}{2} \right) \right]$$

$$M_N = N \left(\frac{l_w}{2} - x_{cg} \right)$$

$$M_p = \sum_{m=1}^{n} F_{p,m}. \left[z_m - \left(x_{cg} - \frac{l_w}{2} \right) \right]$$

where,

M_t is the total section bending moment;
M_a is the contribution of the steel bars to the bending moment;
M_p is the contribution of the steel bars to the bending moment;
M_N is the contribution of the axial load to the bending moment;
$F_{p,m}$ is the force installed in the post-tensioning bar m.

Table 5.35: Summary of the hybrid system wall bending moments.

M_a (kNm)	M_N (kNm)	M_p (kNm)	M_t (kNm)	λ	M_w (kNm)	M_t/M_w $-$
12799.4	6070.3	10128.8	28998.5	1.27	25188.4	1.15

Analysing the section response, the resulting recentring ratio was 1.27, very close to the targeted value 1.25. This difference can be neglected with no need to update the calculations for a recentring ratio of 1.27.

5.9 Discussion of the results and conclusions

The maximum displacement demand expected for the steel angles was 0.033 m, as shown in Table 5.32. The cyclic maximum displacement allowable for the prescribed angle was not determined and more experimental tests should be made in this area. The maximum displacement depends essentially on the thickness of the angles, the type of steel, the distance of the first line of bolts to the vertical leg (distance g in Figure 5.16) and on the demand cycles.

In the experimental tests described in Chapters 3 and 4, the steel angles with similar setup achieved maximum displacements of 0.030 m and 0.023 m in the tensile testing machine and in the wall test, respectively. Taking into account that the tested specimens had a distance g of 0.089 m instead of the 0.145 m of the solution in this example, this last setup should sustain much higher displacements. From EN 10025-2 (2004), the minimum percentage elongation after fracture of the S355 steel should be 22% and for the S275 steel 23%, so the difference between the tested angles (S275) and the prescribed ones (S355) in this case study can be neglected. The last parameter to be considered should be the thickness of the steel angles. In the tests this was 0.016 m whilst in the case study it was 0.023 m so a smaller maximum displacement can be expected. Taking all this parameters into account, the displacement of 0.033 m it is expected to be smaller than the rupture displacement for the steel angles used in this case study.

The objective of this chapter was to show an example of a hybrid system design as tested in Chapter 4. The system tested was a wall submitted to cyclic displacements, being the bending moment due to post-tensioning and external steel angles. The main purpose of the post-tensioning was the recentring of the wall, whilst the role of the steel angles was to dissipate energy.

For this case study, a regular structure was considered. This structure had a frame system in one direction and a wall system in the other direction. Due to the scope of the present study, only the wall direction was designed. To compare with a possible

traditional solution, an equivalent monolithic system was also considered in the case study. The traditional solution would always have a higher damping, leading to a solution with smaller forces. The hybrid solution should have negligible residual displacements with little damage after a seismic action. The expected damage for this hybrid solution is confined to the steel angles, which are easy to replace.

In the case study presented in this chapter, the forces for the hybrid system were considerably higher than for the equivalent monolithic system. This difference was not only due to the differences between the systems, but also due to the smaller design drift imposed in the hybrid system. This smaller design drift was needed to limit the maximum displacement of steel angles. These higher forces lead to a hybrid wall with more reinforcement than was desired with regard to the steel angles and the post-tensioning. A more optimised solution would have been to have a longer wall for the hybrid system, however it was decided to use a wall with the same dimensions as for the equivalent monolithic solution.

If a longer wall had been used it could have been necessary to change the locations of the steel angles. In this case study, the option was to have the angles located near the edges of the wall, where the lever arm is longer. With this option, the bending moment that each angle mobilises for the wall forces is maximised as well as the displacement. A higher displacement has the advantage of leading to higher forces acting in the angles but increases the demand on ductility. If the option had been to have all the angles in the middle of the wall base cross section, the lever arm would have been smaller, but more angles would have been under tension, leading to a higher force. Hereupon, it can be concluded that it is possible to have a similar bending moment with the angles located in the middle of the cross section. With this last option the angles would have a lower demand on ductility.

Chapter 6

Summary, conclusions and future work

6.1 Summary and conclusions

Post-tensioned rocking walls solutions with and without energy dissipaters under seismic actions were studied. The post-tensioned solutions without energy dissipaters are walls connected to the foundation using post-tensioning systems alone. The solutions with energy dissipaters (or hybrid solutions) result from the combination of an elastic response and a plastic response. The elastic response derives from the post-tensioning force and the axial force in the wall. The post-tensioning force is designed to remain in the elastic range during the seismic action. The plastic response comes from the plastic behaviour of energy dissipaters. The energy dissipaters increase the damping of the structure and remain with plastic deformations after an earthquake. The objective of the design is to balance these two components in a way that the structure will return to the initial position, remaining with negligible residual displacements.

The behaviour of these systems, during the seismic action, is characterised by rotations of the wall base in relation to its foundation, that results in relative displacements (gaps) between the wall base and the foundation. The post-tensioning steel should have an unbonded length to accommodate the connection relative displacement in the elastic range. The energy dissipaters have to be designed to follow the connection relative displacements. Several energy dissipater solutions have already been studied and some are implemented in real buildings. The energy dissipaters can be used internally as common reinforcing bars with an unbonded length, using similar bars fixed externally to the wall and to the foundation or even between walls in coupled wall systems.

In this study, the post-tensioning force was applied with two straight unbonded strands

and the energy dissipaters used were steel angles externally fixed to the wall and to the foundation. This external energy dissipater solution was chosen for being easy to replace after an earthquake. The steel angles are also easy to find in steel suppliers and to adjust for the desired function.

The experimental study was divided into two phases, the first being the development of the steel angle solutions and the second was the experimental tests on the rocking walls. The research on the steel angle solutions aimed to reach a stable cyclic behaviour with forces in the order of magnitude needed for hybrid walls. The rocking wall test research had the purpose of testing the hybrid solutions using the developed energy dissipaters. The hybrid rocking wall solutions should respond with the desired strength and be able to recover from the deformed position with negligible residual displacements.

The experimental studies were complemented by numerical and analytical models to support the experimental work and to predict the responses of the systems. In the steel angles research a finite elements program was used to model the tests and an analytical procedure was presented for design purposes. In the rocking walls research, analytical models were used to predict the response of the tests and as a design proposal.

Finally, a case study is presented to exemplify the application of these systems to a real structure. The comparison between a equivalent monolithic system and a precast hybrid system was made and a displacement-based designed procedure was used to estimate the seismic forces acting in the structure.

6.1.1 Steel angles

The steel angles were studied to work as external energy dissipaters in the post-tensioned hybrid systems. From the literature review different solutions were found but some doubts remained as for the ideal one to be used for cyclic actions. As this study was centred on walls, the preliminary calculations resulted in the need for steel angles with significative forces acting on them. For this reason the angles had to be thick and with small gage lengths (the distance between the bolt in the horizontal leg and the heel of the angle). These angles have prying forces that are difficult to control and limited ductility.

The steel angles were designed to have a failure mode caused by flexure and never by bolt failure. For this reason the bolts were oversized, either those mainly under tension forces or those mainly under shear forces.

To optimise the behaviour and increase the efficiency of the angles as energy dissipaters, several solutions were tested experimentally and numerically. The traditional solution described in the literature to fix the angles to the base is to use only one line of bolts in the horizontal leg of the angles. With only one line of bolts, when a tensile displacement

is applied to the angle, the edge of the horizontal leg of the angles is compressed against the base and the leg goes into the plastic range. After the reaching of the maximum displacement, the movement is reversed and the edge of the leg lifts, persisting its plastic deformation at the end of the cycle. In the following cycle the plastic hinge that had occurred in the line of the bolts will not develop any bending moment until the edge of the leg touches the base. This reduces the energy dissipation of the system. To solve this problem the first choice was to use a washer plate and to oversize the bolts, but the stiffness of this set was not sufficient. Two solutions were tested to eliminate this prying effect: the first one was to weld the edge to the base and the second one was to have a second line of bolts. The first solution is usually avoided to eliminate the need for welding on a construction site but may be necessary when small angles are used. The second solution is recommended for construction site assembly but requires larger angles. The welding has the disadvantage of restraining not only the vertical displacement to the base, but also the horizontal displacements, resulting in higher tensions in the legs.

The two final solutions that presented the desired cyclic behaviour were designed to have similar strength. As the thicknesses of the angles were different, this was compensated by changing the position of the bolts. The forces acting on both steel angle solutions were similar but the maximum displacement was different for the reasons mentioned above. The solution with the welding along the edge reached a displacement of 20 mm while the solution with the second line of bolts reached 30 mm. This difference is significant and can condition the use of the solution with the welding in structural applications. It must be mentioned that this displacement depends on the parameters chosen for the angles, namely the thickness, the steel grade and the position of the bolts as well as the displacement demand of the structure to which these elements are designed for.

6.1.2 Post-tensioned concrete walls

Three preliminary post-tensioned wall tests were carried out followed by two tests on post-tensioned hybrid wall solutions and a final test on a post-tensioned wall. To design these tests a design drift ratio of 2.0% was considered, and the post-tensioning forces at this level of displacement should correspond to the steel stress values close to the characteristic 0.1% proof-stress. Due to the short length of the strands and the corresponding high stiffness, the maximum initial post-tensioning force was conditioned and the maximum drift ratio was also limited.

The preliminary tests (wall specimens RM1, RM2 and RM3) were made with the purpose of testing and optimising the laboratory setup. The post-tensioned solutions were walls with rocking behaviour, connected to the foundation with two post-tensioning strands. The first two specimens, RM1 and RM2, were post-tensioned reinforced concrete walls. The third specimen, RM3, was a post-tensioned reinforced concrete wall including

two resin and cork wedges with the purpose of dissipating energy. Due to a scaling problem, the resin and cork did not respond as expected and there was no significative energy dissipation. In all specimen preliminary tests, low energy dissipation was obtained and no residual displacements were registered. These walls had an almost perfect elastic response, with little spalling of the cover concrete. The main problems faced were the instability in the transversal direction and the loss of post-tensioning forces during the tests. The lateral instability is a laboratory problem as in real structures there is a 3D behaviour that braces the wall in the transversal direction. This problem limited the maximum displacements reached in these tests and was solved in the following tests. The loss of post-tensioning forces that emerged was essentially due to the small length of the strands. The short length of the strands also resulted in high increments in the elongations of the strands with the drift ratio increments. This problem has little importance as in real structures, the length of the strands is expected to be much longer.

The two hybrid wall solutions tested used the two angles described above, one with welding along the edge (wall specimen RM4) and the other one with a second line of bolts (wall specimen RM5).

The wall specimen RM4 reached a maximum drift ratio of about 2.5%. At this drift ratio the shear force was declining. The post-tensioning strands had losses for a drift ratio of 2% that were 6% and 10% in the southern and northern strands, respectively. For the final cycles, the maximum post-tensioning force was 223.7 kN. The angles reached a maximum displacement of about 17.5 mm, showing visible cracks (Figure 4.74). The equivalent viscous damping ratio reached was 12.5% for a drift ratio of 2%.

The wall specimen RM5 reached a maximum drift ratio of approximately 3.0%. At this drift ratio the shear force was declining. The post-tensioning strands had losses for a drift ratio of 2% that were 4% and 6% in the southern and northern strands, respectively. These losses increased to 27% and 25%, as the displacements imposed on this specimen led to post-tensioning forces beyond the characteristic 0.1% proof-stress. For the final cycles, the maximum post-tensioning force was 241.6 kN. The angles reached a maximum displacement of about 22.5 mm, showing visible cracks (Figure 4.87). The equivalent viscous damping ratio reached was 14.0% for a drift ratio of 2%.

The last post-tensioned wall tested reached a maximum drift ratio of about 3.5%. This test had only the post-tensioning and the end of the test was determined by this. The post-tensioning strands had losses of 2% and 5% in the southern and northern strands, respectively for a drift ratio of 2%. These losses increased for higher levels of drift ratios as the strands went beyond the characteristic 0.1% proof-stress. The maximum post-tensioning force was 239.7 kN. This specimen had no energy dissipation, so the equivalent viscous damping ratio was similar for the different drift ratios and was between 2% and 3%.

To summarise, the three final wall specimens were considered to be the goal of this part of the study and their behaviour was as expected. Taking into account the design drift ratio of 2%, the behaviour was as expected, while for drift ratios higher than 2%, a problem emerged due to the reduced length of the strands, which caused losses in the post-tensioning forces. The steel angles responded well at the design drift ratio. Following the tests on the hybrid systems, the damage was concentrated in the steel angles, that would be easy to replace.

6.1.3 Case study

The comparison between the equivalent monolithic system and the precast hybrid system should only be carried out taking into account the fact that the hybrid system presents a negligible residual displacement and its rehabilitation can easily be done by replacing the energy dissipaters. This means that the hybrid system will always have the advantage of having a reduced or zero downtime after a major earthquake while the other solution would result in considerable damage.

The equivalent monolithic system has a higher damping than the precast hybrid system. This difference results in lower design forces than for the hybrid system. In the case study this was amplified due to the need to limit the displacement demand of the steel angles to values that were considered to be reasonable. This means that the design drift ratio considered for the equivalent monolithic system was higher than the one used for the hybrid system. The shear base force for the design of the equivalent monolithic system was 2499.8 kN whilst in the hybrid system it was 3895.2 kN.

In the case study, the angles were located to optimise the tensile forces lever arm, which means that they were near the edges of the wall. This location led to advantages and disadvantages. The lever arm was higher, leading to a higher bending moment due to the tensile force of each angle. The displacements were higher than they would have been if the angles were closer to the wall cross section centre. Higher displacements correspond to higher forces acting on the angles, but also to higher displacement demand that can be difficult to reach. For the example of this study, the displacement demand was within acceptable values for the chosen steel angle solution, but an experimental check on this parameter is recommended.

6.2 Future research recommendations

This research presented solutions using steel angles as energy dissipaters in post-tensioned hybrid walls. In the case study chapter some design parameters for the DDBD procedure were adapted from similar systems, however, to have better estimates for these parameters,

a more complete nonlinear numerical study should be carried out on 2D and 3D models. The displacement shape is a parameter where some doubts remain. For the hybrid system, the displacement shape was assumed equal to a monolithic system at the yield point and equal to a post-tensioned wall system beyond that point. This principle was considered appropriate but should be analysed in detail in future studies.

The prediction for the rupture point of the steel angle should also be investigated. A more complete numerical model should be developed to simultaneously consider cyclic actions and material strain limits. To this end more experimental studies could also be carried out taking into consideration different dimensions for the angles and low-cycle fatigue tests.

Different modes of failure of the steel angles are referred in the literature, although for the developed solutions a parametric study should be made, to evaluate, namely the influence of the thickness of the steel angles and the dimensions of the bolts on the location of the plastic hinge near the bolt holes.

In this study, the steel angles were tested applying a cyclic vertical displacement, although the used setup simplifies the actual demand to the angles when used in hybrid wall systems with rocking behaviour, which also includes rotations that can influence the angles response. These rotations should be included in future studies.

The use of the steel angles in wall systems showed that their use can be limited by their maximum displacement, so the use of steel angles in smaller cross sections, like columns, should be considered.

It is not usual to have post-tensioning with short strands, but systems that could go to high drift ratios using short length strands should be investigated. A possibility to be explored could be to have more flexible anchorages that would deform for force increments in a way that the elongation of the strands would remain within reasonable values.

The cyclic protocol used in this research gives a good perception of the system behaviour when a horizontal displacement is applied, but to evaluate the seismic behaviour a test program using a shaking table should be carried out. The ideal next step would be to have a small scale building tested with a shaking table.

Bibliography

[1] ACI-T1.2-03 (2003). *Special Hybrid Moment Frames Composed of Discretely Jointed Precast and Post-Tensioned Concrete Members (ACI T1.2-03) and commentary (ACI T1.2R-03)*. American Concrete Institute.

[2] Alves, A. P. N. (2010). Durabilidade de argamassas poliméricas de agregados leves (in Portuguese). Master's thesis, FCT/UNL, Lisbon.

[3] Aslam, M., Scalise, D. T., and Godden, W. G. (1980). Earthquake rocking response of rigid bodies. *Journal of the Structural Division*, 106(2):377–392.

[4] Astaneh, A., Nader, M. N., and Malik, L. (1989). Cyclic behavior of double angle connections. *Journal of Structural Engineering*, 115(5):1101–1118.

[5] Bathe, K. J. (2010). *ADINA System*. ADINA R&D Inc.

[6] Belleri, A., Schoettler, M. J., Restrepo, J. I., and Fleischman, R. B. (2014). Dynamic behavior of rocking and hybrid cantilever walls in a precast concrete building. *ACI Structural Journal*, 111(1-6).

[7] Cattanach, A. and Pampanin, S. (2008). 21st century precast: the detailing and manufacture of NZ's first multi-storey presss-building. In *NZ Concrete Industry Conference*, Rotorua, New Zealand.

[8] Christopoulos, C., Filiatrault, A., and Folz, B. (2002a). Seismic response of self-centring hysteretic sdof systems. *Earthquake Engineering & Structural Dynamics*, 31(5):1131–1150.

[9] Christopoulos, C., Filiatrault, A., Uang, C., and Folz, B. (2002b). Posttensioned energy dissipating connections for moment-resisting steel frames. *Journal of Structural Engineering*, 128(9):1111–1120.

[10] Conley, J., Priestley, M., and Sritharan, S. (2002). Wall direction modeling of the five-story PRESSS precast test building. Technical Report SSRP - 99/19, University of California, San Diego, CA.

[11] Dolce, M., Masi, A., Cappa, T., Nigro, D., and Ferrini, M. (2003). Experimental evaluation of effectiveness of local strengthening on columns of r/c existing structures. In *Proceedings of fib-symposium concrete structures in earthquake regions*, Athens, Greece.

[12] Dolce, M., Moroni, C., Nigro, D., Ponzo, F., Santarsiero, G., Di Croce, M., De Canio, G., Ranieri, N., Caponero, M., Berardis, S., Goretti, A., Spina, D., Lamonaca, B., and Marnetto, R. (2006). Trema project: Experimental evaluation of the seismic performance of a r/c $\frac{1}{4}$ scaled model upgraded with the dis-cam system. In *2nd Fib Congress*, pages 5–8, Naples, Italy.

[13] Dywidag (2014). Dywidag ductile connectors. http://www.dsiamerica.com/products/reinforcing/dywidag-ductile-connector/advantages-and-characteristics.html. Accessed: 2014-06-23.

[14] El-Sheikh, M., Pessiki, S., Sause, R., and Lu, L. W. (2000). Moment rotation behavior of unbonded post-tensioned precast concrete beam-column connections. *ACI Structural Journal*, 97(1):122–131.

[15] ElGawady, M. A., Ma, Q. T., Butterworth, J. W., and Ingham, J. M. (2006). Effects of interface material on the dynamic behaviour of rigid blocks. In *19th Australasian Conference on the Mechanics of Structures and Materials*, Christchurch, New Zealand.

[16] EN 10002-1 (2001). *Metallic materials - Tensile testing - Part 1: Method of test at ambient temperature*. European Committee for Standardization, Brussels.

[17] EN 10025-2 (2004). *Hot rolled unalloyed structural steel products - Part 2: Technical delivery conditions for non-alloy structural steels*. European Committee for Standardization, Brussels.

[18] EN 1015-11 (1999). *Methods of test for mortar for masonry - Part 11: Determination of flexural and compressive strentgth of hardened mortar*. EN 1015-11:1999 / A1:2006. European Committee for Standardization, Brussels.

[19] EN 12390-1 (2000). *Testing hardened concrete - Part 1: Shape, dimensions and other requirements for specimens and moulds*. EN 12390-1:2000. European Committee for Standardization, Brussels.

[20] EN 12390-3 (2001). *Testing hardened concrete - Part 3: Compressive strength of test specimens*. EN 12390-3:2001. European Committee for Standardization, Brussels.

[21] EN 1991-1-1 (2002). *Eurocode 1: Actions on structures - Part 1-1: General actions - Densities, self-weight, imposed loads for buildings*. European Committee for Standardization, Brussels.

[22] EN 1992-1-1 (2004). *Eurocode 2: Design of concrete structures - Part 1-1: General rules and rules for buildings*. European Committee for Standardization, Brussels.

[23] EN 1993-1-1 (2005). *Eurocode 3: Design of steel structures - Part 1-1: General rules and rules for buildings*. European Committee for Standardization, Brussels.

[24] EN 1993-1-8 (2005). *Eurocode 3: Design of steel structures - Part 1-8: Design of joints*. European Committee for Standardization, Brussels.

[25] EN 1998-1 (2004). *Eurocode 8: Design of structures for earthquake resistance - Part 1: General rules, seismic actions and rules for buildings*. European Committee for Standardization, Brussels.

[26] Englekirk, R. E. (2002). Design-construction of the paramount - a 39-story precast prestressed concrete apartment building. *PCI JOURNAL*, 47(4):56–71.

[27] FEMA-273 (1997). *NEHRP Guidelines for the Seismic Rehabilitation of Buildings*. Building Seismic Safety Council, Washington, D.C.

[28] fib (2003). *Seismic design of precast concrete building structures*. Bulletin 27. Lausanne.

[29] Garlock, M. M., Ricles, J. M., and Sause, R. (2003). Cyclic load tests and analysis of bolted top-and-seat angle connections. *Journal of Structural Engineering*, 129(12):1615–1625.

[30] Garlock, M. M., Ricles, J. M., and Sause, R. (2005). Experimental studies of full-scale posttensioned steel connections. *Journal of Structural Engineering-Asce*, 131(3):438–448.

[31] Garlock, M. M., Sause, R., and Ricles, J. M. (2007). Behavior and design of posttensioned steel frame systems. *Journal of Structural Engineering-Asce*, 133(3):389–399.

[32] Holden, T., Restrepo, J., and Mander, J. B. (2003). Seismic performance of precast reinforced and prestressed concrete walls. *Journal of Structural Engineering*, 129(3):286–296.

[33] Holden, T. J., Restrepo, J., and Mander, J. B. (2001). A comparison of the seismic performance of precast wall construction: Emulation and hybrid approaches. Technical Report 2001-4, Department of Civil Engineering, University of Canterbury, Christchurch, New Zealand.

[34] Hose, Y. D. and Seible, F. (1999). Performance evaluation database for concrete bridge components and systems under simulated seismic loads. Technical Report PEER 1999/11, Pacific Earthquake Engineering Research Center.

[35] Housner, G. W. (1963). The behavior of inverted pendulum structures during earthquakes. *Bulletin of the Seismological Society of America*, 53(2):403–417.

[36] IBC-2003 (2002). *2003 International Building Code*. International Code Council, Inc.

[37] Iqbal, A., Pampanin, S., and Buchanan, A. (2008). Seismic behaviour of prestressed timber columns under bi-directional loading. In *World Conference on Timber Engineering*, Miyazaki, Japan.

[38] Iqbal, A., Pampanin, S., and Buchanan, A. (2010). Seismic performance of prestressed timber beam-column sub-assemblies. In *New Zealand Society for Earthquake Engineering (NZSEE) Conference*, Wellington, New Zealand.

[39] Iqbal, A., Pampanin, S., Buchanan, A., and Palermo, A. (2007). Improved seismic performance of LVL post-tensioned walls coupled with UFP devices. In *8th Pacific Conference on Earthquake Engineering*, Singapore.

[40] König, G., Nguyen, T., and Ahner, C. (1997). *Consistent safety format*. Bulletin nº239. CEB, Lausanne.

[41] Kurama, Y. (1997). *Seismic Analysis, Behavior, and Design of Unbonded Post-Tensioned Precast Concrete Walls*. PhD thesis, Lehigh University, Bethlehem, PA, Bethlehem, PA.

[42] Kurama, Y. C. and Shen, Q. (2004). Posttensioned hybrid coupled walls under lateral loads. *Journal of Structural Engineering-Asce*, 130(2):297–309.

[43] Kurama, Y. C., Weldon, B. D., and Shen, Q. (2006). Experimental evaluation of posttensioned hybrid coupled wall subassemblages. *Journal of Structural Engineering*, 132(7):1017–1029.

[44] Lin, Y., Sause, R., and Ricles, J. (2013). Seismic performance of steel self-centering, moment-resisting frame: Hybrid simulations under design basis earthquake. *Journal of Structural Engineering*, 139(11):1823–1832.

[45] Ma, Q. T. M. (2010). *The mechanics of rocking structures subjected to ground motion*. PhD thesis, The University of Auckland, Auckland, New Zealand.

[46] Mander, J. B., Priestley, M. J., and Park, R. (1988). Theoretical stress-strain model for confined concrete. *Journal of Structural Engineering*, 114(8):1804–1826.

[47] Marriott, D. (2009). *The Development of High-Performance Post-Tensioned Rocking Systems for the Seismic Design of Structures*. PhD thesis, University of Canterbury, Christchurch, New Zealand.

[48] Marriott, D., Pampanin, S., Bull, D., and Palermo, A. (2008). Dynamic testing of precast, post-tensioned rocking wall systems with alternative dissipating solutions. *Bulletin of New Zealand Society for Earthquake Engineering*, 41(2):90–103.

[49] Martins, E. F. B. (2010). Estudo dos efeitos da composição e das dimensões no comportamento mecânico das argamassas poliméricas de agregados leves (in Portuguese). Master's thesis, FCT/UNL, Lisbon.

[50] Nader, M. N. and Astaneh-Asl, A. (1991). Dynamic behavior of flexible, semirigid and rigid steel frames. *Journal of Constructional Steel Research*, 18(3):179–192.

[51] Nader, M. N. and Astaneh-Asl, A. (1996). Shaking table tests of rigid, semirigid, and flexible steel frames. *Journal of Structural Engineering-Asce*, 122(6):589–596.

[52] Nakaki, S. D., Stanton, J. F., and Sritharan, S. (1999). An overview of the presss five-story precast test building. *PCI JOURNAL*, 44(2):26–39.

[53] NZCS (2010). *PRESSS Design Handbook*. Wellington, New Zealand.

[54] NZS3101 (2006). *Concrete Structures Standard: Part 1-The Design of Concrete Structures*. Standards New Zealand, Wellington.

[55] Ogawa, N. (1977). A study on rocking and overturning of rectangular column. Technical Report 18, National Research Center for Disaster Prevention, Japan.

[56] Palermo, A. (2004). *The Use of Controlled Rocking in the Seismic Design of Bridges*. PhD thesis, Technical University of Milan, Milan, Italy.

[57] Palermo, A., Pampanin, S., and Buchanan, A. (2006a). Experimental investigations on LVL seismic resistant wall and frame subassemblies. In *First European Conference on Earthquake Engineering and Seismology*, Geneva, Switzerland.

[58] Palermo, A., Pampanin, S., Buchanan, A., and Newcombe, M. (2005). Seismic design of multi-storey buildings using laminated veneer lumber (LVL). In *New Zealand Society for Earthquake Engineering (NZSEE) Conference*, Wairakei, New Zealand.

[59] Palermo, A., Pampanin, S., Fragiacomo, M., Buchanan, A. H., Deam, B. L., and Pasticier, L. (2006b). Quasi-static cyclic tests on seismic-resistant beam-to-column and column-to-foundation subassemblies using laminated veneer lumber (LVL). In *19th Australasian Conference on Mechanics of Structures and Materials*.

[60] Palmieri, L., Saqan, E., French, C., and Kreger, M. (1996). Ductile connections for precast concrete frame systems. *ACI Special Publication*, 162:313–356.

[61] Pampanin, S., Priestley, M. J. N., and Sritharan, S. (2001). Analytical modelling of the seismic behaviour of precast concrete frames designed with ductile connections. *Journal of Earthquake Engineering*, 5(3):329–367.

[62] Paulay, T. and Priestley, M. (1992). *Seismic design of reinforced concrete and masonry structures*. J. Wiley & Sons, Inc: New York.

[63] Peña, F., Prieto, F., Lourenço, P. B., Campos Costa, A., and Lemos, J. V. (2007). On the dynamics of rocking motion of single rigid-block structures. *Earthquake Engineering & Structural Dynamics*, 36(15):2383–2399.

[64] Perez, F. J. (2004). *Experimental and Analytical Lateral Load Response of Unbonded Post-Tensioned Precast Concrete Walls*. PhD thesis, Lehigh University, Bethlehem, PA, Bethlehem, PA.

[65] Popovics, S. (1973). A numerical approach to the complete stress-strain curve of concrete. *Cement and concrete research*, 3(5):583–599.

[66] prEN 10138-3 (2004). *Prestressing steels - Part 3: Strand*. European Committee for Standardization, Brussels.

[67] Priestley, M. (1998). Displacement-based approaches to rational limit states design of new structures. In *Closing Lecture Eleventh European Conference on Earthquake Engineering*, Paris.

[68] Priestley, M. (2003). *Myths and fallacies in earthquake engineering revisited, mallet milne lecture*. IUSS Press, Pavia, Italy.

[69] Priestley, M., Calvi, M., and Kowalsky, M. (2007). *Displacement-Based Seismic Design of Structures*. IUSS Press, Pavia.

[70] Priestley, M., Evison, R., and Carr, A. (1978). Seismic response of structures free to rock on their foundations. *Bulletin of the New Zealand National Society for Earthquake Engineering*, 11(3):141–150.

[71] Priestley, M. and Tao, J. (1993). Seismic response of precast prestressed concrete frames with partially debonded tendons. *PCI JOURNAL*, 38(1):58–69.

[72] Priestley, M. J. N. (1996). The presss program - current status and proposed plans for phase III. *PCI JOURNAL*, 41(2):22–40.

[73] Priestley, M. J. N. (2002). Direct displacement-based design of precast/prestressed concrete buildings. *PCI JOURNAL*, 47(6):66–79.

[74] Priestley, M. J. N. and MacRae, G. A. (1996). Seismic tests of precast beam-to-column joint subassemblages with unbonded tendons. *PCI JOURNAL*, 41(1):64–81.

[75] Priestley, M. J. N., Sritharan, S., Conley, J. R., and Pampanin, S. (1999). Preliminary results and conclusions from the presss five-story precast concrete test building. *PCI JOURNAL*, 44(6):42–67.

[76] Priestley, M. N. (1993). Myths and fallacies in earthquake engineering - conflicts between design and reality. *Bulletin of the New Zealand National Society for Earthquake Engineering*, 26(3):329–341.

[77] Priestley, M. N., Seible, F., and Calvi, G. M. (1996). *Seismic design and retrofit of bridges*. John Wiley & Sons, Inc, New York.

[78] Restrepo, J. I., Mander, J. B., and Holden, T. J. (2001). New generation of structural systems for earthquake resistance. In *New Zealand Society for Earthquake Engineering 2001 Conference*, Wairakei, New Zealand. NZSEE.

[79] Restrepo, J. I. and Rahman, A. (2007). Seismic performance of self-centering structural walls incorporating energy dissipators. *Journal of Structural Engineering*, 133(11):1560–1570.

[80] Richart, F. E., Brandtzaeg, A., and Brown, R. L. (1928). A study of the failure of concrete under combined compressive stresses. *University of Illinois Engineering Experiment Station Bulletin*, 185.

[81] Ricles, J. M., Sause, R., Garlock, M. M., and Zhao, C. (2001). Posttensioned seismic-resistant connections for steel frames. *Journal of Structural Engineering-Asce*, 127(2):113–121.

[82] Ricles, J. M., Sause, R., Peng, S. W., and Lu, L. W. (2002). Experimental evaluation of earthquake resistant posttensioned steel connections. *Journal of Structural Engineering*, 128(7):850–859.

[83] Rojas, P., Ricles, J., and Sause, R. (2005). Seismic performance of post-tensioned steel moment resisting frames with friction devices. *Journal of Structural Engineering*, 131(4):529–540.

[84] Schoettler, M. J., Belleri, A., Zhang, D. C., Restrepo, J. I., and Fleischman, R. B. (2009). Preliminary results of the shake-table testing for the development of a diaphragm seismic design methodology. *PCI JOURNAL*, 54(1):100–124.

[85] Schultz, A. E., Tadros, M. K., Huo, X. M., and Magana, R. A. (1994). Seismic resistance of vertical joints in precast shear walls. In (FIP), F. I. d. l. P., editor, *Proceedings of the 12th Congress*, volume Volume 1, pages E25–E27, Washington, DC.

[86] Scott, B., Park, R., and Priestley, M. (1982). Stress-strain behavior of concrete confined by overlapping hoops at low and high strain rates. In *ACI Journal Proceedings*, volume 79. ACI.

[87] Shen, J. and Astaneh-Asl, A. (1999). Hysteretic behavior of bolted-angle connections. *Journal of Constructional Steel Research*, 51(3):201–218.

[88] Shen, J. and Astaneh-Asl, A. (2000). Hysteresis model of bolted-angle connections. *Journal of Constructional Steel Research*, 54(3):317–343.

[89] Shen, Q. (2006). *Seismic analysis, behavior, and design of unbonded post-tensioned hybrid coupled wall structures.* PhD thesis, University of Notre Dame, Notre Dame, IN.

[90] Shen, Q. and Kurama, Y. C. (2002). Nonlinear behavior of posttensioned hybrid coupled wall subassemblages. *Journal of Structural Engineering-Asce*, 128(10):1290–1300.

[91] Smith, B. (2012). *Design, Analysis, and Experimental Evaluation of Hybrid Precast Concrete Shear Walls for Seismic Regions*. PhD thesis, University of Notre Dame, Notre Dame, Indiana.

[92] Smith, T., Auletta, G., Carlo, F., Ponzo, F., Pampanin, S., Carradine, D., Palermo, A., and Nigro, D. (2012). Seismic performance of a post-tensioned glue laminated beam to column joint: Experimental and numerical results. In *12th World Conference on Timber Engineering*.

[93] Smith, T., Ludwig, F., Pampanin, S., Fragiacomo, M., Buchanan, A., Deam, B., and Palermo, A. (2007). Seismic response of hybrid-LVL coupled walls under quasi-static and pseudo-dynamic testing. In *New Zealand Society for Earthquake Engineering Conference*.

[94] Smith, T., Pampanin, S., Carradine, D., Buchanan, A., Ponzo, F., Cesare, A., and Nigro, D. (2011). Experimental investigations into post-tensioned timber frames with advanced damping systems. In *Il XIV Convegno di Ingegneria Sismica*. Associazione Nazionale di Ingegneria Sismica.

[95] Smith, T., Ponzo, F. C., Di Cesare, A., Pampanin, S., Carradine, D., Buchanan, A. H., and Nigro, D. (2014). Post-tensioned glulam beam-column joints with advanced damping systems: Testing and numerical analysis. *Journal of Earthquake Engineering*, 18(1):147–167.

[96] Sousa, H. A. M. (2010). Comportamento às acções cíclicas de argamassas poliméricas com agregados leves (in Portuguese). Master's thesis, FCT/UNL, Lisbon.

[97] Stanton, J., Stone, W. C., and Cheok, G. S. (1997). A hybrid reinforced precast frame for seismic regions. *PCI JOURNAL*, 42(2):20–32.

[98] Wang, Y. C. and Restrepo, J. I. (2001). Investigation of concentrically loaded reinforced concrete columns confined with glass fiber-reinforced polymer jackets. *ACI Structural Journal*, 98(3).

[99] Weldon, B. D. and Kurama, Y. C. (2007). Nonlinear behavior of precast concrete coupling beams under lateral loads. *Journal of Structural Engineering-Asce*, 133(11):1571–1581.

[100] Weldon, B. D. and Kurama, Y. C. (2010). Experimental evaluation of posttensioned precast concrete coupling beams. *Journal of Structural Engineering-Asce*, 136(9):1066–1077.

[101] Wikipedia (2013). The paramount, san francisco. http://en.wikipedia.org/wiki/The_Paramount,_San_Francisco. Accessed: 2014-03-31.

[102] Yang, B. and Tan, K. (2013a). Robustness of bolted-angle connections against progressive collapse: Experimental tests of beam-column joints and development of component-based models. *Journal of Structural Engineering*, 139(9):1498–1514.

[103] Yang, B. and Tan, K. H. (2013b). Robustness of bolted-angle connections against progressive collapse: Mechanical modelling of bolted-angle connections under tension. *Engineering Structures*, 57(0):153–168.